

**Synthesis, Characterization and metal ion sensing applications
of certain Schiff bases**

Thesis submitted to Bharathidasan University

For the award of the degree of

DOCTOR OF PHILOSOPHY

in

CHEMISTRY

By

P.VIJAYAKUMAR, M.Sc., M.Phil.

(Reg. No. 5451)

Research Supervisor

Prof. R.RENGANATHAN, Ph.D.,

UGC-Emeritus Fellow (Retd.)



**School of Chemistry
Bharathidasan University
Tiruchirappalli - 620 024
Tamilnadu, India**

May 2022



School of Chemistry, Bharathidasan University
Tiruchirappalli 620 024
Tamilnadu, India

Prof. R.RENGANATHAN
UGC-Emeritus Fellow (Retd.)

Date :

CERTIFICATE

This is to certify that the thesis entitled “**Synthesis, Characterization and metal ion sensing applications of certain Schiff bases**” is a bonafide work done by **P. VIJAYAKUMAR** (Reg. No. **5451**) under my guidance in the, School of Chemistry, Bharathidasan University, Tiruchirappalli – 620 024 and has not been included in any other thesis submitted previously for the award of any degree.

Dr. R. RENGANATHAN
(Research Supervisor)



School of Chemistry, Bharathidasan University
Tiruchirappalli 620 024
Tamilnadu, India

P.VIJAYAKUMAR

Doctoral Student

Date :

DECLARATION













I, hereby declare that the thesis entitled “**Synthesis, Characterization and metal ion sensing applications of certain Schiff bases**” is based on the original and independent research work done by me under the guidance **Dr. R. RENGANATHAN** Professor, School of Chemistry, Bharathidasan University, Tiruchirappalli – 620 024 and this work has not been submitted in a whole or in a part for any other degree or diploma to this or any other University.

(P. VIJAYAKUMAR)

Document Information

Analyzed document	P.VIJAYAKUMAR - Chemistry - Final Thesis.pdf (D138360298)
Submitted	2022-05-29T17:26:00.0000000
Submitted by	Dr.S.Vanitha
Submitter email	vanitha@bdu.ac.in
Similarity	6%
Analysis address	navitha.bdu@analysis.urkund.com

Sources included in the report

SA	Mohan sir thesis- Final - 11.5.21.pdf Document Mohan sir thesis- Final - 11.5.21.pdf (D111196430)	 6
SA	1517030003-S.doc Document 1517030003-S.doc (D60233947)	 21
SA	Phd Thesis compiled new.pdf Document Phd Thesis compiled new.pdf (D116640847)	 1
SA	Thesis Final-Mani doc 2003.doc Document Thesis Final-Mani doc 2003.doc (D22030816)	 1
SA	Janakipriya CLRI.pdf Document Janakipriya CLRI.pdf (D24193700)	 1
SA	Milan Shyamal PhD Chemistry 281217.pdf Document Milan Shyamal PhD Chemistry 281217.pdf (D34552876)	 3
SA	A Mangaleswari 16MCH202103 M.Phil Chemistry 2016-17.docx Document A Mangaleswari 16MCH202103 M.Phil Chemistry 2016-17.docx (D29822659)	 1
SA	W. Anbu Duari Ph.D Chemistry Thesis.docx Document W. Anbu Duari Ph.D Chemistry Thesis.docx (D63511881)	 2
SA	Rukmani Final.pdf Document Rukmani Final.pdf (D46746499)	 3
SA	1217030009-S.doc Document 1217030009-S.doc (D32510088)	 7
SA	D. DIVYA.pdf Document D. DIVYA.pdf (D116621670)	 2
W	URL: https://link.springer.com/article/10.1007/s10895-021-02722-3 Fetched: 2021-08-17T18:57:24.3530000	 1

ACKNOWLEDGEMENT

First of all, I am very grateful to the God Almighty for without his graces and blessing complete my research periods would not have been possible.

*I sincerely heart full thanks to my guide **Prof. R. Renganathan**, UGC-Emeritus Fellow (Retd.), school of chemistry, Bharathidasan University, Tiruchirappalli, for his guidance and continuous encouragement throughout my during research period. I am always grateful to my guide for his inspiration, patience and care.*

*I would like to convey sincere thanks to my Former doctoral committee members and Present Doctoral committee members; **Dr. P. Thomas Muthiah**, UGC-Emeritus Professor (Retd.), **Dr. S. Arunachalam** (Retd.), **Dr.R.Ramesh**, Professor and Chair, Coordinator, Centre for Organometallic Chemistry (COMC) and **Dr. L. Nagarajan**, UGC-Assistant Professor, School of Chemistry, for their active support and motivation, encouragements, valuable suggestion during the research periods.*

*I express my heartfelt thanks to **Prof. S. Muthusamy**, (Head of the School of Chemistry), Bharathidasan University to gave permission to use the common facilities for research work.*

*I owe my special thanks to **Dr. M. Palaniandavar**, Eminent Professor, **Dr. P. Venuvanalingam** Professor (Retd), **Dr. A. Ilangovan**, Professor and Dean of faculty Science Engineering and Technology, **Dr. K. Srinivasan**, Associate Professor, (Late) **Dr. R.Pothiraja** UGC-Assistant Professor, **Dr. V. Thiyagarajan** UGC-Assistant Professor, School of Chemistry, Bharathidasan University, Tiruchirappalli for their valuable suggestions and discussions.*

I take this opportunity to thank the non-teaching staffs of the school for their assistance throughout my research period.

*I like to express my sincere thanks to **Dr. G. Chandramohan**, Associate Professor (Retd) and **Dr. V. Thirumurugan**, Associate Professor, PG and M.Phil. teacher, AVVM Sri Pushpam college Poondi, Thanjavur, for his valuable advice, constant encouragement and motivation.*

*I wish to express my sincere thanks to my senior **Dr. G. Paramaguru**, and **Dr. S. Jagadeeswari**, School of Chemistry, Bharathidasan University, for their valuable,*

suggestions and discussions during my research periods. I am sincerely grateful to him for spending his precious times in assisting the synthetic and instrument methods and sharing his truthful and illuminating views on a number of issues related to my thesis work.

*I would like to thank my collaborators **Dr. P. Venuvanalingam**, Professor (Retd), **Dr. A. Ilangovan** Professor and Dean of faculty science Engineering and Technology, **Dr. M. Arockia Doss** Assistant Professor, St. Joseph University, Nagaland.*

*I am greatly indebted to my seniors **Dr. Kandavelu**, **Dr. P. Raja**, **Dr. V. Anbazhagan**, **Dr. A. Kathiravan**, **Dr. Aashajhonsi**, **Dr. C. Manivannan**, **Dr. E. Vaishnavi**, **Dr. N. Nagarajan**, **Dr. S. Sambathkumar**, **Dr. E. Kavery** and Colleagues **Dr. S. Muruganantham**, **Dr. S. Tamilmani** and my junior **Mr. G. Prabhu** for their voluntary help during my research work.*

*It is also a pleasure to my mention my M.Sc., project student, **Mrs. S. Gunavathi** for their timely support during their project period.*

*I am especially grateful to **UGC RFSMS-BSR Fellowship** University Grants Commission, New Delhi for granting me financial assistance during my Ph.D. University Grants commission (UGC) and DST, New Delhi are gratefully acknowledged for funding to generate Instruments facilities in our school through Special Assistance Program (SAP) and Fund for Improvement of S & T Infrastructure (FIST) programs respectively.*

*It is significant to express my thanks to **Mr. Nawab Jan - Sheerin Banu** (Nurse) family, **Rev. Antoniraj** family, **Dr. N. Jeeva Jasmine Abel** family, **Dr. S. Angeline vedha - Er. Annadurai** family, **Dr. Y. Manojkumar - Dr. S. Ambika** family, **Dr. R. Vijay Solomon** family, **Dr. G. Vignesh** family and all relatives for their love and affection forever.*

*I would like to heartfelt my thankful to my lovable father **R. P. Pakkiri**, mother **P. Radha**, beloved helder brother **Dr. P. Ramesh-Jasmine Senthamizh Selvi** (Nurse), and beloved helder sister **Mrs. P. Mahalakshmi-Muthu**, and our family kutties **R. Jesnith Hansigan**, **M. Pavendan**, **M. Gurunath**, who has been so caring and supportive to me all the time. They have aided and encouraged me throughout this course period. I warmly appreciate the generosity and understanding of my family. My family has aided and encouraged me throughout this endeavour.*

- P. Vijaykumar

CONTENTS

Page No.

CHAPTER - I

Introduction	1 - 31
1.1. Sensors	1
1.1.1. Chemosensors	2
1.1.2. Advantage of fluorescent chemosensor	5
1.2. Mechanism of fluorescent chemosensor	6
1.2.1. Photo-induced electron transfer (PET)	8
1.2.2. Chelation enhancement of fluorescence (CHEF)	9
1.2.3. Photo-Induced (or) Intramolecular Charge Transfer (PCT/ICT)	10
1.2.4. Paramagnetic Fluorescence Quenching Mechanism	10
1.2.5. Fluorescence Resonance Energy Transfer (FRET)	11
1.2.6. Excited –State Intramolecular Proton Transfer (ESIPT)	12
1.2.7. Exciplex/Excimer Formation	13
1.3. Aggregation-induced Emission (AIE)	14
1.4. Schiff bases	14
1.4.1. Photophysical properties of schiff bases	16
1.4.2. Schiff based fluorescent chemosensor	17
1.5. Sensing Metal ions	18
1.5.1. Detection of chromium ions (Cr^{3+})	19
1.5.2. Detection of Lead ion (Pb^{2+})	20
1.5.3. Detection of Aluminum ion (Al^{3+})	21
1.5.4. Detection of Zinc ion (Zn^{2+})	22
1.5.5. Detection of Nickel ion (Ni^{2+})	22
1.5.6. Detection of Ferric ion (Fe^{3+})	23
1.6. Anticancer activity, Cell viability assay	23
1.7. A Brief Review of Literature	24
1.8. Aim and Scope	27
1.9. References	28

CHAPTER – II

Novel Schiff base Synthesis of E-N-(1-(1H-phenothiazin-2yl)-ethylidene)-3-((E)-(2-phenylhydrazono) methyl) aniline “Turn-on” fluorescent chemosensor for sensitivity and selectivity of detection of Cr³⁺ and Pb²⁺	32 - 57
2.1 Introduction	32
2.2 Experimental Section	34
2.2.1 Materials and Instruments	34
2.2.2 Synthesis of Schiff base AT	34
2.2.3 UV-vis and fluorescence experimentation	35
2.2.4. Cell Culture	35
2.2.5. Anticancer activity, Cell viability assay	35
2.2.6. Fluorescence microscopic study	36
2.3 Results and Discussion	36
2.3.1. Absorption studies	40
2.3.2. Emission studies	41
2.3.3. Binding mechanism	44
2.3.4. Effect of pH	45
2.3.5. Reversibility study	46
2.3.6. Theoretical studies	47
2.3.6.1. HOMO and LUMO analysis	47
2.3.6.2. Molecular electrostatic potential (MEP) and Mulliken charge	48
2.3.6.3. Cytotoxicity	49
2.3.6.4. Living cell imaging	51
2.4 Conclusions	52
2.5 References	53

CHAPTER – III

Novel, Synthesis of E-4-((1-(10H-phenothiazin-2-yl)ethylidene)amino)-N-(pyrimidin-2-yl)benzenesulfonamide fluorescent chemosensor for high sensitivity and selectivity of Al³⁺ ion. 58 - 88

3.1.	Introduction	58
3.2.	Experimental Section	60
3.2.1.	Materials and instruments	60
3.2.2.	Synthesis of Schiff base derivative BT	60
3.2.3.	UV-vis and fluorescence experimentation	63
3.2.4.	Cell culture	63
3.2.5.	Anticancer activity and Cell viability assay	64
3.2.6.	Fluorescence microscopic study	64
3.2.7.	Theoretical studies	65
3.3.	Results and discussion	65
3.3.1.	Absorption studies	66
3.3.2.	Fluorescence studies	68
3.3.3.	Binding mechanism	72
3.3.4.	Competitive metal ion studies	74
3.3.5.	Reversibility	75
3.3.6.	Cytotoxicity activity	76
3.3.7.	Cell Imaging	78
3.3.8.	Theoretical studies	79
3.3.8.1.	HOMO and LUMO analysis	79
3.3.8.2.	Molecular electrostatic potential (MEP) analysis	81
3.3.8.3.	Mulliken charge distribution analysis	82
3.3.9.	NLO effects	83
3.4.	Conclusions	84
3.5.	Reference	85

CHAPTER – IV

Synthesis of Schiff base of (Z)-4-methyl-N'-(phenyl(2-(4-substituted)-1H-benzo[d]imidazol-6-yl)methylene)benzenesulfonohydrazide and their role as chemosensor for Zn²⁺ and Al³⁺ 89 - 129

4.1.	Introduction	89
4.2.	Experimental Section	92
4.2.1.	Spectral analysis of compounds A1 & A2	92
4.2.2.	FT-IR spectral analysis of compounds A1 and A2	97
4.2.3.	¹ H NMR spectral analysis of compounds A1 and A2	98
4.2.4.	¹³ C NMR spectral analysis of A1 and A2	98
4.2.5.	ESI Mass spectra	99
4.3.	Results and Discussion	99
4.3.1.	Absorption studies	99
4.3.2.	Fluorescence studies	102
4.3.3.	Job's plot studies and reversibility	107
4.3.4.	Computational analysis	113
4.3.4.1.	Geometry Optimization	113
4.3.4.2.	Nonlinear optical properties	116
4.3.4.3.	HOMO-LUMO analysis	117
4.3.4.4.	Molecular electrostatic potential	119
4.3.4.5.	Mulliken atomic charge analysis	119
4.3.4.6.	Docking analysis of A1 and A2	121
4.3.4.7.	Cytotoxicity evaluation	122
4.4.	Conclusions	125
4.5.	References	126

CHAPTER – V

Novel Dual Chemosensor for Fe³⁺/ Ni²⁺ ions and its Multi Applications	130 - 162
5.1. Introduction	130
5.2. Experimental Section	131
5.2.1. Synthesis of the compound A3	132
5.2.2. Fluorescence	135
5.2.3. Cell culture	135
5.2.4. Assay for cell viability	135
5.2.5. Cell Imaging Study	136
5.2.6. Computational details	136
5.3. Results and Discussion	136
5.3.1. A3 colorimetric and fluorometric reactions to Fe ³⁺ and Ni ²⁺ ions	137
5.3.2. Metal complexes of A3-EDTA Na ₂ to the Fe ³⁺ and Ni ²⁺ ions	141
5.3.3. The pH range of A3 and A3-Fe ³⁺ & A3-Ni ²⁺ ions	143
5.3.4. FE-SEM of complex A3-Fe ³⁺ and A3-Ni ²⁺	145
5.3.5. Cytotoxicity	149
5.3.6. Living cell imaging	151
5.3.7. Computational Analysis	154
5.3.7.1. Mulliken charge analysis	154
5.3.7.2. Molecular Electrostatic Potential of A3	155
5.3.7.3. FMO analysis of A3	156
5.3.8. NLO activity	157
5.4. Conclusions	159
5.5. References	160

Summary

163 - 166

List of Publications

ABBREVIATIONS

CH ₃ CH ₂ OH	:	Ethanol
Cm	:	Centimeter
DMSO d ₆	:	Deuterated dimethylsulfoxide
EDTA	:	Ethylene diamine tetra acetic acid, disodium salt
Equiv	:	Equivalent
g	:	Gram
h	:	Hour
TLC	:	Thin Layer chromatography
H ₂ O	:	Water
MTT	:	Microculture Tetrazolium Test
HEPES	:	4-(2-Hydroxyethyl)-1-piperazineethanesulfonic acid
DMEM	:	Dulbecco's modified eagle medium
FBS	:	Fetal bovine serum
CYGD	:	The comprehensive Yeast Genome Database
NMR	:	Nuclear magnetic resonance spectroscopy
MHz	:	Megahertz
<i>J</i>	:	Coupling constant
FT-IR	:	Fourier transformed infra-red
KBr	:	Pottasium bromide
M	:	Molar
ml	:	Millilitre
Mg	:	Milligram
mol	:	Mole
mmole	:	Millimole

m.p	:	Melting point
pH	:	Power of hydrogen/ hydronium ion
ppm	:	Parts per million
μM	:	Micromolar
UV-vis	:	Ultra violet- visible
w/v	:	Weight by volume
v/v	:	Volume by volume
PL/FL	:	Photoluminence/ Fluorescence
PET	:	Photo induced electron transfer
Aq	:	Aqueous
DFT	:	Density functional theory
ESI-MS	:	Electrospray ionisation mass spectroscopy
r.t	:	Room temperature
LOD	:	Limit of detection
WHO	:	World health organization
λ_{ex}	:	Excitation wavelength
λ_{emi}	:	Emission wavelength
HOMO	:	Highest occupied molecular orbital
LUMO	:	Lowest occupied molecular orbital

INTRODUCTION

1.1 Sensors

A sensor is a device, module or a machine that can detect and respond to certain types of inputs from its physical environment. The specific environmental inputs are for example light, motion, heat, humidity, pressure, etc., The output is a signal, which is transferred to a readable data display at the sensor location (or) electronically sent over the network for reading and further processing.[1] The sensor produces an electrical signal/optical signal using multiple technologies proportional to the inputs. These signals are either interpreted into a readable format or passed on to the next stage for further processing. Sensors are broadly grouped into analog and digital sensors. Analog sensors measure physical variables status whereas digital the exact value. Sensors make human life significantly more accessible and better in almost every field. At present different variety of sensors are accessible (**Fig-1**) that are temperature, ultrasonic, proximity, light, pressure, smoke, infra-red, accelerometer, alcohol, gas, etc. The best example of a sensor is a mercury-based glass thermometer which measures the temperature of the environment (temperature input), oxygen sensor in automobiles is used as emission control which measures the oxygen level in the exhaust gases. Nowadays a variety of motion sensors are available including automatic doors, entryway lighting, hand dryers, automatic ticket gates, home security lights, bathroom fixtures, etc., which all emit certain types of energy, such as microwaves, ultrasonic waves, or light beams, and detect when the flow of energy is interrupted by something entering its path. Likewise, a photosensor is the sensor of light as well as other magnetic radiations of infrared transmission (IR), ultraviolet, and visible light (UV) energy. [2]

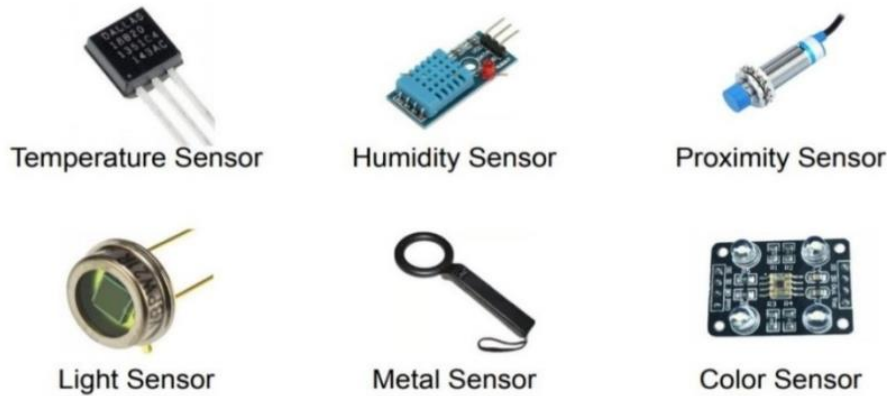


Figure-1: Different types of Sensors

Researchers and experts classify the sensors into active and passive types. The active sensor needs an external trigger/ signal/ power signal to work, on the other hand, passive sensors require no external power to generate the output response. Sensors are integrated into independent devices, conventional products, or machines for smart use. This allows one to measure the amount of noise in a particular system. In smart city solutions, acoustic sensor systems can detect and deliver data to avoid noise pollution. The most common use of sensors can be conceived as a smart building system. The technology can continuously monitor and record physiological and external data as uniquely as sensor technology. Temperature sensors can be used in almost all systems, probably the most adaptive smart sensor. These can monitor, measure, and alert an operator or emergency shutdown system to the temperature of an engine in an industrial environment. This technology can measure and monitor blood flow during various medical procedures, monitor heat losses of buildings and structures, and many more.

1.1.1 Chemosensors

Several types of sensors are described such as pH sensors, metal cation sensors, anion sensors, small-molecule sensors, nucleic acid sensors, protein sensors, cellular sensors. All the sensors are categorized into chemical sensors, biosensors, biological sensors, chemosensors, intrinsic fluorescence probes, conjugate fluorescence probes.

Chemical sensors are the macro (or) microdevices that signal the reversible interaction of the chemical analyte with signal transduction. [3,4] Biological sensors are the macro (or) microdevice that detects the reversible interaction of the biological analyte with signal transduction. Biosensors are molecules from a biotic origin that can signal the presence of energy or matter. Like that chemosensor is the molecule from the abiotic origin which can signal in the presence of energy or matter. A chemosensor is a molecular system of sensory receptors which can accurately interact with the analyte and send the information (interaction and physiochemical changes data) by generating signals. It is also known as a chemoreceptor or molecular sensor which detects certain chemical stimuli in the environment or other hand it's a cell or group of cells that transduce a chemical signal into an action potential. The working action of the chemosensor is depends on the interaction at the molecular level which continuously monitors the interaction of chemical species in given matrix-like blood, solution, tissue, air, drinking water, waste effluent, etc. Usually, all chemosensor designs consist of signaling moiety and recognition group which is connected directly by each other (or) through spacer/connector. Optically based electromagnetic radiation signaling is produced which was raised by changing the UV-Visible emission or absorption behavior of the sensors. Chemosensors are electrochemically based small molecule sensors which are considered analytical devices. It is structurally simple molecules and is a synthetic analog of biosensors. Mostly these molecules are from a synthetic origin that signals the presence of matter or energy. [5] All the chemosensors are sensory receptors that will specifically interact with the analyte (or) mixture of analytes and remit the information by producing detectable signals. Commonly, such chemosensor consists of recognition group as well as signaling moiety. Recognition groups responsible for the efficiency and selectivity of binding and signaling moiety convert the information (data) into detectable signals.

The new and well-organized chemosensors should interact with the targeted analyte in the presence of the co-existing analyte, exhibits the results in an analytical form that can be quantitative and qualitative, should be non-toxic in biological applications, and stable in the range of biological pH. Emissive chemosensor increased interest because of its high sensitive photophysical properties in the microenvironment. Optical signals provide detailed information on its local physical parameters such as rigidity and hydrophobicity, and chemical properties like concentration and pH of the analyte. The evolution of luminescent organometallic and inorganic transition–metal complexes chemosensors gets more attention owing to its long-lived and more intense photoluminescence with large stokes shift. The magnitude of emission energy of such chemosensors can also be controlled by using the numerous organic and inorganic ligands. Moreover, plenty of lanthanide chelates can be applied as the effective sensor that shows narrow emission bands resulting from the f-f transition. In everyday life, chemosensors are applied in numerous science areas such as physiology, biochemistry, chemistry, immunology, medicine, etc. Phenolphthalein is also a sensing device that can detect the concentration of hydrogen ions in the analyte. In addition, it is an abiotic molecule that can also sense the abiotic analyte. It acts as the simplest chemosensor, at sufficient concentration of OH^- ions.

Chemosensors are designed with recognition groups and signaling moiety to detect and signal the single or mixture of analytes in solution. Moreover, it can measure by single measurement or by continuous monitoring. Signaling moiety has been at the signal transducer which converts the information into readable optical response in a reproducible and clear manner. [6] Commonly, the signal is received by measuring several photophysical properties perceived in the emission or absorption when using the different wavelengths of the electromagnetic spectrum. Subsequently, chemosensors can be described as being any colorimetric (ground state) or luminescent (phosphorescent, fluorescent, excited state). Colorimetric chemosensor observes the changes in their absorption properties like

wavelength, absorption intensity (measured by UV-Visible spectroscopy), or chirality (measure by CD spectroscopy and circularly polarized light). In a luminescent chemosensor, the analyte is analyzed by using fluorescence spectroscopy (fluorescence emission or excitation spectra) (**Fig. 2**).

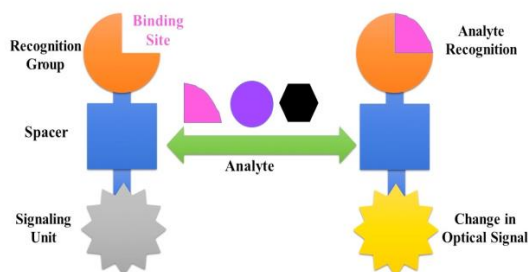


Figure-2: Working action of Chemosensor

1.1.2 Advantage of fluorescent chemosensor

For more than 150 years fluorescent chemosensor-based sensors are investigated by numerous researchers for the detection of environmentally and biologically important species like neutral, anion, and cation types of small molecules and also bio-macromolecules of DNA, proteins, etc. Moreover, analysis executes advanced microscopic imaging technology. In 1867 fluorescent chemosensor was first reported by scientist F. Goppelsroder and developed the method for determining the Al^{3+} ion (aluminum ions) by creating the strongly fluorescent morin chelate.[7] This drive to develop several fluorescent chemosensors which determine the metal ions, over the subsequent decades. In earlier fluorescent chemosensors mainly concentrated the detection of metal ions rather sensing of neutral or anion species which is due to the significant binding ability of metal ions in water being effortless than neutral or anion species. De Silva and Czarnik are the fathers of modern chemosensors (1980) who validated and witness the explosive growth of chemosensors.[8,9]

1.2. Mechanism of fluorescent chemosensor

In past decades the utmost important chemosensors are fluorescent chemosensors in which fluorometry techniques are used to analyze the chemical sensing probes. Nowadays Fluorescence-based sensors are a rapidly developing field in research and are getting more attention in recent days owing to their advantages of simple method, highly sensitive, more selective, very feasible, rapid response time, and have greater potential use in medicinal and environmental research.[10] Sensing multiple analytes using a single chemosensor is a challenging task because it elicits numerous responses by the molecules of different analytes. Such type of molecule should have multiple binding sites to give varied signal transducing units or different binding modes (fluorophores/chromophore/redox-active moiety), varied readout modes, or a combination of the above. Over the past few years, chemosensors with the selectivity of two analytes have significant importance than others. [11] A fluorescent chemosensor is such type of economically beneficial one that senses the two types of analytes. Two analyte molecular receptors are used for the structure of molecular logic gates where an emission output instead of differentiation of response by multiple analytes is important. Intrinsic fluorescence probes are the chemosensors in which the interaction of the analyte with the ligand of fluorophore signaled by signal transduction. Similarly, in conjugate fluorescence probes interaction of the analyte with the ligand of fluorophore π - system (electronically insulated). Signal transduction is the mechanism of interaction of the analyte with the sensor. There are so many mechanisms as well as reasons for choosing fluorescence as the optimal signal transduction. Fluorescence is a highly sensitive technique because it's observed longer wavelength than that of the exciting wavelength. Accordingly, it may read versus zero or near zero for appropriate fluorophores, hence fluorescence of even signal molecules can also be observed.[12] In a recent past investigation of new/advanced mechanism of interaction of signaling group and recognition,

group influences the development of new fluorescent chemosensors. Designing the well-organized and new fluorescent chemosensors is the challenging one practically. From the molecular level fundamental photophysical mechanism and supramolecular chemistry principle concept, chemist develops fluorescent chemosensors.

Fluorescent chemosensors measure the photophysical properties changes of intensity of fluorescence, emission spectra shifts, and molecule's decay life on interacting with an analyte of anion, neutral, or cation molecule via fluorescent modulation. To be successive fluorescent chemosensors, it would selectively bind with the desired analyte in presence of co-existing analytes, in the presence of dissolved oxygen it should be photo-stable, must possess intense fluorescence, less toxic, emission wavelength should exceed 500nm to reduce overlap with the autofluorescence emission of biological analytes/samples. Recognition based on some parameters like solubility of the medium, ionic strength, pH, and nature of the solvent (ability of hydrogen bonding, polarity, aprotic or protic solvents) because which all affects the photophysical character of fluorophore and shifts the fluorescence wavelength, selectivity and efficiency of the binding process. [13] The receptor and fluorophore units are attached in two ways and are described in **Fig. 3**. Firstly, a spacer is placed between the receptor and fluorophore which can avoid conjugations. In a second way, a fluorophore is directly attached with the receptor which has the π -electron of the fluorophore. Several types of signaling mechanisms are reported and are discussed below.

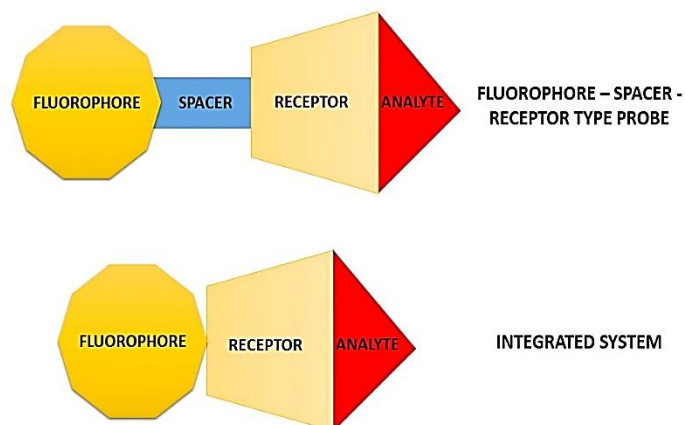


Figure-3: Schematic diagram of two ways of binding of receptor and fluorophore

1.2.1 Photo-induced electron transfer (PET)

PET is the simple process of electron (e^-) transfer mechanism which occurs when light interacts with the particular photoactive material. It is usually a fluorophore-spacer-receptor model which has the fluorophore site for both photonic transactions, receptor site for both the de-complexation and complexation, spacer connects the receptor and fluorophore (close to each other). Because of that, for the recognition of most of the analytes, this mechanism/system is broadly used in florescent type sensors. [14] PET is categorized into TURN – ON and TURN-OFF types. In the absence of an analyte when the PET sensor absorbs energy the electron of a fluorophore is excited from HOMO to LUMO. Simultaneously HOMO of the free receptor is at a higher level it facilitates PET from HOMO of the free receptor to HOMO of the fluorophore that results in the blocking of quenching of fluorescence or emission transition. [15] Once the analyte binds with the receptor, the donor i.e receptor's redox potential increases, and it's lowered the HOMO than the HOMO of the fluorophore. As a consequence, no PET arises that resulted in the fluorescent enhancement of chromophore (**Fig. 4**). In some cases, the receptor is indirectly involved in the photo-physical process. If LUMO of the receptor with the analyte is in between HOMO and LUMO of the fluorophore, the LUMO of the analyte-bound receptor

offers a non-radiative pathway causing quenching of fluorescence. [16] Thus, in Turn-On fluorescent sensor photoinduced electron transfer occurred by involving HOMO and LUMO level of the fluorophore and HOMO level of the free receptor (before analyte binding). While, in the Turn-Off fluorescent sensor PET involves, the HOMO and LUMO level of the fluorophore and LUMO level of the analyte after the complex formation.

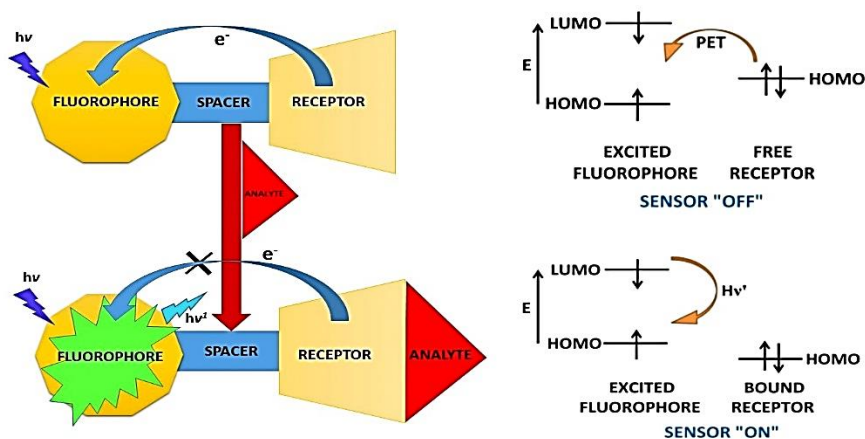


Figure-4: Photo-induced electron transfer (PET) process

1.2.2 Chelation enhancement of fluorescence (CHEF)

In the ground state of a molecule an electron absorbs a photon to be excited to a higher energy state. The resultant excited states lifetime determines the extent to which fluorescence accompanies the return of the electron to the ground state (**Fig. 5**). Often the lifetime of the excited state molecule is shortened so that little, if any, nonradiative dissipation of energy is possible before the excited electron falls back to the ground state, emitting a low energy photon as that absorbed. Under these circumstances the molecule is weakly fluorescent at best and its fluorescence is said to be 'quenched'. If metal ion binds to such a molecule and disables the process which quenches its fluorescence, the molecule will signal the metal ion binding by fluorescing strongly and there by act as a sensor.

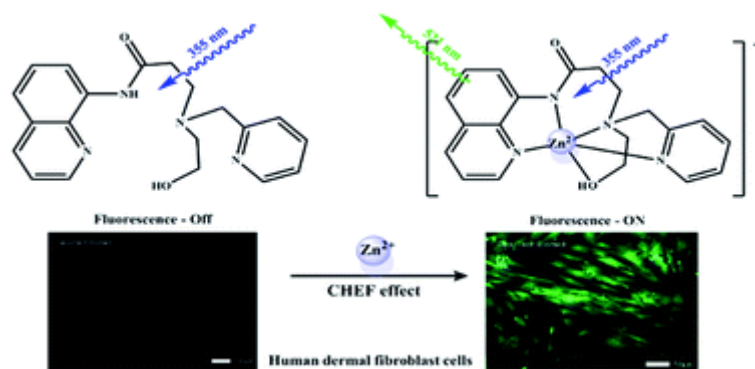


Figure-5. Schematic representation of CHEF-type metal chemosensor

1.2.3. Photo-Induced (or) Intramolecular Charge Transfer (PCT/ICT)

If the fluorophore has the electron-donating groups (-OCH₃, -NH₂, -NMe₂, etc.,) and conjugate with the electron-withdrawing groups (-CN, >C=O, etc.,) the intermolecular charge transfer occurs between the electron donor to electron acceptor at the excitation state which is promoted by the appropriate wavelength of light radiation. [17, 18] PCT commonly takes place with some subsequent changes associated with its dipole moment change, and large Stoke shifts. Similarly, when the electron donor functional group in the receptor interacts with the cation hence the electron-donating capability of the receptor gets reduced. [19] Because of that reduction in conjugation take place and lead to a blue shift of spectra as well as a decrease in the molar extinction coefficient. At the same time, an electron-withdrawing group of receptors interacts with the cation, thus shifting the emission spectra to redshift and along with that it increasing the molar extinction coefficient. [20, 21]

1.2.4. Paramagnetic Fluorescence Quenching Mechanism

Transition metals like Cu²⁺, Fe³⁺, Ni²⁺, Co²⁺, etc form the paramagnetic class of fluorescence quenching mechanism, owing to the half-filled or empty d-orbitals which promote the quenching of intense fluorescence of fluorophore by transferring energy and electron.[22-24] In many metal complexes, such type of phenomenon has occurred, because a half-filled electron in the metal ion will strongly interact with the pi-electrons of a

fluorophore and provides the platform for the intersystem crossing (ISC) process from the singlet excited state of fluorophores to the higher multiplicity state.[25,26]

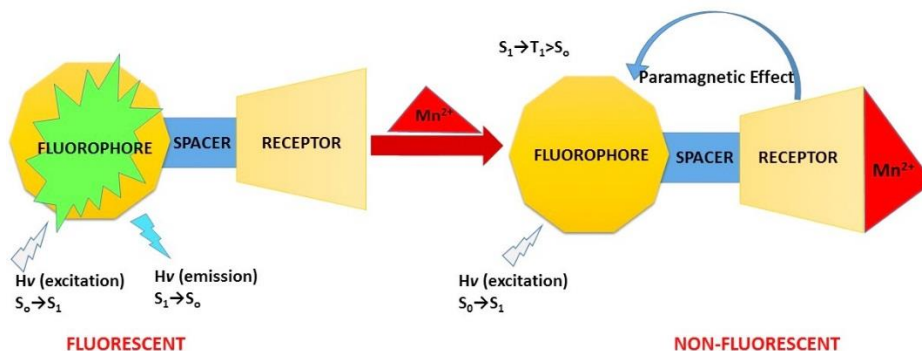


Figure-6: Paramagnetic fluorescence quenching schematic diagram

1.2.5. Fluorescence Resonance Energy Transfer (FRET)

FRET is the distance-dependent physical phenomenon exhibited between the excited states of (electronically) two different fluorophores in that the exciting energy is transferred from the donor to an acceptor fluorophore via a non-radiative dipole-dipole coupling process. If both the fluorophores are fluorescent then the mechanism is called fluorescence resonance energy transfer.[27-29] Forster's theory state some factors to occur in the FRET mechanism and are

- The acceptor fluorophore and donor fluorophore should be close between 10-100Å.
- The donor fluorophores emission spectral should overlay with the absorption spectra of acceptor fluorophore.
- The acceptor absorption moment and the donor emission dipole moments of relative orientation should parallel each other.

In the FRET process, the presence of metal ions can move both the donor and acceptors' fluorophores closer to each other (or) away from each other. When the metal ion

binds the distance between both fluorophores to get decreased as a result the FRET process is enhanced.

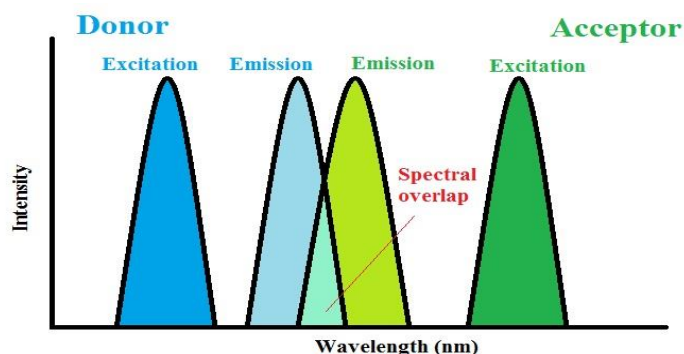


Figure-7: FRET process schematic diagram

1.2.6. Excited –State Intramolecular Proton Transfer (ESIPT)

The most important photophysical phenomenon is ESIPT which is extremely used in fluorescent chemosensors, light-emitting materials, and photochromic switching devices.[30] The ESIPT process exclusively takes place between the proton acceptor (imine nitrogen, carbonyl oxygen, etc.) and proton donors (NH₂, OH, etc.) via intra-molecular hydrogen bonding. At excitation state, the acidic proton move to the basic side and changed the electronic distribution and structure of the chromophore.[31] Zhou et al. studied the fluorescent chemosensor for the detection of Al³⁺ based naphthalimide – rhodamine compound. Initially, at the ground state, the chromophore was in enol form then it is stabilized by the intramolecular hydrogen bonding. On absorption, they excited to the singlet excited state of enol form without any geometrical changes.[32] followed by ultrafast ESIPT by intermolecular hydrogen bonding which is stabilized by the keto form at the singlet excited state. Compared to the fluorescence emission process ESIPT is a very fast process, mostly keto tautomers are responsible for fluorescence emission. Besides, the keto form geometry is relatively different from the enol form. Furthermore, the exo-cyclic double bond

promotes the gap energy reduction between the $S_0 \rightarrow S_1$ of keto form simultaneously it causes the large stoke shift at ESIPT chromophores. [33]

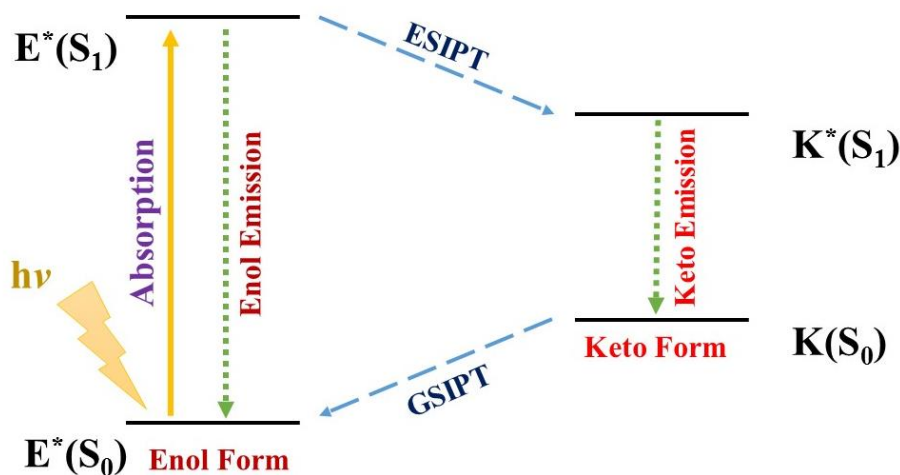


Figure-8: ESIPT Photophysical Cycle

1.2.7. Exciplex/Excimer Formation

Excited dimer or excimer are formed when the aromatic rings were joined by weak interactions of π -stacking, then the electronic interaction of one aromatic ring enhances the other neighboring ring for the interaction. This results from the formation of exciplex which is the collision complexes and is formed at an excited state. These complexes occur between the two distinct species or similar species of a fluorophore. [34,35] It is a reversible process and both the excimer and monomers are luminescent chemical entities. This interaction mainly occurs between the excited state molecules with the nearby ground state molecule that can emit the fluorescence in a longer wavelength (short frequency) than that of monomer. The resulting fluorescence band is mostly weak and broad type. [36] This is when the excimer and analyte interact with each other and influences the strong fluorescence by disturbing or enhancing exciplex/excimer. When two fluorophores species are attached in the fluorescent chemosensor, the analyte complexation affects their mutual distance and the

analyte quantitative measurement is analyzed by finding the fluorescence intensity ratio between the monomer and excimer. [37]

1.3. Aggregation-induced Emission (AIE)

Numerous AIE type fluorescents are known, AIE phenomenon is special, unique, and mostly observed at organic luminescent materials and are applied in biosensors, chemosensors (luminescent sensing materials), and also in light-emitting organic diodes. Most of the organic molecules are planar structural patterns and in the liquid state possess high photoemission efficacy than in the solid-state. [38] Such organic fluorophore's fluorescence efficiency is quenched as aggregated form via ACQ (Aggregation-Caused Quenching) because of the photophysical characteristic effects and it limits their practical applications. [39] To prevent such ACQ effect branched chains and bulky substituents are covalently attached to the organic fluorophores and the chromophore side is protected by cyclic molecular wires (via supramolecular interactions). Even though some organic molecules show weak emission in a liquid state because of unhindered intramolecular movements. When these weak molecules aggregate (i.e. solid form) the vibration, rotation, and intramolecular motions of functional groups are restricted. Also, it exhibits high efficacy of photoemission than in liquid such a process is called as AIE (Aggregation-Induced-Emission) process. [40] The enhancement of photoemission of luminophores in a liquid state than the solid is known as aggregation-induced emission enhancement. This aggregation effect is changed by the guest molecules via the interactions of coordination, electrostatic and hydrophobic (viscosity and polarity effects).

1.4. Schiff bases

Generally, Schiff bases are ketone or aldehyde analog compounds in that carbonyl groups are replaced by the azomethine or imine functional groups which have the general formula of $RR'C=N-R''$. Later, these compounds are named Hugo Schiff and also

structurally known as azomethine or asimine. Schiff base compounds are broadly used for industrial purposes also widely used in biological applications. From the literature reviews, Schiff base compounds reveal promising biological applications such as anti-bacterial, anti-viral, anti-fungal, anti-proliferative, anti-inflammatory, antimalarial, antipyretic, and anti-malarial activities. [41] Primary amines react with ketones or aldehydes under aseptically conditions Schiff base compounds are synthesized. It is an analog of nitrogen of ketone or aldehyde in which the C=O group (carbonyl group) is replaced by an azomethine or imine group. As it is an organic compound, extensively used as dyes and pigments, polymer stabilizers, catalysts, and intermediates in synthesis. [42] Azomethine or imine groups are found in numerous natural, non-natural, and natural derivatives which is the reason for its biological potentials. In 1864 German chemist Hugo Schiff first reported the Schiff base compound by condensing primary amine with the carbonyl compound. After that, he investigated the complexation of metal-salicylaldehyde with the primary amines (2:1 stoichiometry ratio). Series of systematic study and inclusion is achieved and scrutinized by the complexation of Schiff base and its derivatives. Schiff base compounds are performed as highly selective and excellent sensing materials for electrochemical sensors, optical sensors, and membrane sensors (diverse ion sensors). Based on the types and structure of Schiff base the reactivity and its selective towards the metal ions is take place. Other than this the ligand and metal electron configuration, metal ion charges, cavity size of the Schiff base, the unique sizes of the ions, the hard and soft acid-base character of the Schiff base, and metal interfering the reactivity and selectivity of the complexation. The coordination center environment of the Schiff base metal complexes can be changed by attaching the various substituents to the ligand which can affect the reactivity of the compound by modifying its electronic and steric properties. The d-block and p-block metal-based Schiff base complexes effectively act as a catalyst in the synthesis process and also in numerous useful reactions. High quality/class of polymers is synthesized with aid of palladium and

ruthenium Schiff base-complex catalyst. Katsuki's review summarised the salen metal complexes (cis-Metallo-salen) and the Schiff base-related ligands with their structural aspects and their applications in asymmetric catalysis. [43] Oxidation of olefin by Mn(II) amino acid-Schiff base complex synthesized by Wang et al. in 1999. [44] Gupta and Sutar studied the catalytic behavior of transition metal-based Schiff base complexes on various reactions of polymerizations, hydrogenations, ring closures, oxidation, and coupling. In recent days homogeneous and heterogeneous catalysts acquire more attention owing to recyclability and selectivity of the catalysts.[45] Though homogeneous catalysts are more relevant due to their arrival of mechanism, the ligand 2,2'-bis (diphenylphosphino)-1,1'-binaphthyl) (BINAP) is a more popular organophosphorus compound for its stereoselectivity. Chen and Huang reported the BINAP Schiff base compounds as a catalyst for the organic stereoselective transformations of aldol reactions, N-sulfonylaziridine, Diels-Alder reactions, Baeyer-villiger oxidation of aryl cyclobutanone, alkene epoxidation, and hydroxylation of styrene.[46]

1.4.1 Photophysical properties of Schiff bases

In recent years the Schiff base ligands got more attention owing to the wide range of applications in the fields of catalysis, synthesis, and especially in material chemistry. Because of its extensive applications nowadays researchers are tremendously synthesizing the variety of main group and transition metals Schiff base compounds. Schiff base ligands are vastly used as optical pH and metal sensors. However few past years the photophysical properties of the Schiff base are rarely reported in the literature and research papers. Manjaree A.Satam synthesized the series of Schiff base from 3-(1,3-benzothiazole-2-yl)-2-hydroxy naphthalene-1-carbaldehyde and analyzed the photophysical properties of one of the Schiff bases in various solvent systems. The utilization of different solvents changes the polarities, dielectric constants, hydrogen bonding, and refractive indices which can provide a unique and remarkable environment. Thus alter the maxima position at emission and

absorption spectra of the compounds/molecules. Nitro group (electron-withdrawing group) and the weak electron realizing methyl group presence do not give any changes at the absorption maxima. High aprotic solvents of DMSO and DMF showed a redshift in the fluorescence emission spectra and experienced different quantum yields based on the solvent used in the process. [47]

1.4.2. Schiff base based fluorescent chemosensor

Schiff bases are comprehensively used as a catalyst, stabilizers for polymers, pigments, dyes, pharmaceuticals, intermediates in organic synthesis, imaging, biological potent, molecular memory storage, and agro-industries. Chiefly the Schiff base compounds are extensively exploited as strong colorful and absorbing chromophores in the synthesis of chemosensors. Nowadays the Schiff base-designed fluorescent sensors facilitate the detection of numerous toxic analytes and also imaging the analytes in the different biological systems. Mostly the Schiff base ligands and the metal complexes were utilized as the luminescent, modeling of metal bio-active sites, optical material, center for metalloenzyme reactions, and heterogeneous and homogeneous catalyst in various reactions. Research in fluorescent sensors gets more attention due to its practical utilization, high accuracy and sensitivity, environmental and medical applications, and numerous biological effects on targeted metal ions.[48] Especially Schiff-based fluorescent sensors with the transition metal complexations have been applied widely in analytical as well as pharmacological fields owing to the medicinal effect on anti-tumor, anti-bacterial, anti-cancer, anti-fungal, anti-oxidants and also applied as a magnetic material. Most predominantly, Schiff base containing the sulfur and nitrogen chelating groups has exhibited more advantages in many fields owing to specific and diverse properties. Schiff base derivatives are extremely served as superior ligands for complexations of transition metal ions in addition to the transition metal-based Schiff base complex shows the variety of biological efficacies. Derivatives of Schiff base incorporating with the fluorescent moiety

were successfully evidenced the noticeable performance of such model as a fluorescent chemosensor towards the fluorescent sensing of metal ions.[49] Nowadays the Schiff base derivatives are widely utilized as fluorescent chemosensors because of their simple synthesis route, excellent applicability and availability, high selectivity and efficiency, and so forth. To utilize the Schiff base compounds and their derivatives as a fluorescent sensor (for transition metal ions), a strong fluorophore moiety (π -conjugated fluorescent) is required to attach. In the molecular recognition field, Schiff base fluorescent is very essential due to its effective capability of forming a more stable complex with the metal ions. In recent days the mechanism, photochemical properties, and the applications of Schiff base fluorescent probes have been well documented.

1.5. Sensing of Metal ions

In a biological system, metal ions play a vital role in structural and functional actions. Bioanalytical chemistry thoroughly describes the distribution as well as concentration fluctuation of metal ions in the biological system which also explains the applications such as medical developments, enzyme catalysis, and cell signaling. However, some anthropological activities have been mobilized a large number of metal species through waste dumping, corrosion, discharging industrial water, mining, and coal-burning leading to critical health issues and serious environmental problems. Hence metal detection is a necessary and important task for environmental and biological applications. So far, for detection and estimation of metals standard methods like atomic emission/absorption and mass spectroscopies are used. These methods are highly sensitive and accurate even though they are cost-wise high, only available in mega industries and centralized labs, required extensive sample pretreatment, real-time, and in situ measurement. Antibodies act as popular sensors for metal ions but the size of the metal ions is too tiny for direct antibody recognition. Initially, it has to be chelated and it may compromise selectivity. Moreover, antibodies optimally work only specific physiological conditions while environmental

samples may need to be detected under different conditions. On the other hand peptide and protein-based metal sensors also demonstrate metal ion detection but it prone to irreversible denaturation which creates a problem for all proteins. The chemical metal sensors predominantly rely on rational-designed fluorescent chelators. In fluorescent sensors, the metal ions are detected and have two main features: the binding or chelating moiety of metal and the fluorophore (at least one) must capable to absorb and emitting light. To act as a better sensor the metal-binding should alter the molecular or electronic structure of the sensor. Electronic changes in the structure affect the wavelength or intensity of the absorbed or emitted light. While molecular level structure changes alter the orientation or distance of pair of fluorophores of acceptor–donor. Chemical metal sensors distinguish all the metal ions based on their charge, size, and thiophilicity.

1.5.1. Detection of chromium ions (Cr^{3+})

Chromium with the oxidation state of +3 revealed less toxic effect than the other higher oxidation (+4, +6) states to the human body. Cr^{3+} exhibits a vital place in the metabolism of carbohydrates, fats, protein, nucleic acid, and also activates the enzyme, stabilize the nucleic acid and protein. The deficiency of trivalent chromium ions in the human body causes the health problems such as diabetes, cardiovascular diseases, etc. At the same time more than sufficient cation also acts upon the human body binding to DNA, affecting the cellular components and structures. Whereas, anthropogenic uses of Cr^{3+} in textile dyeing, alloying, tanning, and pigmenting of animal hide severely cause environmental contaminations. Hence, detection of trivalent chromium ions by the simple greenway is very important. Hexavalent chromium cation (Cr^{6+}) detection is achieved by fluorescent carbon nanodots type sensor. Metal organic-frame work (MOF) based sensors have been synthesized to detect the $\text{Cr}_2\text{O}_7^{2-}$. In recent days, novel rhodamine types of fluorescent sensors are reported which show low LOD (17.8mM) at 554nm with 100 fold enhancement of fluorescence intensity. [50] The addition of chromium ion (Cr^{3+}) changes

the colorless solution to pink coloration in the presence of the HEPES buffer solution. The enhancement of the fluorescence intensity ring is attributed to the opening of the spirolactum and long conjugation formation. Likewise, rhodamine-cyclohexane diamine type fluorescent probes (turn on) are reported for sensing Cr^{3+} ions which has the limit of sensing up to 7.5mM. Here also 100 fold enhancement of fluorescence is obtained at 580nm which is due to long conjugation formation by ring-opening of spirolactum. The sensor functionality is widely in biological pH from 4 to 8. In the same way, these two probes also examine other metal ions such as Mg^{2+} , Mn^{2+} , Cu^{2+} , Hg^{2+} , Cd^{2+} , Na^+ , K^+ , Ca^{2+} , Fe^{2+} , Zn^{2+} , Fe^{3+} , and Al^{3+} .

1.5.2. Detection of Lead ion (Pb^{2+})

The silver-grey metal is lead even though it has no biological importance but it may be accumulated in the human body and causes severe health issues. Excess exposure to lead can cause weakness, anemia, brain and kidney damage. A very high percentage of lead can lead to death but it is highly utilized in car batteries, cable sheathing, pigments, radiation protection, ammunition, weights for lifting, lead crystal glass, and also in some soldiers. A conjugate base of rhodamine trimethoxy benzaldehyde 'turn on' fluorescent chemosensor which exhibits high selectivity and sensitivity with 15mM LOD on recognition of divalent lead ion (Pb^{2+}) in an aqueous medium over other metal ions.[51] The probe revealed a 100 fold enhancement of intense fluorescence in the presence of divalent lead ions whereas in other metal ions (Mg^{2+} , Mn^{2+} , Cu^{2+} , Hg^{2+} , Cd^{2+} , Na^+ , K^+ , Ca^{2+} , Fe^{2+} , Zn^{2+} , Fe^{3+} , Al^{3+}) not identified such observations. In sensing of Pb^{2+} ions, colorimetric visual color changes from colorless to pink coloration are also observed. This sensor selectively imaging the divalent lead cations only in living cells. Derivative of naphthalene receptor has been employed for a fluorescent probe for only able to sense the Pb^{2+} ions not the other metal ions like Mg^{2+} , Mn^{2+} , Cu^{2+} , Hg^{2+} , Cd^{2+} , Na^+ , K^+ , Ca^{2+} , Fe^{2+} , Zn^{2+} , Ag^+ , Fe^{3+} , and Al^{3+} . It has been exhibited more than 17 fold enhancement of intense fluorescence at 359nm with the LOD of

$5 \times 10^{-7} \text{M}$ in an acetonitrile-water mixture (9:1). Thus, the increase of intensity can eliminate the photoinduced energy transfer process (PET) on the binding of a divalent lead cation. The literature has been reported the semiconducting polymer dots of fluorescent-based sensor for detection of ratiometric lead in the living cells and luminescent of molybdenum disulfide nanosheets based sensor for detection label-free fluorescence sensing of Pb^{2+} .

1.5.3. Detection of Aluminum ion (Al^{3+})

Aluminum, the third most prevalent element and most abundant element (about 8% of the weight of the earth) in the outermost layer of the earth crust, is extensively used in present industry and our daily lives. [52] The widespread of aluminium applied in water purification, food additives, clinical drugs, packing materials. In addition, frequent use of aluminium foil, vessels, and trays for convenience results in moderate increase in the Al^{3+} concentration in food. After absorption, aluminium ions would be distributed among all tissues in humans and animals and eventually accumulate in the bone. Due to the use of aluminum ions in daily life, that increases the risk of people getting aluminum poisoning, causing calcium metabolism disorders, interfering with the iron concentration in the blood, leading to osteomalacia, microcellular hypochromic anemia, and under overload conditions, Al^{3+} may participate in the production of reactive oxygen species causes neurodegenerative diseases. Adverse effect of Al^{3+} ions not only inhibits the plant growth, but also affects the central nervous system of humans and induces Alzheimer's disease, Parkinson's disease and amyotrophic lateral sclerosis. The World Health Organization (WHO) has recommended that the daily average intake of Al^{3+} was around 3-10 mg .Therefore, the development of efficient methods for Al^{3+} detection is quite crucial for the environment and biological systems.

1.5.4. Detection of Zinc ion (Zn^{2+})

Zinc, the second most prevalent transition metal in biological organisms, and it performs major functions in various physiological processes. It is an indispensable cofactor in several enzymes involved in the human body as well as in sea organisms, contains zinc as an essential element. Enzymes, in turn, act as catalysts for biological processes such as cellular metabolism. Less intake of zinc ion possibly leads to growth sexual diseases, epilepsy, degenerative nerve diseases, prostate cancer, Parkinson's disease, Alzheimers diseases etc. Excess intake of zinc ion may lead to health problem. Zinc ions ($45.9 \mu\text{M}$) tolerance in drinking water, the world health organization endores. Therefore, Zinc ions detection to enviraonment monitoring of that ions in biological system constitute an interesting and challenging field of research. [53]

1.5.5. Detection of Nickel ion (Ni^{2+})

Nickel is rarely found in its pure form on the Earth's surface, although it is believed that a significant amount is present at the core. Its most stable oxidation state is +2, while +1 and 0 are only found in organometallic chemistry. It has a very rich coordination chemistry, and can form complexes with different geometries (octahedral, trigonal bipyramidal, tetrahedral, square-based pyramidal and square planar). When compared to copper, zinc is not an abundant element, and trace amounts are present in the Earth's crust. Due to its high reactivity it is rarely found pure in nature. The Zn(II) ion has a $3d^{10}$ electronic configuration, and it cannot be strictly considered as a transition metal ion. Due to this electronic configuration, its compounds are colorless and diamagnetic and there is no ligand-field stabilization energy associated with this ion, for what no particular geometry is preferred in the formation of complexes. [54]

1.5.6. Detection of Ferric ion (Fe³⁺)

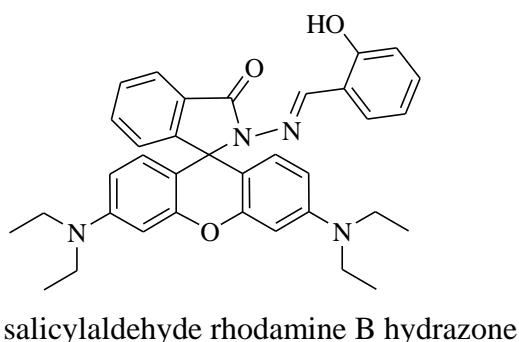
Fe³⁺ is the most essential metal ion in biological systems and plays a crucial role in many biochemical processes, such as in cellular metabolism, in many enzymatic reactions as a cofactor, and in carrying oxygen by heme. Both its deficiency and overloading induce biological disorders in the living body, such as anemia, liver and kidney damage, heart failure, and diabetes [55]. Detection of ferric ions in solution is very difficult using fluorescence techniques because the paramagnetic nature leads to their fluorescence quenching ability. Fluorescence enhancement through chelation of this metal ion with any fluorophore is a challenging task in vitro as well as in vivo. Several groups have successfully detected Fe³⁺ ions in aqueous environments using xanthene derivatives, which can follow either a metal ion induced spirocyclic ring-opening or a FRET mechanism.

1.6. Anticancer activity, Cell viability assay

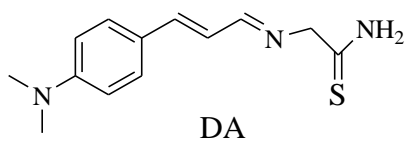
The anticancer activity and cell viability effect of the synthesised compounds were investigated against human liver cancer cell lines HepG2, MCF-7 in this study. National Centre for Cell Science in Pune, India, provided the HepG2 and MCF7 cells. The cell culture was kept at 37 degrees Celsius in a 5% CO₂ atmosphere in DMEM media with 10% FBS, 1% glutamine, and 100 units penicillin–streptomycin. We used the MTT technique to perform a cytotoxicity experiment on produced compounds in HepG2 to determine their anticancer potential. This was accomplished by harvesting exponentially growing cells and seeding 1×10⁵ cells per well in a 96-well plate. After 24 hours of incubation, the old medium was replaced with new media containing various concentrations of produced chemicals (varying from 0.9 to 500 M concentration) and incubated for another 24 hours at 37 °C in a 5 percent CO₂ incubator. The incubation was then continued for another 4 hours by adding 100 µl of MTT solution (5 mg/ml in PBS). The reaction was then stopped with 100 µl of DMSO, and the absorbance was measured at 570 nm. After 24 hours of therapy, substantial cell death was seen in human cancer cells.

1.7. A Brief Review of Literature

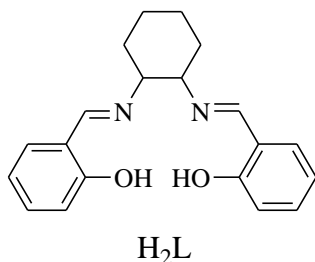
Yu, Xiang and co-worker have reported a new fluorescent Rhodamine was synthesized and selectivity of Cu (II) metal ions absorbance, fluorescence emission above 500nm in neutral buffer medium. The displayed reversible absorption and fluorescence enhancement response to Cu (II) via a 1:1 binding mode. The Cu (II) ions are very high in selectivity due to little interference was observed for other commonly coexistent metal ions. Furthermore, the detection of Cu (II) at a lower micromolar level was successful in buffer aqueous solution.



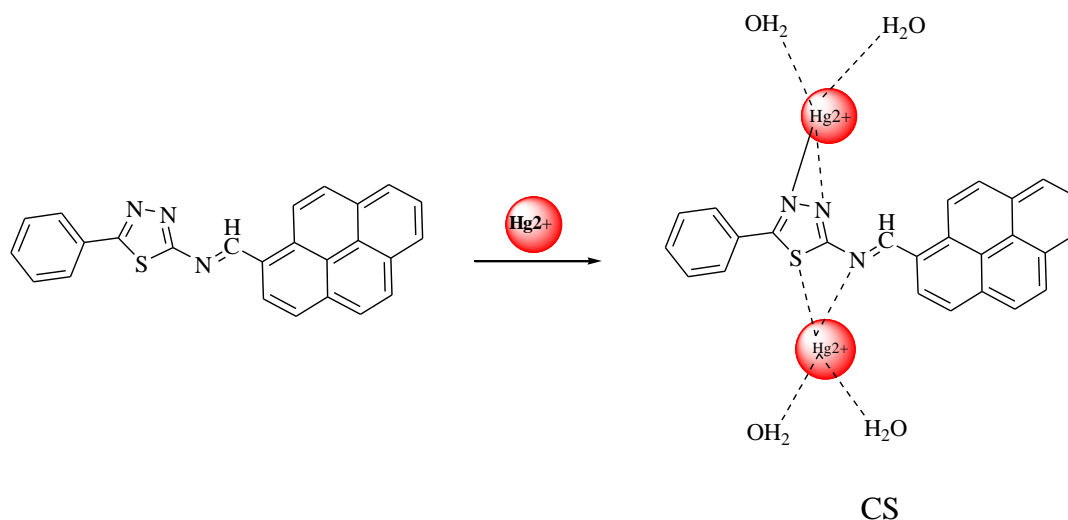
Duong Tuan Quang et al. a new fluorescent chemosensor for Hg^{2+} ions in aqueous medium by a prepared aminothiourea based Schiff base ligand (DA). Addition of 1equiv of Hg^{2+} ions to the aqueous solution of DA gave rise to an obvious fluorescence enhancement and the subsequent addition of more Hg^{2+} induced gradual fluorescence quenching. Other competing ions do not induce any distinct fluorescence changes including Pb^{2+} , Cd^{2+} , Cr^{3+} , Zn^{2+} , Fe^{2+} , Co^{3+} , Ni^{2+} , Ca^{2+} , Mg^{2+} , K^+ and Na^+ , indicating that DA can selectively detect Hg^{2+} ions in aqueous solution.



Nayan Roy et al. a schiff- base (H₂L) fluorescent probe was synthesized and evaluated as a chemoselective Zn²⁺ sensor. Upon treatment with Zn²⁺, the complexation of H₂L with Zn²⁺ resulted in a bathochromic shift with a pronounced enhancement in the fluorescence intensity in ethanol solution. Furthermore, other common alkali, alkaline earth and transition metal ions failed to induce response or minimal spectral changes. Notably, this chemosensor could distinguish clearly Zn²⁺ from Cd²⁺. The stoichiometric ratio and association constant were evaluated using Benesi–Hildebrand relation giving 1:1 stoichiometry. This further corroborated 1:1 complex formation based on Job's plot analyses.



Cui-Bing Bai et al., a novel pyrene based Schiff base molecule (CS) synthesized, and characterized by long-wavelength turn-on fluorescent chemosensor to detect Hg²⁺. In presence other metal ions, CS could effectively recognize Hg²⁺ and produce the turn-on fluorescent emission at 607 nm. And also, the change of the solution color from yellow to orange was directly observed by the naked eye due to absorption spectrum exhibited red-shift. The Hg²⁺ ions interaction with CS confirmed by the Job's plot, SEM, AIMS, and DFT calculations. It was found that the fluorescence of CS could be reversible when I⁻ was added into the solution of CS and Hg²⁺. CS illustrated high selectivity and good sensitivity for Hg²⁺ with the limit of detection of 36 nm. Moreover, CS could be utilized as test strips and silica gel plates to identify Hg²⁺.



Recently Tuhin, Khan et al. reported Salophen, tetradentate Schiff base, fluorescence detection of Al^{3+} ions, we discovered contradicting literature findings on salophen's fluorescence spectral maximum and quantum yield while conducting this research. As a result, the chemical was refined through repeated crystallisation. Fluorescence experiments have been carried out on substances with entirely super impossible absorption and excitation spectra. The refined molecule has a weak fluorescence at 545 nm, which is accompanied by extremely quick fluorescence decay. This is explained by proton transfer in the excited state and torsional motions inside the molecule, which provide efficient non-radiative routes for deactivating the excited state. When salophen is complexed with Zn^{2+} or Al^{3+} , the fluorescence quantum yield rises. When complexed with Al^{3+} , the rise is much greater. The fluorescence maxima of the two complexes, however, are comparable. In the presence of a high excess of Zn^{2+} , fluorescence intensity may not be an appropriate metric for Al^{3+} sensing by salophen. This difficulty can be avoided if the fluorescence lifetime is utilised as the sensing parameter, because the Al^{3+} complex has a life time of nanoseconds, whereas the Zn^{2+} complex has a life time of tens of picoseconds. The following explains the considerable variation in fluorescence quantum yield and lifespan between the two complexes: The Zn^{2+} compound is dimeric, whereas the Al^{3+} complex is monomeric. Quantum chemistry calculations show that around the locally

excited state, there is a larger density of states. This may lead to more efficient non radiative pathways.

1.8. AIM AND SCOPE

The aim of the present work is to design the synthesis of fluorescent chemosensors based on various platforms for heterocyclic schiff base molecules. The investigation of heterocyclic of Schiff bases and related derivatives has provided a new strategy for the design of novel chemosensors. In this research work presented in this thesis an outline on guiding principle for the design of effective Schiff-based chemosensors which are highly sensitive and selective for the detection of metal ions with a focus on the major mechanisms that control luminescence behavior for target molecules is provided. The current study focuses on the behaviour of transition metal ions and d and p block elements towards Schiff bases.

Objectives

- ✓ The synthesis of new heterocyclic compounds of Schiff based chemosensors
- ✓ Characterization of new ligands by spectroscopic techniques ($^1\text{H-NMR}$, $^{13}\text{C-NMR}$, MS, FT-IR) and measurement of UV-vis, fluorescence property.
- ✓ Studies on of transition metal ions like Cr^{3+} , Fe^{3+} , Ni^{2+} , Zn^{2+} and p-block elements like Al^{3+} , Pb^{2+} on the emission behavior of the probes. Furthermore, the capability of Schiff based ligand to sense metal ions with human cancer cell like HepG2- cells and MCF-7 has been explored. Cytotoxic activity and DFT to be studied.
- ✓ The theoretical studies were carried out on the molecular structure using density functional methods (B3LYP) invoking 6-31G basis set. The energy of the highest occupied molecular (HOMO) orbital and lowest unoccupied (LUMO) molecular orbital have been predicted.

1.9 REFERENCES

1. <https://www.smlase.com/entries/automation/what-are-different-types-of-sensors-and-their-applications/>
2. <https://www.taylorfrancis.com/chapters/mono/10.1201/9781420040692-7/optical-sensors-applications-hyungsuck-cho>.
3. Xiaoding . Lou, Daxin. Ou, Qianqian. Li, Zhen. Li, Chem. Commun., 2012, 48, 8462–8477.
4. Poonam, Rani. Chemosensor and its applications. International Refereed Journal of Reviews and Research., 2015, 3, 5.
5. Cuong. Khac, Phu. Truong, Thao Dang. Duy Nguyen1, Ik-Soo, Shin. BioChip J., 2019, 13(3), 203-216.
6. Binghe Wang, Eric V. Anslyn . Chemosensors: Principles, Strategies, and Applications., 2011, 24, 524.
7. Di. Wu, Adam C. Sedgwick, Thorfinnur. Gunnlaugsson, Engin U. Akkaya, Juyoung. Yoon, Tony D. James. Chem. Soc. Rev., 2017, 46, 7105
8. A. Prasanna. de Silva, Thomas S. Moody, Glenn D. Wright., Analyst, 2009, 134, 2385–2393.
9. A. Prasanna. de Silva, R. A. D. Dayasiri, Rupasinghe. J.Chem.Soc., Chem.Comm.,1985.
10. Jiasheng.Wu. Weimin. Liu, Jiechao. Ge, Hongyan. Zhang, Pengfei. Wang, Chem. Soc. Rev., 2011, 40, 3483–3495.
11. A. W. Czarnik, Fluorescent Chemosensors for Ion and Molecule Recognition, American Chemical Society., Washington, DC, 1993.
12. Nahyun, Kwon.; Ying, Hu.; Juyoung, Yoon.; ACS Omega., 2018 3(10), 13731–13751.
13. Fanpeng. Kong, Renpu. Liu, Ranran .Chu, Xu. Wang, Kehua. Xu, Bo. Tang, Chem. Commun., 2013, 49, 9176—9178.
14. Wei. Zhang, Zhao. Ma, Lupei. Du, Minyong, Li. Analyst, 2014, 139, 2641.
15. Longwei. He, Baoli. Dong, Yong. Liu, Weiyong, Lin.Chem. Soc. Rev., 2016, 45, 6449

16. Gholam Babaei, Chalmardi.; Mahmood, Tajbakhsh.; Ahmadreza, Bekhradnia.; Rahman, Hosseinzadeh. *Inorganica Chimica Acta*. 2017, 462, 241–248.
17. J. J. Hopfield, Joseph. Henry, *Biophysical journal*. 1977, 18.
18. Raphael. Pfattner, Egon. Pavlica, Michael. Jaggi, Shi-Xia, Liu, Silvio. Decurtins, Guido. Bratina, Jaume. Veciana, Marta, Mas-Torrent, Concepcio, Roviraa. *J. Mater. Chem. C*, 2013, 1, 398.
19. Songqiu. Yang, Jianyong. Liu, Panwang. Zhou, Keli. Han, Guozhong, He. *Chemical Physics Letters*. 2011, 512, 66–69.
20. Arup. Tarai, Meina. Huang, Pintu. Das, Wenhui. Pan, Jianguo. Zhang, Zhenyu. Gu, Wei. Yan, Junle. Qu, Zhigang. Yang, *Molecules*. 2020, 25, 585.
21. Pronab. Kundu, Dipanwita. Banerjee, Gourhari. Maiti, Nitin, Chattopadhyay. *Phys. Chem. Chem. Phys.*, 2017, 19, 11937-11946.
22. Peng. Wang, Jiang. Wu, Pingru. Su, Cong, Xu Yushu. Ge, Dan. Liu, Weisheng. Liu, Yu, Tang. *Dalton Trans*. 2016, 45, 16246–16254.
23. Roymon. Joseph, Balaji. Ramanujam, Harida. Pal, Chebrolu, P. Rao. *Tetrahedron Letters* 2008, 49, 6257–6261.
24. Sushil K. Dwivedi, Rashid Ali, Manjeet. Singh, Tulika. Gupta, Aditya K. Kar b, Ved Prakash, Anbumani. Sadasivam, Satyakam. Patnaik , Arvind Misra. *Journal of Photochemistry & Photobiology, A: Chemistry* 2020, 403, 112854.
25. Yiqun. Tan, Jiancan, Yu Yuanjing. Cui, Yu. Yang, Zhiyu. Wang, Xiaopeng. Hao, Guodong. Qian, *Analyst*, 2011, 136, 5283–5286.
26. Wenjing. Yang, Xuebo. Chen, Huizhen. Su, Weihai. Fanga, Yong. Zhang, *Chem. Commun.*, 2015, 51, 9616.
27. Forster, T. *Disc. Faraday Soc.*, 1959, 27, 7.
28. Forster, T. *Ann. Phys.*, 1948, 2, 55.
29. Chun-Yan. Li, Yu. Zhou, Young-Fei. Li, Chun-Xiang. Zou, Xue-Fei. Kong, *Sensors and Actuators B: Chemical*, 2013, 186, 360-366.
30. Jianzhang. Zhao, Shaomin. Ji, Yinghui. Chen, Huimin. Guo, Pei, Yang. *Phys. Chem. Chem. Phys.*, 2012, 14, 8803–8817.

31. Ling. Chen, Peng-Yan. Fu, Hai-Ping. Wang, Mei, Pan. *Adv. Optical Mater.* 2021, 2001952.
32. Hem C. Joshi, Liudmil. Antonov. *Molecules.*, 2021, 26, 1475.
33. Adam C. Sedgwick, Luling .Wu, Hai-Hao. Han, Steven D. Bull, Xiao-Peng. He, Tony D. James, Jonathan L. Sessler, Ben Zhong, Tang, He. Tian, Juyoung .Yoon, *Chem. Soc. Rev.*, 2018, 47, 8842.
34. Manikandan. Kadirvel, Biljana. Arsic, Sally, Freeman. Elena, V. Bichenkova, *Org. Biomol. Chem.*, 2008, 6, 1966–1972.
35. Dae Won, Choa, Dae Won. Cho, *New J.Chem.*, 2014, 38, 2233.
36. Jessica C. Berrones-Reyes, Blanca M. Mu noz-Flores, Arelly M. Cant´on-Di´az, Manuel A. Treto-Su´arez, Dayan P´aez-Hern´andez, Eduardo. Schott, Ximena. Zarate, ´ictor M. Jim´enez-P´erez . *RSC Adv.*, 2019, 9, 30778–30789.
37. Yong-Jin Pu, Yuki. Koyama, Daisuke. Otsuki, Minjun. Kim. Hiroya, Chubachi, Yuki. Seino, Kazushi. Enomotoa , Naoya . Aizawa, *Chem. Sci.* 2019, 10, 9203.
38. Qian. Jiang, Mingguang. Zhang, Zhonglong. Wang. Jie, Song, Yiqin. Yang, Wenchao. Li, Wen. Gu, Xu. Xu. Haijun, Xu. Shifa ,Wang. *RSC Ad.*, 2018, 8, 30055.
39. Chendong. Ji, Liming. Lai, Pengyu. Li. Zhen, Wu, Wenyu. Cheng, Meizhen. Yin, *Aggregate.*, 2021, 2, 39.
40. Wenbo. Wu, Bin. Liu, *Natl Sci Rev*, 2021, 8, 222.
41. Wail Al, Zoubi. *International Journal of Organic Chemistry*, 2013, 3, 73-95
42. Asnake. LealemBerhanu, Gaurav. Irshad, Mohiuddin, Ashok. KumarMalik, Jatinder Singh. Aulakh, Vanish. Kumar, Ki-Hyun. Kim, *Trends in Analytical Chemistry* 2019, 116, 74-91.
43. Tsutomu. Katsuki, *Chem. Soc. Rev.*, 2004, 33, 437–444.
44. Rong-Min. Wang, Cheng-Jun. Hao, Yun-Pu. Wang, Shu-Ben. Li, *Journal of Molecular Catalysis A: Chemical.*1999, 147, 173–178.
45. K.C. Gupta, Alekha, Kumar Sutar, *Coordination Chemistry Reviews.*,2008, 252 1420–1450.
46. Chi-Ming. Che, Jie-Sheng. Huang, *Coordination Chemistry Reviews.*, 2003, 242, 97-113`

47. Manjaree. A, Satam Rahul D.Telore, Nagaiyan Sekar, *Dyes and Pigments.*, 2015, 123, 274-284.
48. Duraisamy. Udhayakumari, V. Inbaraj, *Journal of Fluorescence.*, 2020, 30, 1203–1223.
49. Lina.Wang, Juanjuan. Tang, Ning. Sui, Xing. Yang, Luyao. Zhang, Xiaojun. Yao, Qinfei. Zhou, Hailian. Xiao, Shaoping Kuang. William W. Yu, *Anal. Methods*, 2017, 9, 6254-6260.
50. Sunanda. Sahanaa, Gargi. Mishrab, Sri. Sivakumarb, Parimal K. Bharadwaja, *Journal of Photochemistry and Photobiology A: Chemistry.* 2018, 351, 42–49.
51. Omprakash. Sunnapua, Niranjana G. Kotlaa, Balaji. Maddiboyina, Subramanian. Singaravadivel, Gandhi. Sivaraman, *RSC Adv.*, 2016, 6, 656-660.
52. Yuhang.,Xu, Liuqi. Kong, Liping. Bai, Amin. Chen, Na. Li, Lijuan, Cheng, Wenjie. Liu, Xiaoqing. Sun, Farong, Tao. Liping, Wang, Guang, Li., *Tetrahedron*, 2021,79, 131888.
53. Zhaoyan. Tian, Shiqiang. Cuia, Gang. Liua, Renjie. Wanga, Shouzhi, Pua. *J. Phys. Org. Chem.* 2016, 29, 421–429.
54. Gujuluva Gangatharan, Vinoth Kumara, Mookkandi, Palsamy. Kesavana, Murugesan. sankarganesha, Kathiresan, Sakthipandic, Jegathalaprathaban. Rajesha, Gandhi. Sivaraman., *New J. Chem.*, 2018, 42, 2865-2873.
55. Ankush. Gupta, Naresh, Kumar., *RSC Adv.*, 2016, 6, 106413.
56. Yu. Xiang, Aijun. Tong, Peiyuan. Jin, Yong, Ju. *Org. Lett.*, 2006, 8, 13, 2863–2866.
57. Duong. Tuan Quang, Nguyen. Van Hop, Nguyen. Dinh Luyen, Ha. Phuong Thu, Doan Yen. Oanh, Nguyen, Khoa. Hien, Nguyen. Van Hien, Min. Hee, Lee. Jong, Seung Kim. *Luminescence.*, 2013, 28, 222–225.
58. Nayan . Roy, Harun A. R, Pramanik ,Pradip C. Paul, Sanjoy ,T. Singh. *J Fluoresc.*, 2014, 24, 1099-1106.
59. Cui-Bing. Bai, Peng. Xu, Jie. Zhang, Rui. Qiao, Meng-Yu, Chen, Meng-Yu. Mei, Biao. Wei, Chang. Wang, Lin. Zhang, Shui-Sheng, Chen. *ACS Omega.*, 2019, 4, 14621–14625.
60. Tuhin. Khan, Shefali. Vaidya, Darshan S. Mhatre, Anindya, Datta. *J. Phys. Chem. B.*, 2016, 120, 39, 10319–10326.

Chapter II

Novel Schiff base Synthesis of E-N-(1-(1H-phenothiazin-2yl)-ethylidene)-3-((E)-(2-phenylhydrazono) methyl) aniline “Turn-on” fluorescent chemosensor for sensitivity and selectivity of detection of Cr³⁺ and Pb²⁺

2.1. INTRODUCTION

The selection of transition metal ions has potential applications in many fields such as biology, chemistry, medicine, and the environment [1-5]. A variety of effectively fluorescent chemosensors for alkali and alkaline earth metal ions have been developed [1, 3-5]. The soft transition metal ions are fluorescence chemosensors and particularly necessary much attention is paid because of their impact on the environment [6, 7]. Our body could be affected by use this instead of direct. [8] The metal ion Cr³⁺ is a trivalent form and plays a vital role in various biological processes and it assists the metabolism of carbohydrates, nucleic acids, proteins, and fats through stimulated of enzymes as well as by stabilizing the nucleic acids and proteins. [9] Therefore, it is very important to develop a chemosensor for detection of Cr³⁺ ions in biological and also ecological samples. Cr³⁺ could be detected using various instrumentation techniques like reversed phase-high performance liquid chromatography coupled to different spectrometric detection methods, stripping voltammetric analysis, and atomic absorption spectrophotometers. [10-12] Costly instrumentation and time consumption for analysis made chemosensors a significantly analytical tool that can be used to detect ionic species. In current years, fluorescent chemosensors for Cr³⁺ have been reported. [13-17] As a result, the high sensitivity and selectivity to detecting Cr³⁺ ion very quickly in the development of material for ease, and due to it is very simplicity, low cost, and convenience, extensive attention is received by small organic fluorescence basic methods for chemosensors. [18] Fluorescent chemosensor

has several acceptable sensing properties for Pb^{2+} has drawn considerable much attention because of spread of poisonous lead a heavy toxic metal ion from batteries, metallurgy, gasoline, mining, and pigments damage to human health neurological damage, inducing anemia, nerve disorders, kidney disorder, physical growth impairments, memory loss and inhibition of brain developing existing in children. [19-23] However, all reports about the sensing properties of Pb^{2+} ions is only in basic condition that coordinate or substitute effectively for sensor Pb^{2+} ions. [24-33] The Pb^{2+} heavy poisoning could lead the irreversible harm to the growth of teenagers, cognitive development, fetal growth, psychological and behavioral [34-38]. The drinking water can limit to 10ppm, according to the World Health Organization (WHO). [39] Fluorescence chemosensors are interesting in the recognition of various anions, cations and different neutral molecules in number of fields including molecular devices, environmental sensors, biological probes, and detection of nerve gases due to their excellent properties as real-time detection, low cost, low detection limit, operational simplicity high sensitivity and selectivity and adaptability to different platforms [40-46]. The detection of fluorescence signal interacting with a chemical species in fluorescence probes occurs through [47] various mechanisms such as chelation-enhanced fluorescence (CHEF) [48], intramolecular charge transfer (ICT) [49], photoinduced electron/energy transfer (PET) [50], metal-ligand charge transfer (MLCT) [51], excited-state resonance energy transfer (FRET) [52], excimer/excimer formation [53], intramolecular and intermolecular proton transfer (ESIPT) [54] and C=N isomerization [55]. Schiff-base compounds can be used as fluorescence chemosensors due to simple synthesized procedure [56, 57]. In this work we successfully designed fluorescence chemosensor for high sensitively and selectively of Cr^{3+} and Pb^{2+} for “turn-on” platform in aqueous media. Schiff-base-based fluorescent chemosensors, *(E)-N-(1-(1H-phenothiazin-2yl)-ethylidene)-3-((E)-(2-phenylhydrazono)methyl)aniline* was synthesized and characterized by FT-IR, ESI-MS, ^1H NMR, and ^{13}C NMR spectroscopy. The probe AT

showed an excellent fluorescence enrichment towards Cr^{3+} and Pb^{2+} , and sensing mechanisms was proposed based on UV-Vis, Fluorescence titrations, ESI-mass spectrometry analysis, ^1H -NMR titrations, molecular docking, living cell imaging, cytotoxicity, and DFT.

2.2. EXPERIMENTAL METHODS

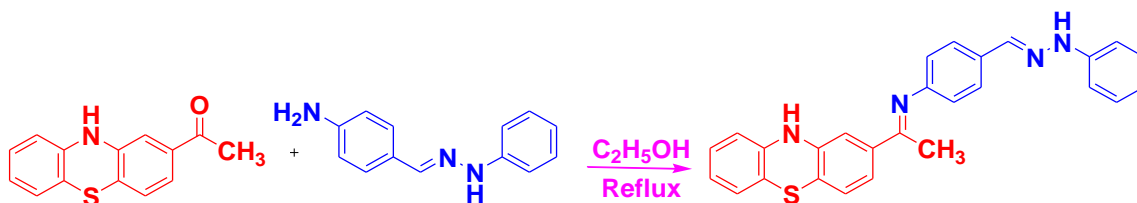
2.2.1 Materials and Instruments

All chemical compounds were purchased and used after purification. Distilled water was used for all experiments. The synthesized compound was characterized by using FT-IR, ^1H & ^{13}C NMR, and ESI-MS spectroscopy. Infrared measurement was made at 4000–400 cm^{-1} region on an Agilent Carry 630 FT-IR (Fourier Transfer Infrared) spectrometer. The ^1H NMR spectrum and ^{13}C NMR were recorded on a Bruker-400MHz and TMS as an internal standard working in $\text{DMSO}-d_6$, respectively. UV and fluorescence measurements were carried out with Perkin-Elmer LS45 fluorescence spectrophotometer at a scan rate of 1200 nm range at room temperature. A Varian RF-5310PC fluorescence spectrometer was used to record fluorescence at ambient temperature.

2.2.2 Synthesis of Schiff base AT

1-(10H-phenothiazin-8-yl)ethanone (0.48g, 2 mmol) and 4-(Phenylhydrazonomethyl)-phenylamine (0.42g, 2 mmol) were dissolved in absolute ethanol and refluxed for 24 h under 60°C atmosphere. Then, the reaction was confirmed by TLC in benzene solvent. After cooling to room temperature the resulting solution was poured into distilled water with stirring, a light yellow precipitate was obtained. The precipitate was filtered off and dried in vacuo. Further, it was recrystallized using absolute ethanol to get the desired product **AT** as shown in **Scheme 1**. Yield: 83%. FT-IR; (C=N) 1597 cm^{-1} , (NH) 3345 cm^{-1} . ^1H NMR (500 MHz, $\text{DMSO}-d_6$) δ 10.14 (s, 1H), 8.06 (s, 1H), 7.30 (s, 1H), 7.284-7.282 (d, $J = 0.8$, 2H), 7.18-7.15 (m, $J = 9.2$, 3H), 7.093-9.055 (m, $J = 1.6$, 2H), 6.985-

6.966 (d, $J = 7.6$, 2H), 6.88 (s, 1H), 6.797-6.771 (m, $J = 10.4$, 3H), 6.644-6.605 (m, $J = 15.4$, 3H), 2.566-2.557 (t, $J = 36$, 3H). ^{13}C NMR (100 MHz, DMSO- d_6), δ (ppm): 196.88, 158.23, 157.15, 152.98, 146.25, 145.16, 141.59, 130.54, 129.18, 128.43, 118.33, 116.49, 115.26, 114.91, 111.41, 26.44. ESI-MS (m/z): calculated for $\text{C}_{27}\text{H}_{22}\text{N}_4\text{S}$ [$\text{M} + \text{H}$] $^+$: 434.1600; found: 435.2747.



Scheme 1. Synthesis of AT compound.

2.2.3 UV-vis and fluorescence experimentation

The stock solutions (0.025 M) of different metal ions (nitrate or chloride salts) were prepared in distilled water. A 1×10^{-5} M stock solution of **AT** prepared in distilled water was used for spectroscopic studies. The absorption and fluorescence spectra measurements were carried out by using a 5 mL mixed solution of **AT** and metal ion in a quartz cell at room temperature. All fluorescence experiments were conducted upon excitation wavelength at 369 nm.

2.2.4. Cell Culture

The human hepatocellular liver carcinoma cells (HepG2 cell lines) (NCCS, Pune, India) were grown in DMEM by addition of 10 % of FBS and antibiotics (streptomycin-50 μg / mL; penicillin-100 μg / mL), at 37 $^\circ\text{C}$, 5 % CO_2 incubator, cells were produced at 95 %.

2.2.5. Anticancer activity, Cell viability assay

The cytotoxicity of **AT** was tested using a 3-(4, 5-dimethylthiazole-2-yl)-2, 5-diphenyl tetrazolium bromide (MTT) assay against HepG2 cell lines. Cells were seeded onto

a 96-well plate at a cell density per dish 1.5×10^4 and incubated at varying concentrations from 1.5 to 500 μM to last 48 hours in a medium containing **AT**. Triplicate wells with 100 μL of MTT added to each well are retained for each operation. It was incubated at 37 °C for 4 h, allowing MTT reaction and metabolically active cells to form crystals of formazan. The medium for MTT was cautiously discarded from the wells. To extract intracellular formazan crystals, 100 μL of DMSO was applied to each well and the dishes shaken for 10 minutes. Using ELISA, at 428 nm, the absorbance was readouts. Using a fluorescent microscope, the photographs of the cells were analyzed. The survival percentage was determined using formula: %survival = [live cell number (test)/live cell number (control)] $\times 100$.

2.2.6. Fluorescence microscopic study

For in-vitro fluorescence imaging of **AT**, the cells were seeded in a 35 mm culture dish at a density of 3×10^5 cells per dish. After completion, 60% confluence for fluorescence microscopy was replaced by mercury nitrate and zinc nitrate (0.3 μM and 0.5 μM) augmented with the serum to absorb $\text{Cr}^{3+}/\text{Pb}^{2+}$ ions by 40-hours developing cells, **AT** (5.0 μM), dissolved in DMSO/ H_2O (99/1), in addition to new media to allow **AT** to be absorbed by cells to form the $\text{Cr}^{3+}/\text{Pb}^{2+}$ - **AT** complex. Under a fluorescence microscope, both excitations of $\text{Cr}^{3+}/\text{Pb}^{2+}$ ions were trypsinized and examined for **AT** images at 428 nm using a 10x fluorescent target. The bright and Fluorescence field knowledge was obtained using the fluorescence microscope 40x-Olympus FV1000-LX81.z, Camedia software, and Adobe Photoshop version 10.0 processed using. For the control trial, the media was stripped off $\text{Cr}^{3+}/\text{Pb}^{2+}$ ions.

2.3. RESULTS AND DISCUSSION

As shown in **Scheme 1**, Schiff base compounds based on the fluorescent chemosensor **AT** (*(E)-N-(1-(1H-phenothiazin-2yl)-ethylidene)-3-((E)-(2-phenylhydrazono)methyl)aniline*) were designed and characterized by FT-IR, ESI-MS, ^1H and ^{13}C NMR

spectroscopic methods (**Fig. S1-S4**, ESI[†]). Further studies, UV-vis, and fluorescence spectroscopic performed using HEPES buffer solution in EtOH: H₂O (1:4, v/v, pH=7.0) and under excitation wavelength at 290 nm. The fluorescence intensity at 428 nm was measured for sensitivity and selectivity of Cr³⁺ and Pb²⁺ ions.

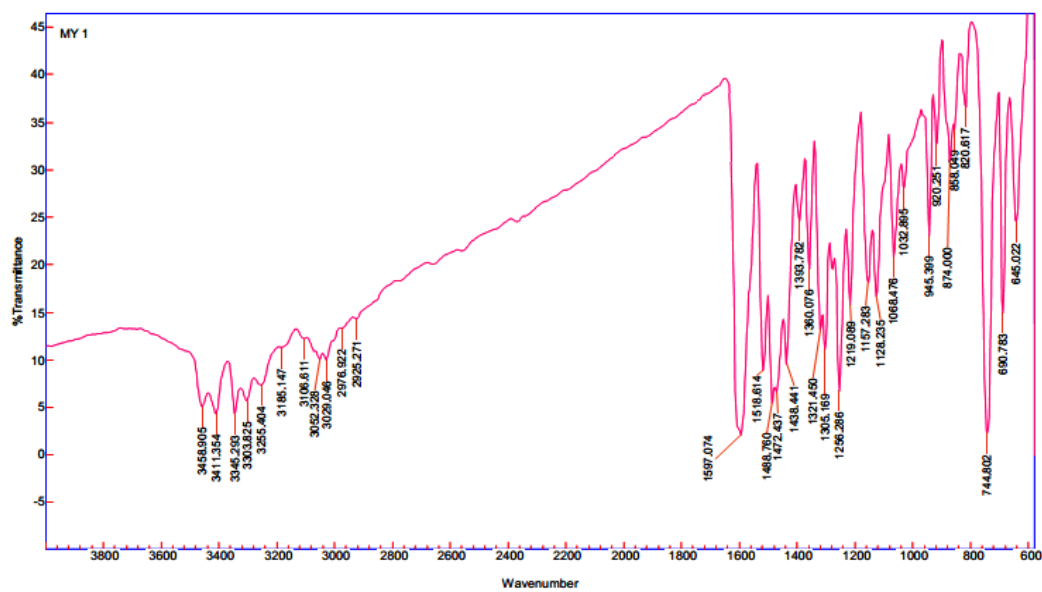


Fig. S1. FT-IR spectrum of AT

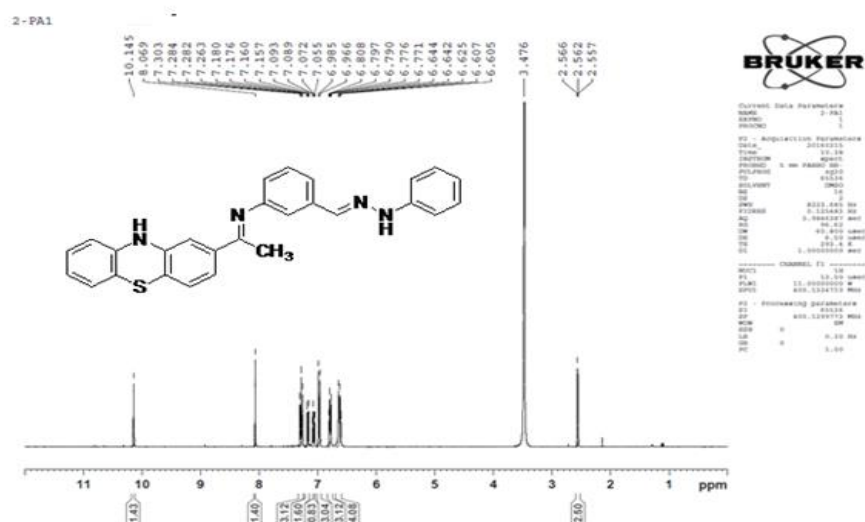
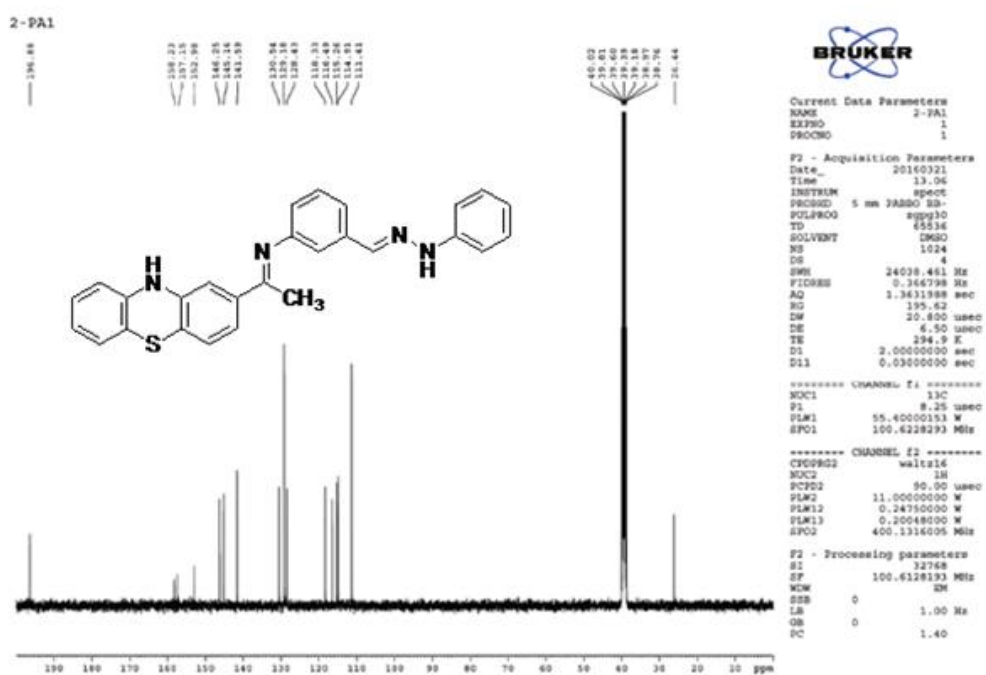


Fig. S2. ¹H spectrum of AT



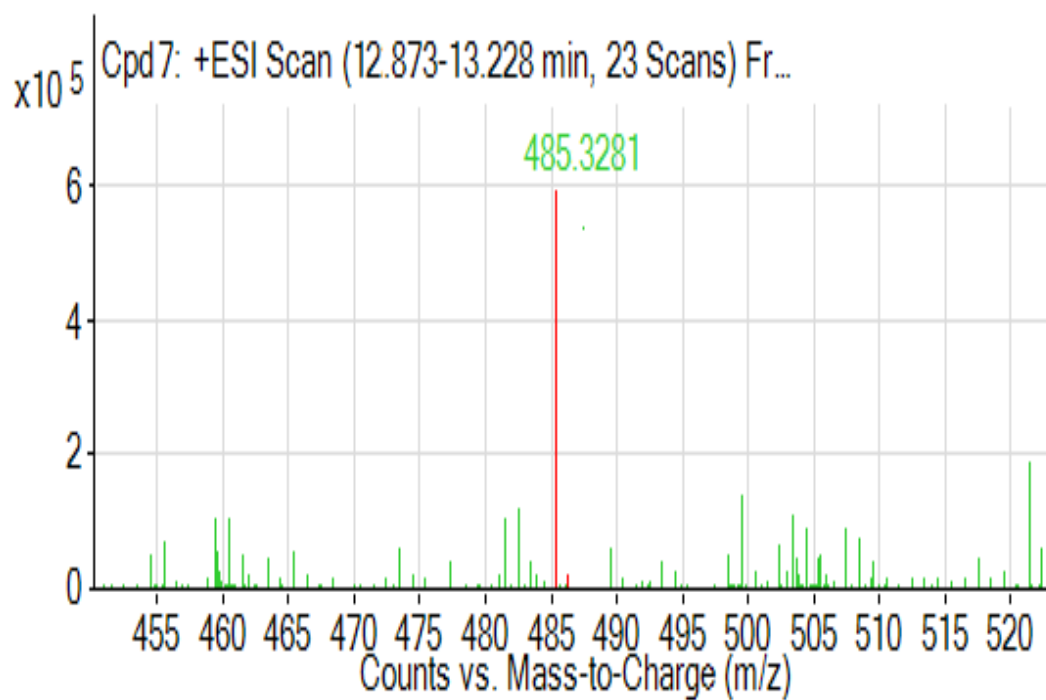


Fig.S5. ESI-MS spectrum of AT+Cr³⁺

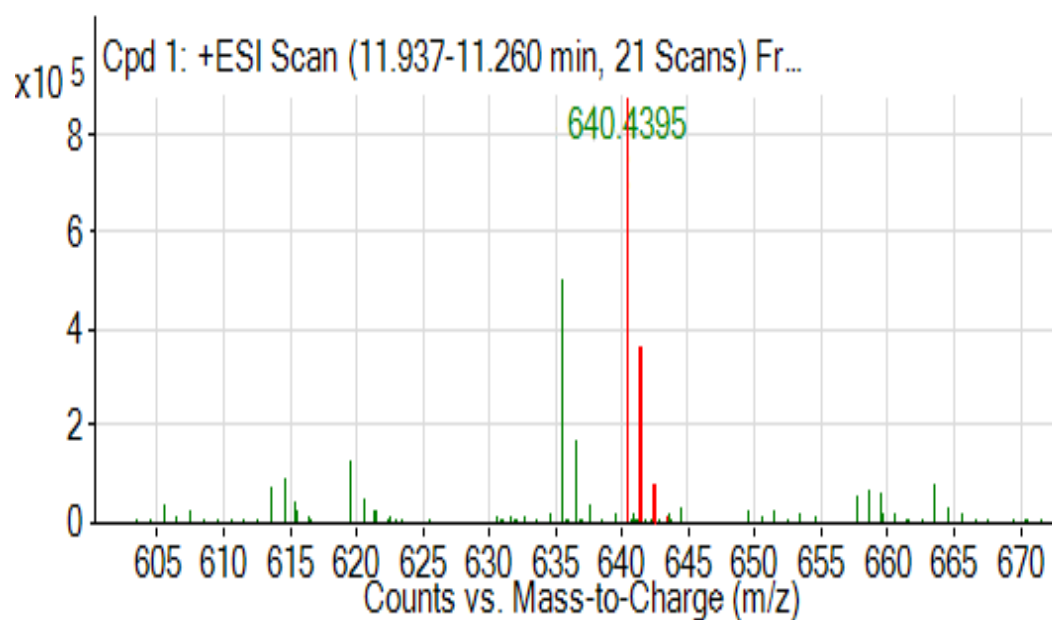


Fig.S6. ESI-MS spectrum of AT+Pb²⁺

2.3.1. Absorption studies

The sensing behavior of **AT** ($1.0 \times 10^{-5} \text{ M}^{-1}$) towards various metal ions such as Zn^{2+} , Sn^{2+} , Sr^{2+} , Cu^{2+} , Fe^{3+} , Mg^{2+} , Cr^{3+} , Cd^{2+} , Hg^{2+} , Al^{3+} , Ca^{2+} , Ni^{2+} , Mn^{2+} , Pb^{2+} , and Ti^{3+} ($1.0 \times 10^{-3} \text{ M}^{-1}$) have been studied in HEPES buffer solution in EtOH: H_2O (1:4, v/v, pH=7.0) investigated by UV-Vis absorption spectroscopic in 100% aqueous solution. The **AT** solution exhibited yellow color to colorless solution in the naked eye under UV-Vis lamp (**Fig.1**) in the presence of two alkali metal ions (Ca^{2+} , Mg^{2+}), one alkali earth metal ion (Mg^{2+}), and transition metal ions (Ag^+ , Cu^{2+} , Fe^{3+} , Co^{2+} , Ni^{2+} , Mn^{2+} , Zn^{2+} , Cd^{2+} , and Mg^{2+}).

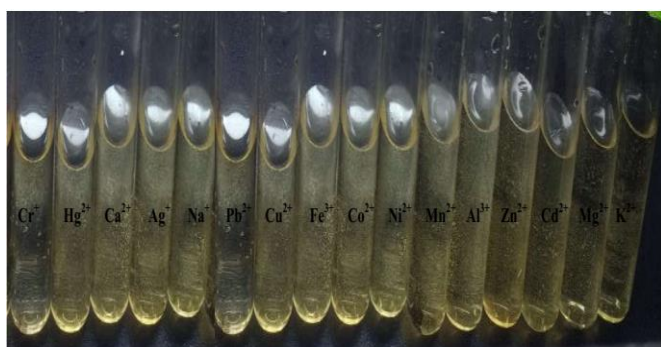


Fig.1. The colourless of metal solution made in compound of **AT**

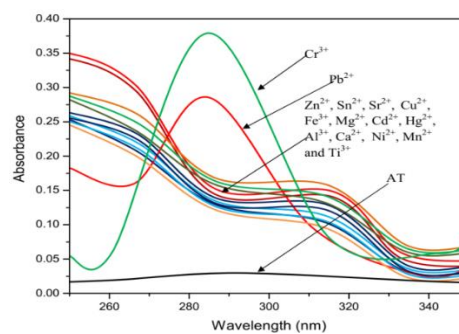


Fig.2. Absorption spectrum of **AT** (100 μM) with different metal ion (100 μM) used in HEPES buffer solution in EtOH:H₂O (1:4, v/v) pH=7.0.

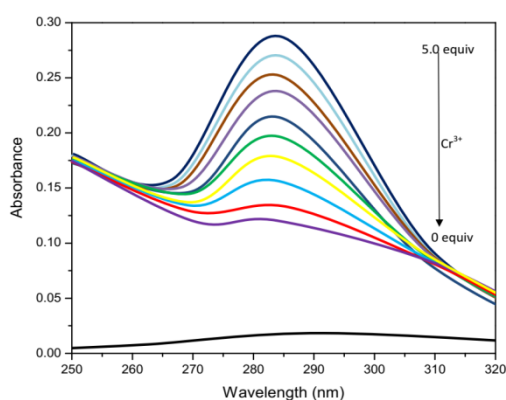


Fig.3. UV-visible titration spectra of **AT** (10 μM) and) in the presence of different concentrations of Cr^{3+} (10 μM) in ethanol.

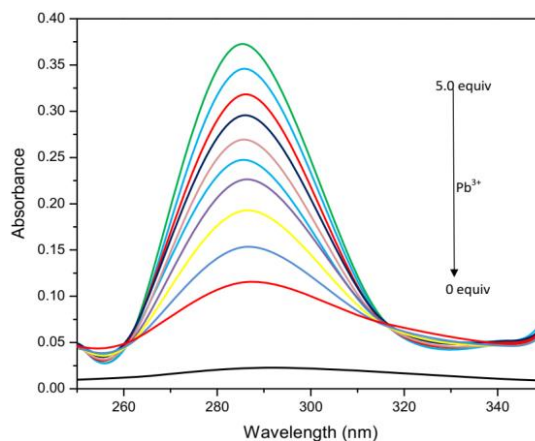


Fig.4. UV-visible titration spectra of **AT** (10 μM) and) in the presence of different concentrations of Pb^{2+} (10 μM) in ethanol.

The **AT** solution demonstrated a strong absorption band around 284 nm observed due to π - π^* electronic transition with detection of Cr^{3+} and Pb^{2+} and without any interference by other metal ions. When **AT** (100 μM) solution was added into different metal ion (100 μM) solutions showed a new absorption band centred at 315 nm observed by blue (hypsochromic) shift and absorption peaks at 284 nm shown in hyperchromic shift (**Fig.2**) The Cr^{3+} and Pb^{2+} (10 μM) solutions was added by incrementally to **AT** (10 μM) in HEPES buffer solution in EtOH: H_2O (1:4, v/v, pH=7.0) (**Fig.3** and **Fig.4**). Then gradually the absorbance intensity at 315 nm was decreased after adding increase concentration of 0, 0.5, 1.0, 1.5, 2.0, 2.5, 3.0, 3.5, 4.0, 4.5, and 5.0 of Cr^{3+} and Pb^{2+} . For Pb^{2+} , two isobestic points at 260 and 317 nm were noticed depending on the increased concentration of Pb^{2+} .

2.3.2. Emission studies

The fluorescence measurements carried out with excitation wavelength at 290 nm **AT** ($1.0 \times 10^{-5} \text{ M}^{-1}$) and metal ions ($1.0 \times 10^{-6} \text{ M}^{-1}$) in (10 mM) HEPES buffer solution of EtOH: H_2O (1:4, v/v, pH=7.0). The pale yellow solution of **AT** changed to light blue for Cr^{3+} ions and colorless for Pb^{2+} ions (**Fig.5**). The probe **AT** (100 μM) solution exhibited enormously weak fluorescence intensity at 428 nm and significantly changed due to role as for dual chemosensor for Cr^{3+} (100 μM) and Pb^{2+} (100 μM) were shifted to longer wavelength due to bathochromic shift (**Fig. 6**).

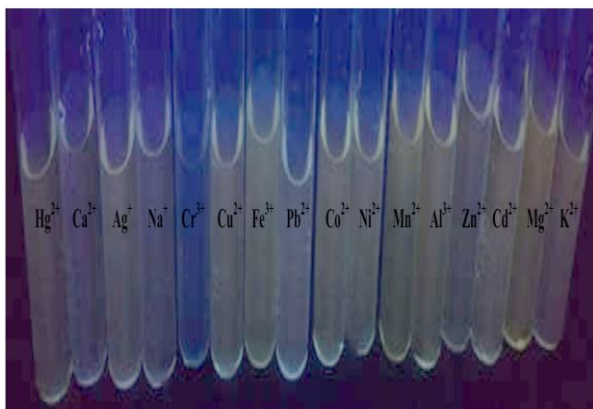


Fig.5. The colourless of metal solution made in compound of **AT**

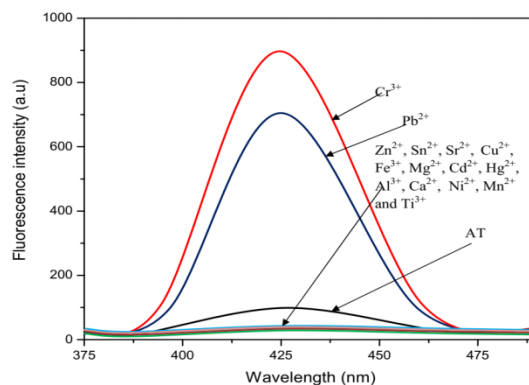


Fig.6. Fluorescence spectrum of **AT** (100 μM) with different metal ion (100 μM) used in 10mM HEPES buffer solution in EtOH: H_2O (1:4, v/v) pH=7.0.

Other metal ions had no influence on the emission intensity. The highly sensitive and selective detection of Cr^{3+} and Pb^{2+} was determined by “turn-on” fluorescence performed in a 100% aqueous solution. This is possibly due to PET (Photoinduced Electron Transfer) mechanism method. Upon addition of 5.0 equiv. of Cr^{3+} and Pb^{2+} (20 μM) to **AT** (20 μM) solution displayed fluorescence enhancement at 428 nm and was successively decreased after adding higher conc. of Cr^{3+} and Pb^{2+} metal ion (**Fig.7** and **Fig.8**).

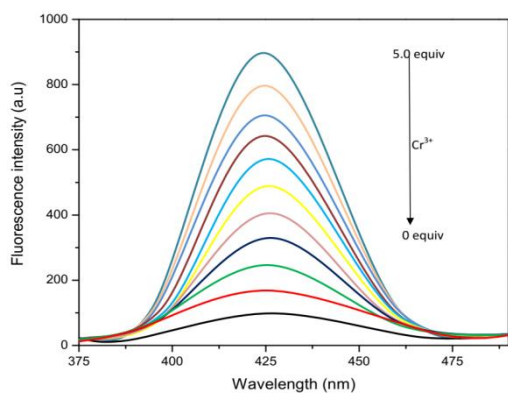


Fig.7. Fluorescence titration spectra of **AT** (20 μM) in the presence of different concentrations of 0.5 equiv. Cr^{3+} (20 μM) in ethanol.

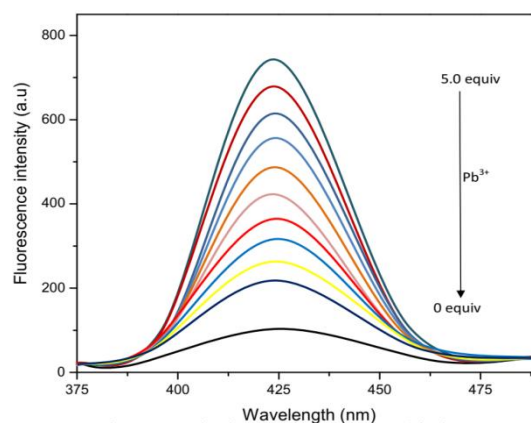


Fig.8. Fluorescence titration spectra of **AT** (20 μM) in the presence of different concentrations of 0.5 equiv Pb^{3+} (20 μM) in ethanol.

The Job plot was constructed by probe **AT** binding with Cr^{3+} and Pb^{2+} , 1:1 stoichiometry complex (0.5 equiv. of Cr^{3+} and Pb^{2+} with **AT** (0.5 equiv.)) has been predicted as 0.6 μM concentration (**Fig.9** and **Fig.10**). The binding constant of **AT** (10 μM) with Cr^{3+} and Pb^{2+} (10 μM) was calculated using fluorescence titration data and found to be $2.13 \times 10^4 \text{ M}^{-1}$ ($R^2=0.9991$) and $2.37 \times 10^4 \text{ M}^{-1}$ ($R^2=0.9996$) according to Benesi-Hildebrand equation (**Fig.11** and **Fig.12**). Furthermore, the detection limit was $8.63 \times 10^{-7} \text{ M}$ ($R^2=0.9992$) and $7.42 \times 10^{-7} \text{ M}$ ($R^2=0.9990$) towards using this equation $3\sigma/k$ (**Fig.13** and **Fig.14**) [58, 59].

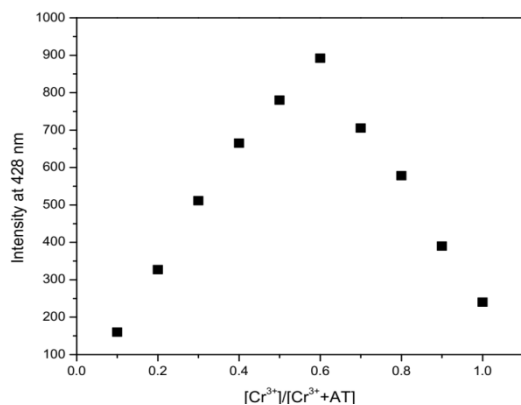


Fig.9. Job's plot of AT (20 μM) solution with Cr^{3+} (20 μM) ion

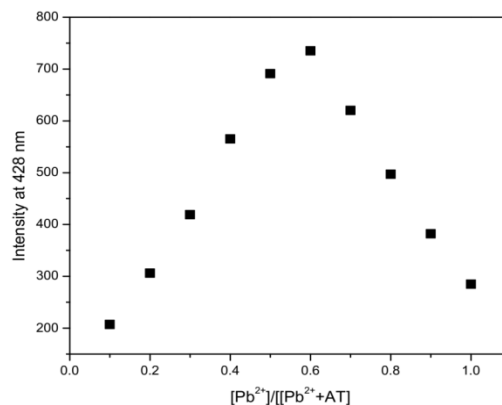


Fig.10. Job's plot of AT (20 μM) solution with Pb^{2+} (20 μM) ion

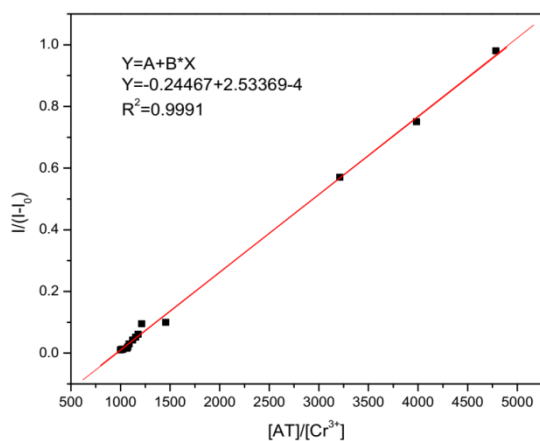


Fig.11. Benesi-Hildebrand equation of AT (10 μM) with different concentration Cr^{3+} (10 μM) ion used in 10mM HEPES buffer solution in EtOH: H_2O (1:4, v/v) pH=7.0.

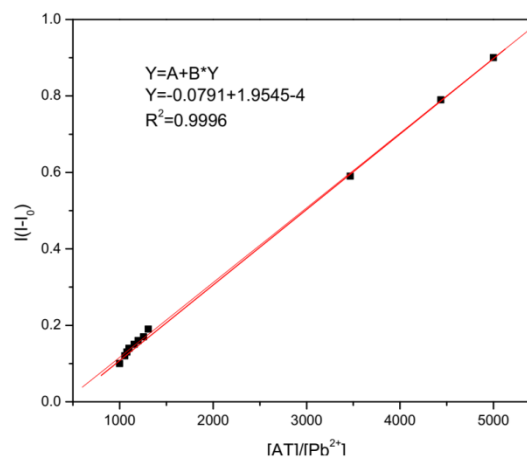


Fig.12. Benesi-Hildebrand equation of AT (10 μM) with different concentration Pb^{2+} (10 μM) ion used in 10mM HEPES buffer solution in EtOH: H_2O (1:4, v/v) pH=7.0.

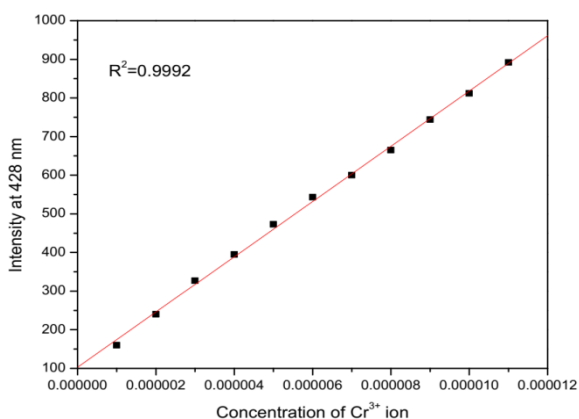


Fig.13. Detection limit of AT (10 μM) with different Cr^{3+} (10 μM) ion used in 10mM HEPES buffer solution in EtOH: H_2O (1:4, v/v) pH=7.0.

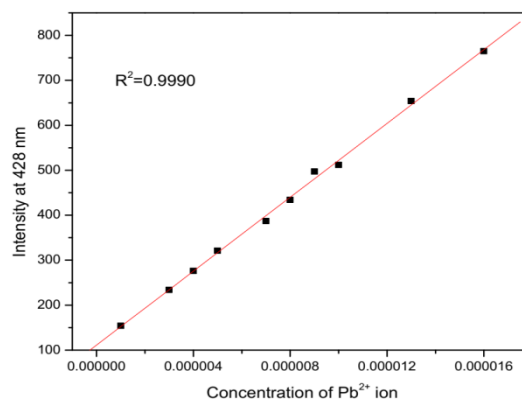


Fig.14. Detection limit of AT (10 μM) with different Pb^{2+} (10 μM) ion used in 10mM HEPES buffer solution in EtOH: H_2O (1:4, v/v) pH=7.0.

Consequently, the performance of **AT** allowed detection of different concentrations of Cr^{3+} and Pb^{2+} in (7.4 μM) in drinking water. Different metal ions (0.5equiv of Sn^{2+} , Sr^{2+} , Cu^{2+} , Fe^{3+} , Mg^{2+} , Cr^{3+} , Cd^{2+} , Hg^{2+} , Al^{3+} , Ca^{2+} , Ni^{2+} , Mn^{2+} , Pb^{2+} and Ti^{3+}) were added into **AT** (10 μM) solution of 20 mM of HEPES buffer solution in EtOH:H₂O (1:4, v/v, pH=7.0) (**Fig.15** and **Fig.16**). The emission intensity at 428 nm for 0.3 equiv of Cr^{3+} and Pb^{2+} shows high values, however, the presence of Cr^{3+} and Pb^{2+} binding with others metal ions did not affect the sensing ability of **AT** (10 μM) against Cr^{3+} and Pb^{2+} .

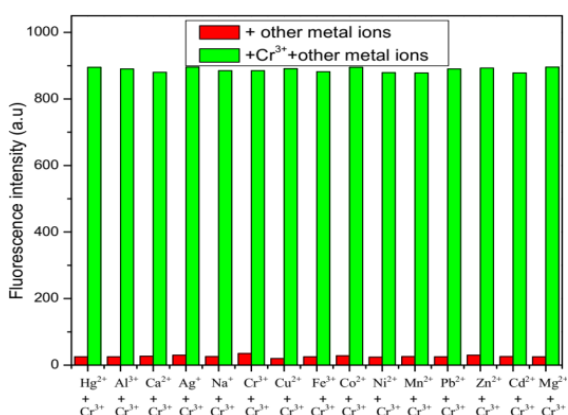


Fig.15. The fluorescence changes of **AT** (10 μM) with Cr^{3+} (5 equiv.) and upon addition of Hg^{2+} , Al^{3+} , Ca^{2+} , Ag^+ , Na^+ , K^+ Cu^{2+} , Fe^{3+} , Co^{2+} , Ni^{2+} , Mn^{2+} , Pb^{2+} , Zn^{2+} , Cd^{2+} , and Mg^{2+} were prepared in 20 mM of HEPES buffer solution EtOH:H₂O (1:4, v/v) pH=7.0.

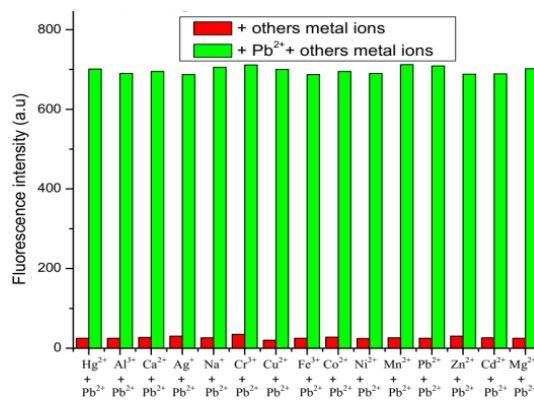
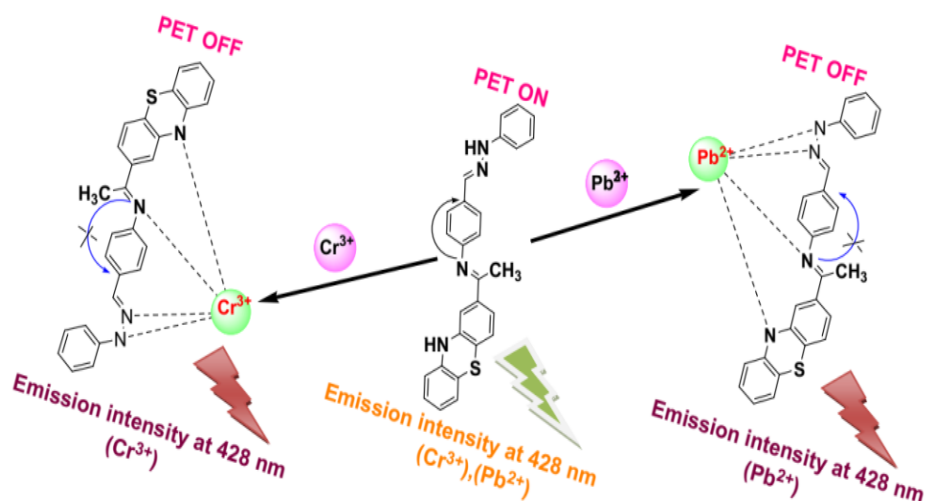


Fig.16. The fluorescence changes of **AT** (10 μM) with Pb^{3+} (5 equiv.) and upon addition of Hg^{2+} , Al^{3+} , Ca^{2+} , Ag^+ , Na^+ , K^+ Cu^{2+} , Fe^{3+} , Co^{2+} , Ni^{2+} , Mn^{2+} , Pb^{2+} , Zn^{2+} , Cd^{2+} , and Mg^{2+} were prepared in 20 mM of HEPES buffer solution. EtOH:H₂O (1:4, v/v) pH=7.0.

2.3.3. Binding mechanism

The fluorescence results indicated photoinduced electron transfer (PET) pathway, and it was caused by the stable complex formation **AT-Cr³⁺** and **AT-Pb²⁺** via complex formation involving imine bond $-\text{CH}=\text{N}-$ and NH resulting due to contribution of lone pairs of imine nitrogen which inhibited PET process. Further, after binding complex Cr^{3+} and Pb^{2+} to **AT**, $\text{C}=\text{N}$ isomerization and the photoinduced electron transfer (PET) effect were hindered [60, 61]. Enhancement of the fluorescence intensity for Cr^{3+} and Pb^{2+} can be explained by PET-ON to PET-OFF with binding. The ESI-mass spectrum confirmed by binding complex and exact molecular weight present at 485.32 m/z shifted from 434.16 m/z

after adding 0.5 equiv of Cr^{3+} into **AT** solution, whereas, after added 0.5equiv. Pb^{2+} concentration into **AT** solution, which provided value at 640.43 m/z, however, it was changed and enormous shifted due to the normal mass value at 434.16 m/z, therefore – $\text{CH}=\text{N}$ - and NH group much potentially participated in complexation of **AT**- Cr^{3+} and **AT**- Pb^{2+} as in **Scheme 2**.



Scheme 2 Synthesis of compound **AT**- Cr^{3+} and Pb^{2+}

2.3.4. Effect of pH

The scope of chemosensor would be much affected by pH value sensing capability hence it is necessary to suitably increment pH value in **AT** solution to detect Cr^{3+} and Pb^{2+} very efficiently. This is revealed in (**Fig.17** and **Fig.18**). Over the pH range of 1-13, **AT** solution of Cr^{3+} and Pb^{2+} shows no significant change. The changes in fluorescence intensity under strong acid condition indicates inhibition of complex formation between **AT** and Cr^{3+} and Pb^{2+} ions due to protonation of Schiff base compound **AT**. Whereas, under the strong basic condition to the formation complexes of **AT** binding with Cr^{3+} and Pb^{2+} prove that inhibited because of sufficiently methyl atom is performed. However, **AT** exhibited

great sensing action to Cr^{3+} and Pb^{2+} over the pH range from 4 to 10, and may successfully detect Cr^{3+} and Pb^{2+} in sensible applications in this large pH range.

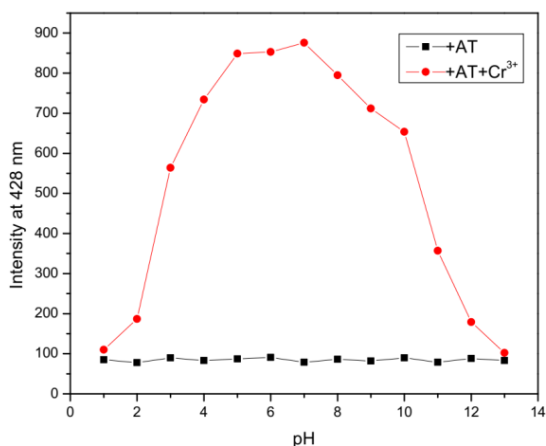


Fig.17. Effect of pH on the fluorescence intensity at 428nm of **AT** (10 μM) in 2 M aqueous solution in the presence of Cr^{3+} .

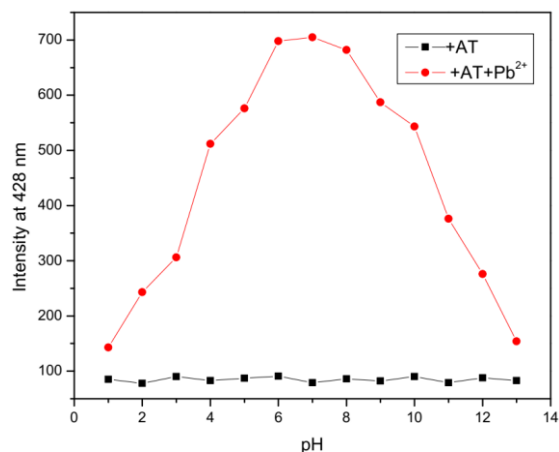


Fig.18. Effect of pH on the fluorescence intensity at 428nm of **AT** (10 μM) in aqueous solution in the presence of Pb^{2+} .

2.3.5. Reversibility study

The reversible response is important for a suitable fluorescent chemosensor. The fluorescence spectrum of **AT**(10 μM) solution with an alternating increase of 3 equiv. of Cr^{3+} and Pb^{2+} and EDTA solution in EtOH:H₂O (1:4, v/v, pH=7.0, 10 mM HEPES buffer) was measured. The emission intensity measured at 436 nm, upon addition was of restored on addition of Cr^{3+} and Pb^{2+} solution to **AT**. Moreover, the fluorescence ON-OFF-ON responsibility upon alternate addition of Cr^{3+} and Pb^{2+} to EDTA solution of **AT** under the UV lamp 365 nm was reversible and could be used and the reversible cycle for at least four times (**Fig.19** and **Fig.20**). Thus, **AT** can be used as an excellent reversible fluorescent chemosensor detecting Cr^{3+} and Pb^{2+} in 100% aqueous solution.

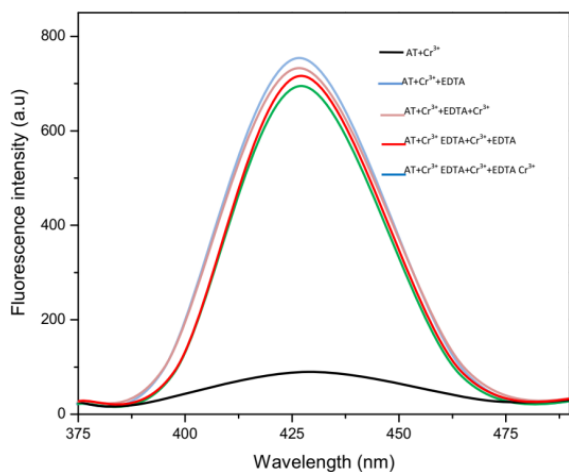


Fig.19. Fluorescence spectrum of AT (10 μM) solution upon addition of Cr^{3+} (3 equiv.) and EDTA (3 equiv.) in HEPES buffer solution EtOH:H₂O (1:4, v/v)

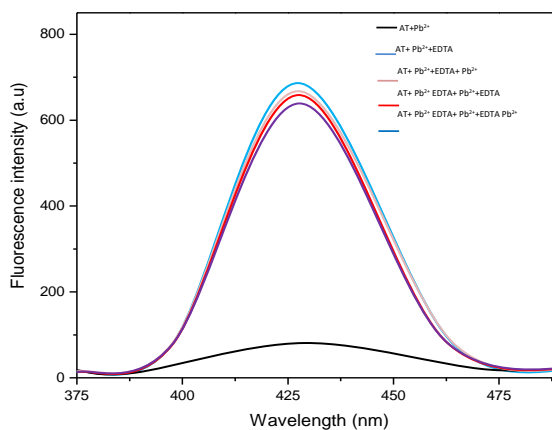


Fig.20. Fluorescence spectrum of AT (10 μM) solution upon addition of Pb^{2+} (3 equiv.) and EDTA (3 equiv.) in HEPES buffer solution EtOH:H₂O (1:4, v/v).

2.3.6. Theoretical studies

2.3.6.1. HOMO and LUMO analysis

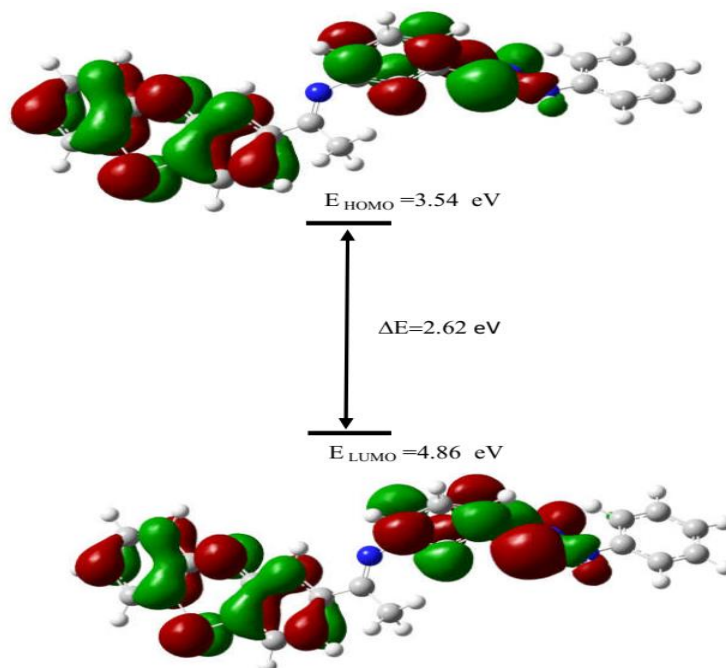


Fig.21. Energy diagram of HOMO and LUMO orbital of AT and its corresponding metal complexes calculated at the DFT level using a B3LYP/6-31G* basis set.

The theoretical calculation studies HOMO-LUMO predict the energy gap value investigated in Gaussian 09. HOMO energy means that the electron-donating ability, whereas, LUMO means that electron-accepting ability for the HOMO-LUMO energy gap as shown in **Fig.21**. The calculated lowest energetic gap is ($\Delta E_{\text{gap}}=2.62\text{eV}$), while the HOMO energy is ($E_{\text{HOMO}}=-3.54\text{eV}$) and the lowest LUMO energy is ($E_{\text{LUMO}}=-4.38\text{eV}$), Therefore, higher energy allowed the greatest electron donor and electron acceptor respectively, and HOMO and LUMO has two parameters and which is related to the orbital energy.

2.3.6.2. Molecular electrostatic potential (MEP) and Mulliken charge

Molecular electrostatic potential (MEP) is sensitive to the charge distribution and depends on the name of electrophilic and nucleophilic reaction. The MEP commonly is used to study hydrogen bonding interaction and even biological detection. The surface complex shows different energy of the molecular electrostatic potential.

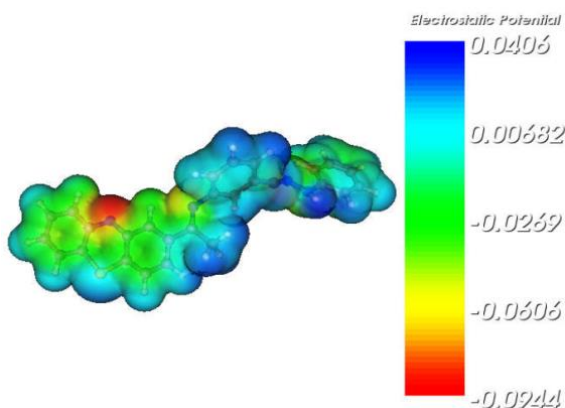


Fig.22. Molecular electrostatic potential surface of **AT**

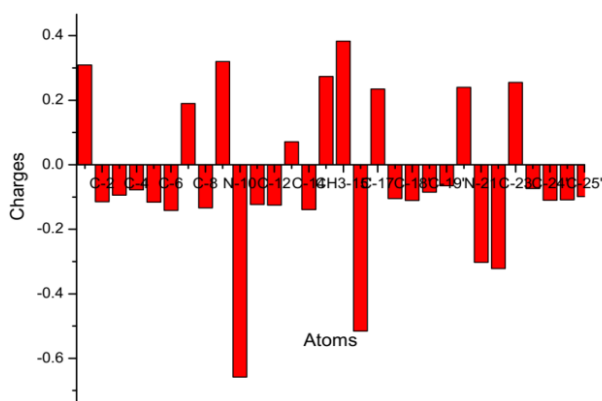


Fig.23. Mulliken atomic charges for **AT**

The result of **AT** expressed increase with potential order blue >green>yellow>red, where blue color is the highest electrostatic potential energy, red color is the lowest electrostatic potential energy and green color is neutral stability as shown in **Fig.22**. The Mulliken charge calculations carried out by computational chemistry are shown in **Fig. 23**,

C19 atom is the highest atomic molecular orbital, N10 is the lowest atomic molecular orbital due to decreased atomic charge and all molecular orbital range is C2 to C25 (**Fig.23**).

2.3.6.3. Cytotoxicity

The cytotoxicity responses of **AT** were studied with various concentrations. This is evident from cellular imaging. Thus, these results show **AT** that as an efficient candidate under intracellular concentration for certain biological conditions and justify its cytotoxic effect and MTT assay in **AT**-treated HepG2 cancer cells for up to 5 h. The 20 μ M concentrations of **AT** demonstrated important cytotoxic effects at least up to 4 h on HepG2 cells. The synthesized **AT** was investigated for cytotoxic activity using the cell line HepG2 in the MTT study, which tests the impact of cellular mitochondrial metabolism on complexes. Tested compounds of ever-increasing concentrations with two days for cells tested. Microscopic images of cancer control cells and morphological changes apoptotic in the **AT**-treated HepG2 cell line presented in **Fig. 24**. The tests showed limited cell death at compound **AT**. At 77 % of IC_{50} values, the demonstrated good inhibition on the HepG2 cell. The **AT-IC₅₀** values (**Fig. 25**) show that an inhibitory action against cancer cells is more potent. The NH group that carries the phenyl group shows the highest IC_{50} value, convincing us that the electronic effect may be one of the determinants of anticancer activity in the compound **AT**. The IC_{50} values of **AT** against HepG2 cell lines are given in **Table. 1**.

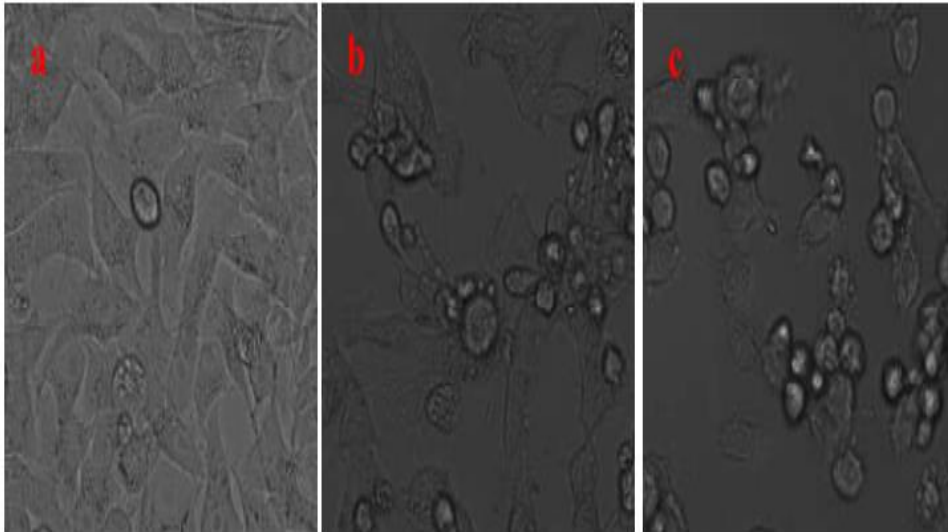


Fig 24. Live cell images of AT: (a) before and (b and c) after treatment with AT examined by fluorescence microscopy.

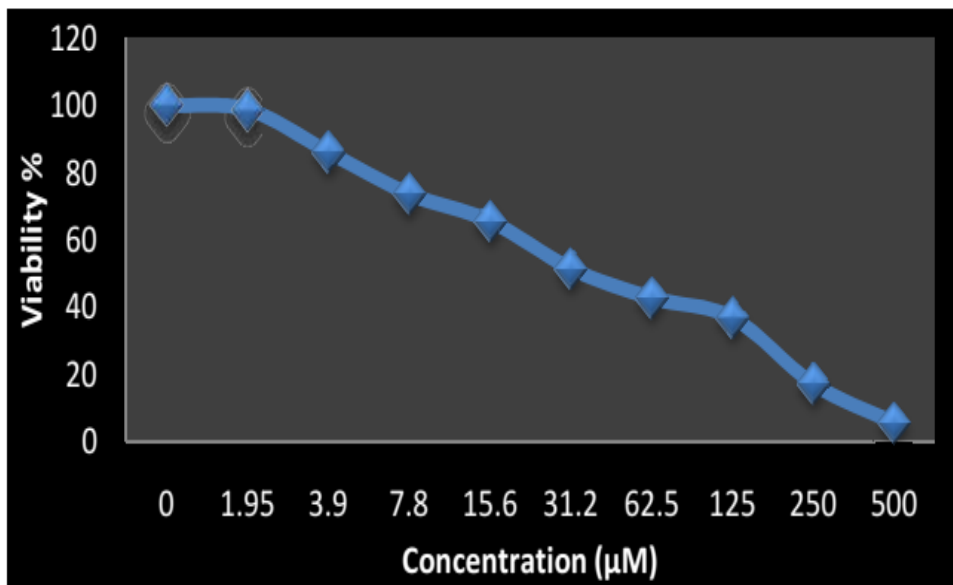


Fig 25. The IC₅₀ values of AT against HepG2 cell lines.

Table 1. The IC₅₀ values of AT against HepG2 cell lines.

Anticancer effect of AT on HepG2 cell line	
Concentration (μM)	Viability %
	AT
0	100
1.95	98.81
3.9	86.15
7.8	73.66
15.6	65.59
31.2	51.45
62.5	42.67
125	36.77
250	17.11
500	5.45

2.3.6.4. Living cell imaging

The **AT** chemosensor is also being tested for imagery of living cells. First, a strong **AT** fluorescence view of HepG2 cell-incubated human liver cancer cells (**Fig. 26**). The overlap of fluorescence and the picture of the bright field reveal the emission of fluorescence within the intracellular region. Good cell membrane permeability was noted for the chemosensor **AT**. The visualization of fluorescence of living cells followed additional treatment with Cr³⁺/Pb²⁺ ions. These observations suggest an efficient binding of chemosensors with **AT** to Cr³⁺/Pb²⁺ ions.

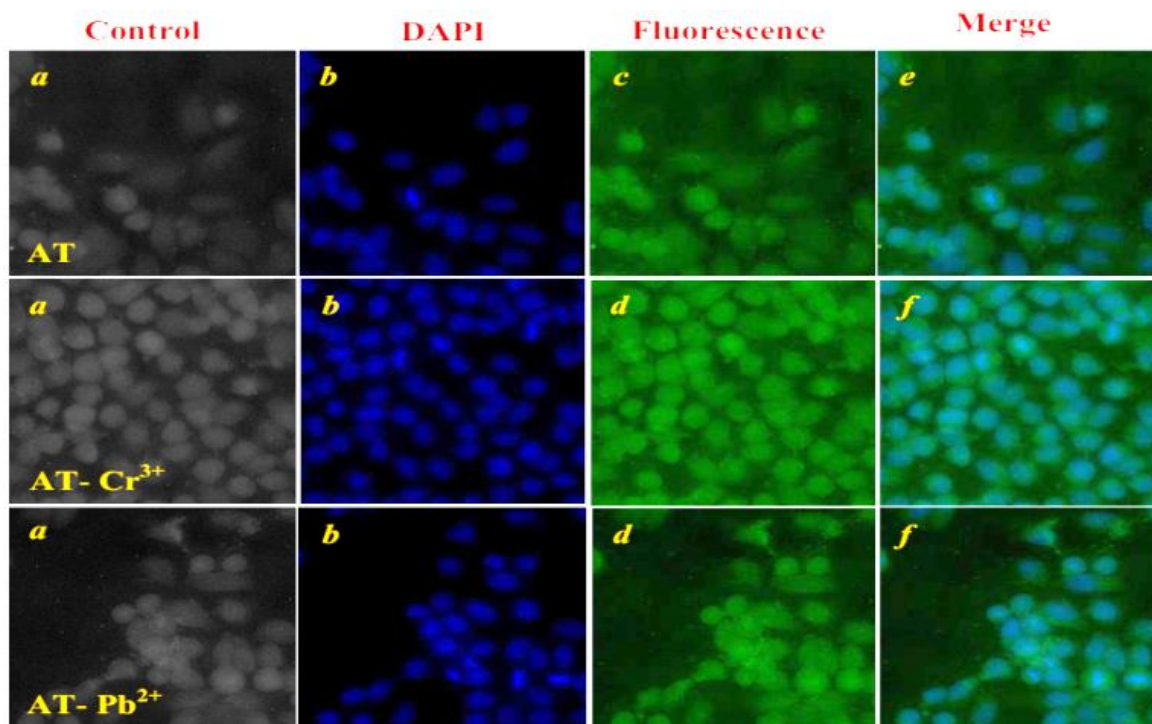


Fig 26. Confocal fluorescence and merged images of HepG2 cells were stained with DAPI, *AT*-Cr³⁺ and *AT*-Pb²⁺, respectively. (a) HepG2 cells incubated with *AT*-Cr³⁺ and *AT*-Pb²⁺ (5 μ M) only, (b) HepG2 cells pre-incubated with *AT*-Cr³⁺ and *AT*-Pb²⁺ (5 μ M) followed by 0.1 mM *AT*, (c) cells were stained with both DAPI and 5 μ M *AT*-Pb²⁺ and *AT*-Cr³⁺; (d) cells of (c) further incubated with *AT* (0.1 mM) for another 30 min, (e) and (f) were merged images. Scale bar, 30 μ m.

2.4. CONCLUSIONS

In summary, the fluorescent chemosensor has been successfully designed and we synthesized as a simple Schiff-base of (E)-N-(1-(1H-phenothiazin-2yl)-ethylidene)-3-((E)-(2-phenylhydrazono) methyl) aniline and studied their PET mechanisms. The experiments indicated report chemosensor **AT** was a highly sensitive and selective chemosensor for Cr³⁺ and Pb²⁺ in a HEPES buffer solution in EtOH: H₂O (1:4, v/v, pH=7.0). Significantly, the probe showed a “turn-on” fluorescence response to Cr³⁺ and Pb²⁺ and emission intensity at 428 nm (excitation wavelength 290). The fluorescence improvement with high selectivity and sensitivity was attributed to photoinduced electron transfer (PET) and also competitive metal studies. The Job plot of **AT** binding with Cr³⁺ and Pb²⁺ demonstrated a 1:1

stoichiometry complex predicted at 0.6 μM concentration. Further, the binding constant was calculated and found to be $2.13 \times 10^4 \text{ M}^{-1}$ ($R^2=0.9991$) and $2.37 \times 10^4 \text{ M}^{-1}$ ($R^2=0.9996$) according to the Benesi-Hildebrand equation and detection limit at $8.63 \times 10^{-7} \text{ M}$ ($R^2=0.9992$) and $7.42 \times 10^{-7} \text{ M}$ ($R^2=0.9990$) towards using this equation $3\sigma/k$ due to WHO (World Health Organization) allowed ($7.4\mu\text{M}$) in drinking water. The pH experiment covered a range from 4-10 in sensing application. EDTA titration was examined and was found to be reversible and irreversible due to Cr^{3+} and Pb^{2+} added into **AT** solution. The theoretical calculation was carried out by B3LYP/6-31*G in Gaussian 09 program. The **AT** has a potent in-vitro HepG2 cell line against the cytotoxic, living cell images. It is worth noting that the receptor **AT** would be a beneficial addition to academia for its optical properties and functional application to biomedical industries which will open door to the establishment of these findings. The molecule is useful in sensing and drug-carrying applications.

2.5. REFERENCES

1. A.P. De Silva, H.Q.N. Gunaratne, T. Gunnlaugsson, A.J. Huxley, C.P. McCoy, J.T. Rademacher, T.E. Rice, Signaling recognition events with fluorescent sensors and switches, *Chem.Rev.*, 1997, 97, 1515–1566.
2. L.Prodi, F.Bolletta, M.Montalti, N.Zaccheronii, Luminescent chemosensors for transition metal ions, *Coord. Chem. Rev.*, 2000, 205, 59–83.
3. J.P. Desvergne, A.W. Czarnik (Eds.), *Chemosensors of Ions and Molecular Recognitions*; NATO ASI Series, Kluwer Academic Dordrecht, the Netherlands, 1997.
4. B.Valeur, I. Leray, Design principles of fluorescent molecular sensors for cation recognition, *Coord. Chem. Rev.*, 2000, 205, 3–40.
5. L. Fabbrizzi, A.Poggi, Sensors and switches from supramolecular chemistry, *Chem. Soc. Rev.*, 1995, 24, 197–202.
6. W.Kaim, B. Schwederski, *Bioinorganic Chemistry: Inorganic Elements in Chemistry of Life, an Introduction and Guide*, Wiley Interscience, New York, 1991.

7. C.D. Klassen, M.D. Amdur, J.Dull, Casarett and Doull's Toxicology, 3rd Ed., MacMillan, New York, 1986.
8. Y.Li, J. Wu, X. Jin, J.Wang, S.Han, W.Wu, J.Xu, W.Liu, X.Yao and Y.Tang, Dalton Trans., 2014, 43, 1881. (b) Z.Zhanga, S.Lu, C.Sha, D.Xu, Sens. Actuators B 208 (2015) 258. (c) J.M. Junga, S. Y. Lee, C. Kim, Sens. Actuators B., 2017, 251, 291. (d) Jo, T. G. Jo, M.Jung, J.Han, M. H. Lim, C.Kim, RSC Adv., 2017, 7, 28723.
9. A. Levina, P. A. Lay, The Nutritional Biochemistry of Chromium (III), Elsevier, 2nd edn, 2019, pp. 281–321 (b) S.Mishra, R. N. Bharagava, J. Environ. Sci. Health, Part C Environ. Carcinog. Ecotoxicol. Rev., 2016, 34, 1 (c) H.Arakawa, R. Ahmad, M.Naoui, H. A. Tajmir- Riahi, J. Biol. Chem., 2000, 275, 10150.
10. E.Jorge, M.Rocha, I.Fonseca, M.Netto, Talanta., 2010, 81, 556-564.
11. C.Capellos, B. H. Bielski, Kinetic systems: mathematical description of chemical kinetics in solution, 1972.
12. M. C. Pannain, R. E. Santelli, Talanta., 1995, 42, 1609-1617.
13. V.Bravo, S.Gil, A.M.Costero, M.N. Kneeteman, U. Llaosa, P.M. Mancini, L.E. Ochando, M.Parra, Tetrahedron., 2012, 68, 4882- 488.
14. J. Y. Jung, S. J. Han, J. Chun, C. Lee, and J.Yoon, Dyes Pigm., 2012, 94, 423-426.
15. D. Li, C-Y. Li, H-R. Qi, K-Y. Tan and Y-F. Li, Sens. Actuators, B., 2016, 223, 705-712.
16. M.Sarkar, S.Banthia, and A. Samanta, Tetrahedron Lett., 2006, 47, 7575-7578.
17. S.Goswami, K.Aich, K. Das, A.Manna, S. Das, RSC Adv., 2013, 3, 2412-2416.
18. T. Q. Lai, L. G. Xiao, K.Deng, T. X. Liang, X. B. Chen, X. B. Peng, Y. Cao, ACS Appl. Mater. Interfaces., 2018, 1, 668- 675 (b) M.Trobe, M.D.Burke, Angew. Chem. Int. Ed., 2018, 16, 4192-4214 (c) J. Feist, J. Galego, F. J. G. Vidal, ACS Photonics., 2018, 1, 205-216.
19. D .Bellinger, H.L. Needleman, in Human Lead Exposure, ed, H. L. Needleman, CRC Press, Boca Raton, 1992, p. 191.
20. H. Needleman, Annu. Rev. Med., 2004, 55, 209.
21. M. L. Riess, J.K.Halm, J.Gen. Intern. Med., 2007, 22, 1212.
22. H. N. Kim, W.X. Ren, J. S. Kim, J.Yoon, Chem. Soc. Rev., 2012, 41, 3210.

23. V. M. Cangelosi V. L. Pecoraro, in *Binding, Transport and Storage of Metal Ions in Biological Cells*, ed. W. Maret, A. Wedd, Royal Society of Chemistry, Cambridge, 2014, p. 843.
24. J. Y. Kwon, Y. J. Yoon, Y. J. Lee, K. M. Kim, M. S. Seo, W. Nam, J. Yoon, *J. Am. Chem. Soc.*, 2005, 127, 10107.
25. L. Marbella, B. Serli-Mitasev, P. Basu, *Angew. Chem., Int. Ed.*, 2009, 48, 3996.
26. H. Lee, D. Bae, J. Park, H. Song, W. Han, J. Jung, *Angew. Chem., Int. Ed.*, 2009, 48, 1239.
27. T. Li, S. Dong, E. Wang, *J. Am. Chem. Soc.*, 2010, 132, 13156.
28. A. Thakur, D. Mandal, S. Ghosh, *Anal. Chem.*, 2013, 85, 1665.
29. H. Zhu, T. Yu, H. Xu, K. Zhang, H. Jiang, Z. Zhang, Z. Wang, S. Wang, *ACS Appl. Mater. Interfaces.*, 2014, 6, 21461.
30. B. Zhang, L. Lu, Q. Hu, F. Huang, Z. Lin, *Biosens. Bioelectron.*, 2014, 56, 243.
31. V. Luxami, R. Rani, A. Sharma, K. Paul, *J. Photochem. Photobiol. A.*, 2015, 311, 68.
32. S. Kuo, H. Li, P. Wu, C. Chen, Y. Huang, Y. Chan, *Anal. Chem.*, 2015, 87, 4765.
33. S. Deo, H. A. Godwin, *J. Am. Chem. Soc.*, 2000, 122, 174–175.
34. S. Araki, H. Sato, K. Yokoyama, K. Murata, *Am. J. Ind. Med.*, 2000, 37, 193–204.
35. N. Rifai, G. Cohen, M. Wolf, et al, *Ther Drug Monit.*, 1993, 15, 71–74.
36. H. Xue, X. J. Tang, L. Z. Wu, L. P. Zhang, C. H. Tung, *J. Org. Chem.*, 2005, 70, 9727–9734.
37. S. Sirilaksanapong, M. Sukwattanasinitt, P. Rashatasakhon, *Chem. Commun.*, 2012, 48, 293–295.
38. K. M. Lee, X. Chen, W. Fang, J. M. Kim, J. Yoon, *Macromol Rapid Commun.*, 2011, 32, 497–500.
39. Second ed. *Guidelines for Drinking Water Quality*, Vol. 2. Geneva: World Health Organization, 1996.
40. Li, X.H. Gao, X.H. Shi, Ma, W. H.M. *Chem. Rev.*, 2014, 114, 590–659.
41. Y.M. Yang, Q. Zhao, W. Feng, F.Y. Li, *Chem. Rev.*, 2013, 113, 192–270.
42. Z.P. Liu, Z.P. Z.P. He, Z. J. Guo, *Chem. Soc. Rev.*, 2013, 42, 1568–1600.

43. L.E. Kreno, K.Leong, O.K. Farha, M.Allendorf, R.P. Van Duyne, J.T. Hupp, *Chem. Rev.*, 2012, 112, 1105–1125.
44. O. Adegoke, P.B.C. Forbes, *Anal. Chim. Acta.*, 2015, 862, 1–13,.
45. V.K. Gupta, A.K. Singh, M.R. Ganjali, P. Norouzi, F.Faridbod, N. Mergu, *Sens. ctuators B Chem.*, 2013, 182, 642–651.
46. J. Cheng, K.We, X.Ma, X.Zhou, H.Xiang, *J. Phys. Chem., C* 2013, 117, 16552–16563.
47. B.Valeur, *Molecular Fluorescence Principles and Applications*, Wiley-VCH Verlag GmbH, New York, 2001 p. 341.
48. Mameli, M. Aragoni, M. C. Arca, M. Caltagirone, C. Demartin, F. Farruggia, G. deFilippo, G. Devillanova, F. A. Garau, A. Isaia, F. A Selective, Nontoxic, OFF–ON FluorescentMolecular Sensor Based on 8-Hydroxyquinoline for Probing Cd²⁺ in Living Cells, *Chem. Eur. J.*, 2010, 16, 919–930.
49. Z. Xu, Y. Xiao, X. Qian, J. Cui, D. Cui, Ratiometric and Selective Fluorescent Sensor for CuII Based on Internal Charge Transfer (ICT), *Org. Lett.*, 2005, 7, 889.
50. R.Alam, T.Mistri, P. Mondal, D.Das, S. K. Mandal, A. R. Khuda-Bukhsh, M.Ali, Anovel copper (II) complex as a nitric oxide turn-on fluorosensor: intracellular applications and DFT calculation, *Dalton Trans.*, 2014, 43, 2566.
51. P. D. Beer, *Transition-Metal Receptor Systems for the Selective Recognition and Sensing of Anionic Guest Species*, *Acc. Chem. Res.*, 1998, 31, 71.
52. H.Ueyama, M.Takagi, S.ATakenaka, Novel Potassium Sensing in Aqueous Media with a Synthetic Oligonucleotide Derivative Fluorescence Resonance Energy Transfer Associated with Guanine Quartet–Potassium Ion Complex Formation, *J. Am. Chem. Soc.*, 2002, 124, 14286–14287.
53. B.Schazmann, N.Alhashimy, D.Diamond, Chloride Selective Calix [4]arene Optical Sensor Combining Urea Functionality with Pyrene Excimer Transduction, *J. Am. Chem.Soc.*, 2006, 128, 8607.
54. X.Zhang, L. Guo, F. Y. Wu, Y. B. Jiang, Development of Fluorescent Sensing of Anions under Excited-State Intermolecular Proton Transfer Signaling Mechanism, *Org. Lett.*, 2003, 5, 2667.
55. J. S. Wu, W. M. Liu, X. Q. Zhuang, F. Wang, P. F. Wang, S. L. Tao, X. H. Zhang, S.K. Wu, S. T. Lee, Fluorescence Turn On of Coumarin Derivatives by Metal Cations: A New Signaling Mechanism Based on C=N Isomerization, *Org. Lett.*, 2007, 9, 33–36.

56. S.Kim, J.Y. Noh, K.Y. Kim, J. H. Kim, H. K. Kang, S. Nam, S.H. Kim, S. Park, C.Kim, *J. Inorg. Chem.*, 2012, 51, 3597–3602.
57. M. Shyamal, P. Mazumdar, S.Maity, G.P. Sahoo, A.Misra, *J. Phys. Chem. A.*, 2016, 120, 210–220.
58. V.Thomsen, D.Schatzlein, D. Mercurio, *Spectroscopy.*, 2003, 18, 112-114.
59. C. R. Lohani, J.M. Kim, S.Y.Chung, J. Yoon, K. H. Lee, *Analyst.*, 2010, 135, 2079-2084.
60. S.Sinha, B.Chowdhury, P. Ghosh, *Inorg. Chem.*, 2016, 55, 9212-9220.
61. L. McDonald, J.Wang, N.Alexander, H.Li, T.Liu, Y.Pang, *J. Mater. Chem. B.*, 2016, 120, 766-772.

Chapter III

Novel, Synthesis of E-4-((1-(10H-phenothiazin-2-yl)ethylidene)amino)-N-(pyrimidin-2-yl)benzenesulfonamide fluorescent chemosensor for high sensitivity and selectivity of Al³⁺ ion

3.1. INTRODUCTION

The development of chemosensors for the recognition of transition metal cations is an important area of research for industrial, biological, and environmental purposes [1,2]. In these conditions, owing to their facile syntheses, high sensitivity and selectivity, flexibility, and cost-effectiveness, such fluorescence chemosensors have gained exceptional attention [3,4]. One of the great topics among researchers is the selective and sensitive detection of metal cations in the production of chemosensors. In general, chemosensors have three components: receptor (capable of guest binding selectivity), spacer (which interfaces receptor and signaling), an active unit (capable of altering its properties during metal complexation). Different chemosensors of polycyclic aromatic hydrocarbons, aromatic ring, thiocarbazole, heterocyclic rings, carbazole, and even silatranes are reported [5-7]. Aluminium is the most plentiful metal ingredient and biological non-essential ingredient and too much used in manufacturing and everyday life such as food additives, water treatment devices, packaging products, cosmetics, and prescription drugs [8-11]. Compared to other metal ions in fluorescent chemosensors, the highly efficient identification of Al³⁺ in aqueous solutions is important due to its strong hydrated ability, lack of spectroscopic characteristics, and poor coordination power [12-14]. The Schiff base of fluorescent chemosensors has recently attracted a great deal of interest due to good coordination capacity, excellent photophysical efficiency, and simple synthesis [15-17]. Aluminium, on its deposition in the brain due to neuron degeneration followed by various disorders such as

Alzheimer's disease, Parkinson's disease, lateral amyotrophic sclerosis, encephalopathy on dialysis, and even multiple sclerosis has gained more significance and attention [18-21]. Thus it has encouraged ongoing studies on the potentially harmful impact of the atmosphere to enhance effective tools for Al^{3+} identification. These techniques include mass spectrometry, spectrophotometer, electrochemistry, inductively coupled plasma mass spectrometry, graphite furnace atomic absorption spectrometry, voltammetry, and liquid chromatography [22-24]. Sensing mechanisms such as chelation-induced enhanced fluorescence (CHEF), intermolecular charge transfer (ICT), fluorescence resonance energy transfer (FRET), and photoinduced electron transfer (PET) mechanisms are very relevant in fluorescence chemosensors [25-29]. For several more years, the Schiff base compound was used in chemistry [30]. There has been substantial use of non-transition metal complexes [30]. Several complexes of Schiff bases have found interesting uses in materials science [31]. In this case, in turn-on chemosensors, the benzenesulfonamide moieties received considerable attention owing to the formation of excimers and high quantum yield [32,33] due to their ability to show a peculiar shift in their emission wavelengths. Comparison with conventional analytical approaches requires, for example, colorimetric methods that could be accomplished by ultraviolet-visible absorption spectra with specific benefits, such as detection and even ease of operation, which could be carried out using on-site tests [34].

The benzenesulfonamide type Schiff base ligand (E)-4-((1-(10H-phenothiazine-2-yl)ethylidene) amino)-N-(pyrimidine-2-yl)benzene sulfonamide (**BT**) was studied in this work. The chemosensor activity for Al^{3+} ions in ethanol/water HEPES buffer solution (5 mM, pH 7.0; 1: 4 v/v) was demonstrated by the UV-visible and fluorescent spectroscopic system at room temperature. For PET process calculations, the complexation of **BT** with Al^{3+} metal ion was analyzed by FT-IR and ESI-MS research.

3.2. EXPERIMENTAL METHODS

3.2.1. Materials and instruments

All the chemical compounds were purchased commercially and used with more purification techniques. During the whole of the tests, distilled water was used. The chlorate or nitrate salts, solutions of various metal ions salts such as Zn^{2+} , Sn^{2+} , Sr^{2+} , Cu^{2+} , Fe^{3+} , Mg^{2+} , Cd^{2+} , Hg^{2+} , Al^{3+} , Ca^{2+} , Ni^{2+} , Mn^{2+} , Pb^{2+} , Cr^{3+} , and Ti^{3+} were prepared. The synthesized compound was confirmed by FT-IR, ^1H & ^{13}C NMR, and ESI-MS spectroscopy. Infrared measurement was calculated at $4000\text{--}400\text{ cm}^{-1}$ region on an Agilent Carry 630 FT-IR (Fourier Transfer Infrared) spectrometer. Initially, the ^1H NMR spectrum was recorded on a Bruker-400MHz and ^{13}C NMR 100 MHz enhancement of the employed TMS as an internal standard working in DMSO- d_6 , respectively. Fluorescence measurements were conducted with the Perkin-Elmer LS45 fluorescence spectrophotometer with a scan rate of 1200 nm range at room temperature.

3.2.2. Synthesis of Schiff base derivative BT

1-(10H-phenothiazin-2-yl)ethanone (0.48g, 2 mmol) and 4-amino-N-(pyrimidin-2-yl)benzenesulfonamide (0.42g, 2 mmol) were dissolved in absolute ethanol and stirred for 24 h at 60°C temperature. Then, the reaction was confirmed by TLC in benzene solvent used. After cooling to room temperature the resulting solution was poured into distilled water with stirring, a light yellow precipitate was obtained. The precipitate was filtered off and dried in vacuo. Further, it was recrystallized using absolute ethanol to get the desired product **BT**. Yield: 83%. FT-IR; (C=N) 1591 cm^{-1} , (NH) 3345 cm^{-1} **Fig.S1 (ESI †)**. ^1H NMR (500 MHz, DMSO- d_6) δ 8.53 (s, 1H), 8.54 (s, 1H), 8.83 (s, 1H), 7.682-7.661 (d, $J = 8.4$, 2H), 7.409-7.404 (D, $J = 2.0$, 2H), 7.389-7.384 (d, $J = 2.0$, 2H), 7.099-7.039 ($J = 2.4$, 2H), 6.980-6.961 (d, $J = 7.6$, 2H), 6.841-6.820 (m, $J = 8.4$, 2H), 6.723-6.700 (m, $J = 10.4$, 2H), 6.632-6.610 (2, $J = 8.0$, 2H), **Fig.S2 (ESI †)**. ^{13}C NMR (100 MHz, DMSO- d_6), δ (ppm):196.88, 158.23, 157.15, 152.98, 141.97, 141.16, 136.06, 129.77, 126.25, 126.11,

124.76, 123.25, 122.52, 122.17, 114.53, 112.62, 112.09, 26.44 **Fig.S3 (ESI†)**. ESI-MS (m/z): calculated for $C_{27}H_{19}N_5O_5S_2$ $[M + H]^+$: 473.1600; found: 473.2721 as shown in **Fig.S4 (ESI†)**..

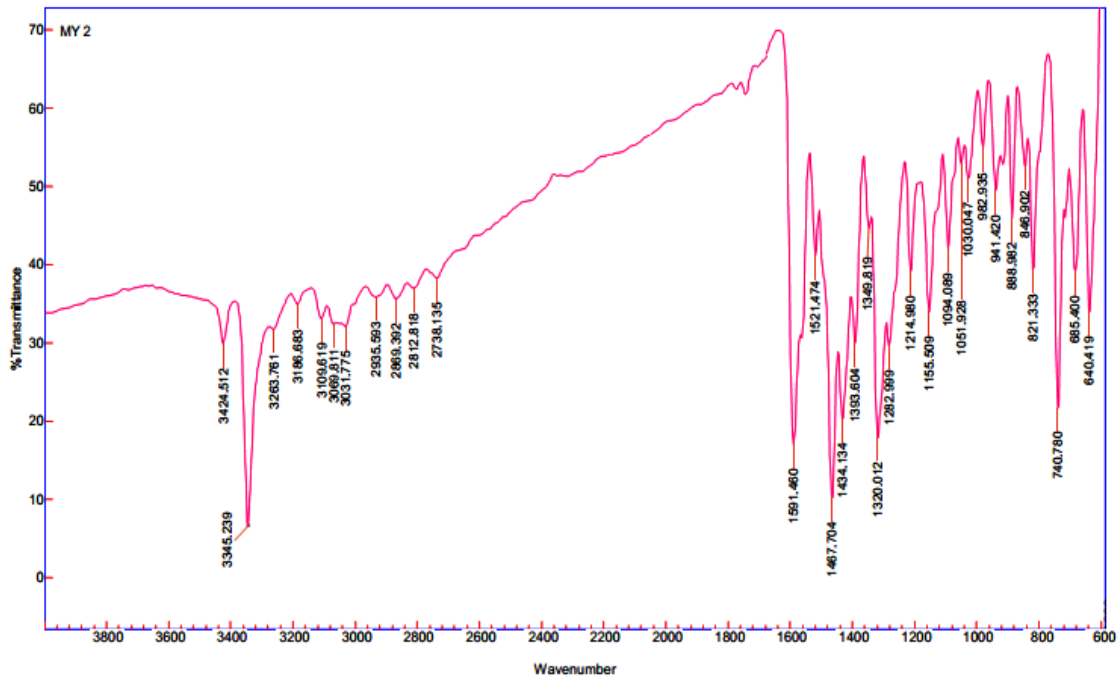


Fig.S1. FT-IR spectrum of BT

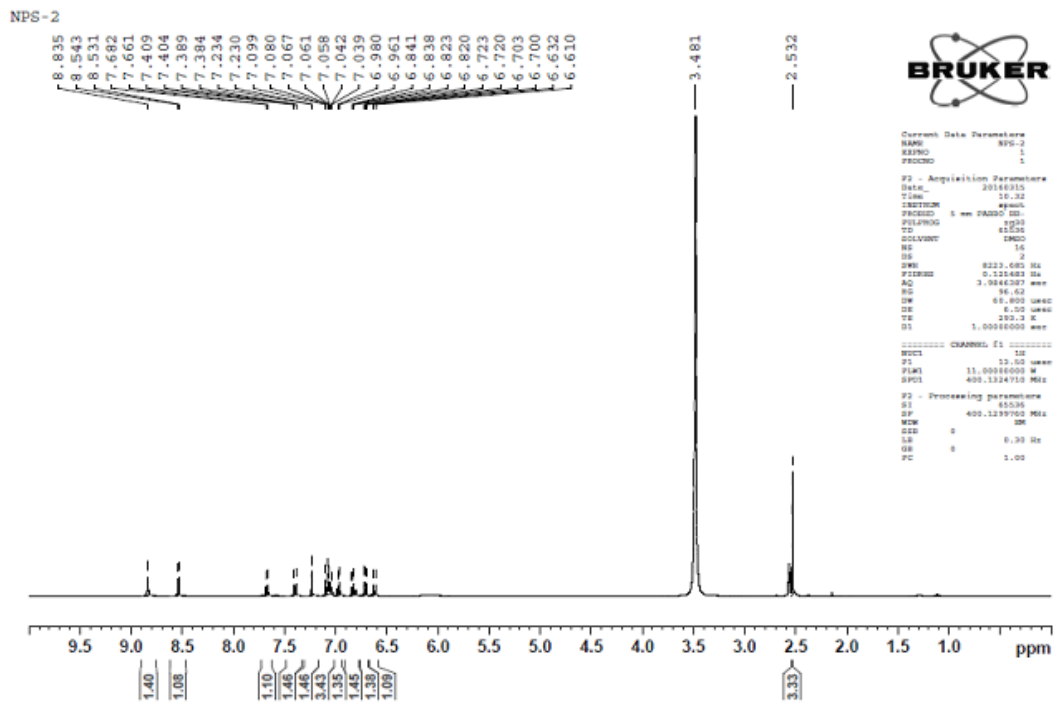


Fig.S2. 1H -NMR spectrum of BT

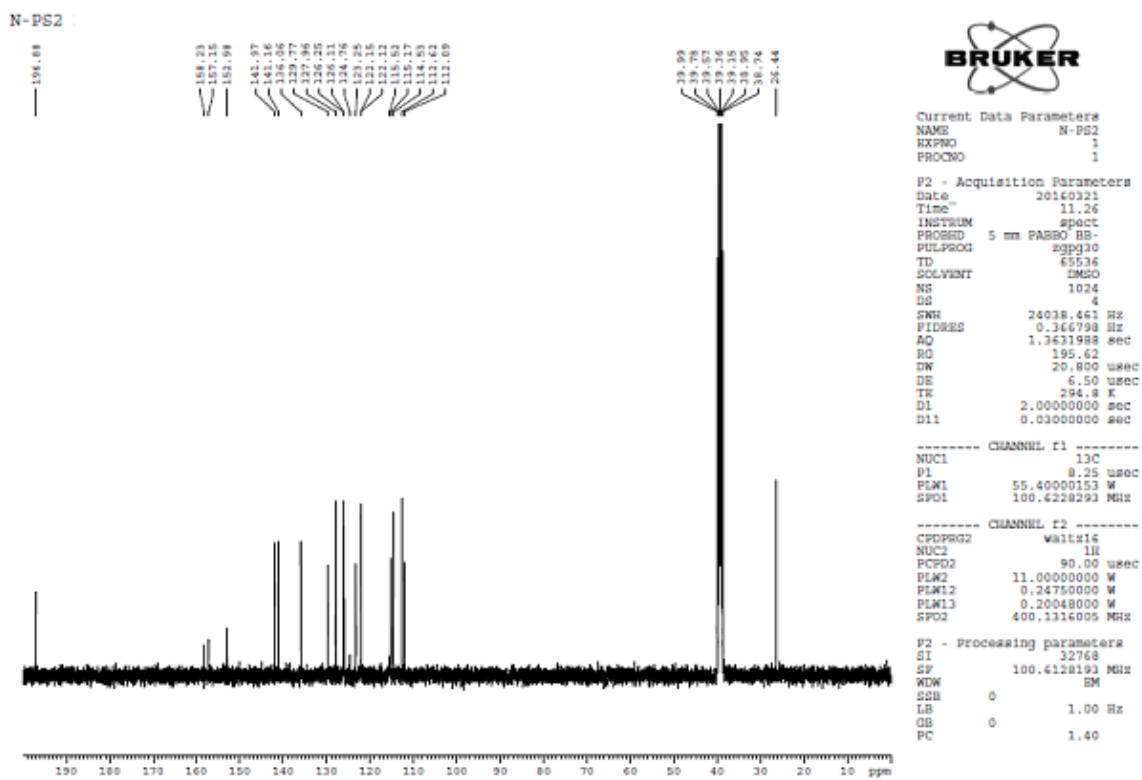


Fig.S3. ^{13}C -NMR spectrum of BT

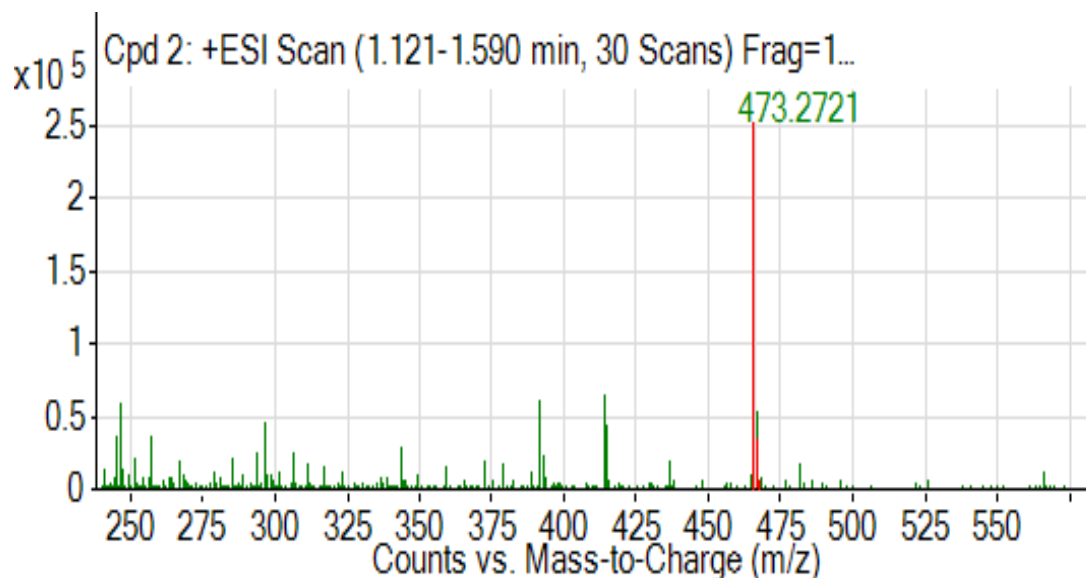


Fig.S4. ESI-MS spectrum of **BT**

3.2.3. UV-vis and fluorescence experimentation

The stock solutions of different metal ions nitrate or chloride salts were prepared in aqueous water. The stock solution of **BT** (10 μ M) was prepared in aqueous water for spectroscopic studies. The absorption and fluorescence spectra measurements were carried out by using 5 mL mixed solution of **BT** (10 μ M) solution and metal ion solution with an accurate concentration in a quartz cell used in ethanol/ water HEPES buffer solution (5 mM, 1: 4, v/v, pH 7.4) at room temperature. All fluorescence experiments have been conducted upon excitation wavelength at 290 nm.

3.2.4 Cell culture

The human hepatocellular liver carcinoma cells (HepG2 cell lines) (NCCS, Pune, India) were grown in DMEM in addition to 10 % of FBS and antibiotics (streptomycin-50 μ g / mL; penicillin-100 μ g / mL), at 37 $^{\circ}$ C, 5 % CO₂ incubator, cells were produced at 95 %.

3.2.5. Anticancer activity and Cell viability assay

The cytotoxicity of **BT** was tested using a 3-(4,5-dimethylthiazole-2-yl)-2,5-diphenyl tetrazolium bromide (MTT) assay against HepG2 cell lines. Cells were seeded onto a 96-well plate at a cell density per disc 1.5×10^4 and incubated at varying concentrations from 0.0-500 μM to last 48 hours in a medium containing **BT**. Triplicate wells with 100 μL of MTT added to each well are retained for each operation. It was incubated at 37 °C for 4 h, allowing MTT reaction and metabolically active cells to form crystals of formazan. The medium for MTT was cautiously discarded from the wells. To extract intracellular formazan crystals, 100 μL of DMSO was applied to each well and the dishes shaken for 10 minutes. Using ELISA, at 365 nm, the reader and absorbance were readout. Using a fluorescent microscope, the photographs of the cells were analyzed. The survival percentage was determined using formula: %survival = [live cell number (test)/live cell number (control)] $\times 100$.

3.2.6. Fluorescence microscopic study

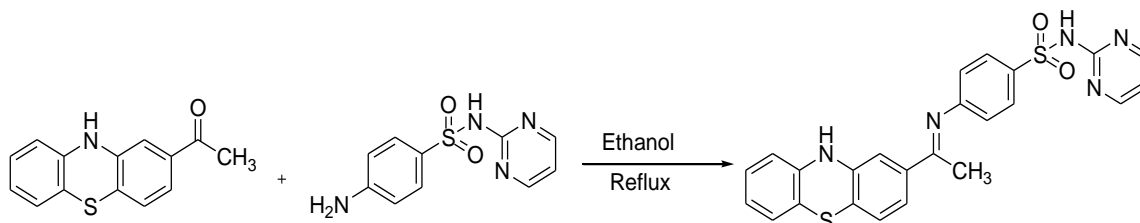
For in-vitro fluorescence imaging of **BT**, the cells were seeded in a 35 mm culture dish at a density of 3×10^5 cells per dish. After completion, 60% confluence for fluorescence microscopy was replaced by aluminium nitrate augmented with the serum to absorb Al^{3+} ion by 40-hours developing cells, **BT** (5.0 μM), dissolved in DMSO/ H_2O (99/1), in addition to new media to allow **BT** to be absorbed by cells to form the Al^{3+} -**BT** complex. Three hours of incubation followed afterward. Under a fluorescence microscope, both excitations of Al^{3+} ion were trypsinized and examined for **BT** images at 365 nm using a 10x fluorescent target. The bright and fluorescence field knowledge was obtained using the fluorescence microscope 40x-Olympus FV1000-LX81.z, Camedia software, and Adobe Photoshop version 10.0 processed using. For the control trial, the media was stripped off Al^{3+} ion.

3.2.7. Theoretical studies

Computational calculations were performed in the Gaussian09 program [35]. The geometry optimization was performed with the B3LYP method by using minimize structure. Mulliken atomic charges and Molecular Electrostatic Potentials (MEPs) of benzenesulfonamide were plotted in a 3D diagram carried out by optimized structures at the same level theory. Moreover, HOMO and LUMO energy values were calculated and energy gap for benzenesulfonamide were calculated by using the B3LYP method with a 6-31G (d,p) basis set. Besides, the dipole moment, polarisability, and hyper polarisability were established from molecular polarizabilities based on theoretical calculations.

3.3. RESULTS AND DISCUSSION

As shown in **Scheme 1**, Schiff base compounds based on the fluorescent chemosensor **BT**, (E)-4-((1-(10H-phenothiazin-2-yl)ethylidene)amino)-N-(pyrimidin-2-yl)benzenesulfonamide (**BT**) was synthesized (**Scheme 1**) and characterized by FT-IR, ESI-MS, ^1H , and ^{13}C NMR spectroscopic methods. Further, colorimetric studies with naked eye UV-vis and fluorescence spectroscopic performed HEPES buffer solution in EtOH: H₂O (1:4, v/v, pH=7.0) and under excitation wavelength at 290 nm. The fluorescent chemosensor **BT** solution was explored for different metal ions and fluorescence intensity at 516 nm for high sensitivity and selectivity of Al³⁺ ion and further investigated such competitive metals ion by EDTA titration method, and theoretical calculation used in Gaussian 09 program.



Scheme 1. The synthesis compound of **BT**

3.3.1. Absorption studies

The UV-Visible absorption technique was carried out to study the interaction of analytes with chemosensors [36-39]. All experiments were carried out in ethanol/water HEPES buffer (5 mM 1:4, v/v, pH=7.0) at room temperature. The colorimetric studies for **BT** solution exhibited a bright yellow color to light yellow color appeared by the naked eye under UV lamp (**Fig.1**). As shown in **Fig.2**, the compound **BT** exhibited a three absorption band maximum at 252, 272, and 295 nm, which might have appeared due to intra-ligand $\pi \rightarrow \pi^*$ electronic transition and another absorption band at 327 nm, which might be caused due to $n \rightarrow \pi^*$ electronic transitions from non-bonding orbitals on the heteroatoms to π^* orbitals of **BT**. The absorbance of **BT** was explored with different metal ions such as alkali metal ion (Ca^{2+} , Mg^{2+}), one alkali earth metal ions (Mg^{2+}), and transition metal ions (Ag^+ , Cu^{2+} , Fe^{3+} , Co^{2+} , Ni^{2+} , Mn^{2+} , Zn^{2+} , Cd^{2+} , and Mg^{2+}) in ethanol/water HEPES buffer (5 mM 1:4, v/v, pH=7.0) at room temperature was studied. The absorption spectra of **BT** demonstrated considerable shift in the presence of Al^{3+} ion with various wavelengths, while the other metal ions did not generate any significant changes in the absorption spectrum (**Fig.2**). After the addition of the Al^{3+} ions, the spectrum of **BT** shows a new absorption at 327 nm and two new isosbestic points band at 308 nm and 340 nm appeared during the titration of **BT** with Al^{3+} (**Fig. 3**). The redshift (bathochromic) in absorption is because of the donor atoms in **BT** binding to the metal ion (Al^{3+}) to generate a chelate ring; therefore conjugation is extended which is possibly the reason for the redshift in the absorption intensity.

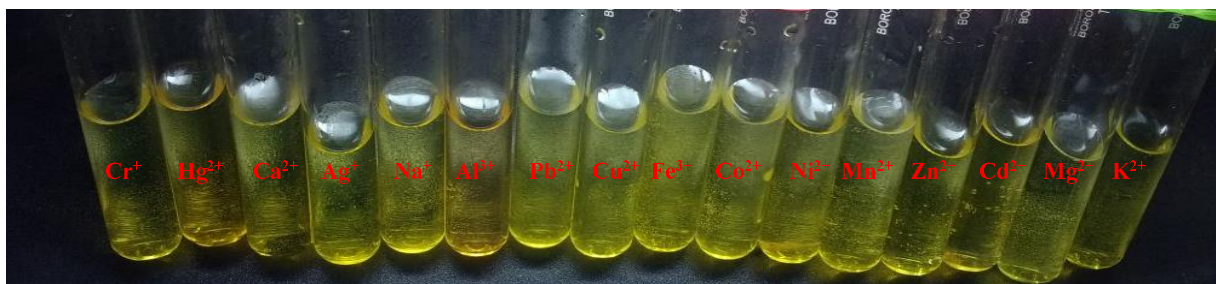


Fig. 1 The colorimetric studies for **BT** (10 μ M)

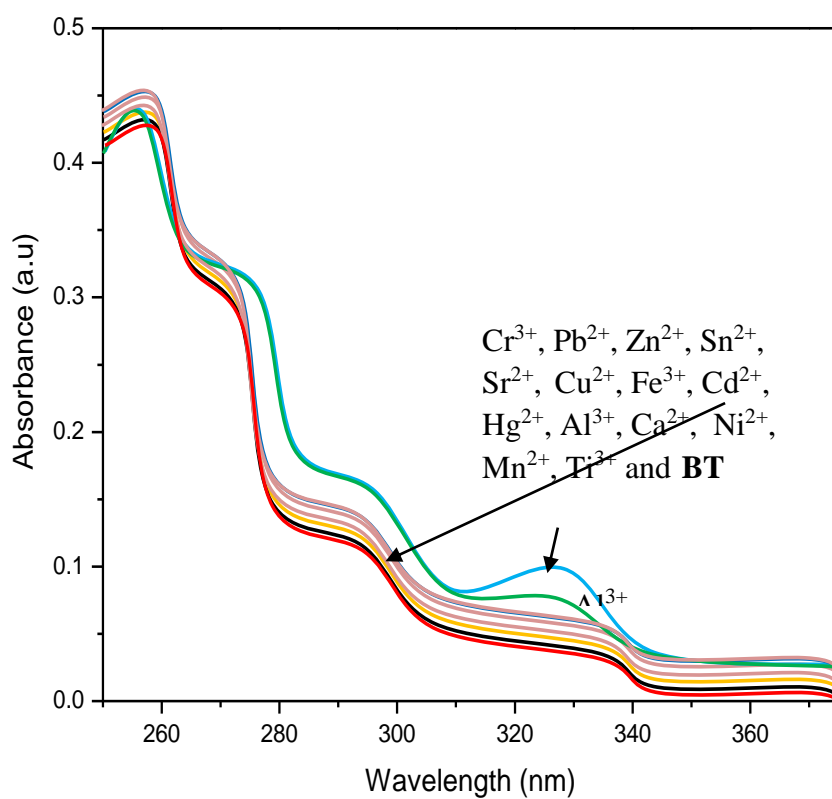


Fig.2. Absorption spectrum of **BT** (10 μ M) with different metal ion (5 equiv) used in ethanol/water HEPES buffer solution in EtOH:H₂O (5 mM, 1:4, v/v) pH=7.0.

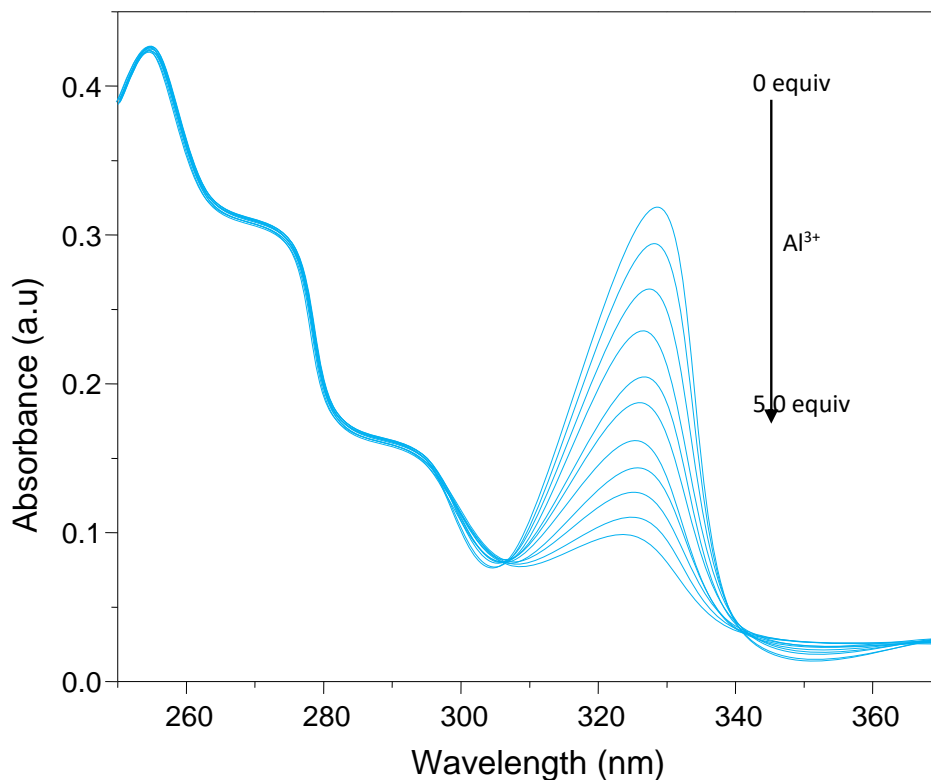


Fig.3. Absorption spectrum of **BT** (10 μM) with increase concentration of Al^{3+} ion used in ethanol/water HEPES buffer solution (5 mM, 1:4, v/v) pH=7.0.

3.3.2. Fluorescence studies

The selectivity of **BT** was initially evaluated by fluorescence lamp due to pale yellow color change to blue color appeared, because with all metal ions no color change was observed by fluorescence under 365 nm UV lamp (**Fig. 4**). An equimolar solutions of **BT** (10 μM) was added to solutions of different heavy transition metal ions such as Cr^{3+} , Pb^{2+} , Zn^{2+} , Sn^{2+} , Sr^{2+} , Cu^{2+} , Fe^{3+} , Cd^{2+} , Hg^{2+} , Al^{3+} , Ca^{2+} , Ni^{2+} , Mn^{2+} , Ti^{3+} and Al^{3+} ion in ethanol/water HEPES buffer (2 mM 1:4, v/v, pH=7.0) at room temperature explored by fluorescence spectroscopy. The emission study demonstrated that the compound **BT** shows weak emission maximum intensity at 516 nm was observed on excitation wavelength at 290 nm (**Fig. 5**). On the addition of Al^{3+} for the emission intensity at 516 nm was redshifted; however, other metal ions did not produce any significant change in the fluorescence spectrum. The metal-ligand binding induced switch-ON fluorescence of **BT** was completely selective towards Al^{3+} ions. The binding of the **BT**- Al^{3+} complex study was examined by

various spectroscopic techniques. From the titration on the addition of 2 equiv. of Al^{3+} gradually decreased the fluorescence emission intensity at 516 nm, (**Fig. 6**) become stable representing the coordination of **BT** ($10\ \mu\text{M}$) with Al^{3+} in stoichiometric complex 1:1 binding mode. Job plots adopted from the fluorescence data also indicated 1:1 stoichiometric for the Complexation of **BT**- Al^{3+} (**Fig. 7**). The binding constant (K) estimated from the fluorescence intensity at 516 nm using the Benesi-Hildebrand plot was found to be $3.27 \times 10^7\ \text{M}^{-1}(\text{Al}^{3+})$, representing the capable binding of **BT** with Al^{3+} (**Fig. 8**). The detection limit of Al^{3+} was predicted at $R^2=0.9965$ using the equation $\text{DL} = 3\sigma/k$, where σ is the standard deviation of empty measurements; k is the slope of intensity versus sample concentration (**Fig. 9**) to understand the binding properties of **BT** as a receptor for Al^{3+} titration of **BT** was accomplished with increasing gradually Al^{3+} for all calculation methods.

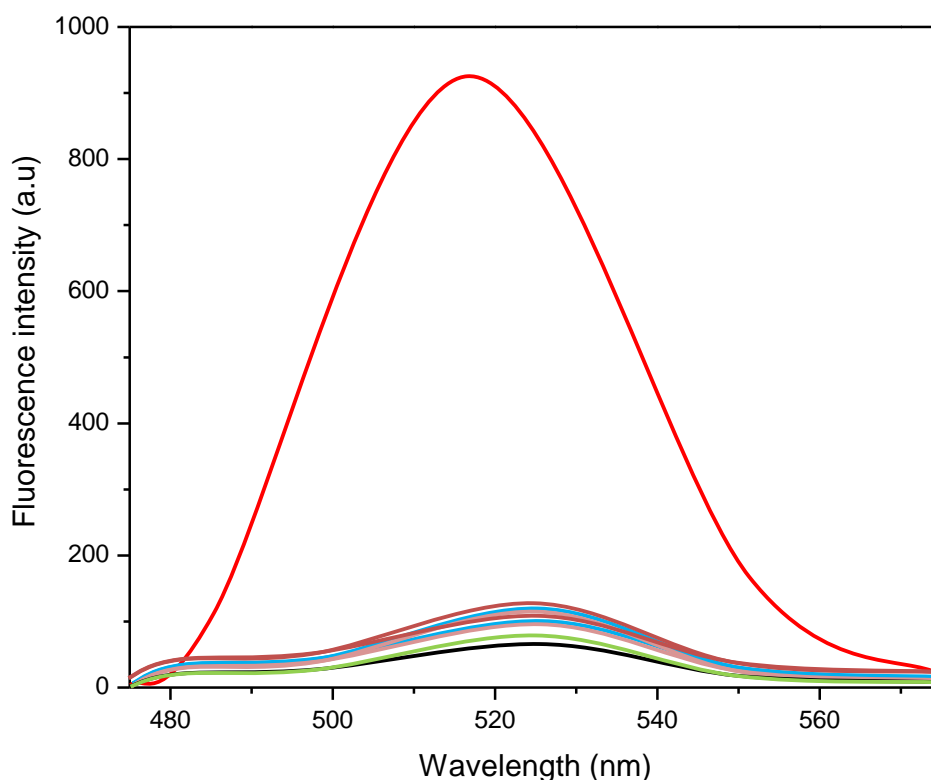


Fig.5. Fluorescence spectrum of **BT** ($10\ \mu\text{M}$) with different metal ion (5 equiv) used in ethanol/water HEPES buffer solution in EtOH:H₂O (5 mM, 1:4, v/v) pH=7.0.

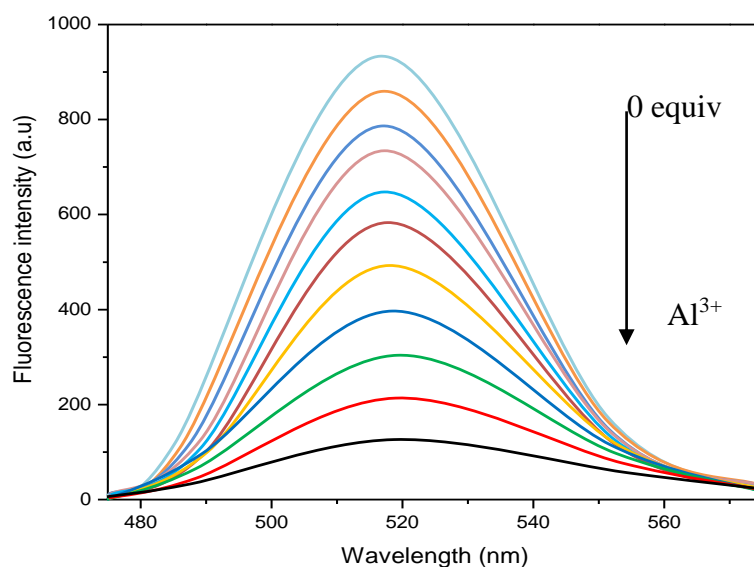


Fig.6. Fluorescence spectrum BT (10 μM) with increase concentration of Al^{3+} ion used in ethanol/water HEPES buffer solution (5 mM, 1:4, v/v) pH=7.0.

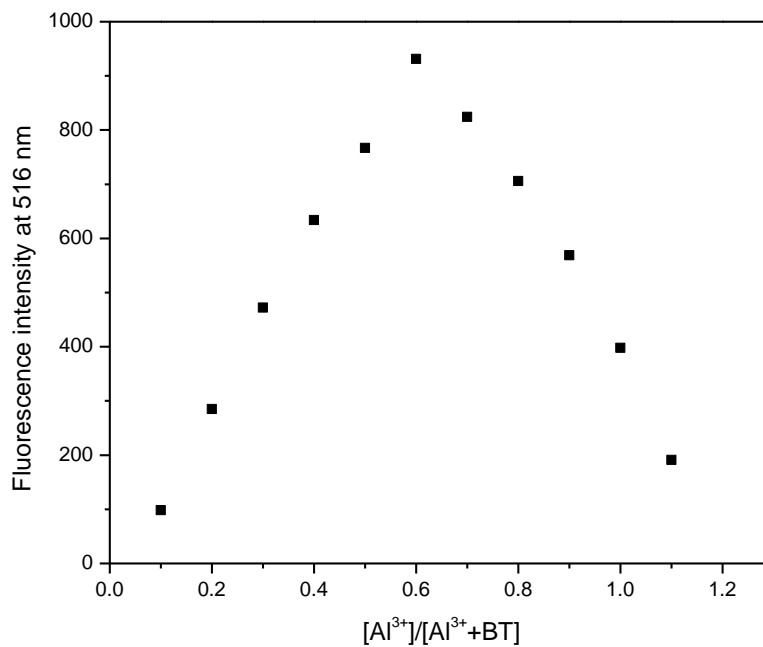


Fig.7. The job's plot of BT+ Al^{3+} used different concentration.

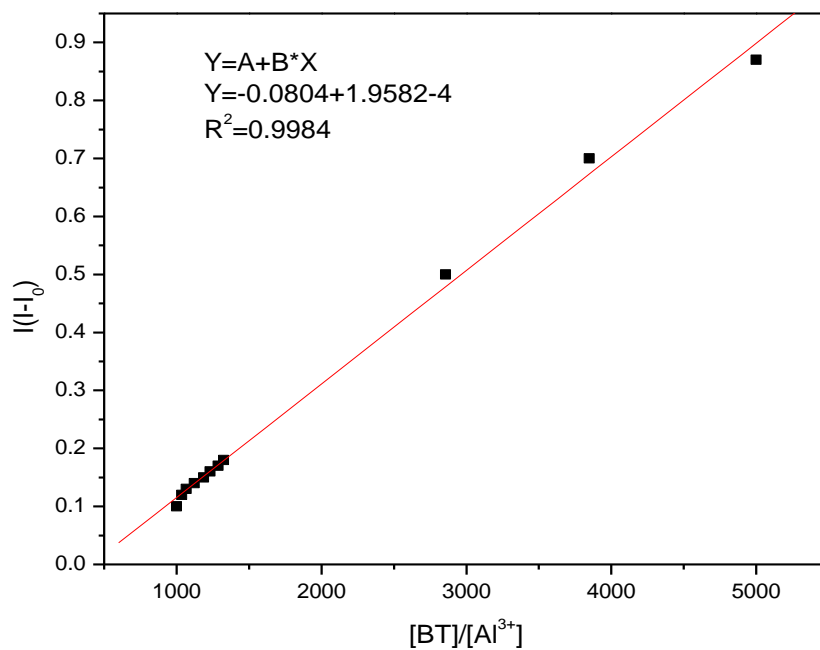


Fig.8. Benesi-Hildebrand plot from fluorescence titration data of with concentration **BT+Al³⁺**.

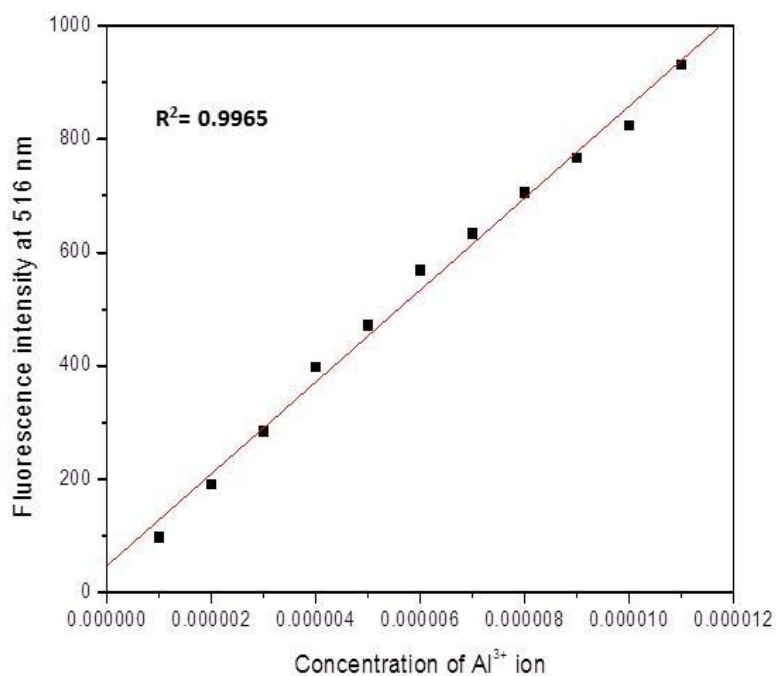
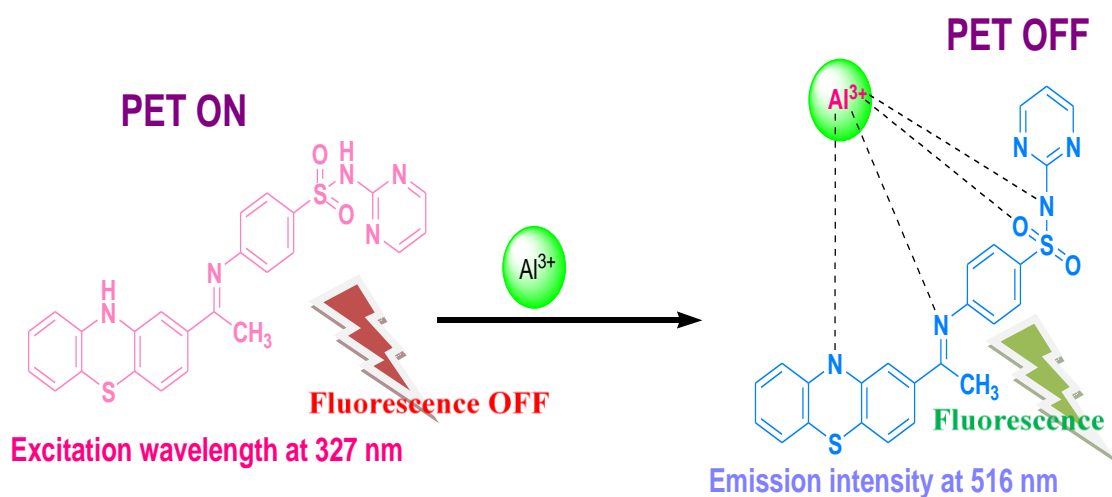


Fig.9. The determination of limit **BT** (10 μ M) with different concentration of **Al³⁺**.

3.3.3. Binding mechanism

Binding studies demonstrate that **BT** is sensitive and selective for Al^{3+} as shown by fluorescence changes observed at 516 nm. The chelation of Al^{3+} with O and N donors of **BT** increase the rigidity of the molecular association (CHEF) through the inhibition of the rotation due to the rigid azomethine nitrogen ($\text{CH}=\text{N}$). The fluorescence of **BT**, because of the delocalization of accessible lone pairs of electron on the imine ($\text{C}=\text{N}$) nitrogen atom to the aromatic moiety leads to the quenching effect of fluorescence through the photoinduced electron transfer (PET) process (**Scheme 2**). The emission enhancement was observed by two effects (PET and CHEF) that are responsible for titration methods. The PET mechanism was confirmed by further studies such as IR and Mass spectroscopy. Initially, NH stretching peak at 3345 cm^{-1} disappeared and a new peak appeared 3316 cm^{-1} , the functional group of the imine peak at 1591 cm^{-1} disappeared, while a new peak at 1601 cm^{-1} appeared due to the addition of 0.5 equiv of Al^{3+} (**Fig.S5, ESI†**). The ESI-MS spectrum showed exact molecular weight present in 498.1849 m/z after adding Al^{3+} (1 equiv) into **BT** solution and compared to the original compound exact mass present at 473.2721 m/z (**BT**), Job's plot confirmed by 1:1 stoichiometry for **BT**- Al^{3+} (**Fig.S6, ESI†**).



Scheme 2 The synthesis compound of **BT**+ Al^{3+}

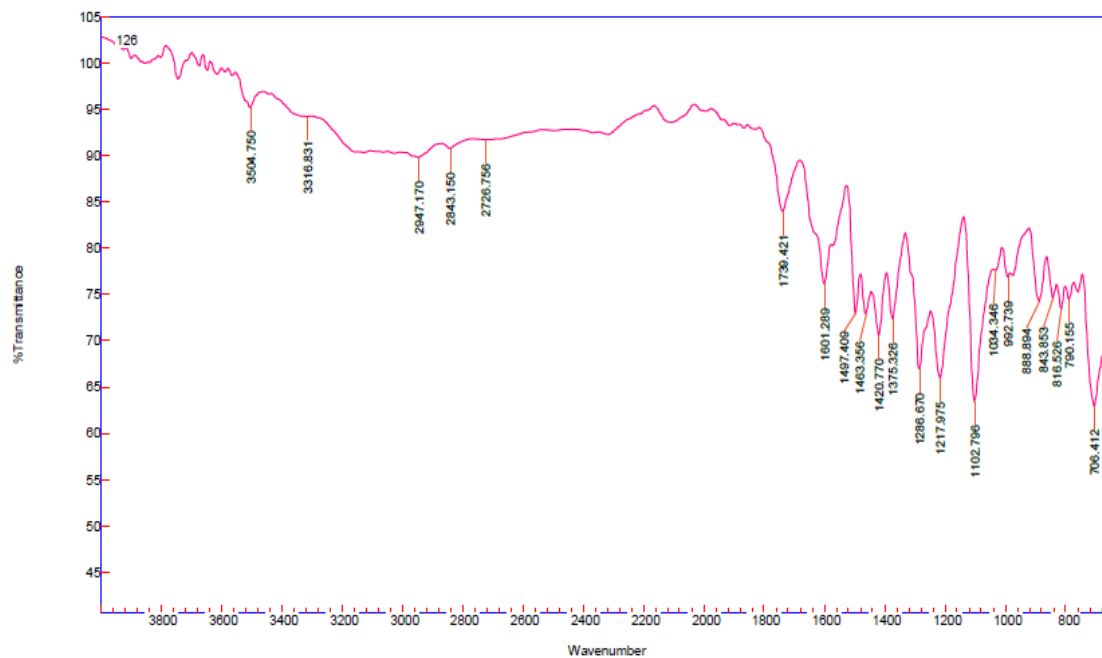


Fig.S5. ESI-MS spectrum of **BT+Al³⁺**

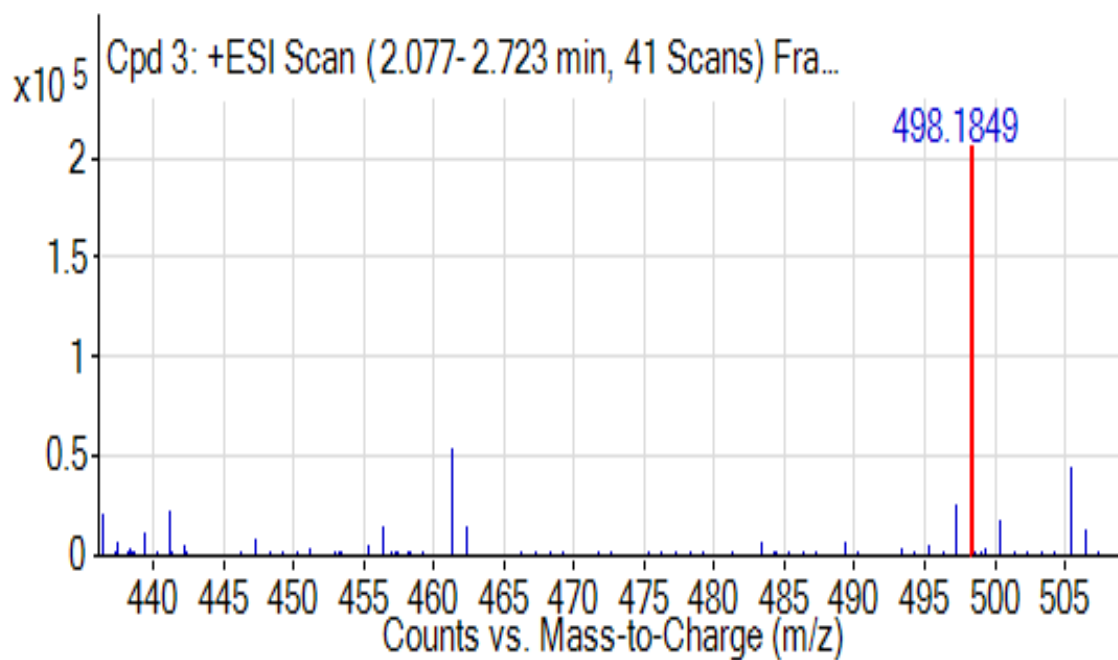


Fig.S6. ESI-MS spectrum of **BT+Al³⁺**

3.3.4. Competitive metal ion studies

The fluorescence intensity of **BT**- Al^{3+} was examined with other interfering metal ions such as Cr^{3+} , Pb^{2+} , Zn^{2+} , Sn^{2+} , Sr^{2+} , Cu^{2+} , Fe^{3+} , Cd^{2+} , Hg^{2+} , Al^{3+} , Ca^{2+} , Ni^{2+} , Mn^{2+} , Ti^{3+} and Al^{3+} in ethanol/water HEPES buffer (5 mM 1:4, v/v, pH=7.0) at room temperature. It intervened with the estimate of Al^{3+} ion. As shown in **Fig. 10**, excitation wavelength 290 initially used, and emission intensity at 516 nm was observed respectively. The fluorescence spectrum of **BT** exhibited increase intensity at 516 nm in the presence of Al^{3+} ions ($\lambda_{\text{ex}} = 290$ nm), but when including other metal ions with Al^{3+} might not make any noteworthy sensing in the emission intensity of **BT** at 516 nm.

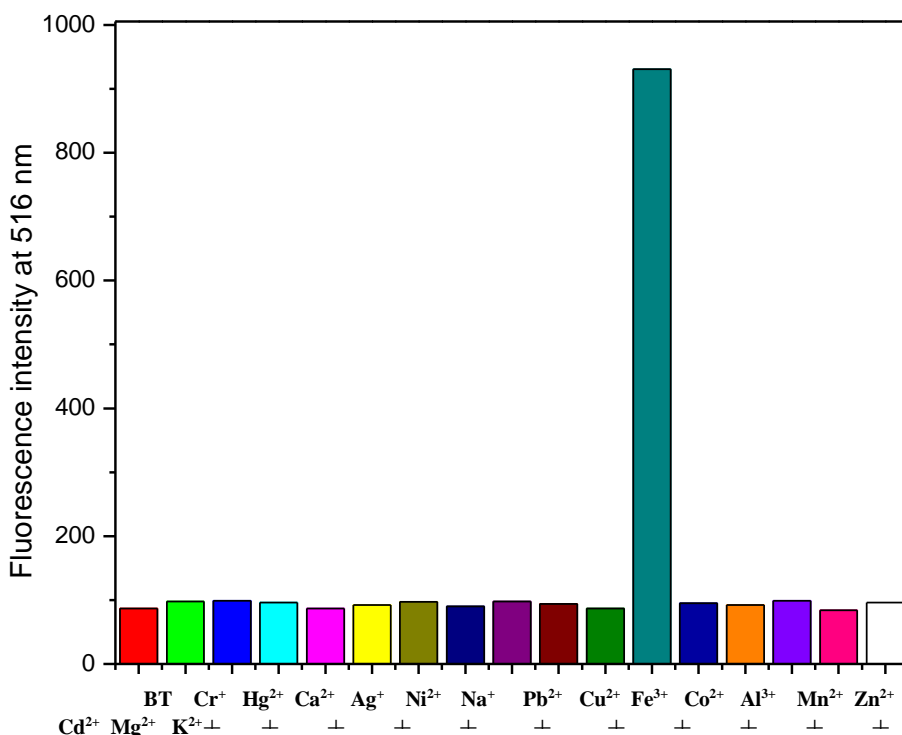


Fig.10. Emission intensity of **BT** (10 μM) at $\lambda_{\text{em}} = 516$ nm and the presence of various metal ions (5 equiv.) in ethanol/water HEPES buffer (5 mM, pH 7.0; 1 : 4,

However; different metal ions might have an effect on the fluorescence intensity of the **BT** with equimolar Al^{3+} ions. To estimate the major effect of various metal ions, the fluorescence intensity at 516 nm ($\lambda_{\text{ex}} = 290$ nm) was monitored when the **BT** is mixed with Al^{3+} ion, respectively (**Fig. 11**). The fluorescence emission intensity of **BT** mixed with Al^{3+}

did not significantly change in the presence of other metal ions. The obtained results demonstrate that **BT** could be used to detect Al^{3+} ion even in the presence of other metal ions relatively.

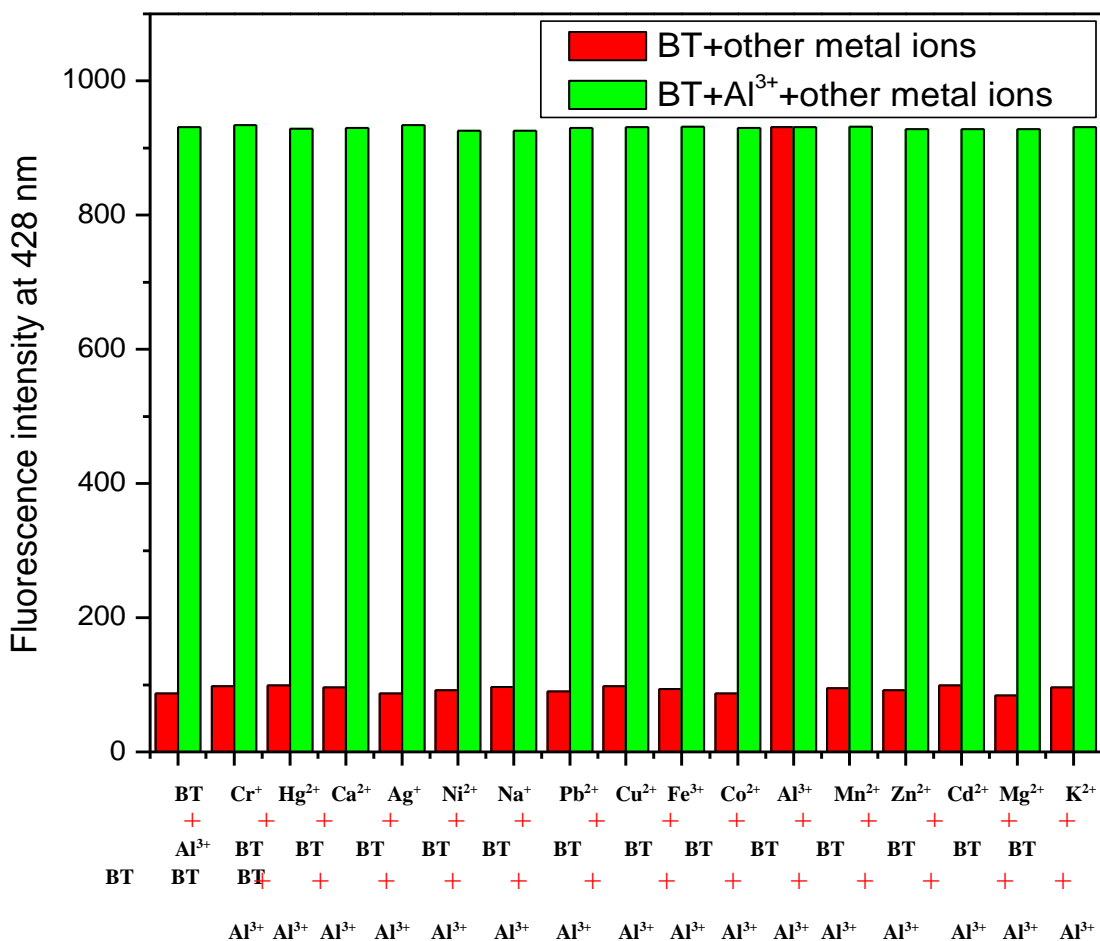


Fig.11. Competitive metal studies **BT** (10 μM) at $\lambda_{\text{em}} = 516 \text{ nm}$ and the presence of various metal ions (5 equiv.) in ethanol/water HEPES buffer (5 mM, pH 7.0; 1 : 4, v/v) at room temperature.

3.3.5. Reversibility

The reusability of the probe is a remarkable quality for predicted its probability for its application and hereafter reversibility tests of **BT** with both Al^{3+} ion was carried out in ethanol/water HEPES buffer (5 mM 1:4, v/v, pH=7.0) at room temperature (**Fig.12**). The fluorescence spectra of the **BT** have been recorded with 2 equiv. of Al^{3+} ion at 516 nm respectively. The emission intensity of metal complexes was quenched after adding an

increased concentration of the chelating agent EDTA solution, which can be seen as the regeneration of the free **BT**. For a second time, the addition of the Al^{3+} ion into the **BT** solution mixture caused fluorescence enhancement completed within 5 min and further added the chelating agent EDTA solution induced the quenching of fluorescence intensity. The obtained results showed that **BT** was a reversible and reusable sensor up to three cycles for Al^{3+} ion by the gradual addition of suitable strong chelating reagents such as EDTA.

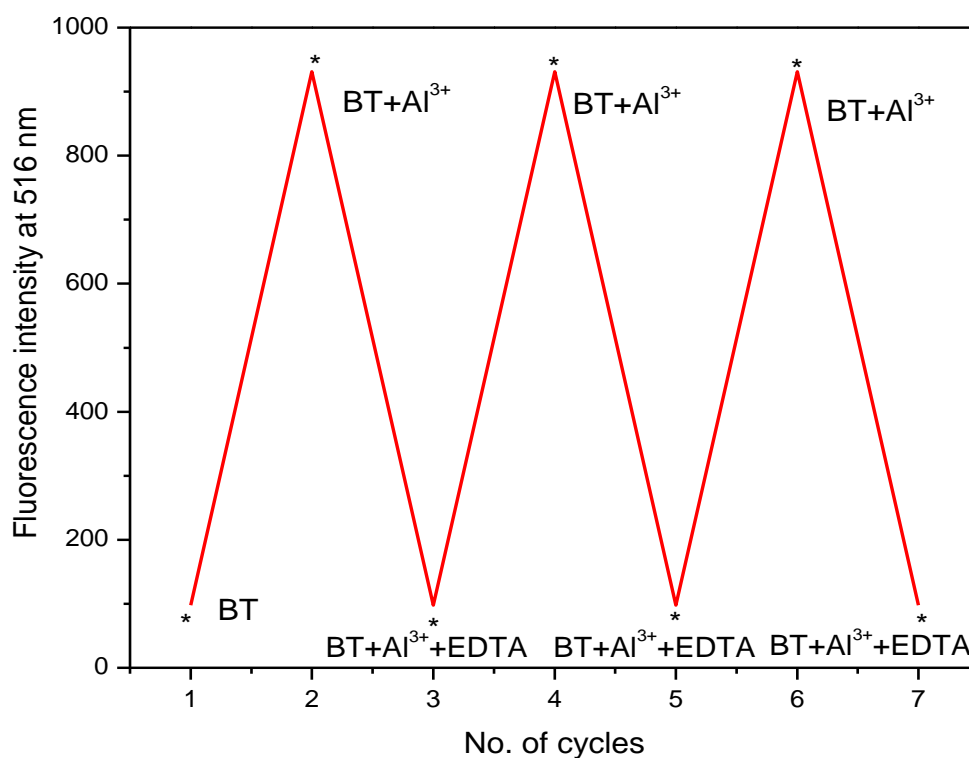


Fig.12. Emission intensity of **BT** (10 μM) at $\lambda_{\text{em}} = 516 \text{ nm}$ and the presence of various metal ions (5 equiv.) in ethanol/water HEPES buffer (5 mM, pH 7.0; 1 : 4, v/v) at room temperature.

3.3.6. Cytotoxicity activity

The anticancer effects of newly synthesized materials against liver cancer cell (HepG2) were measured by the MTT based metabolic assay as the procedure described previously (Mosmann et al., 1983). Briefly, the cells (approximately ten thousand cells) were seeded in well (96-well plate) containing 100 μL of fresh medium and extended for 24 h incubation. Then, cells were undergone for 100 μL of different concentrations (ranging

from 0.0–500 μM concentration) treatment with of the newly produced compound in each well, respectively. After 24 h of treatment, 100 μL of MTT was added and incubated for 2-4 h. Then, the reaction was arrested using 100 μL volumes of DMSO and the measurement was carried at 360 nm. The cytotoxicity of synthesized compound was indicated as concentration of the extracts inhibiting cell growth by 50% (IC_{50}), the IC_{50} values of synthesized compound shown in (**Fig. 13**) and (**Table 1**). The compound **BT** showed anticancer activity (47.15 μM) against human liver cancer cells shows in (**Fig. 14**). Anticancer activity results revealed that the synthesized compound showed potent inhibition of liver cancer cell proliferation.

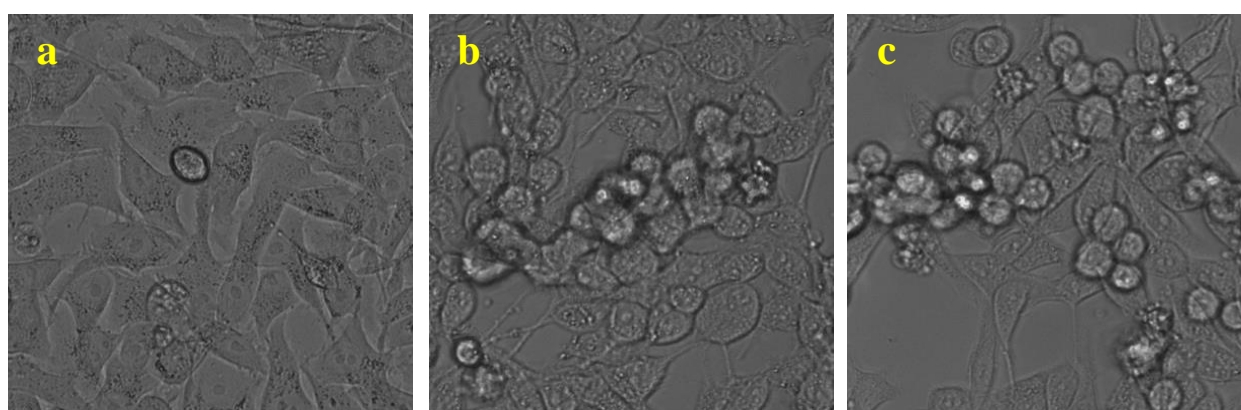


Fig.13. Live cell images of **BT**: (a) before and (b and c) after treatment with **BT** examined by fluorescence microscopy

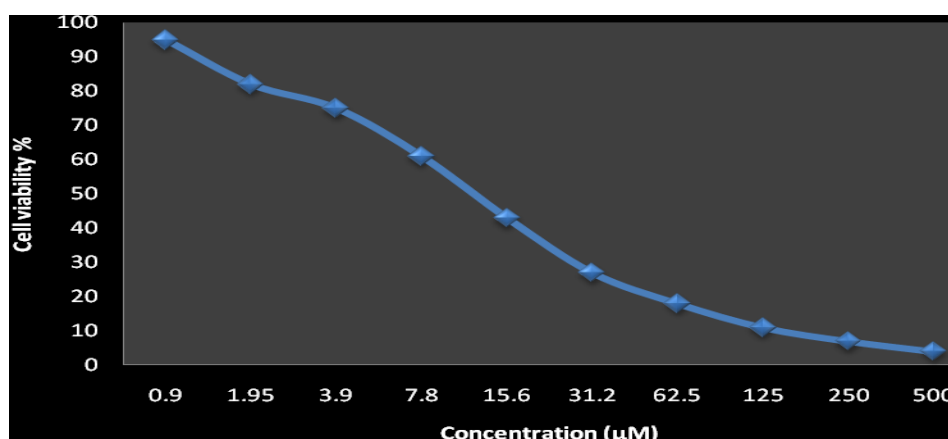


Fig. 14 The IC_{50} values of **BT** against MCF7 cell lines

Table 1. The IC₅₀ values of **BT** against MCF7 cell lines.

Anticancer effect of BT on HepG2 cell line	
Concentration (μM)	Cell Viability %
	BT
0	100
0.9	95
1.9	82
3.9	75
7.8	61
15.6	43
31.25	27
62.5	18
125	11
250	7
500	3

3.3.7. Cell Imaging

HepG2 cancer cells were incubated with Al^{3+} (0-100 $\mu\text{g}/\text{mL}$) and exposed to compound **BT** for 30 min at 37 °C. Compound **BT**- Al^{3+} have been selected for cell imaging process due to their strong emission intensity in presence of the probe. (**Fig. 15**) represents the confocal fluorescence images of HepG2 cell lines upon separate treatment of DAPI control, metal salts, probe, and its complexes. Gradual increase in the sensor concentration (0, 20, 50, and 100 $\mu\text{g}/\text{mL}$) follows a proportional relationship with respect to fluorescence intensity for Al^{3+} complex (**Fig. 15**). Magnified images (**Fig. 15**) can clearly distinguish the motif of binding inside the living cell. Hence, the receptor **BT** has good cell permeable character can be used for the easy detection of Al^{3+} ion inside the living cell. Moreover, resemblance in cell imaging was also observed when HepG2 cell lines were used instead of HepG2 cells (**Fig. 15**).

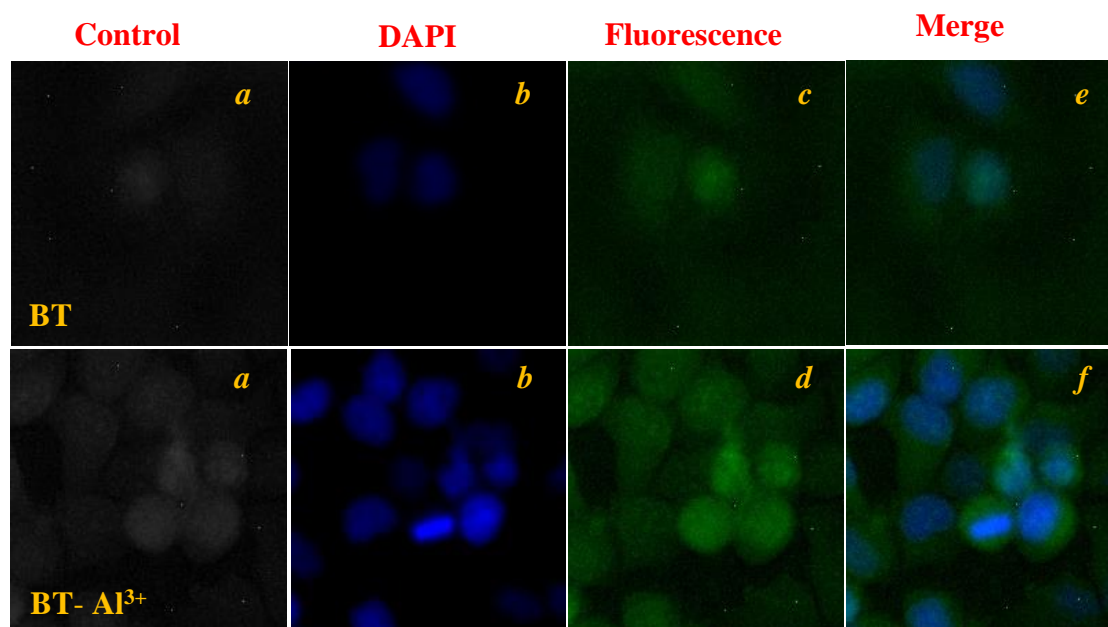


Fig.15. Confocal fluorescence and merged images of HepG2 cells were stained with DAPI, **BT-Al³⁺**, respectively. (a) HepG2 cells incubated with **BT-Al³⁺** (5 μ M) only, (b) HepG2 cells pre-incubated with **BT-Al³⁺** (5 μ M) followed by 0.1 mM **BT**, (c) cells were stained with both DAPI and 5 μ M **BT-Al³⁺**; (d) cells of (c) further incubated with **BT** (0.1 mM) for another 30 min, (e) and (f) were merged images. Scale bar, 30 μ m.

3.3.8. Theoretical studies

3.3.8.1. HOMO and LUMO analysis

The HOMO and LUMO are delocalized from the whole molecule for all study with the Schiff bases compound. The energy level of HOMO and LUMO is an extremely important parameter to define the relativities of molecules because they generally take part in chemical reactions. The lower molecule EHOMO has a weak electron-donating capability. However, the higher molecule EHOMO means the good electron donor [40]. The DFT method was used in the B3LYP/6-31G(d,p) basis set, and calculated energy level. The molecules with a methyl group in substituted benzenesulfonamide and NH group in ring. The largest EHOMO value at 3.24 eV and the lowest ELUMO value at 2.43 eV for compound **BT**, both calculated the bandgap energy level at 1.64 eV, because of the decrease in the LUMO value (**Fig. 16**). This compound has a stronger electron-donating ability than other Schiff bases. In the meantime, the other calculation method include is dipole moment,

polarizability, and hyperpolarisability are given data in **Table 2**. The present work obtained results that the existence of a structure resembles benzenesulfonamide-ring increase the HOMO orbitals.

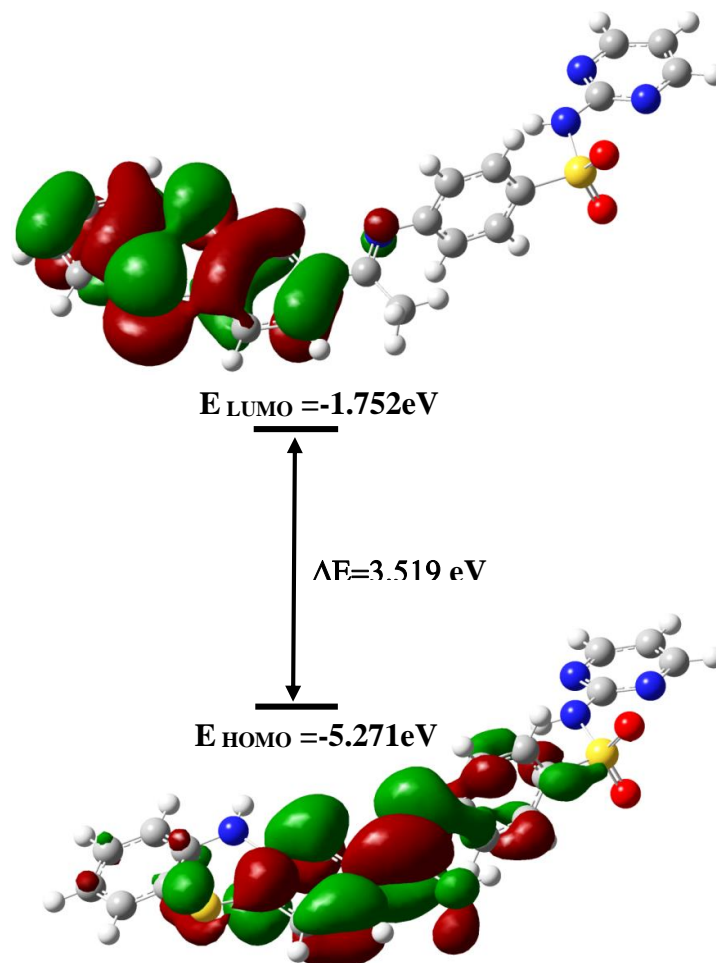


Fig.16. Energy level diagram of **BT**

Table 2 Calculated energy values (eV) of compound **BT** in gas phase

B3LYP/6-311++G(d,p)	BT
E_{HOMO}	-5.2715
E_{LUMO}	-1.752
$E_{\text{LUMO-HOMO}}$	3.5194
Electronegativity	-3.5118
Hardness	1.7595
Electrophilicity index	3.5042
Softness	7.731

3.3.8.2. Molecular electrostatic potential (MEP) analysis

The MEP is an essential tool for the molecular interactions within a given molecule. The hydrogen-bonding interactions and electrophilic and nucleophilic attacking are very useful for predicting and interpreting relevant reactivity sites for [41,43]. The 3D plot of the MEP diagram for the Schiff molecules (**BT**) is shown in **Fig. 17** and calculated by using the optimized structure of molecular at the B3LYP/6-31G(d,p) basis set. The compound **BT** has noticed the molecular electrostatic potentials at the surface for the molecule which was shown in different colors. As a result, that the red colors represent negative electrostatic potential, the blue colors represent positive electrostatic potential, and green colors represent the regions of zero potential. The corresponding of the negative electrostatic potential of the attraction of the proton, whereas, corresponds to the repulsion of the proton with positive electrostatic potential.

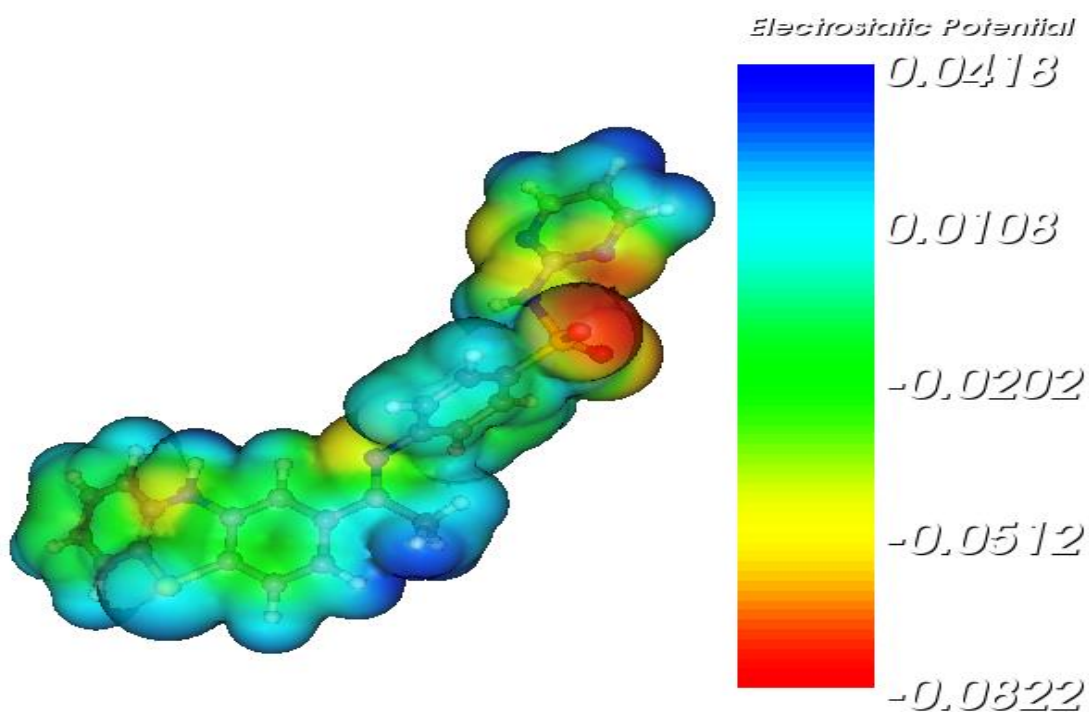


Fig.17. Molecular electrostatic potential surface of **BT**

3.3.8.3. Mulliken charge distribution analysis

Mulliken charge population investigation leads to the same conclusion of charge distributions for all Schiff bases of organic compounds. The charge distributions above all atoms propose the formation of donor and acceptor pairs relative to the charge transfer in this molecule, the highest negative charge density which is placed on O and N atoms, further responsible for a strong bond between the substrate surface and Schiff base. The Mulliken charge distribution of the molecule is calculated by B3LYP at 6-31G (d,p) level theory. The synthesized compound **BT**, charge distribution shows that all the nitrogen and oxygen highly negative charges and Mulliken charges are very low compared with natural charges (**Fig. 18**). In further negative charge could spread all over C1, C3, C5, C6, C8, C11, C15, C18', and C19', therefore due to these atoms attached all the molecules. While, other atoms attached to a molecule such as N10, CH₃15', N16, N22, S21, N22, N24, and N24' are given in **Table 3**. In concluding that design and synthesis this compound ready for nucleophilic substitution reactions.

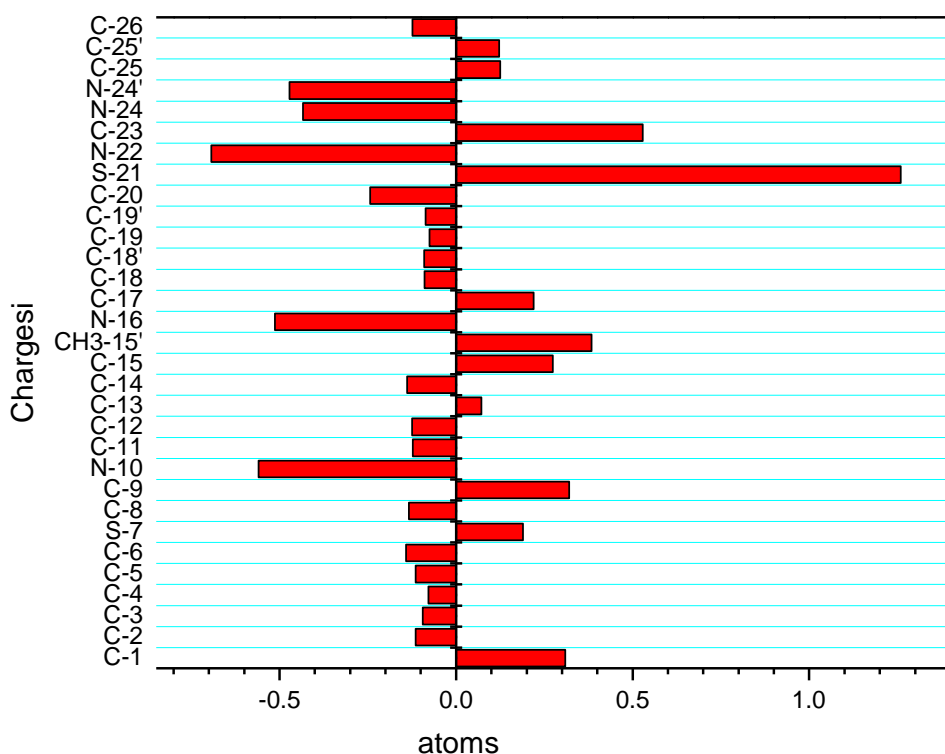


Fig.18.Mulliken atomic charges for **BT**

Table 3 Mulliken atomic charges of compound **BT**

Atom	BT	Atom	BT
C-1	0.309	N-16	-0.513
C-2	-0.115	C-17	0.22
C-3	-0.094	C-18	-0.089
C-4	-0.078	C-18'	-0.09
C-5	-0.115	C-19	-0.075
C-6	-0.142	C-19'	-0.086
S-7	0.189	C-20	-0.243
C-8	-0.134	S-21	1.259
C-9	0.32	N-22	-0.693
N-10	-0.559	C-23	0.529
C-11	-0.123	N-24	-0.434
C-12	-0.125	N-24'	-0.472
C-13	0.072	C-25	0.125
C-14	-0.139	C-25'	0.122
C-15	0.274	C-26	-0.124
CH3-15'	0.384		

3.3.9. NLO effects

Nonlinear optical is a forerunner of current research that provides key functions of optical switching, optical modulation, optical logic frequency shifting, and optical memory in emerging technologies such as optical interconnections signal processing and telecommunications. When describing nonlinear optical properties an external radiation field is often approximated as an external dipole moment caused by a polarization molecule caused by an induced dipole moment. This molecular system of first hyperpolarizability (β_0) is calculated using the B3LYP/6-31G(d,p) method, based on a finite field approach. The estimated **BT** values for hyperpolarizability are given in **Table 4** Urea is one of the reference molecules used in molecular systems to test NLO properties and also used for comparative purposes. The compound **BT** measured first hyperpolarizability (β_{tot}) is 139.906×10^{-30} esu,

which is six times greater than that of urea (β_0 1.21×10^{-30}). Thus, this molecule may serve as a nonlinear optical material for a prospective building block.

Table 4 Dipole moment, Polarisability, Hyperpolarizability values of compound **BT**

Parameter	Dipolemoment (Debye)	Hyperpolarizability (a.u)	
	BT		
μ_x	9794.942	β_{xxx}	-159.606
μ_y	4546.899	β_{yyy}	4.3205
μ_z	5231.86	β_{zzz}	1.0394
μ_{total}	139.906	β_{xyy}	-47.817
Parameter	Polarisability (a.u)	β_{xxy}	59.3327
α_{xx}	-204.44	β_{xxz}	-68.893
α_{yy}	-175.20	β_{xzz}	108.453
α_{zz}	-183.08	β_{yzz}	-2.432
α_{xy}	-9.77	β_{yyz}	3.7775
α_{xz}	4.56	β_{xyz}	-4.4776
α_{yz}	4.26	β_0 (esu) $\times 10^{-30}$	1.21
α_0 (esu) $\times 10^{-23}$	2.8	$\Delta\alpha$ (esu) $\times 10^{-24}$	4.42

3.4. CONCLUSIONS

In the present work, the benzenesulfonamide is based on the Schiff base of **BT** characterized by FT-IR, ^1H NMR, and ^{13}C NMR spectroscopy and mass spectrometry. The compound **BT** exhibited that the recognition for Al^{3+} in ethanol/ water HEPES buffer solution (5 mM, 1: 4, v/v, pH 7.4) at room temperature in a UV-Visible and fluorescence spectroscopy. The fluorescence emission intensity at 516 nm (excitation wavelength at 290 nm), fluorescence “turn-on” due to the presence of Al^{3+} ion with a high peak below all metal ions. Photoinduced Electron Transfer (PET) and stimulating the Chelation Enhanced Fluorescence (CHEF) process for **BT**+ Al^{3+} is coordinated through the NH group and imine nitrogen inhibited and blocked. Job’s plot was shown by 1:1 stoichiometric for **BT**- Al^{3+} . The binding constant (K) was determined fluorescence intensity at 516 nm, Benesi-

Hildebrand plot at $3.27 \times 10^7 \text{ M}^{-1}$ (Al^{3+}), The detection limit of **BT** for Al^{3+} was observed $R^2=0.9965$. Competitive metal ions extensively study for the presence of Al^{3+} , whereas, after the EDTA solution added into **BT**+ Al^{3+} was examine that reversible and irreversible. The theoretical calculation used in Gaussian 09 program followed by the B3LYP/6-31G(d,p) basis set.

3.5. REFERENCE

1. L. J. Fana, Y. Zhanga, C. B. Murphya, S. E. Angell, M. F. L. Parkera, B. R. Flynn and W. E. Jones Jr, *Coord. Chem. Rev.*, 2009, 253, 410–422.
2. X. Zhang, J. Yin and J. Yoon, *Chem. Rev.*, 2014, 114, 4918–4959.
3. (a) F. Wang, L. Wang, X. Chen and J. Yoon, *Chem. Soc. Rev.*, 2014, 43, 4312; (b) Y. M. Yang, Q. Zhao, W. Feng and F. Y. Li, *Chem. Rev.*, 2013, 113, 192; (c) J. F. Zhang, Y. Zhou, J. Yoon and J. S. Kim, *Chem. Soc. Rev.*, 2011, 40, 3416.
4. (a) H. F. Xiang, J. H. Cheng, X. F. Ma, X. G. Zhou and J. J. Chruma, *Chem. Soc. Rev.*, 2013, 42, 6128; (b) Y. Feng, J. H. Cheng, L. Zhou, X. G. Zhou and H. F. Xiang, *Analyst*, 2012, 137, 4885; (c) D. C. E. Persch, D. C. O. Dumele and F. Diederich, *Angew. Chem., Int. Ed.*, 2015, 54, 3290.
5. G. Singh, A. Singh, P. Satija, G. Sharma, Shilpy, J. Singh, J. Singh, K. N. Singh and A. Kaur, *New J. Chem.*, 2019, 43, 5525–5530.
6. G. Singh, J. Singh, S. S. Mangat, J. Singh and S. Rani, *RSC Adv.*, 2015, 5, 12644–12654.
7. G. Singh, S. Rani, A. Saroa, S. Girdhar, J. Singh, A. Arora, D. Aulakh and M. Wriedt, *RSC Adv.*, 2015, 5, 65963–65974.
8. B. Naskar, R. Modak, Y. Sikdar, D.K. Maiti, A. Bauzá, A. Frontera, A. Katarkar, K. Chaudhuri and S. Goswami, *Sens. Actuators B*, 2017, 239, 1194-1204.
9. K. Boonkitpatarakul, J. Wang, N. Niamnont, B. Liu, L. Mcdonald, Y. Pang and M. Sukwattanasinitt, *ACS Sens.*, 2016, 1, 144-150.
10. S. Gui, Y. Huang, F. Hu, Y. Jin, G. Zhang, L. Yan and R. Zhao, *Anal. Chem.*, 2015, 87, 1470-1474.
11. E. Yıldız, Ş. Saçmacı, M. Saçmacı and A. Ülgen, *Food Chem.*, 2017, 237, 942-947.

12. K. S. Ku, P. Muthukumar, S. Angupillai and Y. A. Son, *Sens. Actuators B*, 2016, 236, 184-191.
13. L. Tang, S. Ding, K. Zhong, S. Hou, Y. Bian and X. Yan, *Spectrochim. Acta A*, 2017, 174, 70-74.
14. Z. Li, W. Chen, L. Dong, Y. Song, R. Li, Q. Li, D. Qu, H. Zhang, Q. Yang and Y. Li, *New J. Chem.*, 2020, 44, 3261-3267.
15. S. Wang, G. Men, L. Zhao, Q. Hou and S. Jiang, *Sens. Actuators B*, 2010, 145, 826-831.
16. H. Y. Jeong, S. Y. Lee, J. Han, M. H. Lim and C. Kim, *Tetrahedron*, 2017, 73, 2690-2697.
17. Y. Xu, L. Yang, H. Wang, Y. Zhang, X. Yang, M. Pei and G. Zhang, *J. Photoch. Photobio. A*, 2020, 391, 112372.
18. J. A. Edwardson, J. M. Candy, P. G. Ince, F. K. McArthur, C. M. Morris, A. E. Oakley, G. A. Taylor and E. Bjertness, *Ciba Found. Symp.*, 1992, 169, 165-185.
19. M. Kawahara, *J. Alzheimer Dis.*, 2005, 8, 171-182.
20. J. Savory, M. M. Herman, C. D. Katsetos and M. R. Wills, in: M. Nicolini, P.F. Zatta, B. Corain (Eds.), *Aluminum in Chemistry Biology and Medicine*, Cortina International/ Raven Press, Verona/New York, 1991, p. 45.
21. C. Exley, G. Mamutse, O. Korchazhkina, E. Pye, S. Srekopytov, A. Polwart and C. Hawkins, *Mult. Scler.*, 2006, 12, 533-540.
22. S. Mondal, A.K. Bhanja, D. Ojha, T.K. Mondal, D. Chattopadhyay and C. Sinha, *Fluorescence sensing and intracellular imaging of Al³⁺ ions by using naphthalene based sulfonamide chemosensor: structure, computation and biological studies*, *RSC Adv.*, 2015, 5, 73626-73638.
23. S.Y. Li, D.B. Zhang, J.Y. Wang, R.M. Lu, C.H. Zheng and S.Z. Pu, *A novel diarylethenehydrazinopyridine- based probe for fluorescent detection of aluminum ion and naked-eye detection of hydroxide ion*, *Sens. Actuators, B*, 2017, 245, 263-272.
24. G. Bartwal, K. Aggarwal and J.M. Khurana, *An ampyrone based azo dye as pH-responsive and chemo-reversible colorimetric fluorescent probe for Al³⁺ in semi-aqueous medium: implication towards logic gate analysis*, *New J. Chem.*, 2018, 42, 2224-2231.

25. (a) S. K. Sahoo, G. D. Kim and H. J. Choi, *J. Photochem. Photobiol. C*, 2016, 27, 30–53; (b) S. K. Sahoo, D. Sharma, R. K. Bera, G. Crisponi and J. F. Callan, *Chem. Soc. Rev.*, 2012, 41, 7195–7227.
26. (a) Y. Dong, R. Fan, W. Chen, P. Wang and Y. Yang, *Dalton Trans.*, 2017, 46, 6769–6775; (b) S. Goswami, A. Manna, S. Paul, K. Aich, A. K. Das and S. Chakraborty, *Dalton Trans.*, 2013, 42, 8078–8085.
27. K. P. Carter, A. M. Young and A. E. Palmer, *Chem. Rev.*, 2014, 114, 4564–4601.
28. W. N. Lipscomb and N. Straeter, *Chem. Rev.*, 1996, 96, 2375–2434.
29. A. K. Bhanja, C. Patra, S. Mondal, D. Ojha, D. Chattopadhyay and C. Sinha, *RSC Adv.*, 2015, 5, 48997–49005.
30. (a) K. Zhang, L. Zhang, S. Zhang, Y. Hu, Y. Zheng and W. Huang, *Inorg. Chem.*, 2015, 54, 5295–5300; (b) N. Ahmed, C. Das, S. Vaidya, A. K. Srivastava, S. K. Langley, K. S. Murray and M. Shanmugam, *Dalton Trans.*, 2014, 43, 17375–17384; (c) X. Yang, D. Schipper, R. A. Jones, L. A. Lytwak, B. J. Holliday and S. Huang, *J. Am. Chem. Soc.*, 2013, 135, 8468–8471.
31. (a) X. Liu and J.-R. Hamon, *Coord. Chem. Rev.*, 2019, 389, 94–118; (b) N. Cao, R. Jiang, L. Hao, L. Tian, R. Moc, Y. Fan, J. Zhao and L. Ren, *Mater. Lett.*, 2019, 250, 182–185.
32. T. Simon, M. Shellaiah, V. Srinivasadesikan, C.-C. Lin, F.-H. Ko, K. W. Sun and M.-C. Lin, *Sens. Actuators, B*, 2016, 231, 18–29.
33. A. Singh, R. Singh, M. Shellaiah, E. C. Prakash, H.-C. Chang, P. Raghunath, M.-C. Lin and H.-C. Lin, *Sens. Actuators, B*, 2015, 207, 338–345.
34. Wan, J.; Zhang, K.; Li, C.; Li, Y.; Niu, S. A novel fluorescent chemosensor based on a rhodamine 6G derivative for the detection of Pb²⁺ ion. *Sensors and Actuators B: Chemical*, 246, 2017, 696-702.
35. M.J. Frisch, G.W. Trucks, H.B. Schlegel, G.E. Scuseria, M.A. Robb, J.R. Cheeseman, G. Scalmani, V. Barone, B. Mennucci, G.A. Petersson, *et al.*, *Gaussian 09*, Revision C.01, in, Gaussian, Inc., Wallingford CT, 2009.
36. Z. Wang, N. Wang, X. Han, R. Wang and J. Chang, Interaction of two flavonols with fat mass and obesity-associated protein investigated by fluorescence quenching and molecular docking, *J. Biomol. Struct. Dyn.*, 2018, 36, 3388-3397.
37. Z. Li, Z. Wang, N. Wang, X. Han, W. Yu, R. Wang and J. Chang, Identification of the binding between three fluoronucleoside analogues and fat mass and obesity-

- associated protein by isothermal titration calorimetry and spectroscopic techniques, *J. Pharm. Biomed. Anal.*, 2018, 149, 290-295.
38. T. Ren, Z. Wang, L. Zhang, N. Wang, X. Han, R. Wang and J. Chang, Study of the Binding between Camptothecin Analogs and FTO by Spectroscopy and Molecular Docking, *J. Fluoresc.*, 2017, 27, 1467-1477.
39. L. Zhang, T. Ren, X. Tian, Z. Wang, W. Yu, R. Wang and J. Chang, Investigation of the Interaction between 1,3-Diazaheterocyclic Compounds and the Fat Mass and Obesity-Associated Protein by Fluorescence Spectroscopy and Molecular Modeling, *J. Fluoresc.*, 2017, 27, 369-378.
40. S. Antonczak, *J. Mol. Struct.*, 2008, 856, 38–45.
41. I. Lukovits, E. K´alm´an and F. Zucchi, Corrosion Inhibitors— Correlation Between Electronic Structure and Efficiency, *Corrosion*, 2001, 57(1), 3–8.
42. E. Scrocco, J. Tomasi, *Adv. Quantum. Chem.* 1978, 103, 115.
43. V. Arjunan, P.S. Balamourougane, C.V. Mythili, S. Mohan, V. Nandhakumar, *J. Mol. Struct.* 2011, 1006, 247.

Chapter IV

Synthesis of Schiff base of (Z)-4-methyl-N'-(phenyl(2-(4-substituted)-1H-benzo[d]imidazol-6-yl)methylene)benzenesulfonylhydrazide and their role as chemosensor for Zn²⁺ and Al³⁺

4.1. INTRODUCTION

The careful selection of various receptors, each equipped with specific response groups capable of displaying optical, magnetic, or electrochemical signals, might allow for the selective detection of target molecules/species. The fluorescence sensing process[1,2] is one of the most extensively used sensing techniques due to its simple operating procedure and instrumentation. [3] In addition, this approach has a short measurement time, high selectivity, and high sensitivity for probing analyte molecules. [4-7] Cationic, anionic, or neutral molecules/species are likely to be targeted, with Zn²⁺ and Al³⁺ standing out. Zn²⁺ is the second most common transition metal in biological systems, behind iron. [8] The quantity of Zn²⁺ in the human body varies a great deal. The Zn²⁺ ion is found in intracellular serum at a concentration of 12 M, but only 0.1-0.5 M in brain and nerve tissues. [9,10] In proteins and peptides, the Zn²⁺ ion is tightly bound. In the brain,[11] pancreas,[12] spermatozoa,[13] paneth cells in the colon, mast cells, granulocytes, pituitary cells, and CNS neurons, Zn²⁺ ions can be present in free or chelatable form. [14] In the brain, the Zn²⁺ ion is trapped in the vesicles of presynaptic neurons, where it is released in an inactive state. [15] The Zn²⁺ ions cause the formation of -amyloid (A), which is associated with the etiology of Alzheimer's disease. [16,17] In amyloid plaques, Zn²⁺ ion concentrations are high, ranging from 0.2-1 mM. Pancreatic -cells generate chelatable Zn²⁺ ion and insulin at the same time, with a local Zn²⁺ ion concentration of 0.48 mM around stimulated -cells recorded. [18] The ability to track Zn²⁺ ion release from -cells in vivo will help researchers

better understand the development and management of diabetes. [19] The Zn^{2+} ion is a d^{10} system with electronic properties comparable to those of Cd^{2+} ions. As a result, designing fluorescent chemosensors for the selective and sensitive detection of zinc ions, especially in biological environments, is challenging. [20].

Because of its multifaceted role and numerous uses of Al-containing compounds, Al^{3+} ions have a major influence on human civilization. The catalytic activity of the $-AlF_3$ molecule converts the ozone-depleting reagent CFCs into environmentally acceptable HFCs. [21] Al^{3+} MOFs (Al-MOFs) might be used for sorption, separations, water, and air purification, heterogeneous catalysis, and sensing, among other things. [22] According to the European Food Safety Agency, the tolerance for Al^{3+} is 1 mg Al/kg of body weight per week (EFSA). [23] In 1976, Al^{3+} toxicity was first detected in haemodialysis patients. In 1978, the first case of [24] osteomalacia, commonly referred to as "aluminium-induced bone disease" (AIBD), was identified. [25] Acid rain causes mineral formations to emit Al^{3+} , which then becomes a pollutant in the environment. [26] Coffee and tea plants cultivated in acidic soil have a lot of Al^{3+} . Because of these plants, humans are exposed to Al^{3+} through their diet. [27,28] Workers in the Al^{3+} industry get bladder,[29] leukemia, lung, renal, pancreatic, and brain cancer as a result of increased Al^{3+} exposure. [30] Al^{3+} poisoning decreases the activity of superoxide dismutase (SOD) and catalase, causing changes in nitric oxide generation in both glia and neurons as well as increased DNA breakage. [31-33] Al^{3+} accumulation in the brain causes neuron degeneration, which leads to diseases including Alzheimer's, Parkinson's, amyotrophic lateral sclerosis, dialysis encephalopathy, and multiple sclerosis. [34-37]

Inductively coupled plasma atomic emission spectroscopy and graphite furnace atomic absorption spectrometry are the most often used Al^{3+} ion detection techniques for

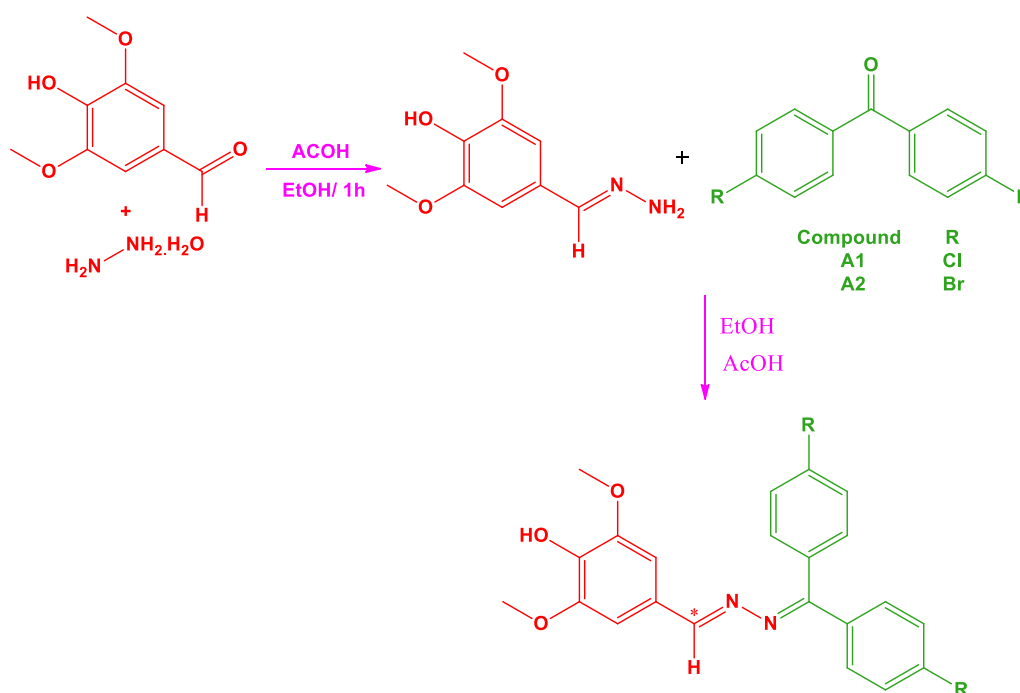
real sample examination. Preparing a fluorescent chemosensor for selective detection of Al^{3+} ions is difficult due to its low coordination ability and high hydration ability. The detection of Al^{3+} ions is frequently hampered by trivalent ions such as Fe^{3+} and Cr^{3+} . In Al^{3+} ion detecting chemosensors, anthraquinone, BODIPY, coumarin, rhodamine, fluorescein, salicylaldehyde, and other fluorophoric units are typically encountered. [38-44] Zn^{2+} detecting chemosensors include di-2-picolyamine, quinoline, bipyridyl[45-56], and others. Fluorescence sensing modalities such as CHEF, ICT, FRET, and PET are all significant. [56,57-60]

In this work, we created asymmetrical azines of **A1** and **A2** for the detection of Zn^{2+} and Al^{3+} ions. Presence of fluorescence excitation wavelength in the UV area is the fundamental drawback of quinoline-based chemosensors. But in both chemosensors (**A1** & **A2**) fluorescence excitation wavelengths appear in the visible area. These compounds are interesting probes in the realm of biological research because of their visible range of excitation wavelengths. The synthesis of both chemosensors by just altering a substituent in the ligand framework is an intriguing part of this work. The chloro-substituted chemosensor detects Al^{3+} ions preferentially due to its hard basic nature. Due to its comparably soft rather intermediate basic nature, bromo-substituted chemosensors predominantly detect Zn^{2+} ions. The detection limits (LOD) of **A1** and **A2** against Zn^{2+} and Al^{3+} ions, respectively, are $1.06 \times 10^{-5} \text{ M}^{-1}$ and $1.13 \times 10^{-5} \text{ M}^{-1}$, indicating that the probes can detect Zn^{2+} and Al^{3+} ions in biological systems. Fluorescence enhancement is controlled via PET Off CHEF On. These biocompatible chemosensors also display cell permeability and detect intracellular ions in the MCF7 cancer cell line.

4.2. EXPERIMENTAL SECTION

4.2.1. Spectral analysis of compounds A1 & A2

The compounds **A1** and **A2** were obtained by refluxing 1:1 molar ratio (*E*)-4-(hydrazonomethyl)-2,6-dimethoxyphenol with various substituted benzophenone in ethanol. The starting material (*E*)-4-(hydrazonomethyl)-2,6-dimethoxyphenol was synthesized by refluxing equimolar amount of C₉H₁₀O₄ and hydrazinehydrate in presence of three drops of CH₃COOH in C₆H₅OH. The reaction pathway is summarized in **Scheme 1**.



Scheme 1. Synthesis of asymmetrical azine compounds A1 and A2

The ¹H&¹³C-NMR, Mass, and FT-IR spectra are used to describe the molecular structure of produced compounds **A1** and **A2**. Table 1 shows the different types of spectra observed for the produced substances. The spectra of asymmetrical azine compounds **A1** and **A2** (FT-IR, ¹H&¹³C-NMR, and ESI-Mass) are shown in **plates 1-8**.

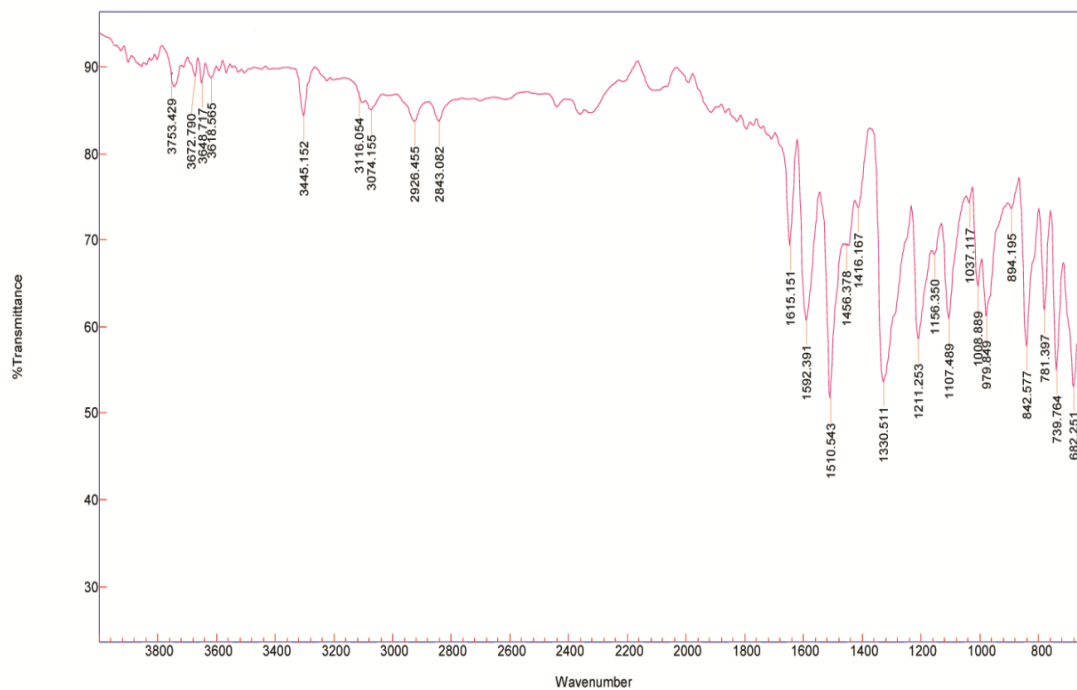


Plate 1. FT-IR spectrum of compound A1

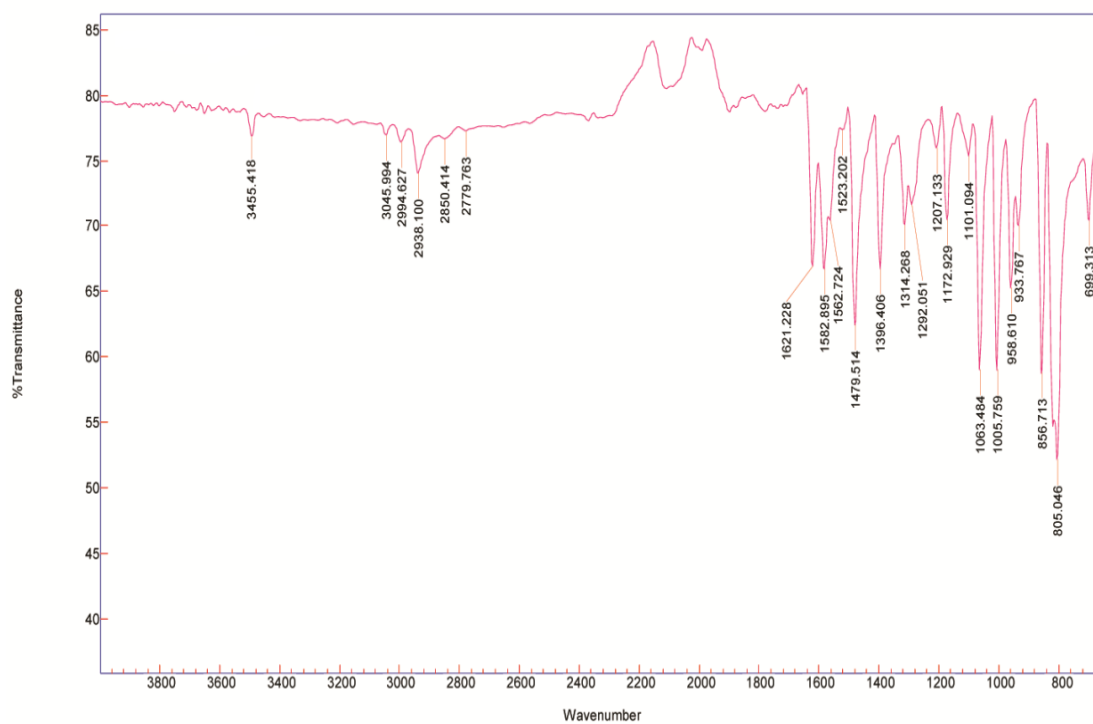
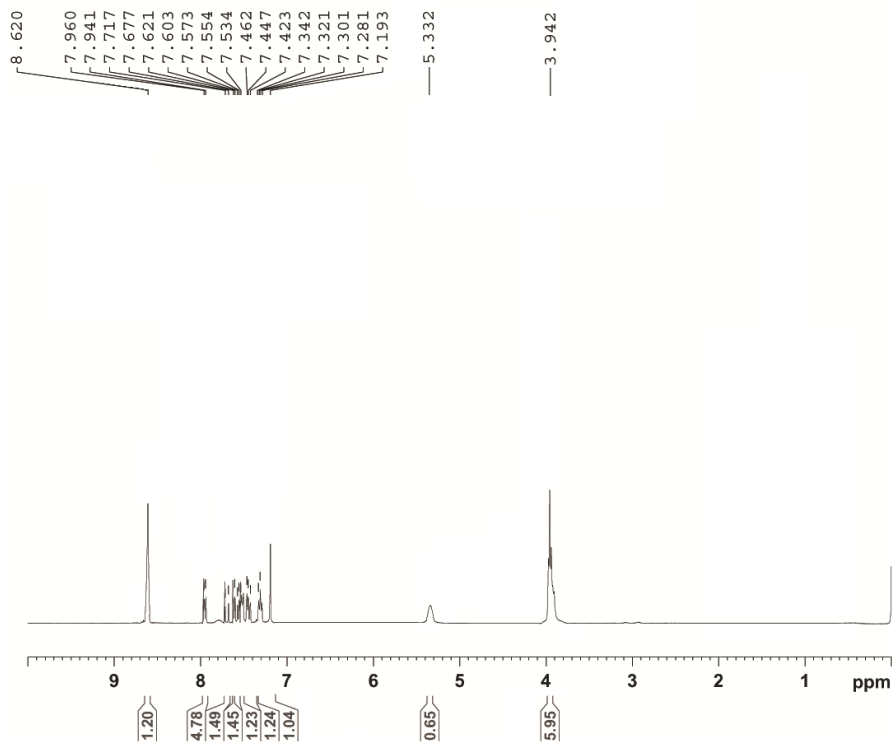


Plate 2. FT-IR spectrum of compound A2



```

Current Data Parameters
NAME          11
EXPNO         1
PROCNO        1

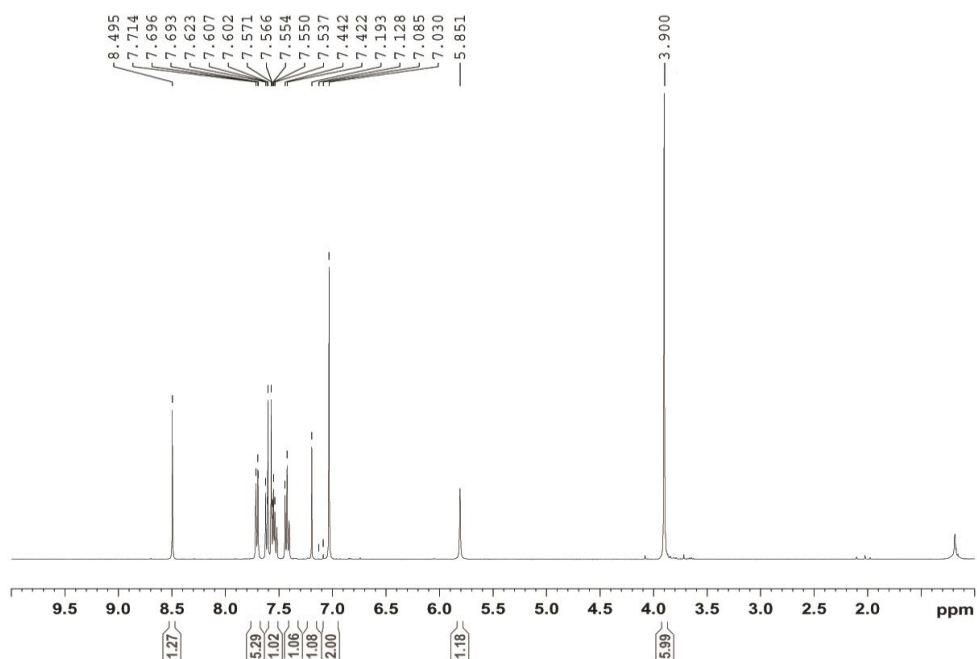
F2 - Acquisition Parameters
Date_         20190131
Time          10.41
INSTRUM       spect
PROBHD        5 mm PABBO BB-
PULPROG       zg30
TD            65536
SOLVENT       CDCl3
NS            16
DS            2
SWH           8012.820 Hz
FIDRES        0.122266 Hz
AQ            4.0894465 sec
RG            174.41
DW            62.400 usec
DE            6.50 usec
TE            294.6 K
D1            1.00000000 sec
TDO           1

===== CHANNEL f1 =====
SFO1          400.1324710 MHz
NUC1          1H
P1            13.50 usec
PLW1          11.00000000 W

F2 - Processing parameters
SI            65536
SF            400.1300361 MHz
WDW           EM
SSB           0
LB            0.30 Hz
GB            0
PC            1.00

```

Plate 3. ^1H NMR Spectrum of compound A1



```

Current Data Parameters
NAME          20
EXPNO         1
PROCNO        1

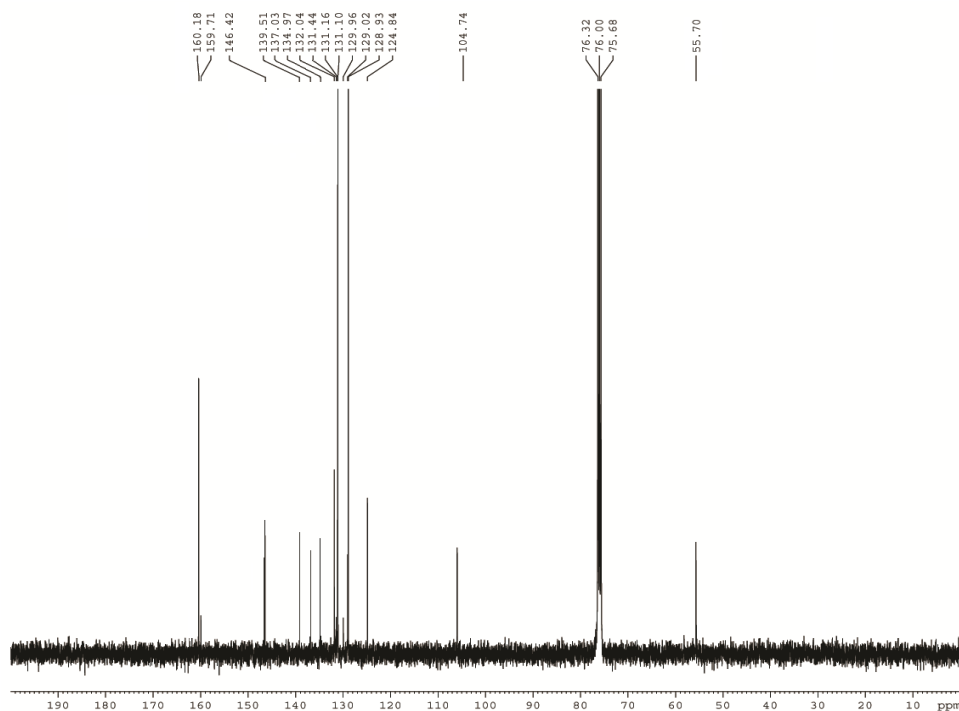
F2 - Acquisition Parameters
Date_         20180911
Time          10.35
INSTRUM       spect
PROBHD        5 mm PABBO BB-
PULPROG       zg30
TD            65536
SOLVENT       CDCl3
NS            16
DS            2
SWH           8012.820 Hz
FIDRES        0.122266 Hz
AQ            4.0894465 sec
RG            174.41
DW            62.400 usec
DE            6.50 usec
TE            294.6 K
D1            1.00000000 sec
TDO           1

===== CHANNEL f1 =====
SFO1          400.1324710 MHz
NUC1          1H
P1            13.50 usec
PLW1          11.00000000 W

F2 - Processing parameters
SI            65536
SF            400.1300361 MHz
WDW           EM
SSB           0
LB            0.30 Hz
GB            0
PC            1.00

```

Plate 4. ^1H NMR Spectrum of compound A2



```

Current Data Parameters
NAME          11
EXPNO         1
PROCNO        1

F2 - Acquisition Parameters
Date_         20180827
Time          14.27
INSTRUM      spect
PROBHD       5 mm PABBO BB-
PULPROG      zgpg30
TD            65536
SOLVENT      CDCl3
NS            2500
DS            4
SWH           24038.461 Hz
FIDRES       0.366798 Hz
AQ            1.3631488 sec
RG            195.62
DW            20.800 usec
DE            6.50 usec
TE            297.8 K
D1            2.0000000 sec
D11           0.0300000 sec
TDO           1

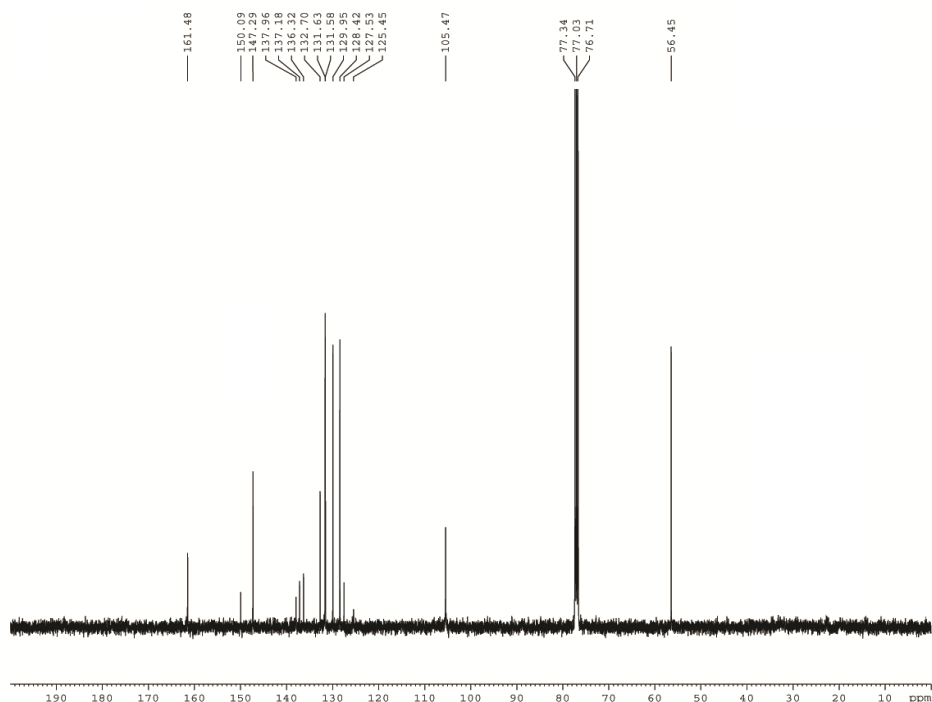
===== CHANNEL f1 =====
SFO1          100.6228293 MHz
NUC1           13C
P1             9.00 usec
PLW1           55.40000153 W

===== CHANNEL f2 =====
SFO2          400.1316005 MHz
NUC2            1H
CPDPRG[2]     waltz16
PCPD2         90.00 usec
PLW2          11.00000000 W
PLW12         0.24750000 W
PLW13         0.20048000 W

F2 - Processing parameters
SI             32768
SF            100.6128723 MHz
WDW            EM
SSB            0
LB             1.00 Hz
GB             0
PC             1.40

```

Plate 5. ^{13}C NMR Spectrum of compound A1



```

Current Data Parameters
NAME          20
EXPNO         1
PROCNO        1

F2 - Acquisition Parameters
Date_         20180927
Time          20.21
INSTRUM      spect
PROBHD       5 mm PABBO BB-
PULPROG      zgpg30
TD            65536
SOLVENT      CDCl3
NS            3000
DS            4
SWH           24038.461 Hz
FIDRES       0.366798 Hz
AQ            1.3631488 sec
RG            195.62
DW            20.800 usec
DE            6.50 usec
TE            298.2 K
D1            2.0000000 sec
D11           0.0300000 sec
TDO           1

===== CHANNEL f1 =====
SFO1          100.6228293 MHz
NUC1           13C
P1             9.00 usec
PLW1           55.40000153 W

===== CHANNEL f2 =====
SFO2          400.1316005 MHz
NUC2            1H
CPDPRG[2]     waltz16
PCPD2         90.00 usec
PLW2          11.00000000 W
PLW12         0.24750000 W
PLW13         0.20048000 W

F2 - Processing parameters
SI             32768
SF            100.6127685 MHz
WDW            EM
SSB            0
LB             1.00 Hz
GB             0
PC             1.40

```

Plate 6. ^{13}C NMR Spectrum of compound A2

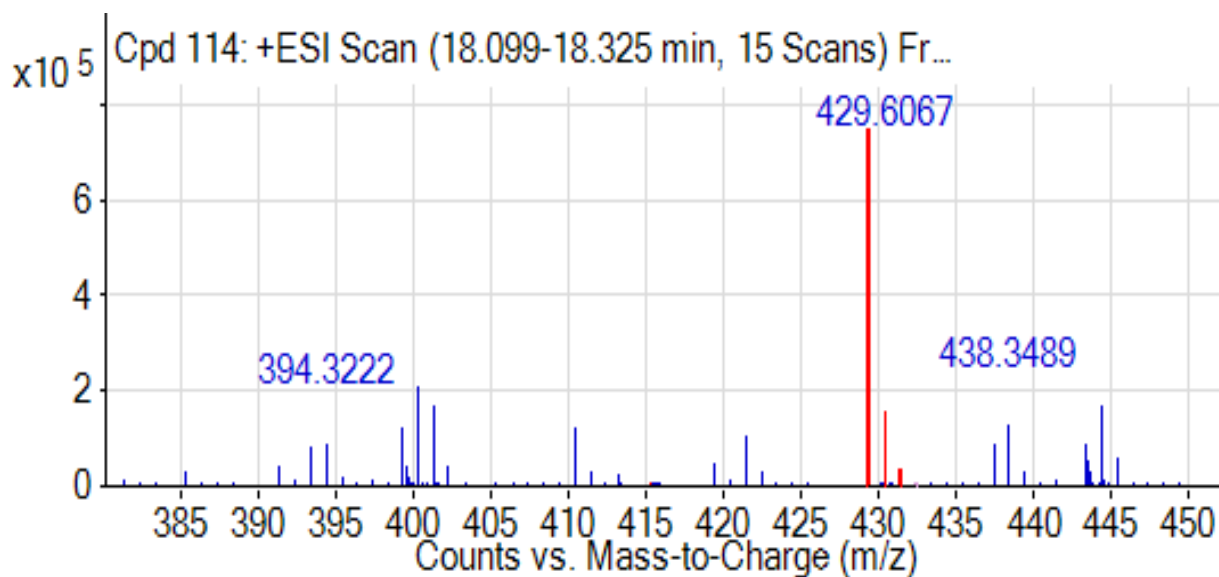


Plate 7. Mass Spectrum of compound A1

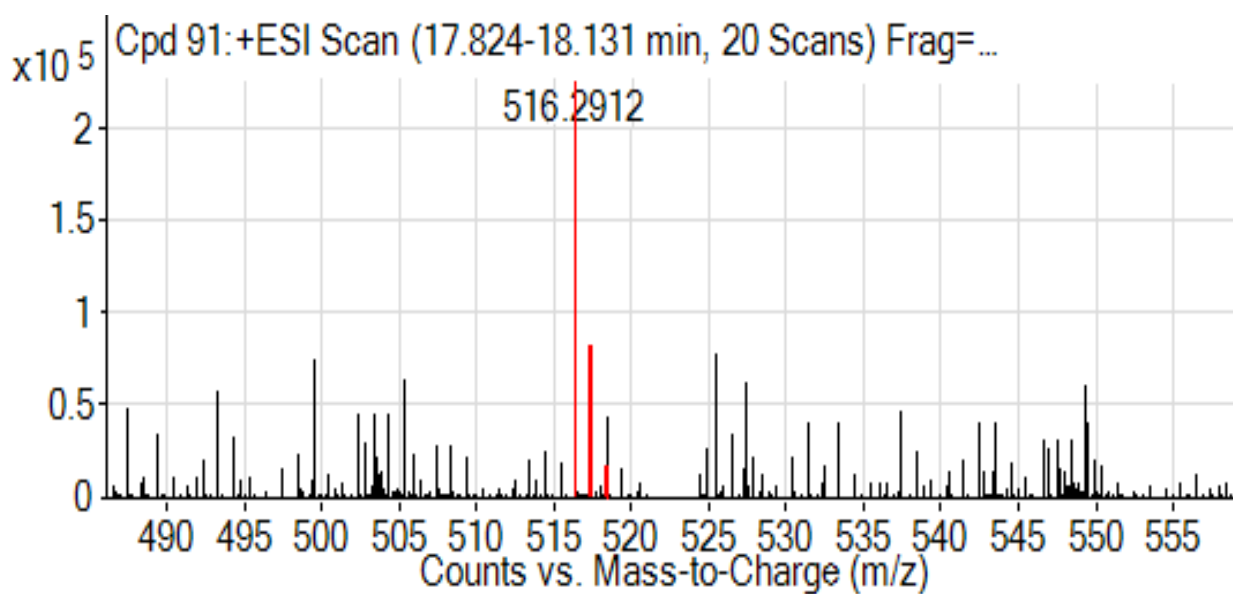


Plate 8. Mass Spectrum of compound A2

Table 1. Type of the spectra recorded for the synthesized compounds A1 and A2

Compounds	IR	¹ H NMR	¹³ C NMR	ESI-Mass
A1	✓	✓	✓	✓
A2	✓	✓	✓	✓

4.2.2. FT-IR spectral analysis of compounds A1 and A2

The FT-IR spectrum of **A1** and **A2** is given in **plates 1** and **2**. In general, the prominent peak occurs in the region of 1615-1621 cm⁻¹ of compounds **A1** and **A2** is assigned to stretching C=N vibration and stretching aromatic C-H vibration attributed in the region of 3045-3074 cm⁻¹. The absorption bands noticed in the region of 1510-1523 cm⁻¹ are ascribed to C=C stretching frequencies. The O-H stretching frequencies appeared at 3445-3445 cm⁻¹. The methoxy group occurs in the region of 2926-2938 cm⁻¹ for compounds **A1** and **A2**. **Table 2** displays the experimental values.

Table 2. Compounds A1 and A2 of vibrational frequencies

Assignments	Compounds	ν _{C=N}	ν _{C=C}	ν _{C-H}	ν _{O-H}	ν _{OCH₃}
Vibrational frequency (cm ⁻¹)	A1	1615	1510	3074	3445	2926
	A2	1621	1523	3045	3445	2938

4.2.3. ¹H NMR spectral analysis of compounds A1 and A2

The NMR spectra were performed in CDCl₃. The ¹H NMR spectrum of synthesized compounds **A1** and **A2** are displayed in **Plates 3** and **4**. The high resolution ¹H NMR spectra are recorded for compounds **A1** and **A2**. The placements and integrals of the signals were used to allocate them. The downfield signal at 8.49-8.62 ppm is azomethine proton in general. The aromatic proton signal is found in the 7.08-7.71 ppm range. OH proton is assigned to the upfield signal that appeared in the range of 5.33-5.40 ppm. Furthermore, for compounds **A1** and **A2**, the OCH₃ group was found in the range of 3.94-3.97 ppm. **Table 3** summarizes the tentative assignment of experimental ¹H NMR data of compounds **A1** and **A2**.

Table 3. ¹H NMR chemical shift (ppm) of A1 and A2

Compounds	Protons			
	CH=N	Aromatic proton	OH	OCH ₃
A1	8.62	7.28-7.71	5.33	3.94
A2	8.49	7.08-7.71	5.85	3.90

4.2.4. ¹³C NMR spectral analysis of A1 and A2

The ¹³C NMR spectrum of compounds **A1** and **A2** at 100 MHz was recorded in CDCl₃. The ¹³C NMR spectrum of compounds **A1** and **A2** are displayed in **plates 5** and **6**. The C₂₀H₂₉NO carbons are allocated to the high frequency signals at 160.78-161.48 ppm. The ipso carbon signal attributed at 159.71-150.09 ppm. The aromatic carbon appeared at 104.74-147.29 ppm, the methoxy group attributed in the range of 56.67-55.70 ppm respectively. The experimental carbon chemical shifts are presented in **Table 4**.

Table 4. ^{13}C NMR spectral analysis of **A1** and **A2**

Compounds	Carbons			
	CH=N	C=N	Aromatic carbon	OCH ₃
A1	160.78	159.71	104.74-146.42	55.70
A2	161.48	150.09	105.47-147.29	56.45

4.2.5. ESI Mass spectra

The **A1** and **A2** ESI-Mass spectra were obtained and are shown on **plates 7** and **8**. The mass spectrum of chemical **A1** shows an ion peak with $m/z = 429.60$, which corresponds to the molecular structure computed [428.07]. The compound **A2** had an ion peak of $m/z = 516.29$ $[\text{M}+\text{H}]^+$ computed [515.97], which corresponded to a molecular structure that was almost identical to their estimated m/z values..

4.3. RESULTS AND DISCUSSION

4.3.1. Absorption studies

The colorless solution of **A1** exhibited a change in color to become yellow visible to the naked eye. Using HEPES buffer solution in $\text{H}_2\text{O}:\text{EtOH}$ (4:1, v/v) medium at $\text{pH}=7.0$, UV-visible investigations were conducted to investigate the sensor behaviour of **A1** ($1.0 \times 10^{-3} \text{ M}^{-1}$) with different metal ions such as Zn^{2+} , Al^{3+} , Hg^{2+} , Ag^+ , Ca^{2+} , Na^+ , Fe^{3+} , Ni^{2+} , Co^{2+} , Mn^{2+} , Pb^{2+} , Mg^{2+} , Zn^{2+} , Cd^{2+} , and K^+ . The absorption band at 330 nm is related to the Zn^{2+} complex, whereas the absorption band at 335 nm is due to the **A1** (10 mM) spectrum studied with various metal ions showed in **Fig. 1**. In the presence of alkali and alkali earth metal ions, this interaction demonstrates great selectivity of Zn^{2+} with the sensor. In **Fig. 2**, the absorption spectra of sensor **A1** ($1.0 \times 10^{-3} \text{ M}^{-1}$) with Zn^{2+} (10-110M) in HEPES buffer solution in $\text{H}_2\text{O}:\text{EtOH}$ (4:1, v/v) medium at $\text{pH}=7.0$, with a strong absorption intensity at 335 nm, are displayed. It should be observed that when the concentration of Zn^{2+} ions increases, the intensity of absorbance decreases.

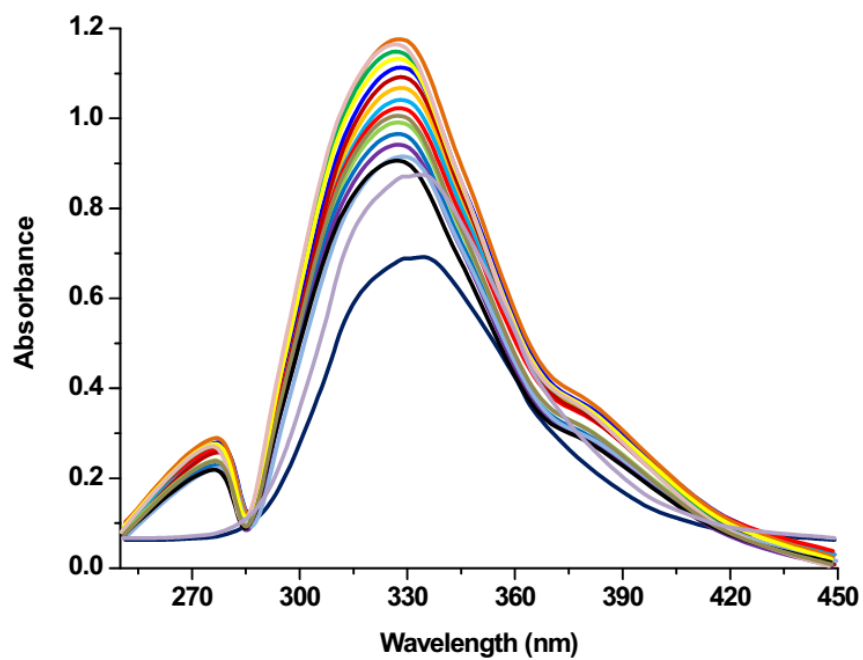


Fig. 1 The **A1** ($1.0 \times 10^{-3} \text{ M}^{-1}$) absorption spectra in EtOH with various metal ions employed in HEPES buffer solution: (1:4, v/v) H_2O pH=7.0

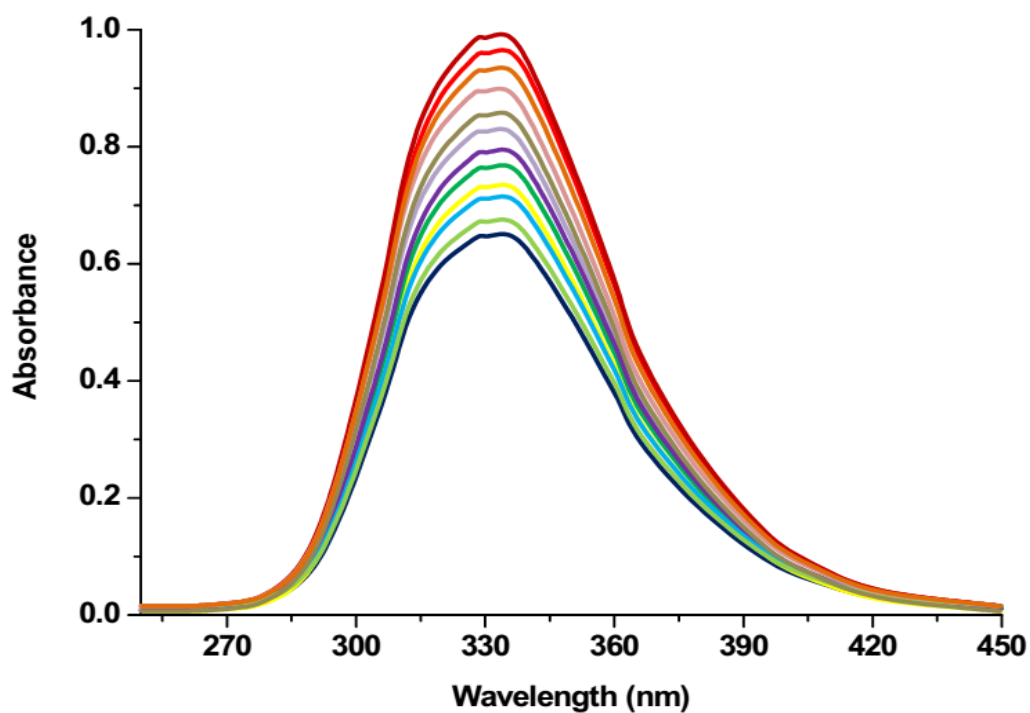


Fig. 2 UV-visible spectra of **A1** ($1.0 \times 10^{-3} \text{ M}^{-1}$) in ethanol with various concentrations of Zn^{2+} (10^{-10} - 10^{-11} M)

Using HEPES buffer solution in EtOH:H₂O (1:4, v/v) pH=7.0) medium, UV-visible studies of sensor **A2** ($1.0 \times 10^{-3} \text{ M}^{-1}$) were carried out with different metal ions such as Zn²⁺, Al³⁺, Hg²⁺, Ag⁺, Ca²⁺, Na⁺, Fe³⁺, Ni²⁺, Co²⁺, Mn²⁺, Pb²⁺, Mg²⁺, Zn²⁺, Cd²⁺, and K⁺. In the presence of Al³⁺ ion, the colourless solution of **A2** changed to yellow very instantly. The absorption spectrum of **A2** (10 mM) with different metal ions provided absorption band at 290 nm overall, but another absorption band at 307 nm was observed due to complexation with Al³⁺ ion, as shown in **Fig. 3**. Two alkali earth metal ions (Mg²⁺, Ca²⁺), and transition metal ions Mg²⁺, Fe³⁺, Ni²⁺, Cd²⁺, Co²⁺, Mn²⁺, Cu²⁺, Zn²⁺, and Ag⁺). In **Fig. 4**, the absorption spectra of **A2** ($1.0 \times 10^{-3} \text{ M}^{-1}$) with Al³⁺ ion in HEPES buffer solution EtOH:H₂O (1:4, v/v) pH=7.0, the strong absorption intensity at 295 nm progressively decreased with the addition of Al³⁺ ion (10-110M).

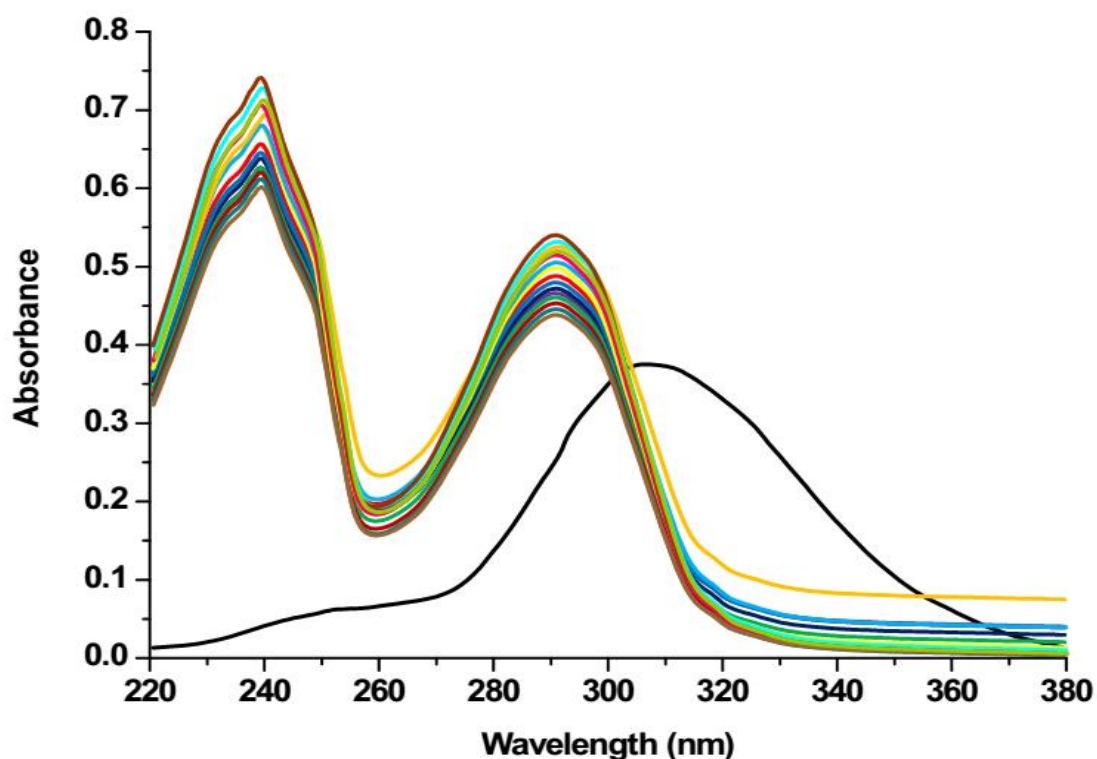


Fig. 3 The **A2** absorption spectra in EtOH with various metal ions in HEPES buffer solution: pH=7.0 H₂O (1:4, v/v)

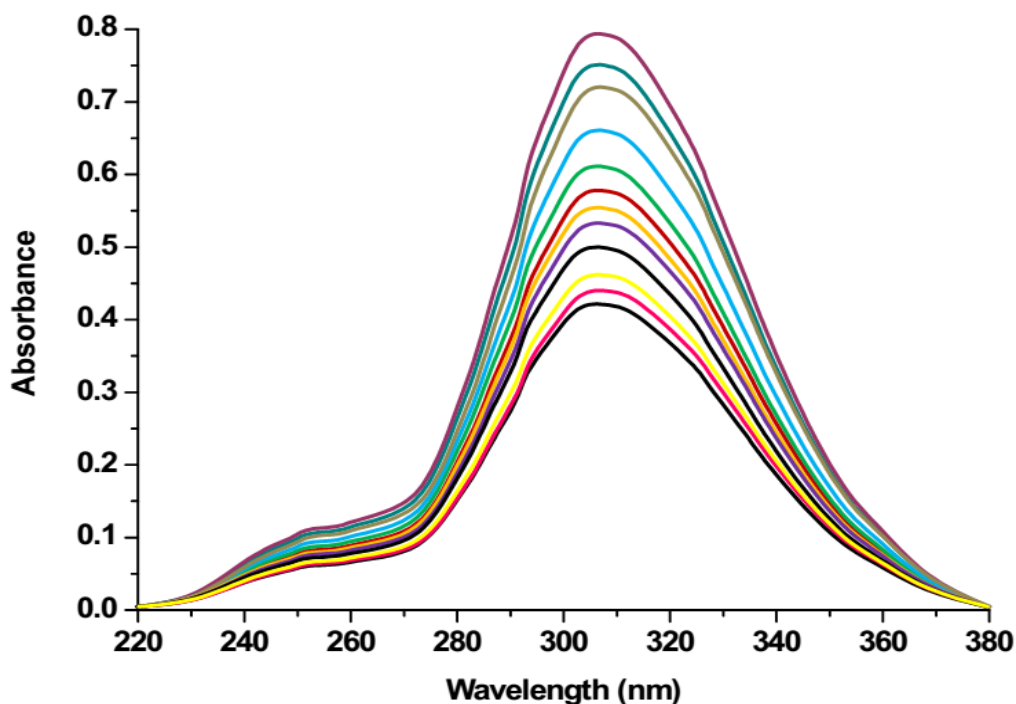


Fig. 4 UV-visible titration spectra of **A2** (10 mM) in ethanol with various amounts of Al^{3+} ion

4.3.2. Fluorescence studies

The sensor **A1** demonstrated a significant fluorescence intensity at 525 nm with all metal ions, as shown in **Fig. 5**. (while excitation wavelength 325 nm). Further, the sensor **A1** displayed selectivity of Zn^{2+} ion by turn-off fluorescence signaling by binding with chemosensor, whereas, all other metal ions slight increase. In a 10 mM HEPES buffer solution in H_2O : EtOH (4:1, v/v) at pH=7.0, binding interaction of sensor **A1** ($1.0 \times 10^{-6} \text{ M}^{-1}$) with Zn^{2+} ($5.0 \times 10^{-6} \text{ M}^{-1}$) was performed. When Zn^{2+} (10^{-110} M) is added to the sensor, the fluorescence intensity at 450 nm gradually decreases (**Fig. 6**). In a 10mM HEPES buffer solution in H_2O : EtOH (4:1, v/v) pH=7.0, the fluorescence spectrum of the **A2** ($1.0 \times 10^{-6} \text{ M}^{-1}$) was examined with various metal ions such as Zn^{2+} , Al^{3+} , Hg^{2+} , Ag^+ , Ca^{2+} , Na^+ , Fe^{3+} , Ni^{2+} , Co^{2+} , Mn^{2+} , Pb^{2+} , Mg^{2+} , Zn^{2+} , Cd^{2+} , and K^+ . Fluorescence intensity appeared at 455 nm, as illustrated in **Fig. 7**. (while excitation wavelength 450 and 470 nm). The sensor **A2** displayed selectivity of Al^{3+} ion in turn-on fluorescence signal but other metal ions showed no change. The great selectivity for Al^{3+} caused the "turn-on" fluorescent signal of **A2** at

455nm, but there was no significant change in fluorescence in the presence of Ca^{2+} , Ag^+ , or Hg^{2+} (**Fig 7**). In a 10mM HEPES buffer solution in H_2O : EtOH (4:1, v/v) pH=7.0, binding sensor **A2** ($1.0 \times 10^{-6} \text{ M}^{-1}$) interacts with Al^{3+} ($5.0 \times 10^{-6} \text{ M}^{-1}$). As shown in **Fig. 8**, adding Al^{3+} steadily enhanced the intensity of **A2** (10-110M) at 455 nm, indicating Al^{3+} ion binding and complex formation

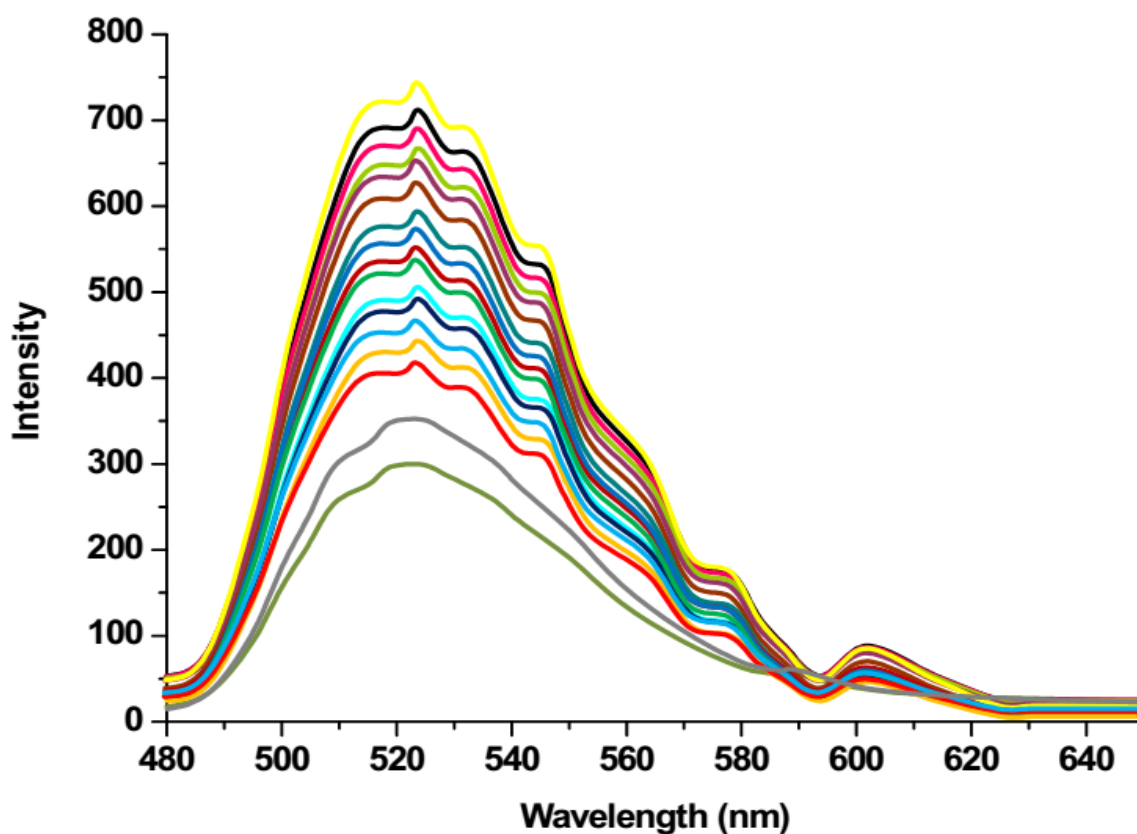


Fig. 5 Fluorescence spectra of **A1** in 10 mM HEPES buffer solution in H_2O with various metal ions: (4:1, v/v) EtOH pH=7.0

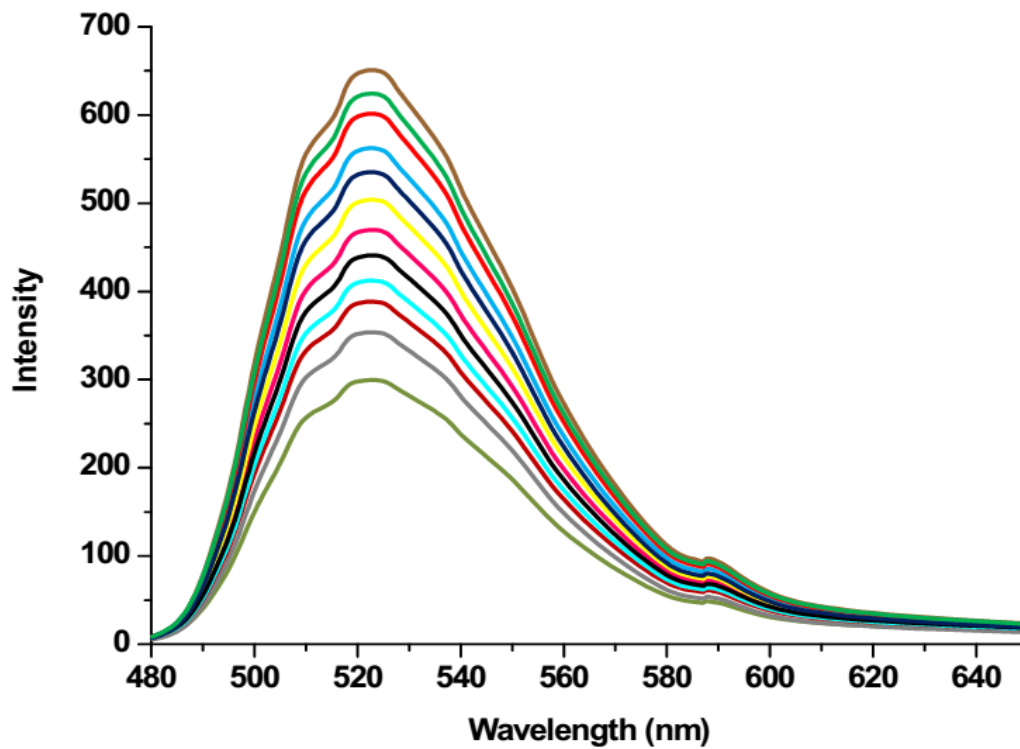


Fig. 6 Fluorescence spectra of **A1** ($1.0 \times 10^{-5} \text{ M}^{-1}$) in the presence of various Zn^{2+} concentrations (10-110M) in ethanol

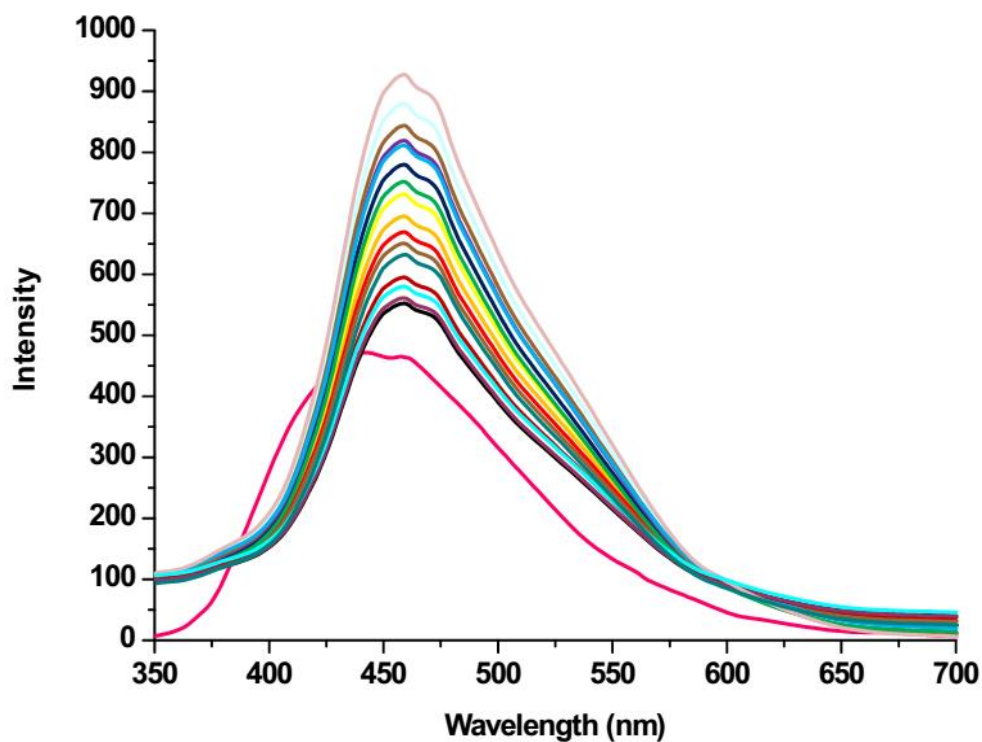


Fig. 7 Fluorescence spectra of **A2** in 10 mM HEPES buffer solution in EtOH with various metal ions: (1:4, v/v) H_2O pH=7.0

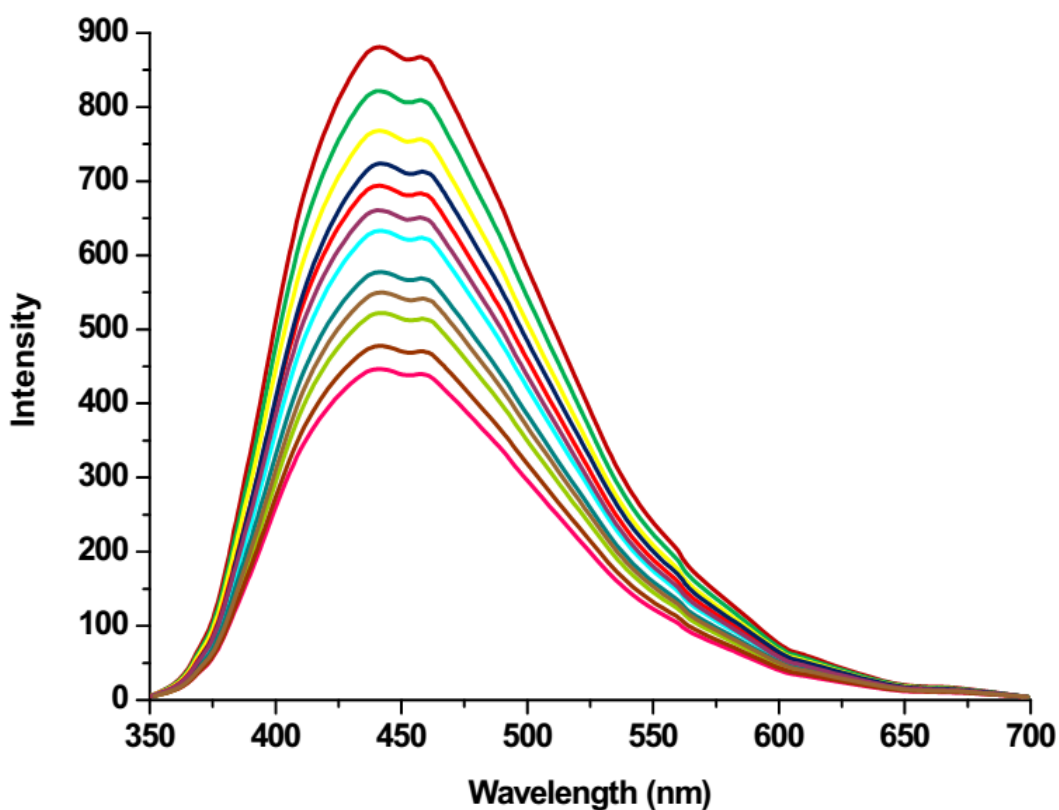


Fig. 8 Fluorescence titration spectra of **A2** (10 mM) in the presence of different concentrations of Al^{3+} in ethanol

In HEPES buffer solution in $\text{H}_2\text{O}:\text{EtOH}$ (4:1, v/v) at $\text{pH}=7.0$, the role of sensor **A1** with coupled competitive metal ions was investigated towards Zn^{2+} . For all metal ions, the sensor **A1** showed fluorescence intensity at 295 and 325 nm, although there was a "turn-off" fluorescence effect for Zn^{2+} . As a result, even in the presence of other metal ions as seen in **Fig. 9**, the strong paramagnetic character of Zn^{2+} entirely quenched the fluorescence intensity. For Al^{3+} in HEPES buffer solution in $\text{H}_2\text{O}:\text{EtOH}$ (4:1, v/v) $\text{pH}=7.0$, the usage of sensor **A2** with coupled competitive metal ions was investigated. The fluorescence intensity 455 nm of the sensors **A2** was stable for all metal ions, however it slightly dropped and rose to a variable amount in the presence of Al^{3+} . Therefore, fluorescence is obviously changed Al^{3+} complex. The fluorescence signal caused by **A2**- Al^{3+} complex was much altered in presence of other metal ions like Fe^{3+} , Mg^{2+} , & Ag^+ due to paramagnetism (**Fig. 10**). Second,

sensor **A2** was examined, and it was discovered that the fluorescence intensity at 455 nm was slightly reduced and increased to a different size in comparison to the presence of Al^{3+} ions, indicating that they had a required "turn-on" fluorescence signal to give effect for the recognition of Al^{3+} . From **Fig 10** it is clear that Al^{3+} caused a constant change in fluorescence intensity at **AT** while other metal ions lead to appreciate variation.

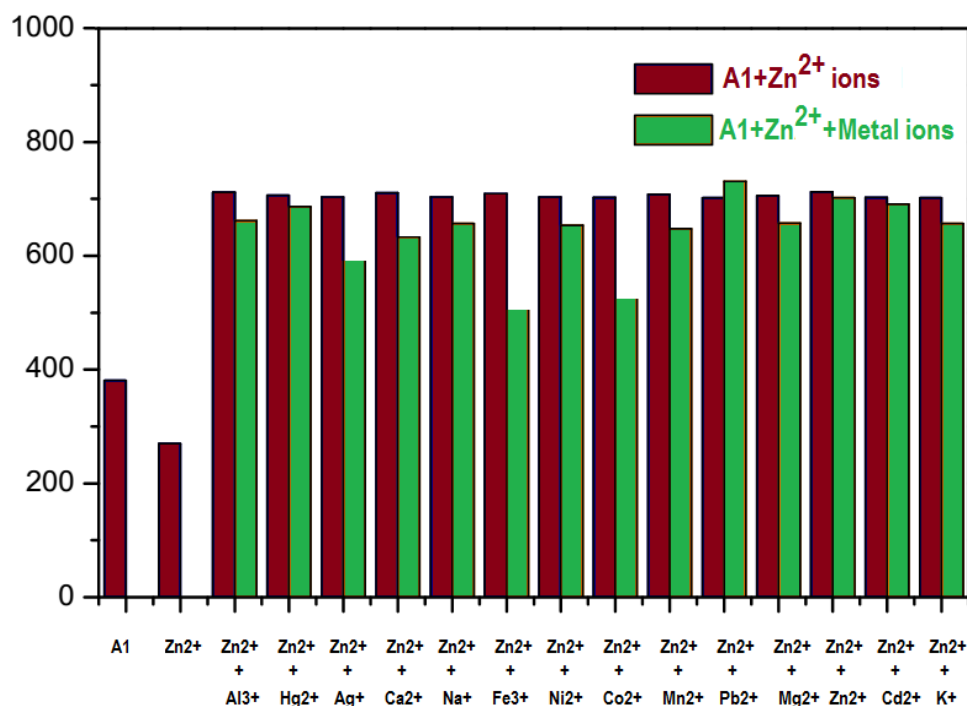


Fig. 9 The fluorescence changes of **A1** (10 mM) with Zn^{2+} (10 mM) and upon addition of Zn^{2+} , Al^{3+} , Hg^{2+} , Ag^+ , Ca^{2+} , Na^+ , Fe^{3+} , Ni^{2+} , Co^{2+} , Mn^{2+} , Pb^{2+} , Mg^{2+} , Cd^{2+} , and K^+ (10 mM) were prepared in HEPES buffer solution $\text{H}_2\text{O}:\text{EtOH}$ (4:1, v/v)

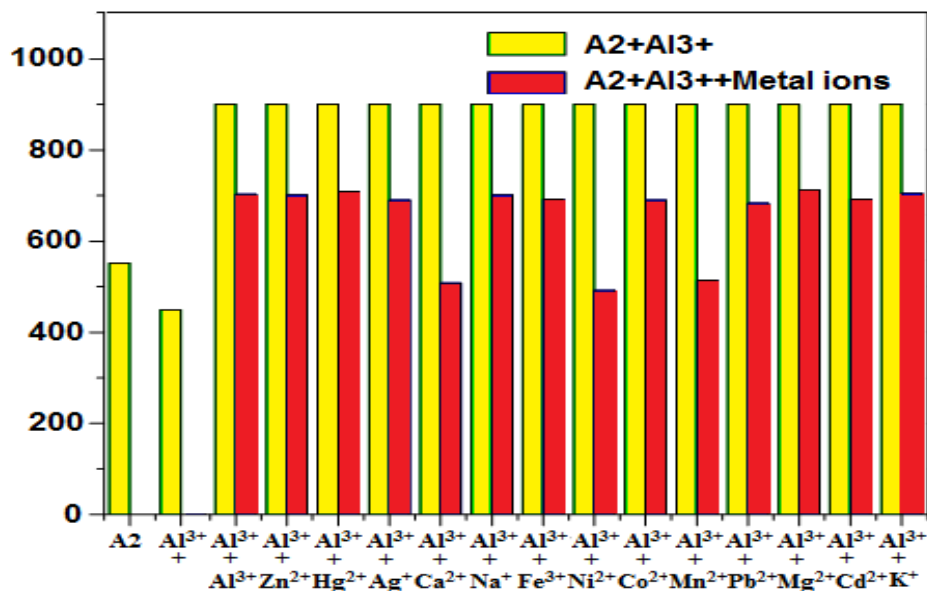


Fig. 10 The fluorescence changes of A2 (10 mM) with Al³⁺ (10 mM) and upon addition of Zn²⁺, Al³⁺, Hg²⁺, Ag⁺, Ca²⁺, Na⁺, Fe³⁺, Ni²⁺, Co²⁺, Mn²⁺, Pb²⁺, Mg²⁺, Cd²⁺, and K⁺ (10 mM) were prepared in HEPES buffer solution H₂O:EtOH (4:1, v/v)

4.3.3. Job's plot studies and reversibility

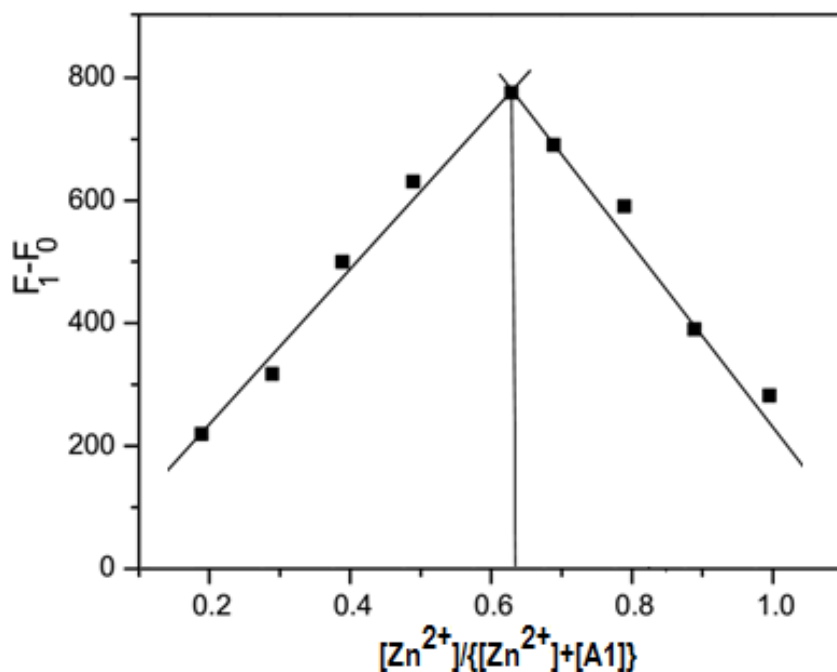


Fig. 11 Job's plot of a 1: 1 complex of A1 (30 mM) and Zn²⁺ ions.

In this study the presence of Zn^{2+} binding with **A1** forming metal complex was proved with 1:1 stoichiometry. This was evidenced by k_a maximum value of 0.62 (K_a) as noted in the plot of F_1-F_0 versus $Zn^{2+}/\{[Zn^{2+}]+[A1]\}$ (Fig 11). The corresponding association constant was found to be $1.13 \times 10^5 M^{-1}$ as determined by Benesi-Hildebrandt (Fig 12).

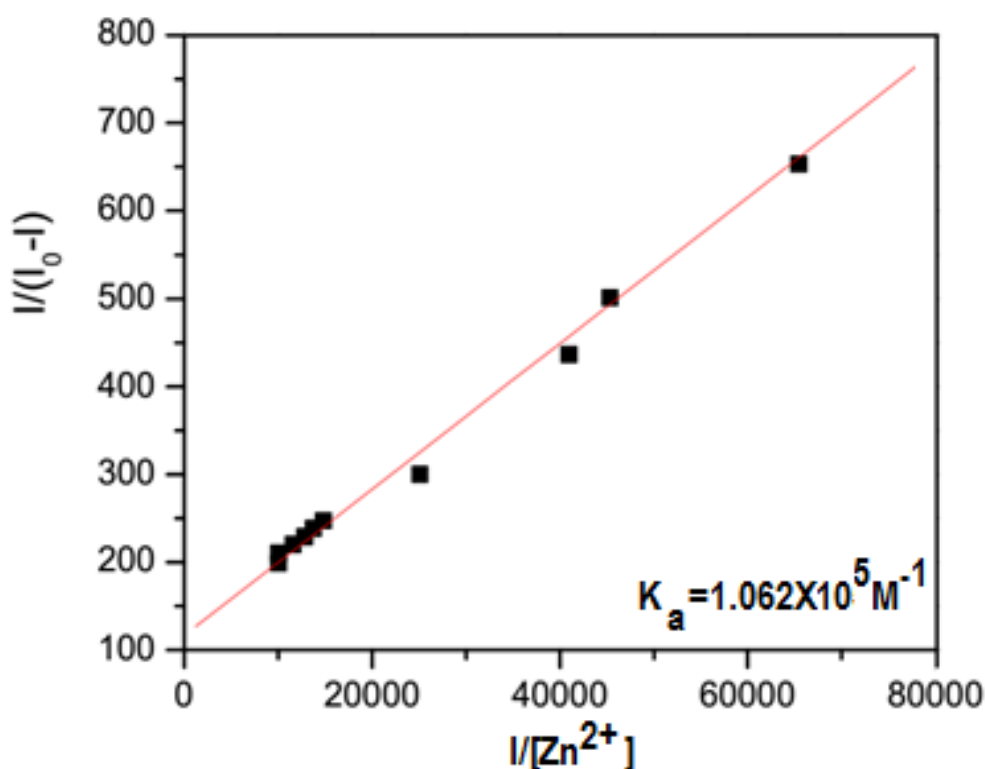


Fig. 12 Benesi-Hildebrandt plot of **A1** (10 mM) using 1:1 stoichiometric for association between **A1** and Zn^{2+} .

The detection limit was calculated as $1.06 \times 10^5 M^{-1}$ as shown in the plot of F vs $[Zn^{2+}]$ (**Fig. 13**). The possible binding mechanism of **A1** with Zn^{2+} which lead to the fluorescence quenching is shown in **Scheme 2**. Sensor **A1** containing one keto group and two amide group bind with Zn^{2+} , by hydrogen atom transfer. To analyse the binding ability and reversibility of **A1** to Zn^{2+} ions, it was titrated using ethylenediaminetetraacetic acid

(EDTA). The addition of EDTA solution to the **A1**-Zn²⁺ complex leads to suddenly changed “turn-on” fluorescence intensity. Chemosensor with Zn²⁺ ion exhibited fluorescence quenching while the addition of EDTA reverses the complex formation.

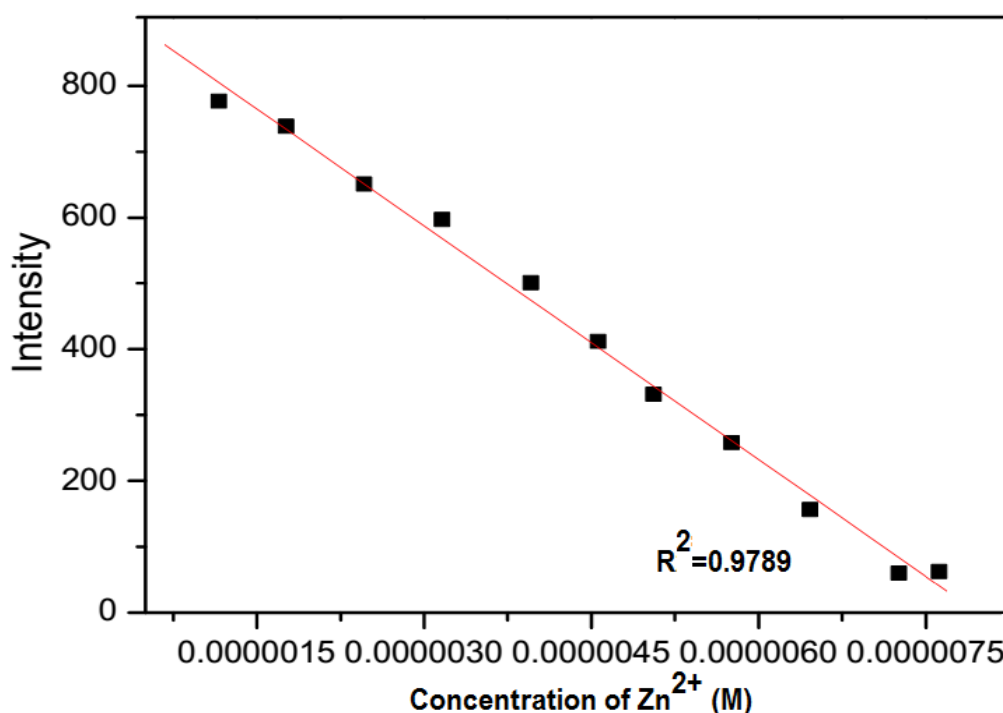


Fig. 13 Detection limit of change of **A1** (10 mM) with the total concentration of Zn²⁺ ion

Therefore, sensor **A1** is reversible in the presence of EDTA, which implements the presence of Al³⁺ binding with metal complex formation. The binding of stoichiometric complex of **A2** for Al³⁺, showed 1:1 complex formation (**Fig.14**). This complex of **A2**-Al³⁺ formation suggested 1:1 ratio was determined by the association constants (K_a) for **A2**-Al³⁺ and determined by Benesi-Hildebrand method was calculated $1.13 \times 10^5 \text{ M}^{-1}$ (**Fig. 15**). The detection limit was calculated as $1.13 \times 10^5 \text{ M}^{-1}$ as shown in K_a plot (**Fig. 16**).

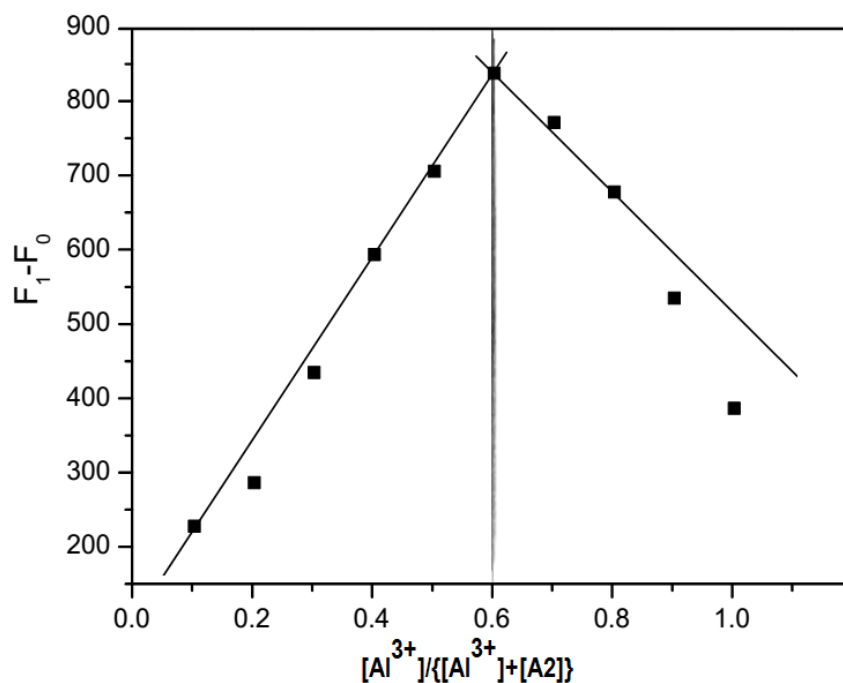


Fig. 14 Job's plot of a 1: 1 complex of **A2** (30 mM) and Al^{3+} ions.

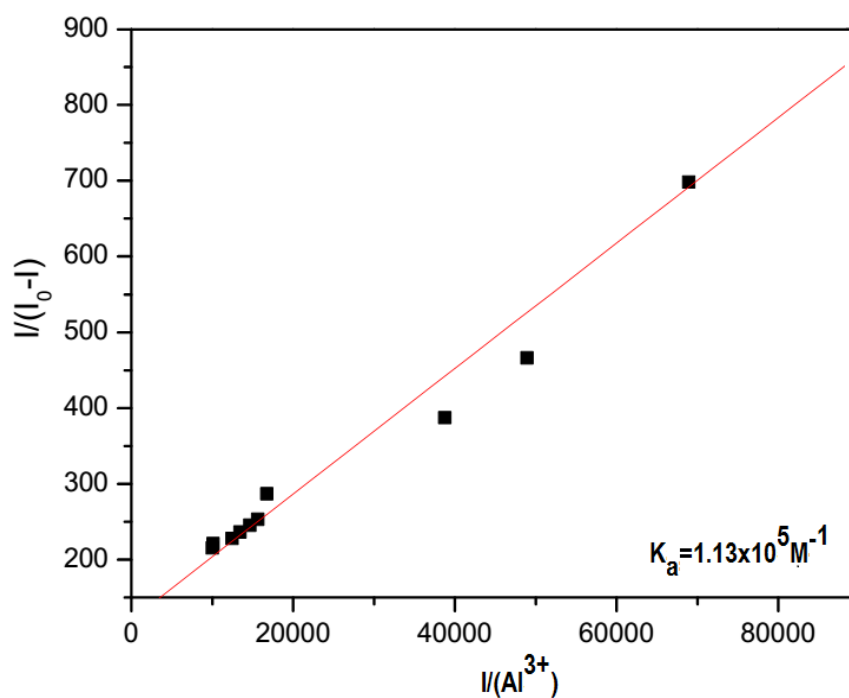


Fig. 15 Benesi-Hildebrand plot of **A2** (10 mM) using 1:1 stoichiometry for association between **A2** and Al^{3+} .

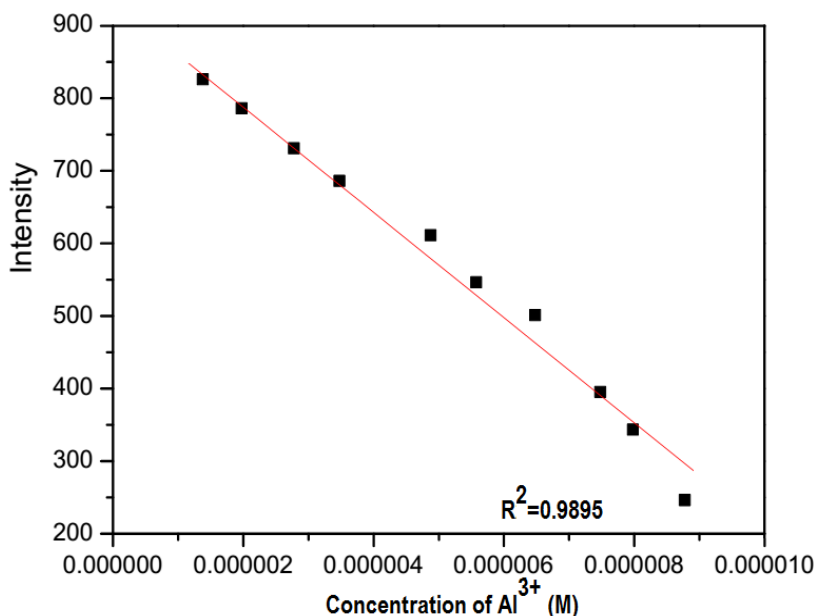


Fig. 16 Detection limit of change of **A2**

The binding ability and reversibility of **A1** to selectivity for Zn^{2+} ions was found by using ethylenediaminetetraacetic acid (EDTA). The addition of EDTA solution to **A1**- Zn^{2+} complex leads to sudden decrease of fluorescence intensity (**Figs. 17**). In HEPES buffer solution (1:4, v/v) EtOH: H₂O, fluorescence spectrum variations of **A2** (10 mM) and Al^{3+} with EDTA solution were generated. The fluorescence intensity at 365 nm was recorded after adding Al^{3+} again. Even after several cycles with sequential replacements of Zn^{2+} and an EDTA, the fluorescence shifted to reversible. As a result of the findings, chemosensor **A1** must be recycled using an appropriate reagent such as EDTA solution. Instead, the addition of EDTA solution with **A2** and Al^{3+} complex indicated that no obviously changed fluorescence intensities (**Fig. 18**), that **A2**- Al^{3+} complex formation was irreversible with EDTA. It indicated that completely reversible property by EDTA solution is very comfortable, because it could be different **A2**- Al^{3+} binding complex. Furthermore, because of the fluorescence signal "turn-on" procedure, **A2** might be beneficial for recognizing Al^{3+} . Although sensor **A2** would have recognized Al^{3+} in the presence of a specific metal ion, it did not demonstrate "turn-on" fluorescence. Finally it is conducted that, sensor **A1** shows reversible property of EDTA indicating that **A1** sensor is selective to Zn^{2+} while **A2** is selective for Al^{3+} .

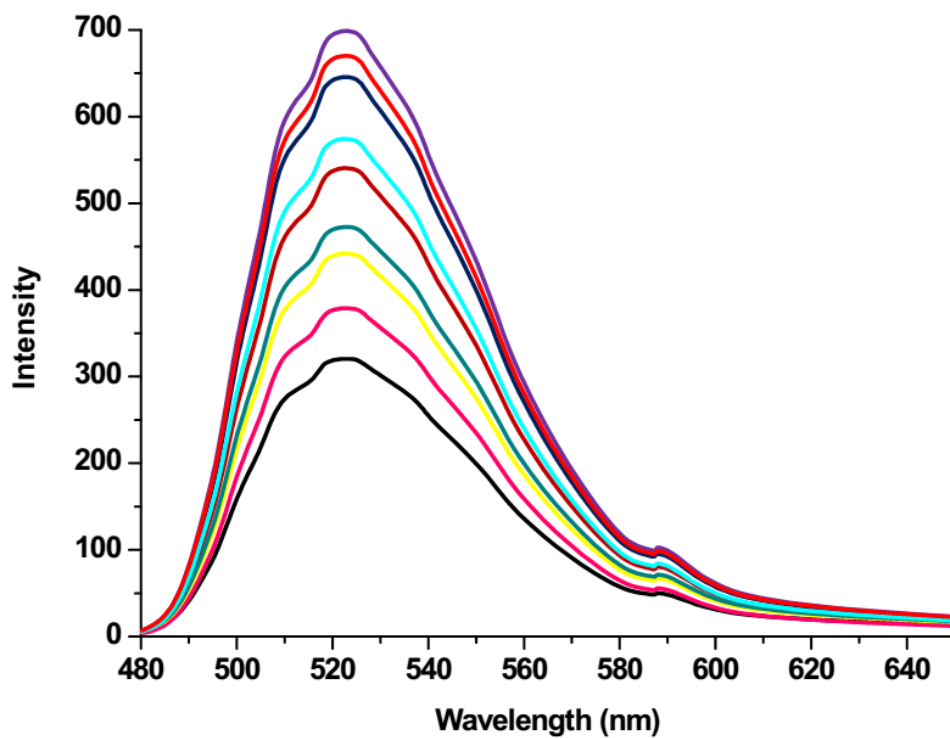


Fig. 17 Fluorescence spectral changes of **A1** (10 mM) and Zn²⁺ with EDTA solution solution (1:4, v/v) EtOH:H₂O

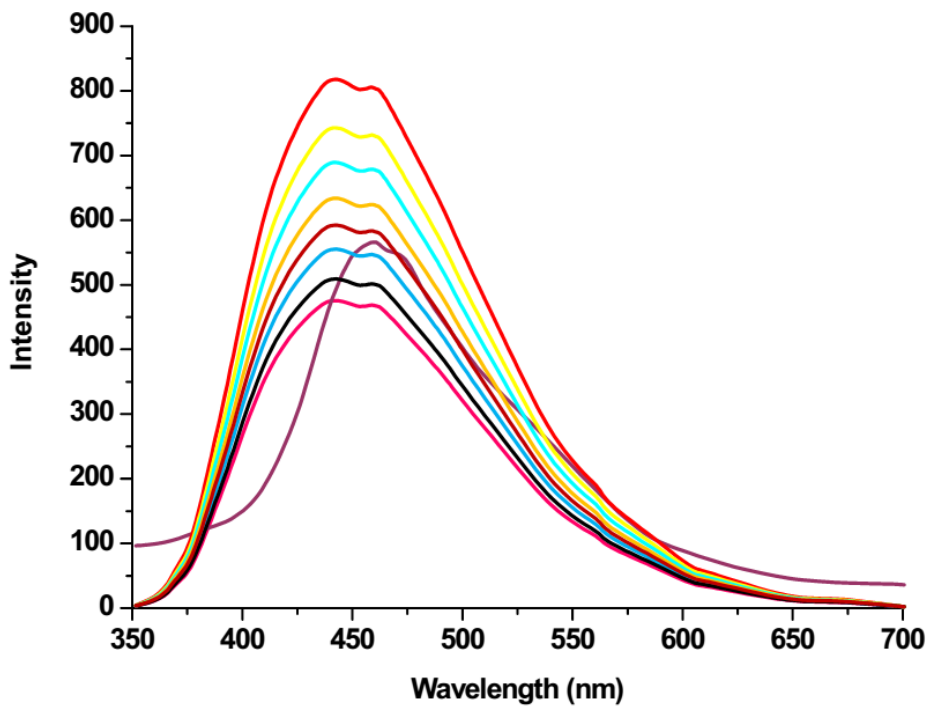
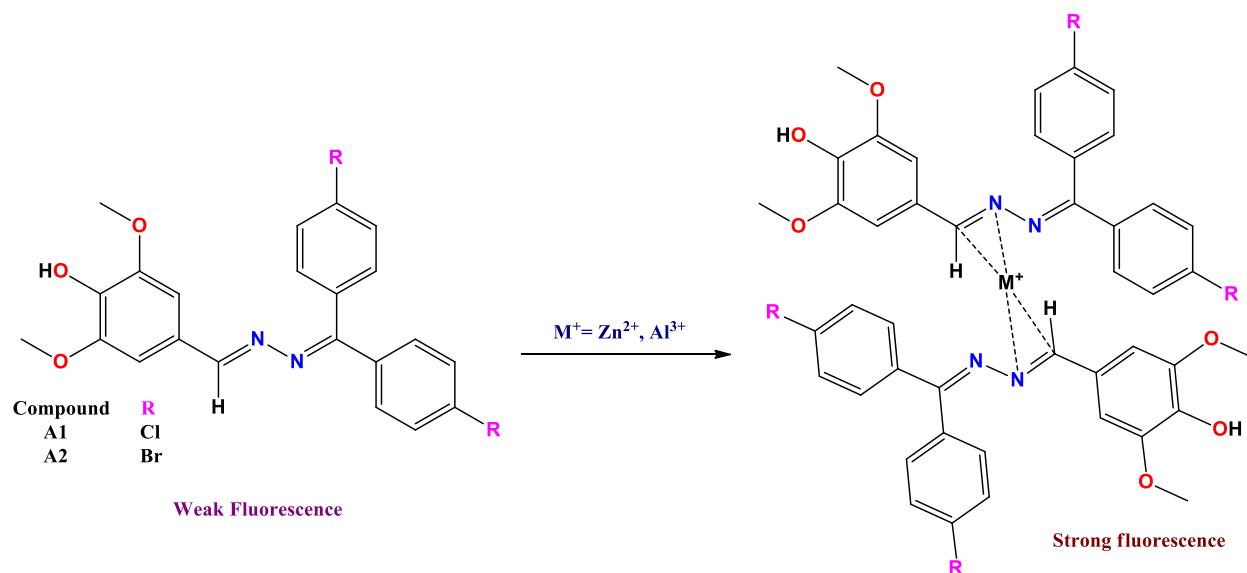


Fig. 18 Fluorescence spectral changes of **A2** (10 mM) and Al³⁺ with EDTA solution (1:4, v/v) EtOH:H₂O



Scheme 2. Sensing mechanism of A1 and A2

4.3.4. Computational analysis

4.3.4.1. Geometry Optimization

The DFT approach was used to optimise the molecular characteristics of **A1** and **A2** (bond angles, bond lengths, and dihedral angles of compounds **A1** and **A2**), as shown in **Table 5** and **Fig. 19**. The C-N bond distance values for compounds **A1** and **A2** are noteworthy at C16-N15 and C13-N14. These differences in chloro and bromo bond lengths show that X251-C25 corresponds to 1.91 and 1.75, respectively, while N15-N14 bond length is 1.38.

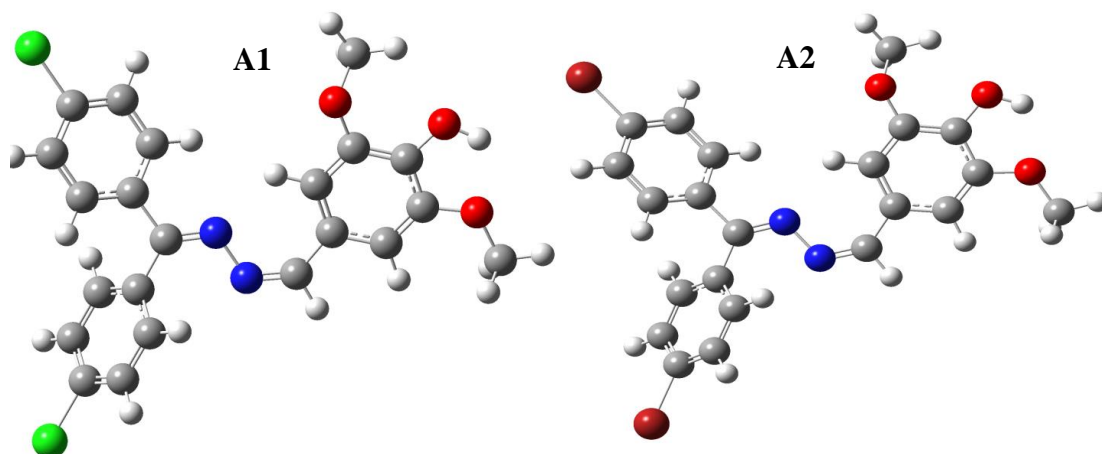


Fig. 19. Optimization structure of the A1 and A2

Table 5. Optimized geometrical parameters of **A1** and **A2**

Geometric parameters	Compounds	Geometric parameters	Compound
	A1	Bond length (Å)	A2
Bond length (Å)			
C1-C2	1.40	C1-C2	1.40
C2-C3	1.38	C2-C3	1.39
C3-C4	1.40	C3-C4	1.40
C5-C6	1.39	C5-C6	1.38
O7-C10	1.37	O7-C10	1.43
C4-O8	1.35	C4-O8	1.37
O9-C12	1.43	O9-C12	1.42
C1-C13	1.45	C1-C13	1.45
C13-N14	1.29	C13-N14	1.29
N14-N15	1.38	N14-N15	1.38
N15-C16	1.29	N15-C16	1.29
C17-C18	1.40	C17-C18	1.40
C18-C19	1.39	C18-C19	1.39
C19-C20	1.39	C19-C20	1.39
C21-C22	1.39	C21-C22	1.39
C23-C24	1.40	C23-C24	1.40
C25-C26	1.39	C25-C26	1.39
C27-C28	1.39	C27-C28	1.39
C25-X251	1.75	C25-X251	1.91

Bond angle (°)			
C1-C2-C3	118.71	C1-C2-C3	119.38
C4-C5-O9	121.45	C4-C5-O9	112.69
C4-C3-O7	112.96	C4-C3-O7	122.24
C2-C3-O7	126.16	C2-C3-O7	118.43
C1-C13-N14	122.41	C1-C13-N14	112.18
C13-N14-N15	115.75	C13-N14-N15	112.18
N15-C16-C17	125.19	N15-C16-C17	124.96
C18-C19-C20	120.26	C18-C19-C20	120.08
C21-C22-C17	120.67	C21-C22-C17	120.52
C24-C25-C26	121.00	C24-C25-C26	121.04
C27-C26-X261	119.43	C27-C26-X261	119.49
Torsional angle (°)			
C1-C2-C3-C4	0.34	C1-C2-C3-C4	0.31
C4-C5-O9-C12	64.32	C4-C5-O9-C12	179.05
C6-C1-C13-N14	0.11	C6-C1-C13-N14	0.75
N14-N15-C16-C17	-176.73	N14-N15-C16-C17	4.52
C18-C19-C20-C21	0.39	C18-C19-C20-C21	-0.44
C23-C24-C25-C26	0.31	C23-C24-C25-C26	0.31
C26-C27-C28-C23	-0.21	C26-C27-C28-C23	0.21
C24-C25-C26-X261	-178.42	C24-C25-C26-X261	-179.82

4.3.4.2. Nonlinear optical properties

The calculated NLO activity of the compound **A1** specimen are, $\alpha_{\text{tot}} = 3.610 \times 10^{-33}$ esu, $\beta_{\text{tot}} = 7.152 \times 10^{-24}$ esu, $\mu = -0.283$ and compound **A2** are $\alpha_{\text{tot}} = 3.469 \times 10^{-24}$ esu, $\beta_{\text{tot}} = 8.942 \times 10^{-33}$ esu, $\mu = 4.659$ as shown in **Table 6**.

Table 6. The NLO activity of **A1** and **A2**

A1	Parameters	A2
Dipole moment		
3.589	μ_x	-2.727
-1.667	μ_y	3.527
-0.283	μ_z	-1.355
-0.283	μ	4.659
Polarizability		
163.49	α_{xx}	171.85
143.43	α_{yy}	152.50
165.03	α_{zz}	173.04
26.19	α_{xy}	5.39
2.65	α_{xz}	8.43
2.25	α_{yz}	3.44
7.152X10⁻²⁴	α_o	3.469X10⁻²⁴
Hyperpolarizability		
296.593	β_{xxx}	-22.259
-34.727	β_{yyy}	-13.982
-1.349	β_{zzz}	-3.873
-43.751	β_{xxy}	54.985
-19.587	β_{xxz}	-67.335
25.598	β_{xzz}	51.205
3.623	β_{yzz}	-7.462
-4.514	β_{yyz}	-22.473
-4.514	β_{xyz}	-13.552
3.610X10⁻³³	β_o	8.942X10⁻³³

It is indicated that β_{tot} has its highest portion of β_{xxx} along the X-direction which means that electron cloud delocalization is more in this direction. The DFT/6-31G (d,p) technique yielded a β_{total} value of 0.382×10^{-33} esu for urea. The β value of **A1** is 9.45 times that of urea, while the β value of **A2** is 23.40 times that of urea. The urea molecule is used as a model for nonlinear optical characteristics. The NLO feature comes from the strongest intramolecular and intermolecular hydrogen bonding interactions, which boost the β value.

4.3.4.3. HOMO-LUMO analysis

The highest occupied molecular orbital and the lowest empty molecular orbital are found in frontier molecular orbitals, and the energy gap is one of the most efficient characteristics. FMOs were extremely useful in measuring molecular dynamics and describing chemical reactions. The total energy, HOMO and LUMO energies, the energy difference, the ionizing potential (I), the dipole moment (D), the absolute electronegativity (χ), the electron affinity (A), softness (S), and the absolute hardness (η) for the **A1** and **A2** were computed on the basis of the B3LYP/6-31G (d, p) foundation. The HOMO-LUMO orbitals are depicted in diagrams in **Fig. 20**. Compounds **A1** and **A2** have distinct energy values of 6.9372 eV and 6.1726 eV, respectively. Correspondingly, the energy gap for compound **A1** is higher while for **A2** its value is smaller. The HOMO-LUMO energy difference values are given in **Table 7**.

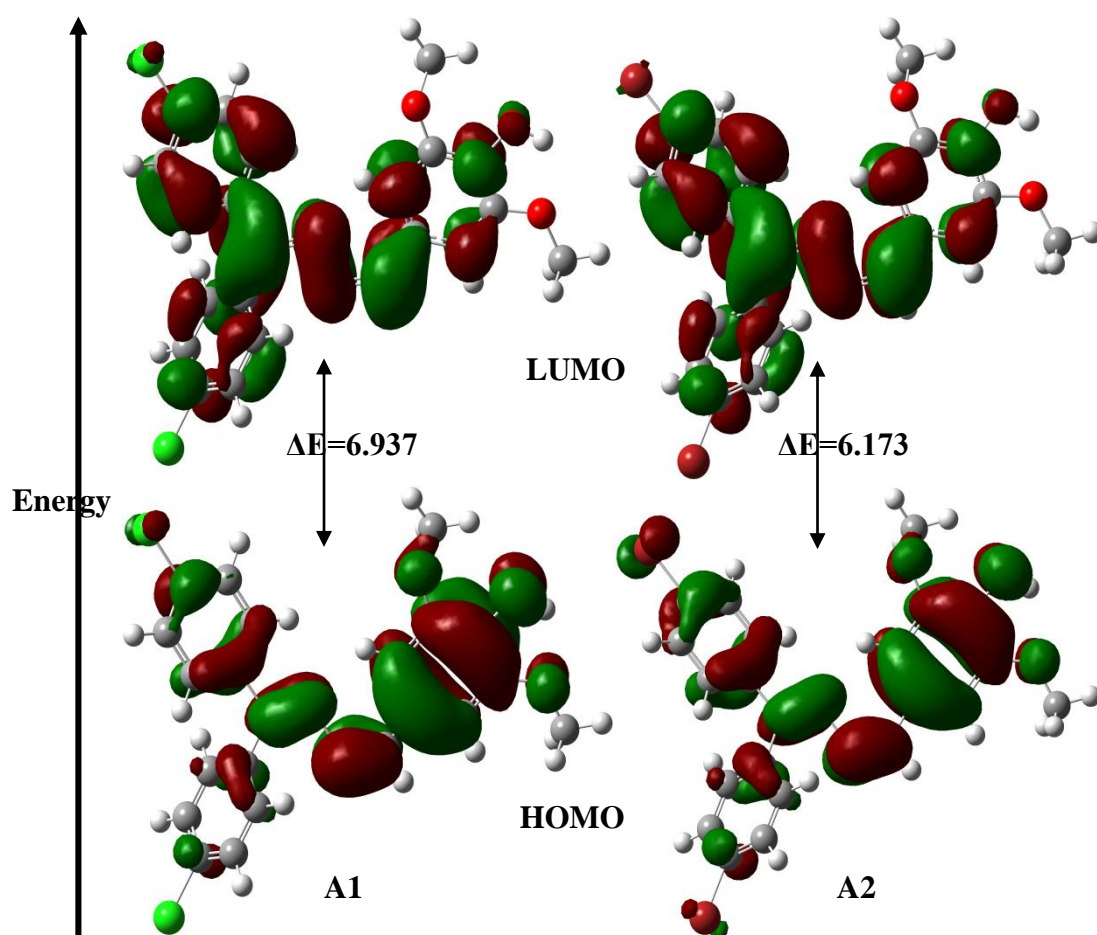


Fig. 20. HOMO and LUMO diagram of A1 and A2

Table 7. Compounds A1 and A2 Calculated energy values (eV)

Molecular property (in eV)	E_{HOMO}	E_{LUMO}	$E_{\text{LUMO}} - E_{\text{HOMO}}$	Electro-negativity (χ)	Chemical hardness (η)	Electrophilicity index (φ)	Softness (s)
A1	-6.4825	-0.4547	6.9372	3.0139	3.4686	1.3094	0.14415
A2	-6.609	-0.4364	6.1726	3.5227	3.0863	2.0104	0.1620

4.3.4.4. Molecular electrostatic potential

MEP analysis displays a plot of electrostatic potential projected on the fixed potential electron density surface, which may be used to determine the reactivity of positively and negatively charged reactants, examine H-bond interactions, and enzyme-substrate interactions. The MEPs of **A1** and **A2** investigated are shown in **Fig. 21**. From blue to red, the potential values drop. The blue hues are the most appealing, while the red colors are the most revolting.

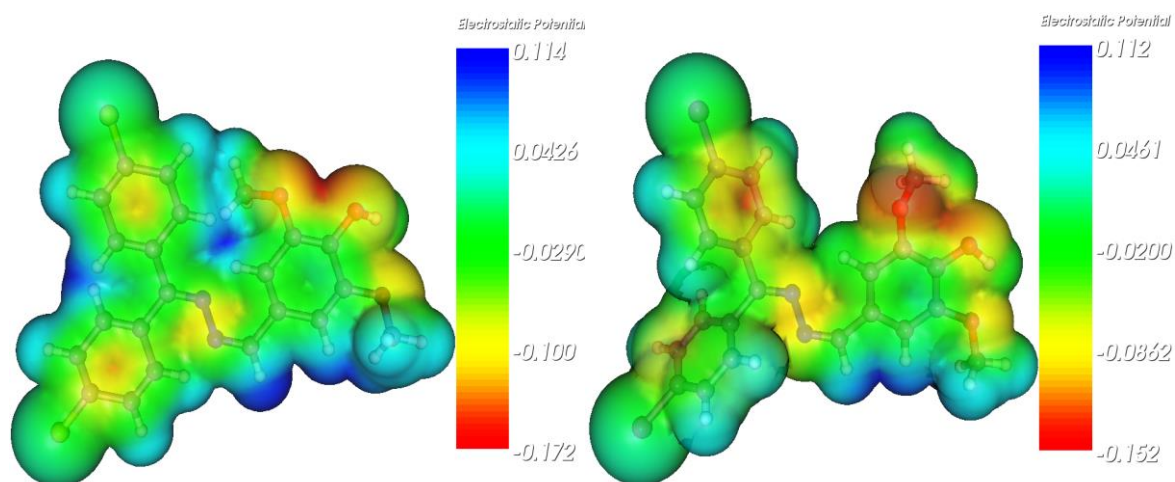


Fig. 21. MEP diagram of **A1** and **A2**

4.3.4.5. Mulliken atomic charge analysis

The electronic charge on atoms within a molecule is a critical element in determining the molecule's binding ability. The electron density distribution over the molecule is depicted by the atomic charge of the molecule. **Table 8** and **Fig. 22** show the estimated Mulliken atomic charge of **A1** and **A2**. The hydrogen atoms that are coupled to the N and O atoms have a higher positive charge than the other hydrogen atoms. The atoms of hydrogen are positively charged. These final data demonstrate their electronegative charge binding effect. It's worth mentioning that the intermolecular hydrogen bonds formed in this molecule support these findings. H11 appears to have the largest Mulliken charge among the hydrogen atoms in **A1** and **A2** (0.337). Compound **A1** has the most electronegative

charge values (-0.569, -0.561, -0.53), while compound **A2** has the most electronegative charge values (-0.569, -0.561, -0.53). (-0.533, -0.562, -0.571, respectively). The Mulliken charge value for N atoms in the azomethine group is expected for the electronegativity of these compounds. When compared to other atoms, the oxygen atom has the highest atomic charge because of the methoxy group of highly electronegative atoms.

Table 8. Compounds A1 and A2 of Mulliken atomic charge

S.No	A1	Mulliken atom	A2
1	0.072	C1	0.069
2	-0.174	C2	-0.164
3	0.332	C3	0.310
4	0.269	C4	0.270
5	0.317	C5	0.342
6	-0.148	C6	-0.163
7	-0.569	O7	-0.533
8	-0.561	O8	-0.562
9	-0.531	O9	-0.571
10	-0.078	C10	-0.841
11	0.337	H11	0.337
12	-0.083	C12	-0.079
13	0.129	C13	0.132
14	-0.312	N14	-0.314
15	-0.346	N15	-0.342
16	0.198	C16	0.197
17	0.072	C17	0.072
18	-0.105	C18	-0.105
19	-0.091	C19	-0.092
20	-0.078	C20	-0.080
21	-0.098	C21	-0.102
22	-0.071	C22	-0.073
23	0.076	C23	0.080
24	-0.091	C24	-0.095
25	-0.077	C25	-0.095
26	-0.092	C26	0.056
27	-0.078	C27	-0.096
28	-0.121	C28	-0.125
29	-0.023	C251	-0.129

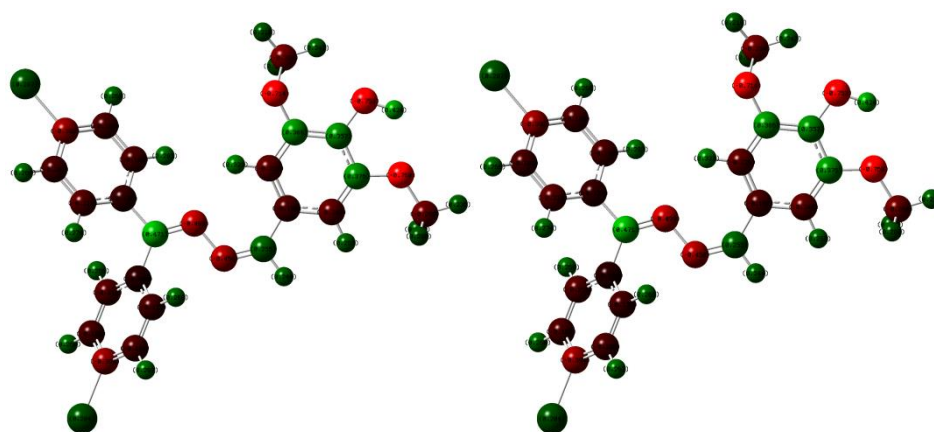


Fig. 22. Mulliken atomic charge distribution and **A1** and **A2** Mulliken plot

4.3.4.6. Docking analysis of **A1** and **A2**

Schrodinger software was used to analyze molecular docking investigations (Maestro 11.2). The docking data revealed the binding with different ligands **A1** and **A2** of the human estrogen receptor along with regorafenib, which is the standard drug for breast cancer to computationally evaluate the protein binding activity. The molecular docking process established the binding affinity and inhibitory constant which demonstrated the excellent values of almost the ligands.

Table 9. Molecular docking studies of **A1** and **A2**

	Regorafenib	A1	A2
glide energy	-50.71	-38.32	-38.11
glide ecoul	-7.07	-1.73	-1.576
glide evdw	-43.64	-36.59	-36.54
glide gscore	-9.00	-6.45	-6.32
Interacting Residues	-	LEU 387, TRP 383, LEU 384, MET 388, GLU 353	ILE 424, MET 528, GLY 420, GLU 419, MET 421
glide ecoul = Coulomb interaction energies, glide evdw = van der Waals interaction energies			

The molecular docking studies show that chemicals **A1** and **A2** attach to the target protein's active site with different corroboration positions and energy levels. Given identical conformational behavior within the active area of the target protein, **Fig. 23** depicted the binding pattern of **A1** and **A2**. The binding sites **A1** and **A2** revealed some common residues to bind with the receptor protein which are Leu₃₈₄, Trb₃₈₃, Ala₃₅₀, Leu₃₄₉, Lys₅₂₉, Ile₄₂₄, Met₄₂₁, Gly₄₂₀, Glu₄₁₉, Phe₄₀₄, Thr₃₄₇, Met₃₄₃. The binding energy results of the docked compounds **A1** and **A2** are displayed in **Table 9**.

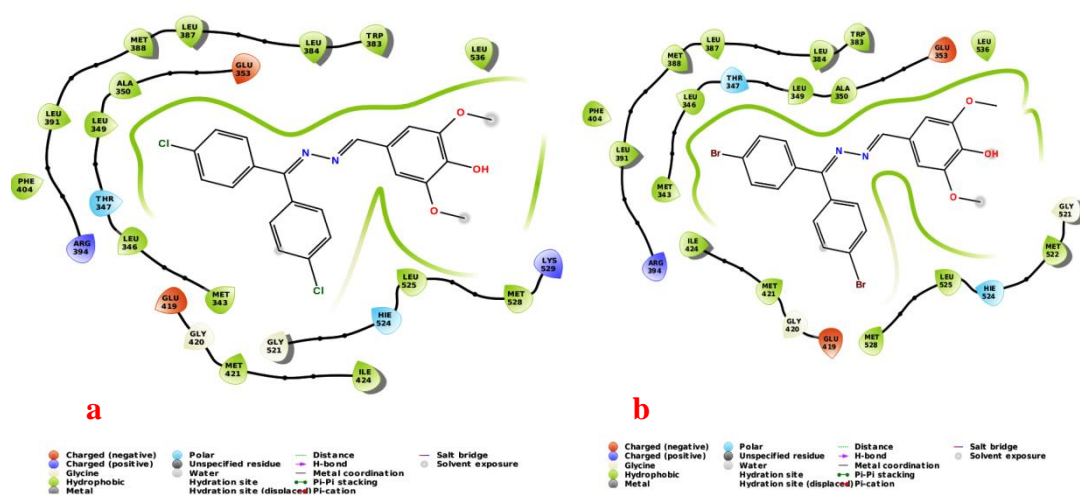


Fig. 23. The 2D diagram (a,b) docking image of compounds **A1** and **A2**

4.3.4.7. Cytotoxicity evaluation

The typical metrics for determining the biocompatibility of compounds are cytotoxicity and cell viability. In comparison to MCF-7 cell lines, azine chemicals have a more cytotoxic impact. The cytotoxicity reactions of **A1** and **A2** at various doses are disclosed, and cellular imaging clearly demonstrates this. It has been shown to be an effective candidate for monitoring intracellular concentration changes under particular biological situations, and its cytotoxicity and MTT assay have been validated in MCF-7 cancer cells treated for up to 5 hours with varied doses of **A1** and **A2** azine chemicals.

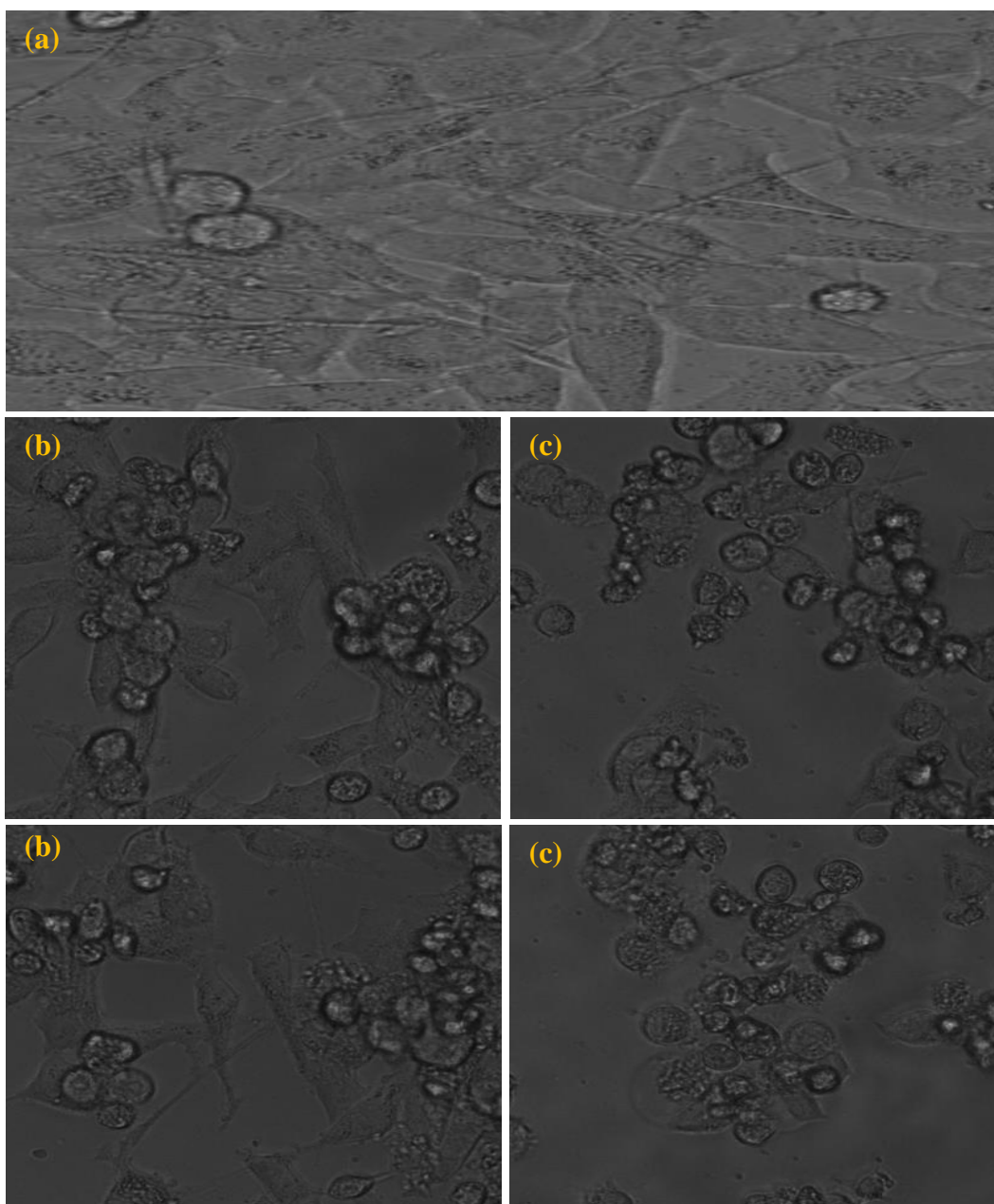


Fig. 24. MCF-7 live cell pictures of **A1** and **A2**: (a) before and (b & c) after confocal microscopy examination with **A1** and **A2**

The cytotoxic action of the **A1** and **A2** was tested on the MCF-7 cell line using an MTT assay, which allows us to assess the effect of complexes on cellular mitochondrial metabolism. The cells were exposed to increasing doses of the chemicals for two days. **Figure 24** shows microscopic pictures of control tumor cells and apoptotic morphological changes in compounds-treated MCF-7 cell lines, whereas **Figure 25** shows a bar diagram.

On the MCF-7 cell lines, the compounds show significant cytotoxicity with IC₅₀ values of 73.3. In comparison to MCF-7 cancer cells, the azine compounds **A1** and **A2** had a more effective inhibitory impact and had the higher IC₅₀ value. **Table 10** shows the IC₅₀ values of compounds in contrast to MCF-7 cell line results. We are persuaded to suggest that the electrical effect might be one of the elements behind the anticancer properties of chemicals.

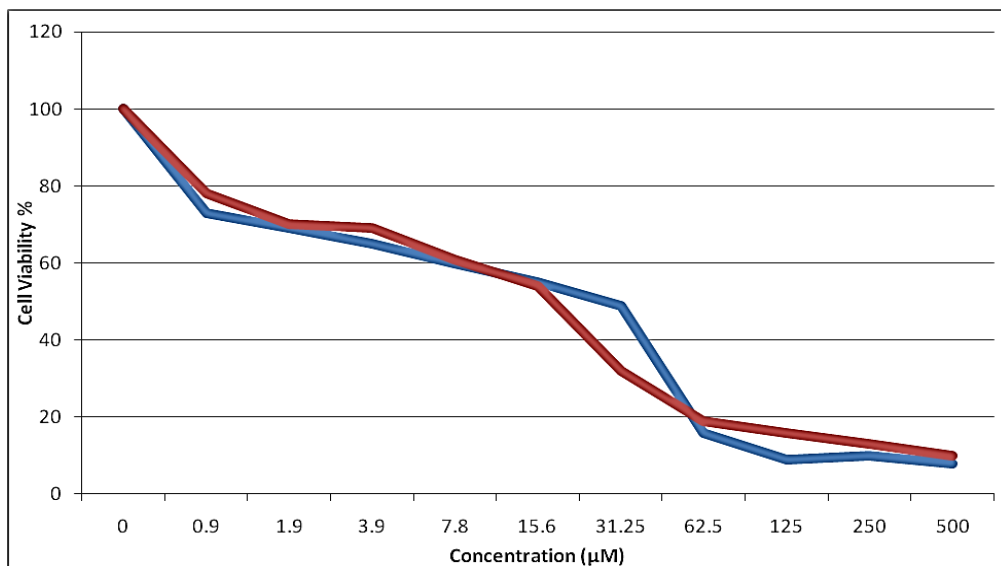


Fig. 25. Compounds **A1** and **A2** IC₅₀ values against MCF-7 cell lines

Table 10. The IC₅₀ values of compounds **A1** and **A2**

MCF7 cell line on Anticancer effect of A1-A2		
Concentration (µM)	Cell Viability %	
	A1	A2
0	100	100
0.9	73	78
1.9	69	70
3.9	65	69
7.8	60	61
15.6	55	54
31.25	49	32
62.5	16	19
125	9	16
250	10	13
500	8	10

4.4. CONCLUSIONS

In summary, new and simple water-soluble fluorescent chemosensors namely asymmetrical azine derivatives viz., **A1** and **A2** were synthesized. The FT-IR, ^1H , and ^{13}C NMR, and ESI-MS spectrum investigations were used to identify the produced compounds. The mass spectra of **A1** and **A2** are quite close to the chemical formulas provided for the respective substances. Chemosensors **A1** and **A2** show an increase in emission intensity when Zn^{2+} and Al^{3+} ions are present. The detection limits (LOD) of **A1** and **A2** versus Zn^{2+} and Al^{3+} ions, respectively, are $1.062 \times 10^5 \text{ M}^{-1}$ and $1.13 \times 10^5 \text{ M}^{-1}$, indicating that the probes can sense Zn^{2+} and Al^{3+} ions in biological systems. The binding affinity including both metal ions for chemosensors, as well as the k_a values of metal-bound chemosensors, indicate that the probes have a strong affinity for the respective metal ions. The structure of both Zn^{2+} and Al^{3+} ions linked chemosensors in **A1** and **A2** proves the PET-OFF-CHEF-ON process. All compounds **A1** and **A2** were theoretically computed using the DFT/6-31G (d,p) basis set, and their optimal bond properties were determined. The oxygen atom will be the most active site for electrophilic assault, whereas the hydrogen atom will be the most reactive site for the nucleophilic attack, according to Mulliken Analysis and Molecular Electrostatic Potential. The investigation on docking studies for compounds **A1-A2** was carried with 3ERT protein. The docking results showed an outstanding docking score -6.45 and -6.32 (kcal/mol) for compounds **A1** and **A2**. The compounds **A1-A2** showed wide inhibition on the MCF-7 cell line, with IC_{50} values of 50.51 and 63.19 M, respectively, according to the MTT experiment. According to the obtained IC_{50} values, compound **A1** had a stronger inhibitory impact on cancer cells.

4.5. REFERENCES

1. (a) M. Zhao, J. Wang, H. Yu, Y. He and T. Duan, *Sensors & Actuators: B. Chemical.*, 2020, 307, 127664; (b) R. Ai and Y. He, *Sensors & Actuators: B. Chemical.*, 2020, 304, 127372.
2. (a) J. Liu, Y. –Q. Fan, Q. –P. Zhang, H. Yao, Y. –M. Zhang, T. –B. Wei and Q. Lin, *Soft Matter.*, 2019, 15, 999–1004; (b) Q. Lin, X. –W. Guan, Y. –M. Zhang, J. Wang, Y. –Q. Fan, H. Yao and T. –B. Wei, *ACS Sustainable Chem. Eng.*, 2019, 7, 14775–14784.
3. (a) H. Wang, W. P. Lustig and J. Li, *Chem. Soc. Rev.*, 47 (2018) 4729–4743; (b) S. Yang, W. Jiang, Y. Tang, L. Xu, B. Gao and H. Xu, *RSC Adv.*, 8 (2018) 37828–37834.
4. M. Li, X. J. Jiang, H. H. Wu, H. L. Lu, H. Y. Li, H. Xu, S. Q. Zang and T. C. W. Mak, *Dalton Trans.*, 2015, 44, 17326–17334.
5. L. Wang, D. D. Ye, W. X. Li, Y. Y. Liu, L. H. Li, W. L. Zhang and L. Ni, *Spectrochim. Acta A.*, 2017, 183, 291–297.
6. G. Chen, Z. Guo, G. Zeng and L. Tang, *Analyst.*, 2015, 140, 5400–5443.
7. D. T. Quang and J. S. Kim, *Chem. Rev.*, 2010, 110, 6280–6301.
8. C. F. Mills, *Zinc in Human Biology*; Springer-Verlag: New York, (1989).
9. (a) R. B. Thompson, D. Peterson, W. Mahoney, M. Cramer, B. P. Maliwal, S. W. Suh, C. Frederickson, C. Fierke and P. Herman, *J. Neurosci. Methods*, 2002, 118, 63–75; (b) L. A. Finney, T. V. O’Halloran, *Science*, 2003, 300, 931–936.
10. C. J. Frederickson, M. A. Klitenick, W. I. Manton and J. B. Kirkpatrick, *Brain Res.*, 1983, 273, 335–339.
11. (a) C. J. Frederickson and A. I. Bush, *Biometals.*, 200, 14, 353–366; (b) Y. Li, C. Hough and J. Sarvey, *Sci. STKE.*, 2003, 182, 19.
12. (a) W. J. Qian, K. R. Gee and R. T. Kennedy, *Anal. Chem.*, 2003, 75, 3468–3475.
13. P. D. Zalewski, X. Jian, L. L. L. Soon, W. G. Breed, R. F. Seamark, S. F. Lincoln, A. D. Ward and F. Z. Sun, *Reprod. Fertil. Dev.*, 1996, 8, 1097–1105.
14. R. B. Thompson, D. Peterson, W. Mahoney, M. Cramer, B. P. Maliwal, S. W. Suh, C. Frederickson, C. Fierke and P. Herman, *J. Neurosci. Methods*, 2002, 118, 63–75.

15. E. Mocchegiani, C. Bertoni-Freddari, F. Marcellini and M. Malavolta, *Prog. Neurobiol.*, 2005, 75, 367–390.
16. J. Hardy and D. J. Selkoe, *Science*, 2002, 297, 353–356.
17. J. Hardy, *Curr. Alzheimer Res.*, 2006, 3, 71–73.
18. B. J. Kim, Y. H. Kim, S. Kim, J. W. Kim, J. Y. Koh, S. H. Oh, M. K. Lee, K. W. Kim and M. S. Lee, *Diabetes.*, 2000, 49, 367–372.
19. A. B. Chausmer, *J. Am. Coll. Nutr.*, 1998, 17, 109–115.
20. (a) E. M. Nolan and S. J. Lippard, *Acc. Chem. Res.*, 2009, 42, 193–203.
21. D. Dambournet, A. Demourgues, C. Martineau, S. Pechev, J. Lhoste, J. Majimel, A. Vimont, J. –C. Lavalley, C. Legein, J. –Y. Buzaré, F. Fayon and A. Tressaud, *Chem. Mater.*, 2008, 20, 1459–1469.
22. A. Samokhvalov, *Coordination Chemistry Reviews*, 2018, 374, 236–253.
23. Scientific Opinion of the Panel on Food Additives, Flavourings, Processing Aids and Food Contact Materials (AFC), *The EFSA Journal*, 2008, 754, 1–34.
24. A. C. Alfrey, G. R. LeGendre and W. D. Kaehny, *New Engl. J. Med.*, 1976, 294, 184–188.
25. M. K. Ward, T. G. Feest, H. A. Ellis, I. S. Parkinson and D. N. Kerr, *Lancet.*, 1978, 1, 841–845.
26. S. E. Jorgensen and A. Jensen, *Metal Ions Biol. Syst.*, 1984, 18, 61.
27. S. Jansen, T. Watanabe, E. Smets and S. Jansen, *Annals of Botany.*, 2002, 90, 53–64.
28. A. Frankova, O. Drabek, J. Havlik, J. Szakova and A. Vanek, *J. Inorg. Biochem.*, 2009, 103, 1480–1485.
29. G. Theriault, C. Tremblay, S. Cordier and S. Cingras, *Lancet.*, 1984, 1, 947–950.
30. A. Ronneberg and F. Langmark, *Am. J. Ind. Med.*, 1992, 22, 573–590.
31. C. Swain and G. B. N. Chainy, *J. Trace Elem. Med. Biol.*, 1997, 11, 77–82.
32. C. Cuccarella, C. Montoliu, C. Hermenegildo, R. Saez, L. Manzo, M. D. Minana and V. Felipo, *J. Neurochem.*, 1998, 70, 1609–1614.
33. Y. Hojo, T. Kobayashi, Y. Shigemitsu and T. Tanabe, *Jpn. J. Toxicol. Environ. Health.*, 1998, 44, P–10.

34. J. A. Edwardson, J. M. Candy, P. G. Ince, F. K. McArthur, C. M. Morris, A. E. Oakley, G. A. Taylor and E. Bjertness, *Ciba Found. Symp.*, 1992, 169, 165–185.
35. M. Kawahara, *J. Alzheimer Dis.*, 2005, 8, 171–182.
36. J. Savory, M. M. Herman, C. D. Katsetos and M. R. Wills, in: M. Nicolini, P.F. Zatta, B. Corain (Eds.), *Aluminum in Chemistry Biology and Medicine*, Cortina International/Raven Press, Verona/New York, 1991 p. 45.
37. C. Exley, G. Mamutse, O. Korchazhkina, E. Pye, S. Srekopytov, A. Polwart and C. Hawkins, *Mult. Scler.*, 2006, 12, 533–540.
38. Y. Lu, S. Huang, Y. Liu, S. He, L. Zhao and X. Zeng, *Org. Lett.*, 2011, 13, 5274–5277.
39. Y. Tachapermpon, S. Thavornpradit, A. Charoenpanich, J. Sirirak, K. Burgess and N. Wanichacheva, *Dalton Trans.*, 2017, 46, 16251–16256.
40. L. Hou, J. Feng, Y. Wang, C. Dong, S. Shuang and Y. Wang, *Sens. Actuators B*, 2017, 247, 451–460.
41. X. Chen, T. Pradhan, F. Wang, J. S. Kim and J. Yoon, *Chem. Rev.*, 2012, 112, 1910–1956.
42. H. N. Kim, M. H. Lee, H. J. Kim, J. S. Kim and J. Yoon, *Chem. Soc. Rev.*, 2008, 37, 1465–1472.
43. V. Dujols, F. Ford and A. W. Czarnik, *J. Am. Chem. Soc.*, 1997, 119, 7386–7387.
44. D. T. Quang and J. S. Kim, *Chem. Rev.*, 2010, 110, 6280–6301.
45. B. A. Wong, S. Friedle and S. J. Lippard, *J. Am. Chem. Soc.*, 2009, 131, 7142–7152.
46. X. Zhang, D. Hayes, S. J. Smith, S. Friedle and S. J. Lippard, *J. Am. Chem. Soc.*, 2008, 130, 15788–15789.
47. L. Xue, G. Li, D. Zhu, Q. Liu and H. Jiang, *Inorg. Chem.*, 2012, 51, 10842–10849.
48. L. Xue, Q. Liu and H. Jiang, *Org. Lett.*, 2009, 11, 3454–3457.
49. (a) H. Liu, Y. Dong, B. Zhang, F. Liu, C. Tan, Y. Tan and Y. Jiang, *Sens. Actuators B*, 2016, 234, 616–624; (b) S. M. Z. Al-Kindy, Z. Al-Mafrigi, M. S. Shongwe and F. E. O. Suliman, *Luminescence.*, 2011, 26, 462–470.
50. Z. Xu, J. Yoon and D. R. Spring, *Chem. Soc. Rev.*, 2010, 39, 1996–2006.
51. Y. Fu, C. Fan, G. Liu, S. Cui and S. Pu, *Dyes Pigm.*, 2016, 126, 121–130.

52. C. He, Z. Lin, Z. He, C. Duan, C. Xu, Z. Wang and C. Yan, *Angew. Chem., Int. Ed.*, 2008, 47, 877–881.
53. I. Ravikumar and P. Ghosh, *Inorg. Chem.*, 2011, 50, 4229–4231.
54. D. Maity and T. Govindaraju, *Chem. Commun.*, 2012, 48, 1039–1041.
55. (a) M. Sohrabi, M. Amirnasr, S. Meghdadi, M. Lutz, M. B. Torbati and H. Farrokhpour, *New J. Chem.*, 2018, 42, 12595–12606; (b) Q. –F. Li, J. –T. Wang, S. Wu, G. –W. Ge, J. Huang, Z. Wang, P. Yang and J. Lin, *Sensors and Actuators B*, 2018, 259, 484–491.
56. S. K. Sahoo, G. D. Kim and H. J. Choi, *J. Photochem. Photobiol. C*, 2016, 27, 30–53.
57. Y. Dong, R. Fan, W. Chen, P. Wang and Y. Yang, *Dalton Trans.*, 2017, 46, 6769–6775.
58. K. P. Carter, A. M. Young and A. E. Palmer, *Chem. Rev.*, 2014, 114, 4564–4601.
59. W. N. Lipscomb and N. Straeter, *Chem. Rev.*, 1996, 96, 2375–2434.
60. A. K. Bhanja, C. Patra, S. Mondal, D. Ojha, D. Chattopadhyay and C. Sinha, *RSC Adv.*, 2015, 5, 48997–49005.

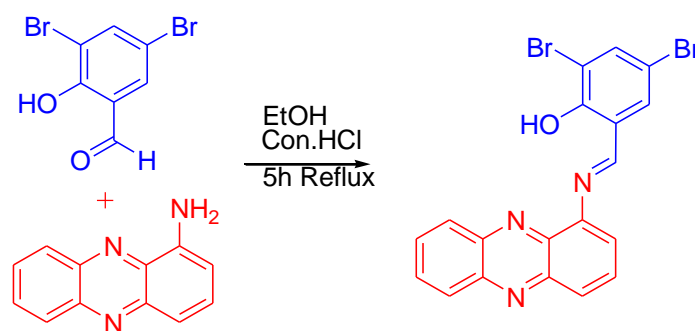
Novel Dual Chemosensor for Fe³⁺/ Ni²⁺ ions and its Multi Applications

5.1. INTRODUCTION

Due to their relevance in the environmental, biology, and chemistry sectors, the development of extremely sensitive and selective chemosensors has sparked a lot of interest in detecting heavy metals in recent years.[1–10] Iron, the world's third most abundant metal, is a frequent component of living cells and a pervasive element in the environment. It is involved in enzymatic activity, cellular metabolism, gene expression, and oxygen transport, among other biological processes.[11–16] A variety of illnesses can be caused by both lack and excess.[17] Atomic absorption spectroscopy, inductively coupled plasma-atomic emission spectroscopy, mass spectrometry, electrochemical, and fluorescence spectroscopic examination are some of the current qualitative and quantitative approaches for Fe³⁺ ions.[18–22] These approaches are hampered by either the complex nature and high cost of equipment or the time-consuming sample preparation procedures.[23,24] It is vital to create simple, highly sensitive, and selective chemosensors for Fe³⁺ detection. So far, only a few chemosensors using functionalized nanoparticles or conjugated organic chromophores have been developed. [25–32] Only a few of them can be used as practical probes due to their limited sensitivity and selectivity, as well as their incompatibility with aquatic circumstances. [33–37] The Hg²⁺, Zn²⁺, and Cu²⁺, for example, have several properties that are similar to Fe³⁺ and may cause Fe³⁺ detection to fail. [38]

Nickel is required for biological processes including biosynthesis, respiration, and metabolism. Electroless nickel plating, electronics cleaning, electrochromic devices, rechargeable batteries, supercapacitors, and catalytic precursors are just a few of the industrial uses for a nickel.[39,40] Inhaling too much of this metal has detrimental consequences for the respiratory system, kidneys, lungs, and blood, resulting in asthma,

allergies, CNS dysfunction, carcinogenesis, and nasal cavity diseases.[41–44] Nickel compounds are likewise classified as group one carcinogens by the World Health Organization's International Agency for Research on Cancer (IARC) (WHO). Despite this, due to its high hydration and poor coordinating complexation ability, interference from other metal ions and fluorescence quenching qualities associated with the paramagnetic nature of Ni²⁺ ion have proved challenging to detect.[45-47] With these factors in mind, we selected to test *E*-2,4-dibromo-6-((phenazin-1-ylimino)methyl)phenol A1C4 as a novel Schiff base. Only two instances exist of quenching and enhancement-based detection of Fe³⁺ and Ni²⁺ ions, such as Pb²⁺, Al³⁺, Hg²⁺, and Cr²⁺ ions, which is a tough undertaking because these ions are predominantly quarks (**Scheme 1**). These fluorescent probes show preferential binding to Fe³⁺ and Ni²⁺ ions in aqueous environments. We also demonstrate how to employ these probes in a straightforward and cost-effective manner. These two metal ions allowed A1C4 to light "on and off" in an aqueous solution. The relevance of Fe³⁺ and Ni²⁺ ions in biological systems was further confirmed by fluorescent imaging studies in live HepG2 cells. Theoretical simulations back up the Fe³⁺ and Ni²⁺ ions sensing mechanisms.



Scheme 1 Synthesis route of compound A3

5.2. EXPERIMENTAL SECTION

All of the compounds (spectral and laboratory grade) were purchased commercially from Sigma-Aldrich and used as-is. To investigate the characteristics of probe compounds towards various metal ions, nitrate or chloride salts of Fe³⁺, Ni²⁺, Pb²⁺, Sr²⁺, Cr³⁺, Sn²⁺, Mn²⁺, Ag⁺, Mg²⁺, Al³⁺, Hg²⁺, Zn²⁺, Zr²⁺, Cu²⁺, Cd²⁺, and Bi³⁺ ions were utilized. The FT-IR

spectra (in KBr pellets) were obtained using an Agilent-Cary 630 spectrophotometer in the 4000-400 cm^{-1} range. Elements (CHN) testing was carried out using a VARIOMICRO V2.2.0 analyzer. Mass spectra were calculated using a SCIEX-API 2000 spectrometer. On a Bruker Avance-III (400 MHz for ^1H and 100 MHz for ^{13}C) spectrometer, ^1H and ^{13}C NMR spectra were collected in CDCl_3 as a solvent. FE-SEM with EDS was utilized on platinum-coated samples with a JEOL JSM-5610 to explore the surface morphology of the corresponding complex with Fe^{3+} and Ni^{2+} ions. On a UV-2450 Shimadzu photometer, UV-Vis absorption spectra were acquired by dissolving the sample in $\text{CH}_3\text{CH}_2\text{OH}$ and H_2O and using a 1cm path-length quartz cell. A PerkinElmer LS55 fluorescence spectrometer was used to capture the fluorescence spectra at room temperature. At a magnification of 40X, the confocal pictures were obtained with a Leica DM3000 from Germany. The Gaussian 03W application software was used to compute theoretical values on a personal laptop. The DFT approach was used to improve the 6-31G (d,p) basis sets.

5.2.1. Synthesis of the compound A3

As shown in **Scheme 1**, chemosensor synthesis may be accomplished in a single condensation procedure. To 30 mL of ethanol containing phenazin-1-amine (1 mmol), two drops of Con. HCl was added, followed by 3,5-dibromo-2-hydroxybenzaldehyde (1 mmol). The mixture was then brought to reflux for 5 hr. After cooling to room temperature, the residue was filtered and rinsed with distilled water many times. E-2,4-dibromo-6-((phenazin-1-ylimino)methyl) phenol synthesis (**A3**). m.p ($^{\circ}\text{C}$): 205-208; yield (%): 71; brown colour crystal $\text{C}_{19}\text{H}_{11}\text{Br}_2\text{N}_3\text{O}$: MF: CHN (elemental analysis): C, 49.92; H, 2.43; N, 9.19; found (%): C, 48.99; H, 2.38; N, 9.15; FT-IR (KBr, cm^{-1}) 3524 (C=OH), 3049 (Ar-CH), 1589 (C=N), (400 MHz, CDCl_3 , δ , ppm) ^1H NMR 8.39-8.53 (CH=N); 7.08-7.69 (Aromatic proton); 9.86 (OH). ^{13}C NMR 105.69-148.73 (C=N); 150.76-161.75 (C=N); 105.69-148.73 (C=N); (Aromatic carbon). Calcd. 454.93; found: 453.16 (m/z). **Figures 1–4** depict spectral images.

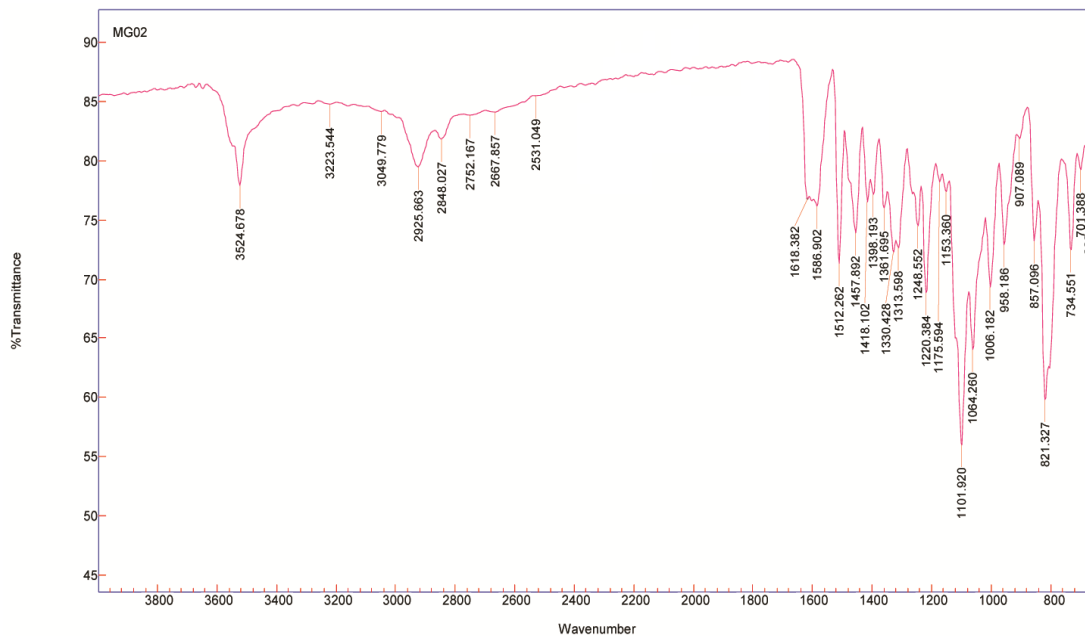


Fig 1. FT-IR Spectrum of compound A3

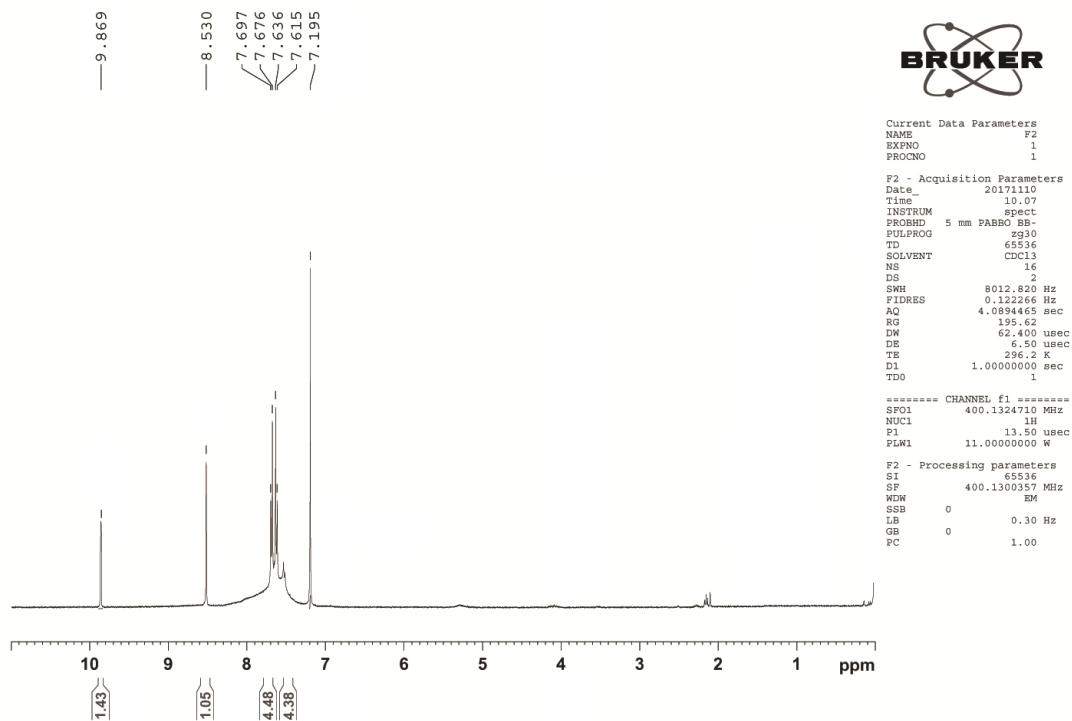


Fig 2. ¹H Spectrum of compound A3

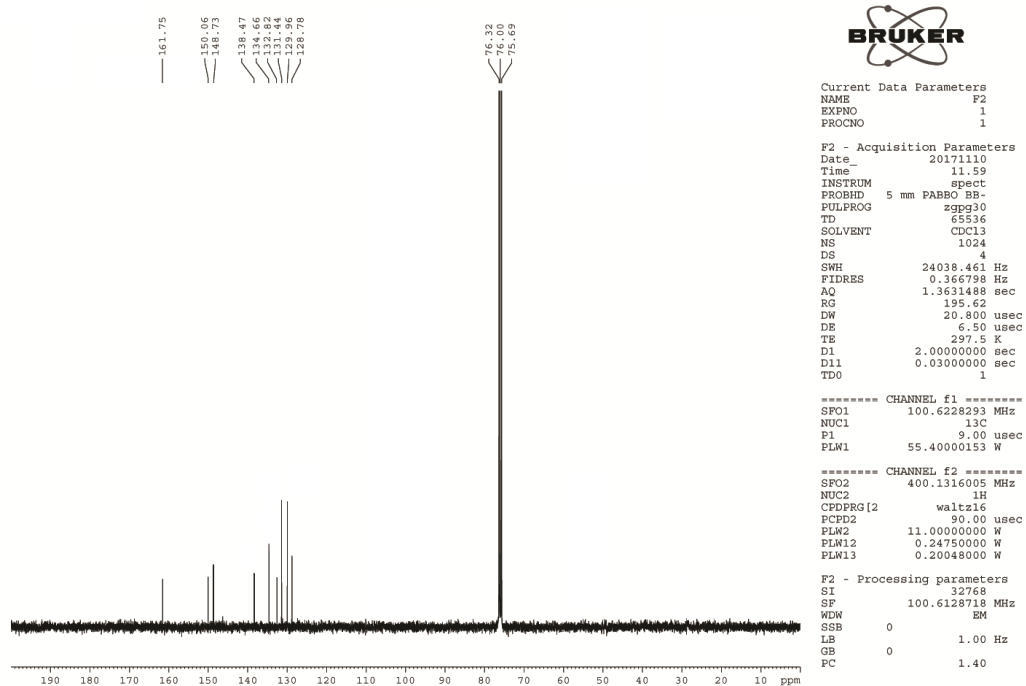


Fig 3. ¹³C Spectrum of compound A3

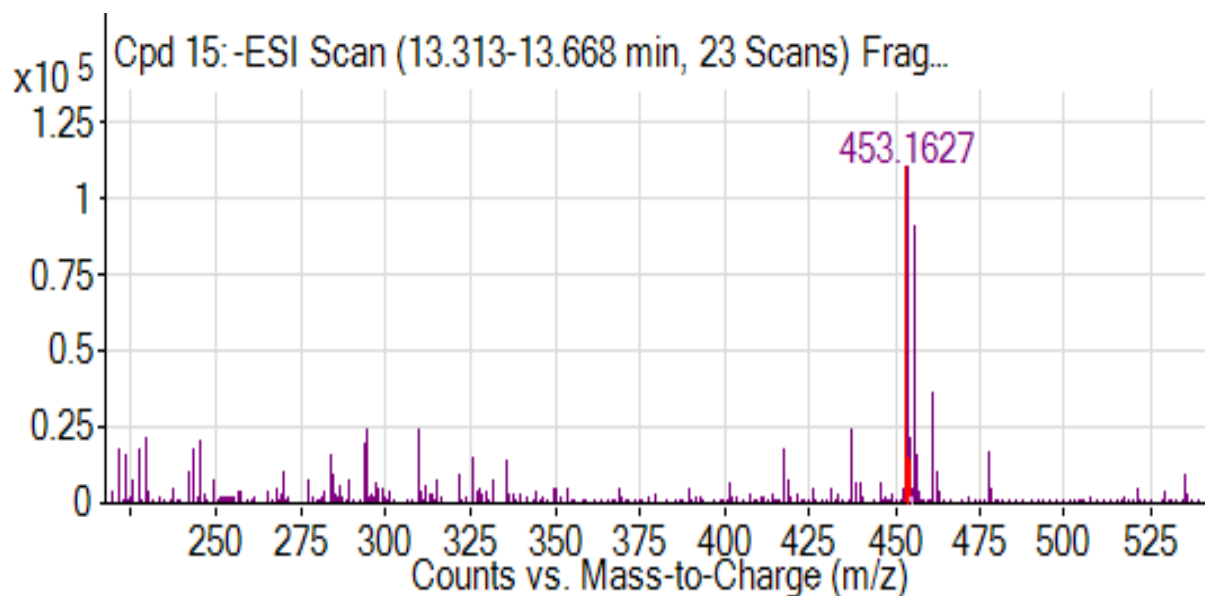


Fig 4. Mass Spectrum of compound A3

5.2.2. Fluorescence

For UV-vis and fluorescence titration, a stock solution of compound **A3** (3.0×10^{-3} mol L⁻¹) was prepared in EtOH: H₂O (4:1, v/v). The receptor solution was then diluted to 1×10^{-5} mol L⁻¹ in EtOH/H₂O solution (4:1, v/v, 10 M HEPES buffer, pH=7.0). In each titration experiment, the ligand solution (1×10^{-5} mol L⁻¹) was put in an exceeding quartz optical cell with a 10 mm optical path length, and the ion stock solution was gradually supplied to the cell using a micropipette. To use their individual metal ions, the guest ions solutions were prepared in deionized water at pH=7.0 using nitrate or chloride salts in the order of (1×10^{-4} M). Separate solutions with increasing cation strength and various detector concentrations are created. The spectra of these solutions were recorded using fluorescence and UV-vis methods.

5.2.3. Cell culture

The human hepatocellular liver carcinoma (HepG2) cell line was donated by NCCS (Pune). Cells were placed on 18 mm diameter glass coverslips and allowed to adhere for 24 hours. In a humidified atmosphere of 5% CO₂, the cells were cultured at 37 °C in DMEM (Dulbecco's Modified Eagle's Medium) with 10% FBS (Fetal Bovine Serum) and antibiotics (100 mg/mL streptomycin and 100 U/mL penicillin).

5.2.4. Assay for cell viability

The cytotoxicity of **A3** against HepG2 cell lines was determined using the MTT (3-(4,5-dimethylthiazole-2-yl)-2,5-diphenyl tetrazolium bromide) test. The cells were seeded at 1.5×10^4 cells per well in a 96-well plate and incubated for 48 hours in a medium containing **A3** at concentrations ranging from 0.9 to 500 µM. Each treatment was done in triplicate wells, with 100 µL of MTT given to each well and incubated for 4 hours at 37 °C to allow MTT to react with MTT and metabolically active cells to generate formazan crystals. The MTT-containing medium in the wells was carefully removed. 100 µL of

DMSO was added to each well, and the plates were shaken for 10 minutes to dissolve intracellular formazan crystals. An ELISA reader was used to detect the absorbance at 318 nm, and a fluorescence microscope was used to examine the cell pictures. The survival percentage (percentage) was calculated using the following formula: [live cell number (test)/living cell number (control)] x 100 = percent survival.

5.2.5. Cell Imaging Study

1×10^5 HepG2 cells were cultivated and incubated on a coverslip on a 35x10 mm culture plate for 24 hours at 37°C. The HepG2 cells were treated with 10 μ M **A3** (produced by dissolving **A3** in DMSO: Water = 1:9 v/v) for 45 minutes at 37°C. The nuclear staining agent was then DAPI (2-(4-Amidinophenyl)-6-indolecarbamidinedihydro chloride-4,6-Diamidino-2-phen-ylindole). Furthermore, cells were pre-incubated for 3 hours at 37°C with 10, 20 μ M Fe^{3+} and Ni^{2+} ions, washed three times with 1X PBS buffer to remove the extraneous Fe^{3+} and Ni^{2+} ions, and then incubated with 10 μ M compound **A3** for 30 minutes at 37°C. Fluorescence photographs of each culture plate were taken. Fluorescence photographs of each culture plate were taken. When compared to the blue nuclear counter stain of DAPI, compound **A3** shows cytoplasmic red fluorescence due to the formation of **A3-Fe³⁺** and **A3-Ni²⁺** complexes.

5.2.6. Computational details

The Gaussian 03W software package was used to do theoretical studies on **A3** full computations at *ab-initio* DFT levels.

5.3. RESULTS AND DISCUSSION

The FT-IR, ^1H and ^{13}C NMR, and mass spectrum studies were used to characterise and confirm the synthesised target. **Figures 1–4** shows the spectral pictures. The yield of the described chemical was excellent; **Scheme 1** depicts a synthetic technique.

5.3.1. A3 colorimetric and fluorometric reactions to Fe³⁺ and Ni²⁺ ions

Absorption and emission spectroscopy were used to investigate the optical characteristics of chemosensor **A3** (10 μM) at room temperature (EtOH/H₂O = 4/1, v/v, 10 M HEPES buffer, pH = 7.0). Strong absorption bands emerge at 318 nm in the UV-vis spectra of **A3**, which may be ascribed to the π-π* electron transition. In contrast to other metal cations, adding 10 equiv. of Fe³⁺ and Ni²⁺ ions to a solution of **A3** (10 μM) in HEPES buffered solution resulted in a 69 nm blue shift of absorption maxima, resulting in a perceived colour change from colourless to yellow colour that can easily be detected by 'naked eye,' and no significant differences were observed (**Fig. 5a**).

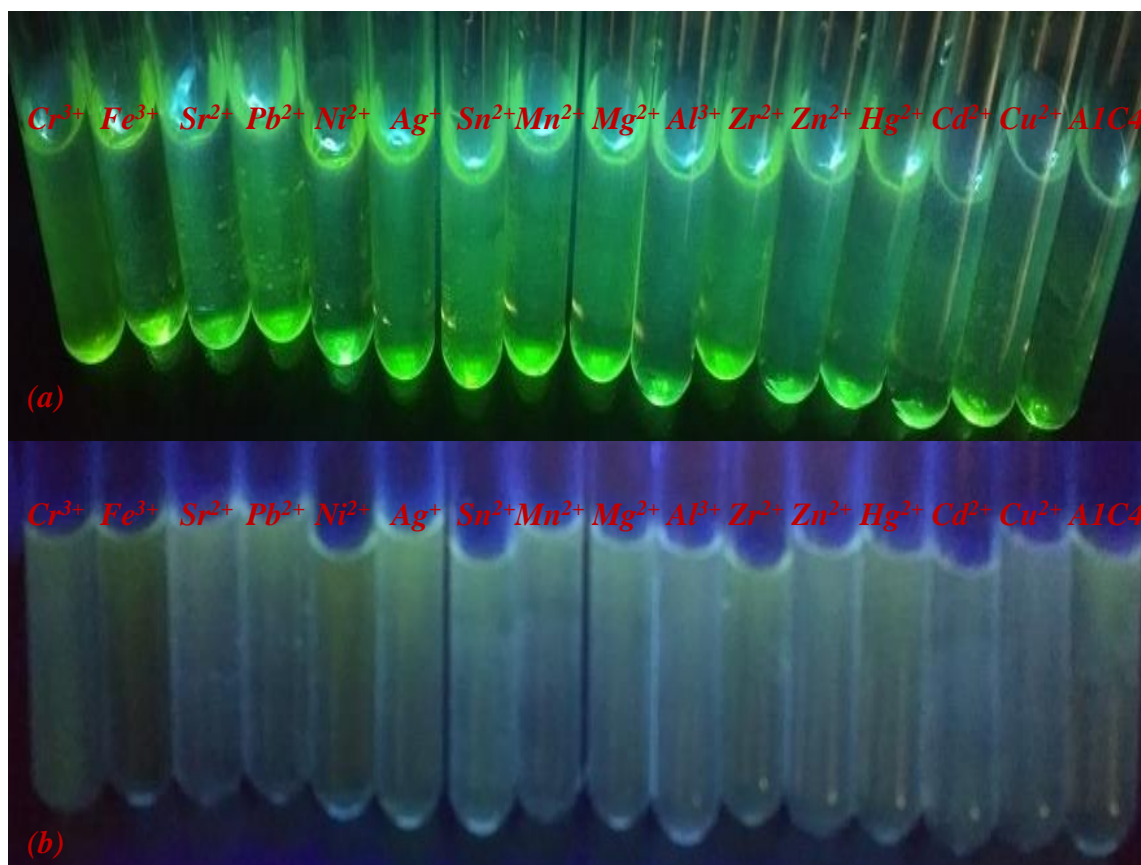


Fig 5. (a) Colourimetric and (b) Fluorometric naked-eye detection of **A3** in absence and presence of different metal ions

A3: Fe^{3+} and **A3**: Ni^{2+} ions combination generate bright sky-blue and light yellow fluorescence under fluorescence light bands appearing at 553 nm. Other cations, however, did not show such obvious colour shifts. These investigations demonstrated that **A3** is selective and appropriate for colorimetric sensing of Fe^{3+} and Ni^{2+} ions, allowing it to be employed as a colorimetric sensor for Fe^{3+} and Ni^{2+} ions qualitative evaluation (**Fig 5b**). In an EtOH/ H_2O medium, the UV-vis absorption and emission characteristics of **A3** were examined, with the compound **A3** having a maximum absorption wavelength of 318 nm.

Compound **A3** displayed a hyperchromic shift centred at 318 nm for Fe^{3+} and Ni^{2+} ions after treatment with Fe^{3+} , Ni^{2+} , Cr^{3+} , Sr^{2+} , Pb^{2+} , Ag^+ , Sn^{2+} , Mn^{2+} , Mg^{2+} , Al^{3+} , Zr^{2+} , Zn^{2+} , Hg^{2+} , Cd^{2+} , and Cu^{2+} ions. This demonstrates the selectivity of compound **A3** for Fe^{3+} and Ni^{2+} ions. The competitive event was observed using fluorescence spectroscopy. **Figures 6** and **7** illustrate the absorbance and emission spectra of **A3** in the presence of all of the various metal ions, revealing a strong hypsochromic and hyper shifts emission envelope exclusively in the presence of Fe^{3+} and Ni^{2+} ions, respectively. When stimulated at 318 nm, **A3** showed modest fluorescence emission when different metal cations. **A3** exhibited significant fluorescence emission at 553 nm after adding the diamagnetic Fe^{3+} molecule. The modest fluorescence was, however, muted by the paramagnetic Ni^{2+} ion. As a result, **A3** serves as a dual sensor for Fe^{3+} ions with enhanced fluorescence and Ni^{2+} ions with quenched fluorescence. Under long-wavelength UV visible light, the visual colour shift of **A3** was detected after the addition of several metal ions. When the Fe^{3+} ion was added to the **A3**, it produced a bright green fluorescence. **Figures 6** and **7** show the fluorescence intensity that resulted.

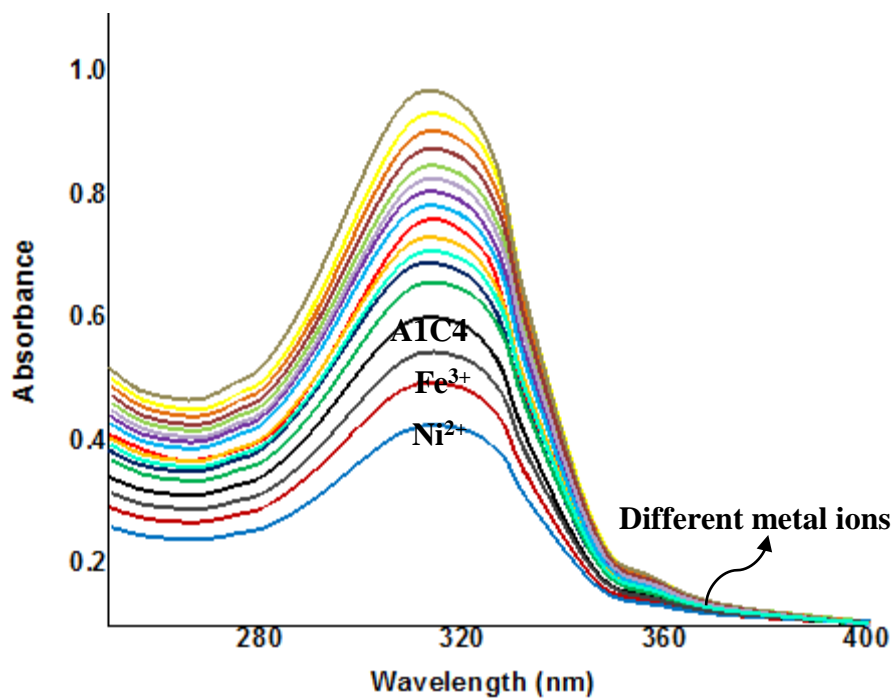


Fig 6. Absorption spectra of A3 with different metal ions

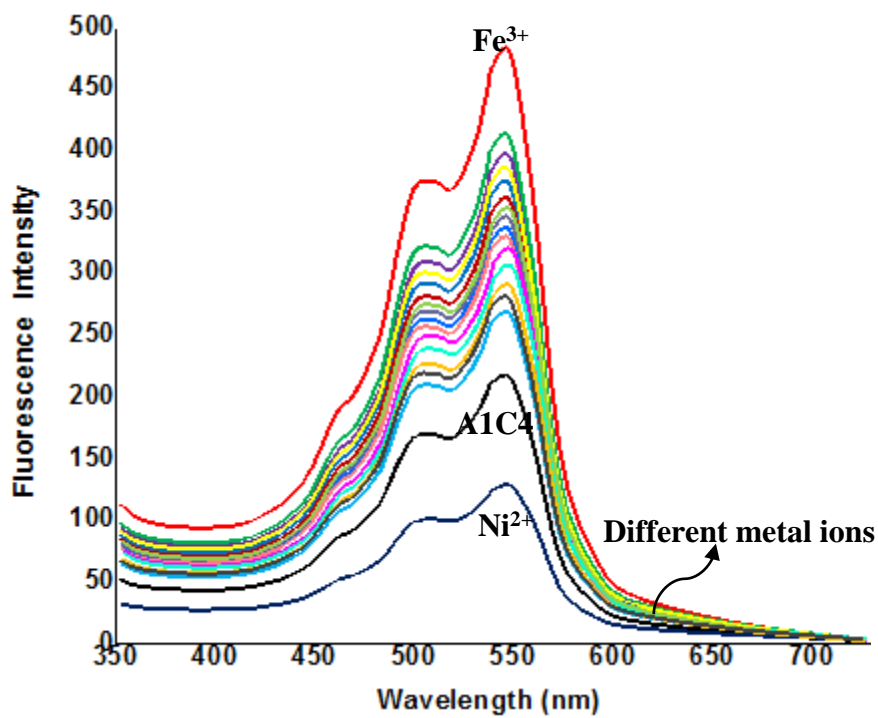


Fig 7. Fluorescence spectra of A3 with different metal ions

The findings clearly show that other metal ions do not interfere with the detection of Fe^{3+} . As shown in **Fig 8**, the fluorescence quenching generated by the Ni^{2+} ion in the presence of most other cations was identical to that caused by the Ni^{2+} ion alone, with no fluctuation in intensity levels. These findings with Fe^{3+} and Ni^{2+} ions over other metal ions point to the probe's use as a Fe^{3+} and Ni^{2+} sensor for a wide variety of cations. The recognition of Fe^{3+} ions by **A3** was initially investigated using emission spectroscopy in EtOH- H_2O . In the first stage, the addition of 0 to 1.4 equivalents of Fe^{3+} ions to compound **A3** yielded a peak point at 553 nm, as shown in **Fig 8**.

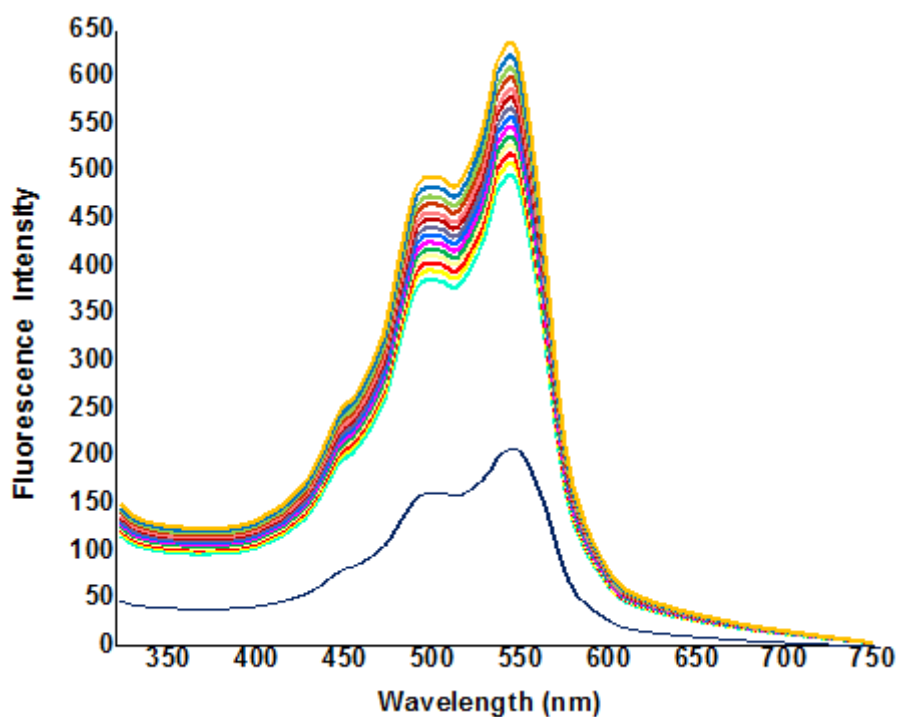


Fig 8. Fluorescence spectra of **A3** in the presence of an increasing Fe^{3+} concentrations

These findings demonstrate a unique structural alteration of **A3** caused by the addition of Fe^{3+} ions, indicating that Fe^{3+} binding causes fluorescence amplification. As a result, the concentration was restricted to 0.6 μM , and the detection limits were 0.8 μM ; beyond that, the fluorescence intensity began to decline. As shown in **Fig 9**, when compound **A3** was treated with 0 to 1.2 equivalents of Ni^{2+} ions, the fluorescence intensity increased until it reached 0.5 μM , after which it progressively decreased. When compared to other

metal cations, the addition of Ni^{2+} ion resulted in significant dampening of emission intensity. In the case of **A3**, the Fe^{3+} ion causes significant enhancement in the emission with a mild redshift ($\text{DI}_{1/4}$ 2 nm), whereas the Ni^{2+} ion causes significant quenching in the emission with a significant blue shift ($\text{DI}_{1/4}$ 11 nm). Because probe **A3** displayed emission amplification in the presence of Fe^{3+} ions, sensing investigations were limited to EtOH/ H_2O =4/1, v/v, 10 M HEPES buffer, pH=7.0. **Figures 8** and **9** depict the changes in the fluorescence intensity of **A3** caused by the addition of Fe^{3+} and Ni^{2+} ions, respectively. With a wavelength change, Fe^{3+} and Ni^{2+} ions showed enhancement and quenching, respectively.

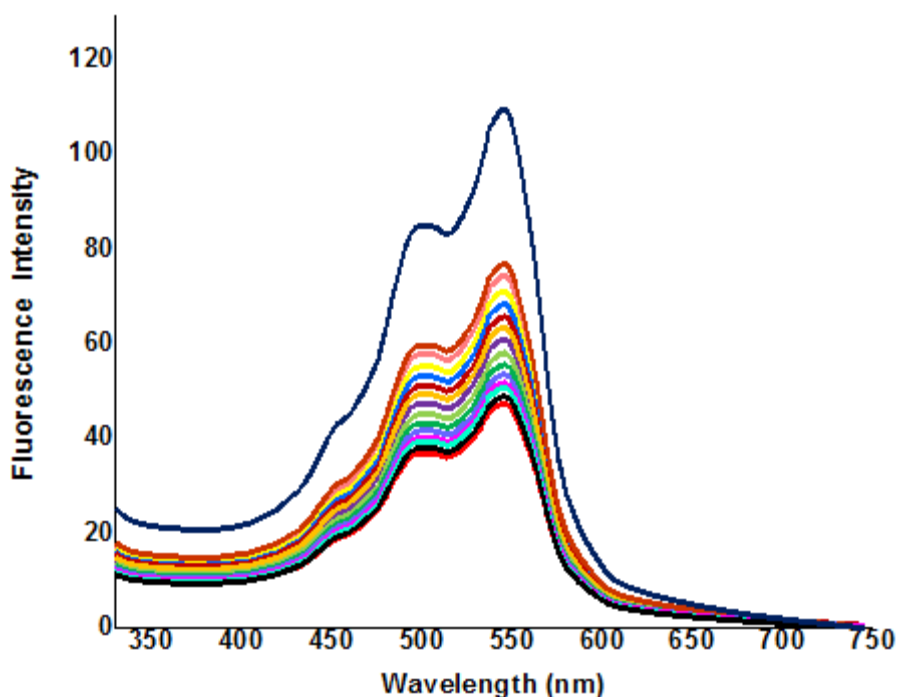


Fig 9. Fluorescence spectra of **A3** in the presence of an increasing Ni^{2+} concentrations

5.3.2. Metal complexes of A3-EDTA Na_2 to the Fe^{3+} and Ni^{2+} ions

The chelating activity of metal with a ligand was investigated using fluorescence spectroscopy. When the metal Fe^{3+} ion (**Fig 10**) was chelated with the chelating reagent EDTA Na_2 , the fluorescence intensities were reversible (1.0 equ). Reversibility of

fluorescence is a must-have property for building practical chemosensors. The reversibility of the sensor **A3** is evaluated by adding an aqueous solution of EDTA Na₂ to the Ni₂₊ metal complex solution. The emission intensity is lowered to that of metal-free sensors when extra EDTANa₂ salt solution is introduced (**Fig 11**). This behaviour implies that this compound might be employed as an "on-off" Fe³⁺ and Ni²⁺ ion sensor (**Fig 10** and **Fig 11**).

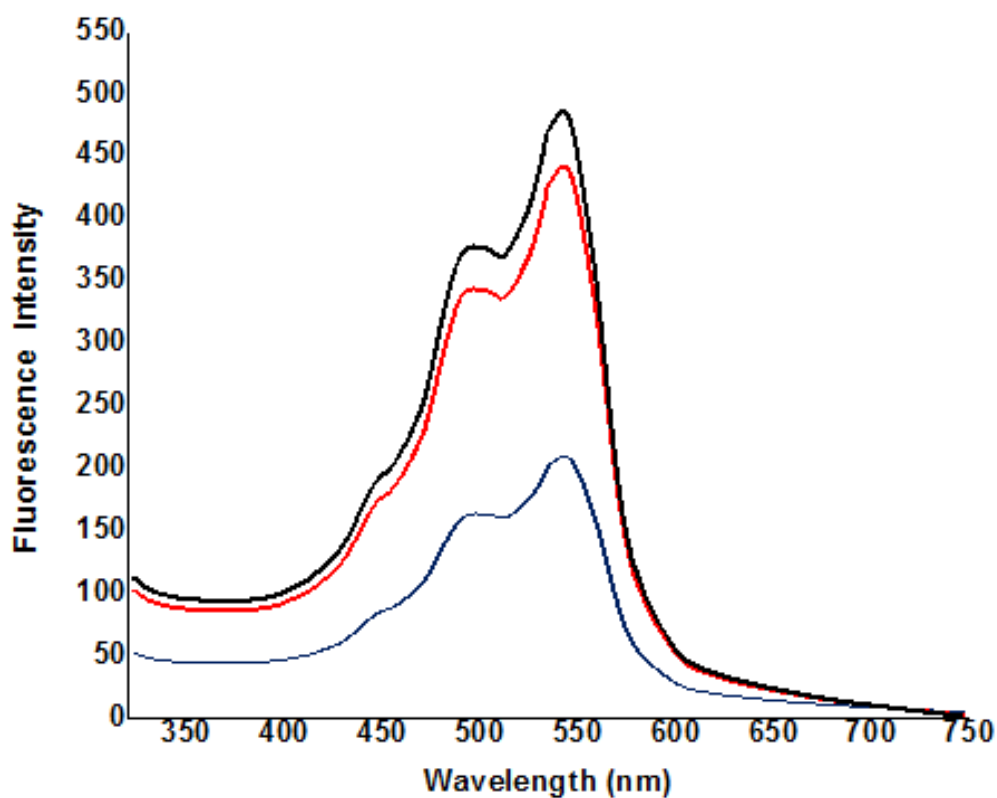


Fig 10. Fluorescence spectra of **A3** + Fe³⁺ and **A3** + Fe³⁺ + EDTANa₂ in EtOH/H₂O = 4/1, v/v solution

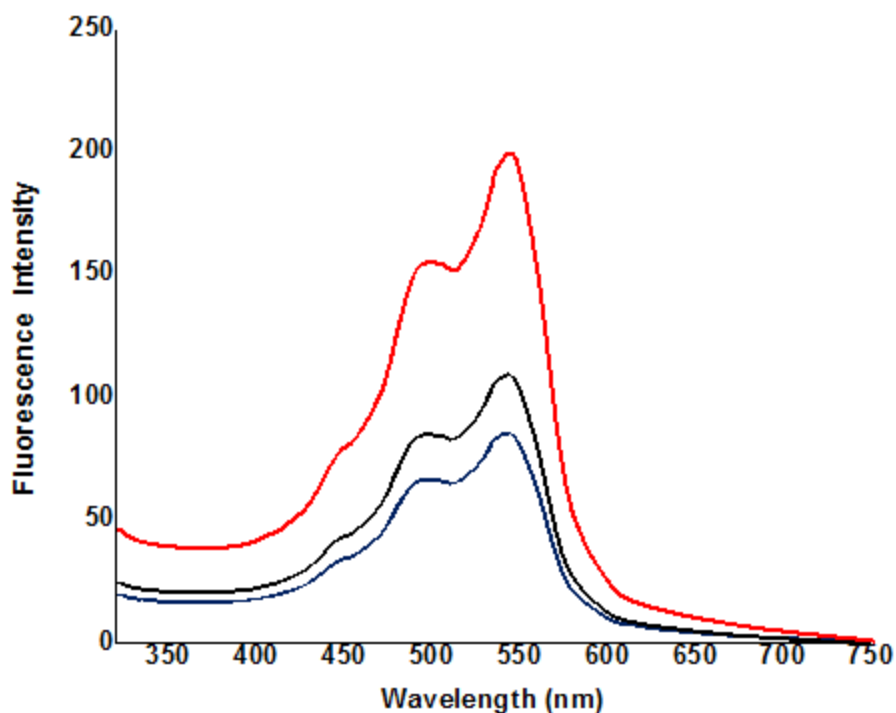


Fig 11. Fluorescence spectra of **A3**+ Ni²⁺ and **A3** + Ni²⁺ + EDTANa₂ in EtOH/H₂O = 4/1, v/v solution

5.3.3. The pH range of **A3** and **A3-Fe³⁺**& **A3-Ni²⁺** ions

For practical applications, the best pH conditions of the ligand **A3**, **A3-Fe³⁺**, and **A3-Ni²⁺** ions were examined using a buffer. The changes in absorption and fluorescence at various pH values are depicted in **Figure 12**. In acidic condition, fluorescence intensity is high. The binding behaviour of metal was justified. The emission band with a core wavelength of 553 nm in **A3** was preserved. The intensity of the fluorescence decreases substantially at pH 9, which might be attributed to a high pH causing an interaction between the metal and -OH, resulting in the creation of metal hydroxides. According to this experiment, the probe detects Fe³⁺ and Ni²⁺ ions in the pH range of 8.0–10.0 (**Fig 12**). This demonstrates that the sensor can detect Fe³⁺ and Ni²⁺ ions.

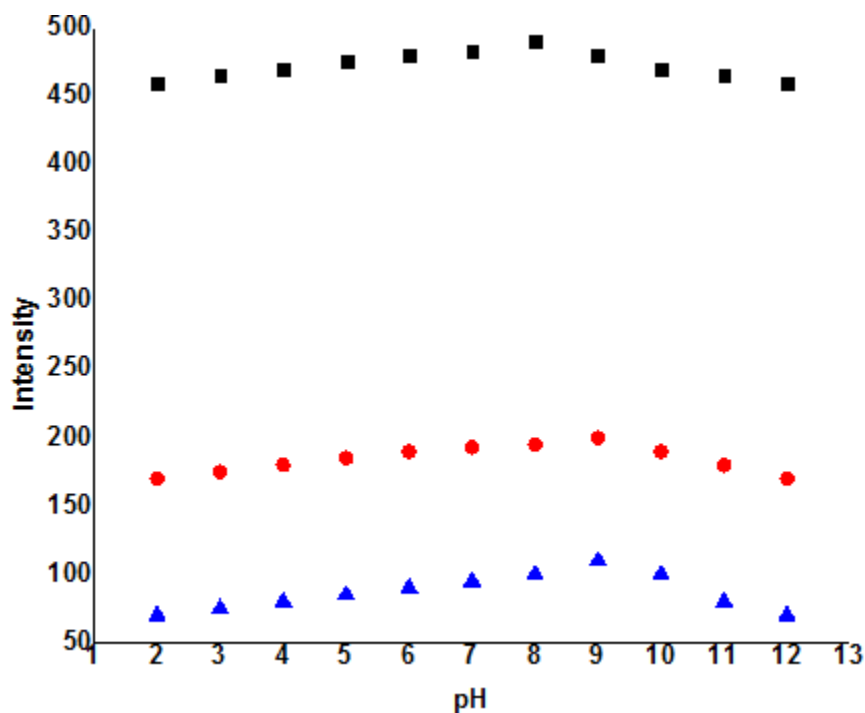
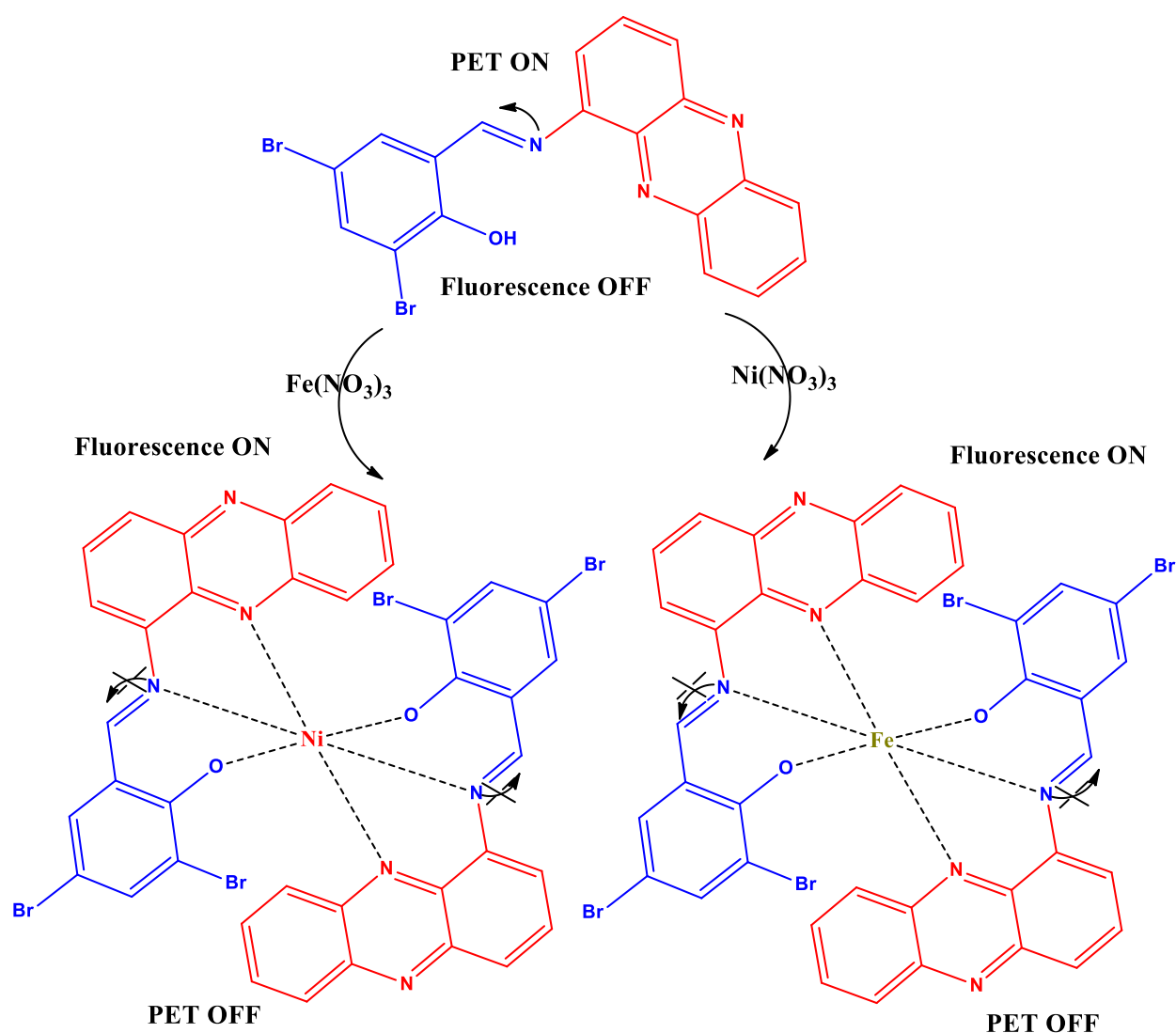


Fig 12. Fluorescence spectra of **A3** in EtOH/H₂O with **A3** + Ni²⁺, and **A3** + Ni²⁺ solution at different pH = 2 to 12

The PET technique, which allows for the amplification and quenching of fluorescence spectra in support of Fe³⁺ and Ni²⁺ ions detection, is significantly influenced by the great binding affinity of Fe³⁺ and Ni²⁺ ions for **A3** (**Scheme 2**). The significant binding constant supports the Fe³⁺ and Ni²⁺ ions' binding to **A3**. After selective coupling of the Fe³⁺ and Ni²⁺ ions, the electron lone pair on the imine atom of **A3** is no longer accessible for the PET method, permitting fluorescence intensification and quenching.



Scheme 2 The Possible binding site of compound A1C4 with Fe^{3+} and Ni^{2+} ions

5.3.4. FE-SEM of complex A3-Fe^{3+} and A3-Ni^{2+}

FE-SEM was used to analyse the presence of N, O, C, Fe, and Ni inside the (corresponding to **A3**) surface of complexes. **Figure 13** depicts the elemental mapping of nitrogen, oxygen, carbon, Fe^{3+} , and Ni^{2+} in FE-SEM complexes (A3-Fe^{3+} and A3-Ni^{2+}). **Figure 13** depicts the densities of nitrogen, oxygen, and carbon. N, O, C, Fe, and Ni are distributed evenly (**Fig 13**). According to elemental mapping, the chemical **A3** combination contains Fe^{3+} and Ni^{2+} ions. It also shows the purity of the complexes (A3-Fe^{3+} and A3-Ni^{2+}

ions). EDS is accurate up to trace quantities of metal present on the surface of complexes. The EDS obtained from the targeted region verifies the existence of N, O, C, Fe, and Ni inside the complexes, as shown in **Fig 13**.

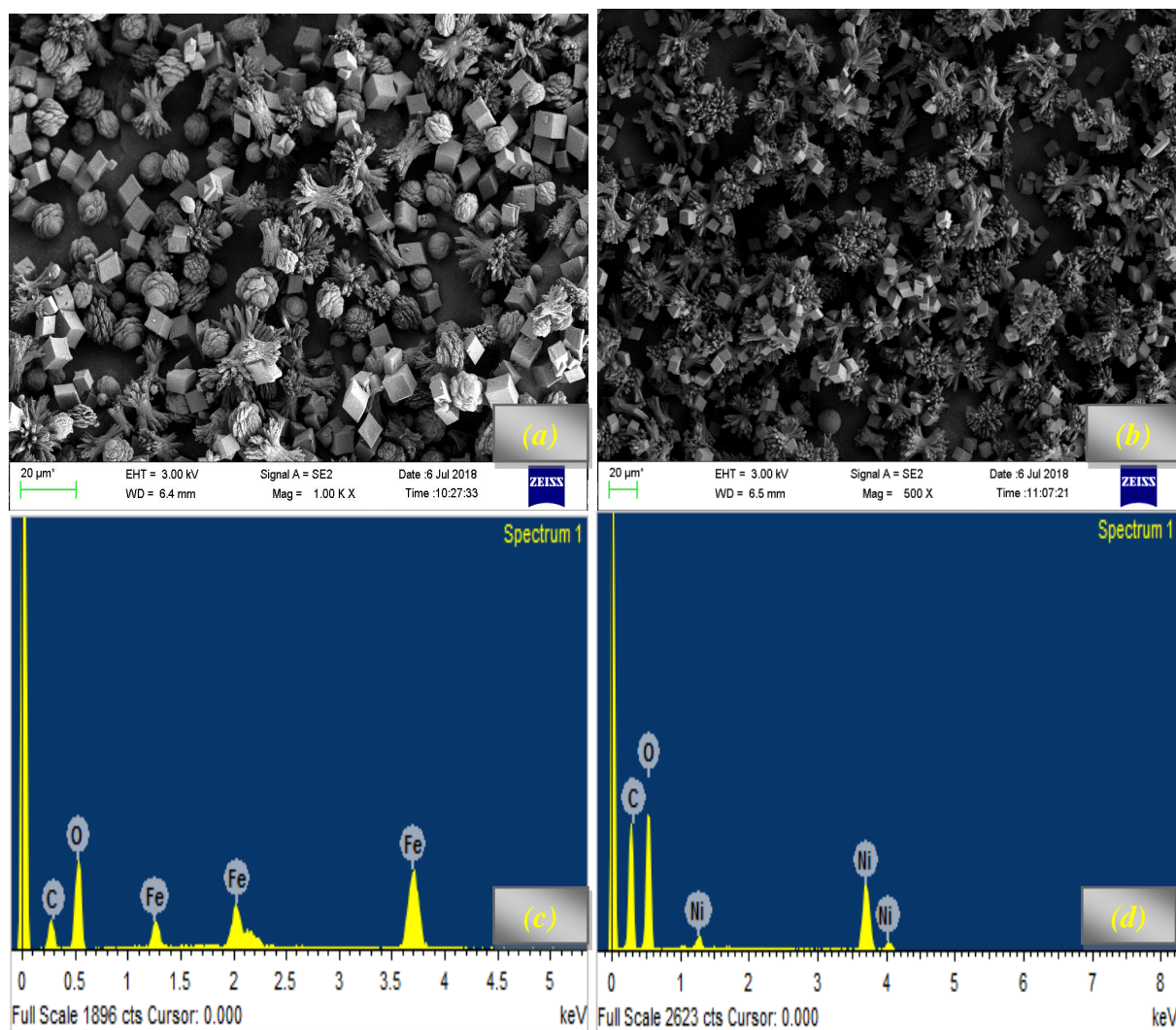


Fig 13. (a, b) FE-SEM of compound **A3** with Fe^{3+} and Ni^{2+} ions, (c, d) EDS of compound **A3** with Fe^{3+} and Ni^{2+} ions

The Stoichiometries of **A3**: Fe^{3+} and **A3**: Ni^{2+} ions were determined using Job's plots between mole fraction and fluorescence emission changes at 553 nm in the presence of Fe^{3+} and Ni^{2+} ions, as shown in **Fig 14** and **Fig 15**. At molar fractions of **A3**/ Fe^{3+} (0.5) and **A3**/ Ni^{2+} (0.5), Job's figure reaches the emission maximum, suggesting a 1:2 complexation binding hypothesis.

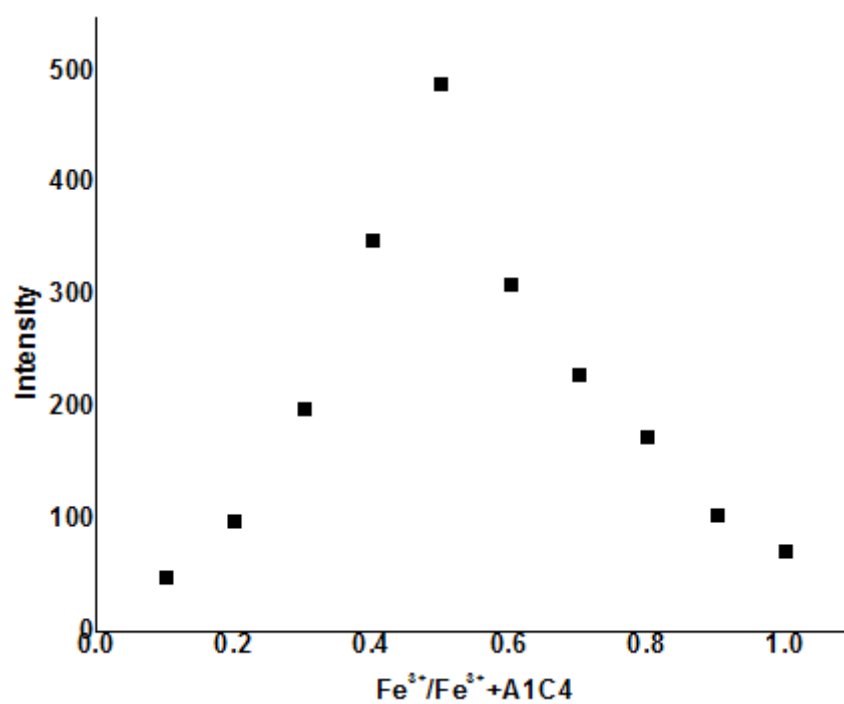


Fig 14. Jop's plot for **A3** with Fe³⁺ ions

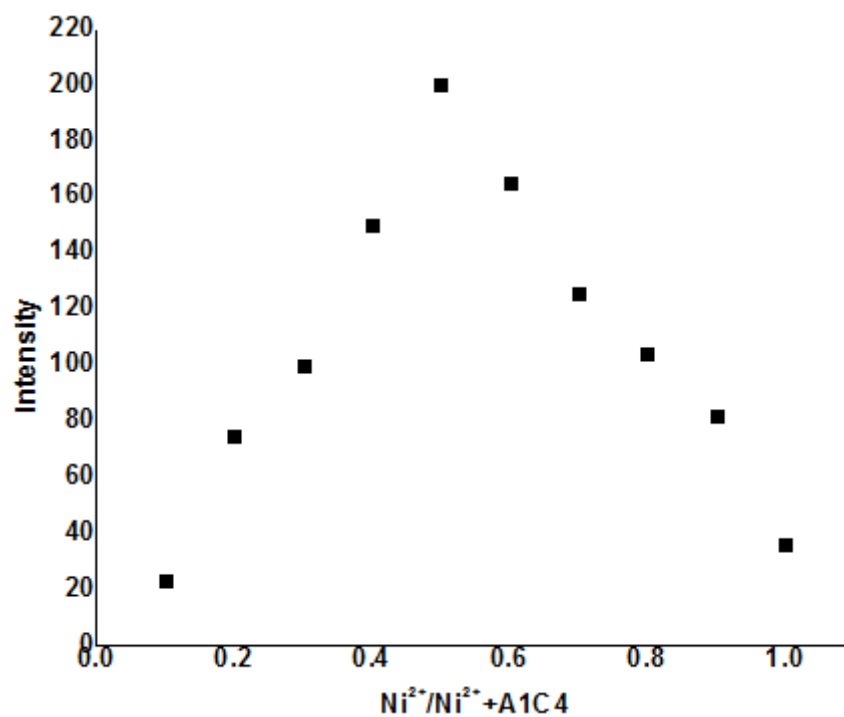


Fig 15. Jop's plot for **A3** with Ni²⁺ ions

To support the stoichiometry, ESI-mass spectra were employed. The **A3-Fe³⁺** m/z peak at 963.03 and the **A3-Ni²⁺** m/z peak at 965.08 confirmed the 1:2 (**A3-Fe³⁺** and **A3-**

Ni²⁺) complexation hypothesis (**Fig 16** and **Fig 17**). When varying amounts of Fe³⁺ and Ni²⁺ ions were introduced to the **A3** fluorogenic response, the sensitivity of the receptor was determined by determining the limit of detection. The values were found to be 0.6 μM and 0.8 μM, respectively (**Fig 18** and **Fig 19**). This suggested that **A3** prefers the Fe³⁺ and Ni²⁺ ions for binding.

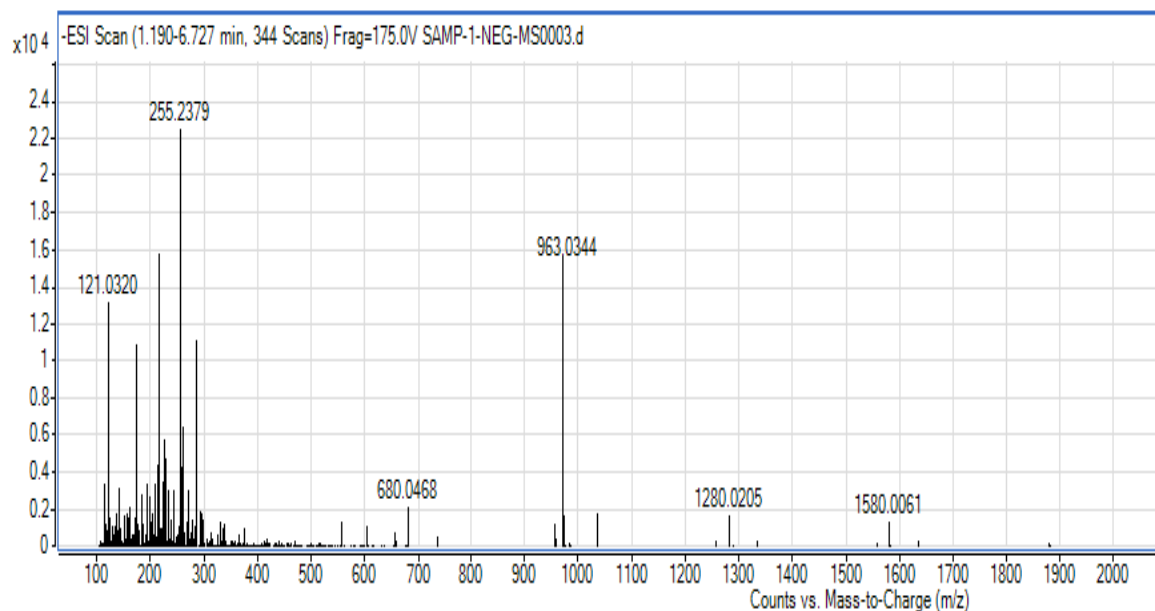


Fig 16. ESI mass spectrum of **A3**/ Fe³⁺ ion complex

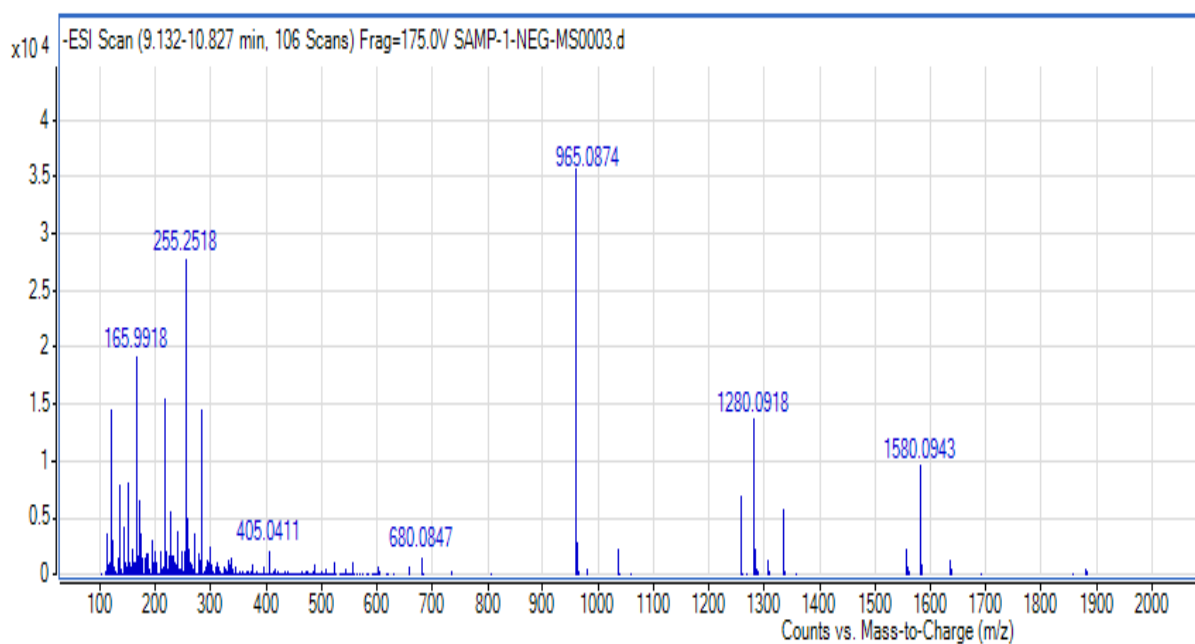


Fig 17. ESI mass spectrum of **A3**/ Ni²⁺ ion complex

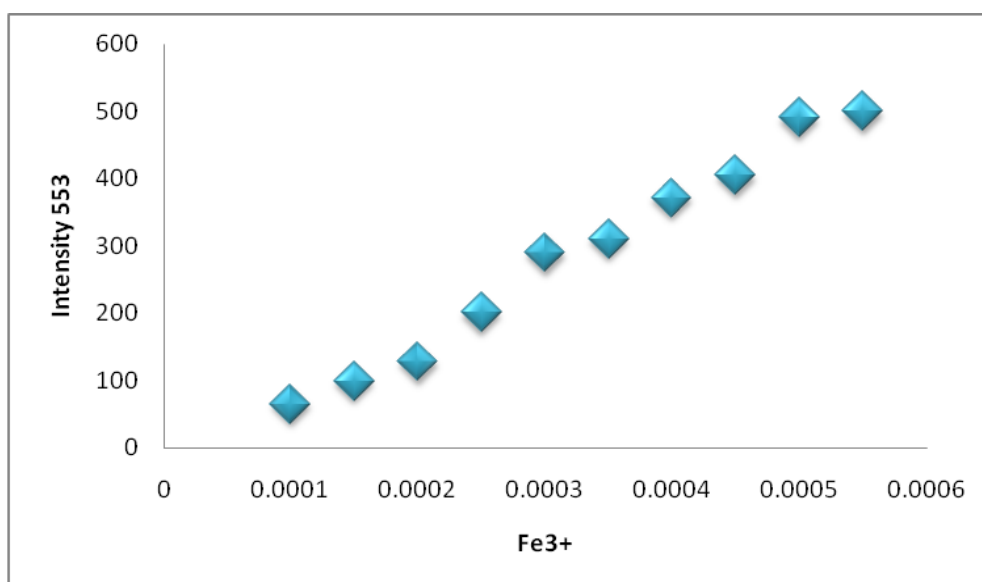


Fig 18. Calibration plot for successive addition of Fe³⁺ ion to **A3** solution in EtOH/H₂O

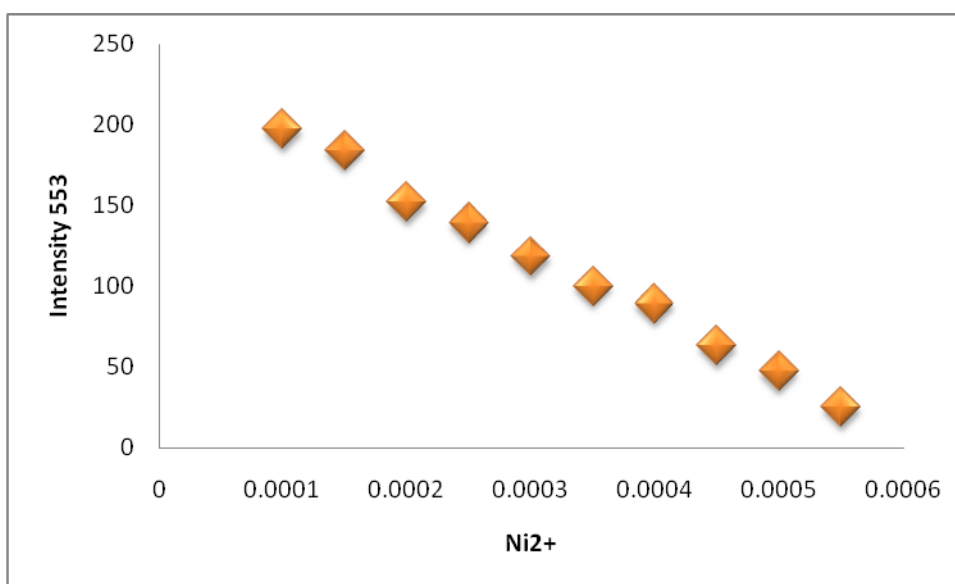


Fig 19. Calibration plot for successive addition of Ni²⁺ ion to **A3** solution in EtOH/H₂O

5.3.5. Cytotoxicity

The cytotoxicity reactions of **A3** at various dosages may be seen via cellular imaging. **A3** has been demonstrated to be cytotoxic using the MTT test in HepG2 cells treated with varied dosages of **A3** for up to 5 hours as a consequence of these findings, and it is an effective candidate for monitoring intracellular concentration changes under

particular biological situations. As shown in **Fig 20**, 20 μM levels of **A3** exhibited a substantial cytotoxic impact on HepG2 cancer cells for at least 4 hours. The activity of the generated **A3** on the HepG2 cell line was tested using the MTT test, which allows us to analyse the effect of complexes on cellular mitochondrial metabolism. For two days, cells were exposed to escalating dosages of the substances. **Figure 21** depicts microscopic pictures of control cancer cells as well as morphological changes associated with apoptosis in the HepG2 cell line treated with **A3**. The **A3** exhibited a low incidence of cell death, according to the data. With IC_{50} values of 62.07 μm , **A3** inhibits the HepG2 cell lines in a wide range of ways. **A3** showed a stronger inhibitory effect on cancer cells, according to the IC_{50} values (**Fig 20**). Because the compound **A3** with the =O group in ortho position has the greatest IC_{50} value, we assume that the electronic result is one of the variables in determining **A3** anticancer activity. The IC_{50} values of **A3** against HepG2 cells are shown in **Table 1**.

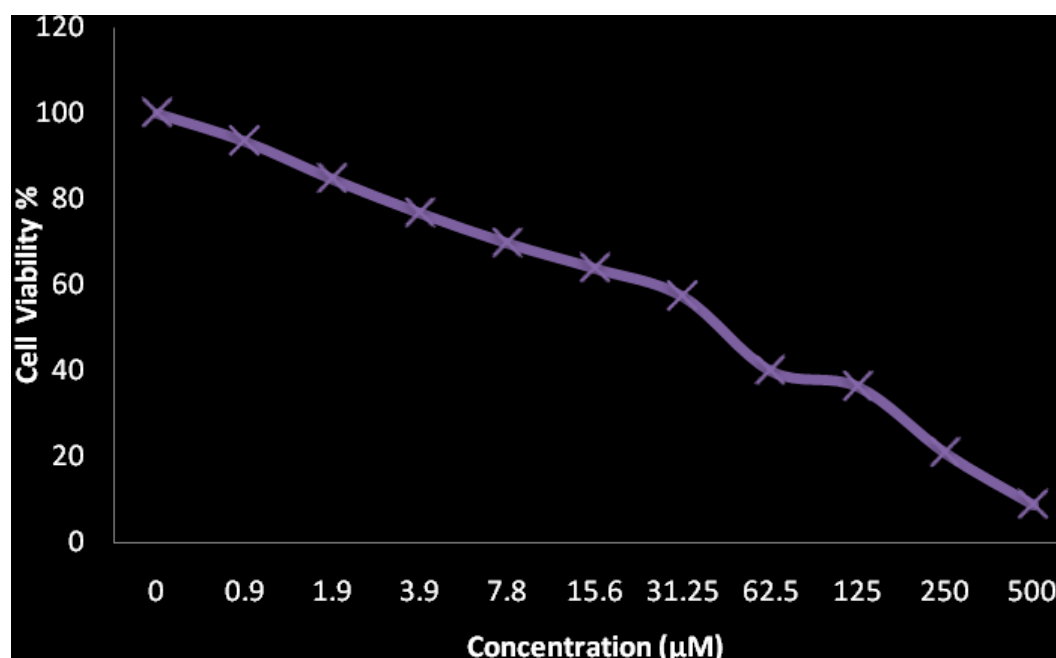


Fig 20. The IC_{50} values of **A3** against HepG2 cell lines

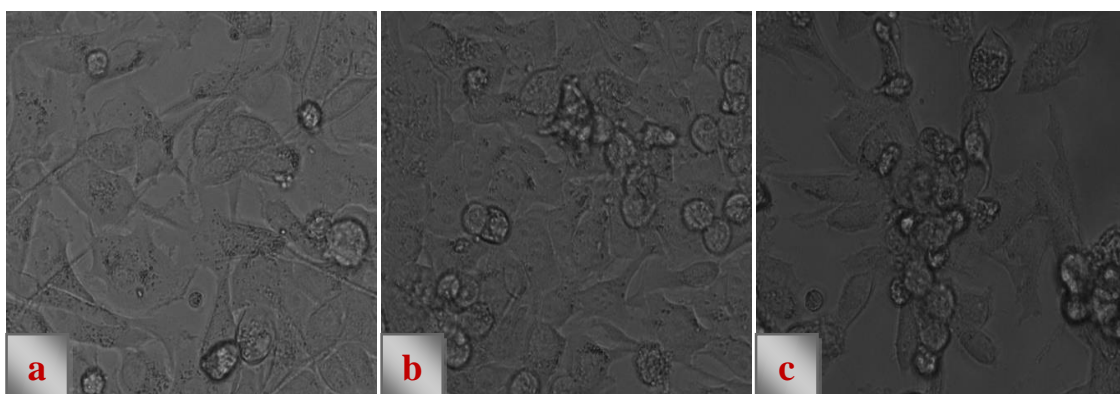


Fig 21. Live cell images of compound **A3**: (a) before and (b and c) after treatment with compound **A3** examined by fluorescence microscopy.

Table 1. The IC₅₀ values of **A3** against HepG2 cell lines

Anticancer effect of A3 on HepG2 cell line	
Concentration (μM)	Viability %
0	100
0.9	89.49
1.9	84.68
3.9	76.79
7.8	69.77
15.6	63.89
31.25	57.33
62.5	40.04
125	36.34
250	20.8
500	8.79

5.3.6. Living cell imaging

Living cell imaging was also explored with the chemosensor **A3**. First, when HepG2 cells were treated with **A3**, they produced a bright fluorescent picture (**Fig 22**).

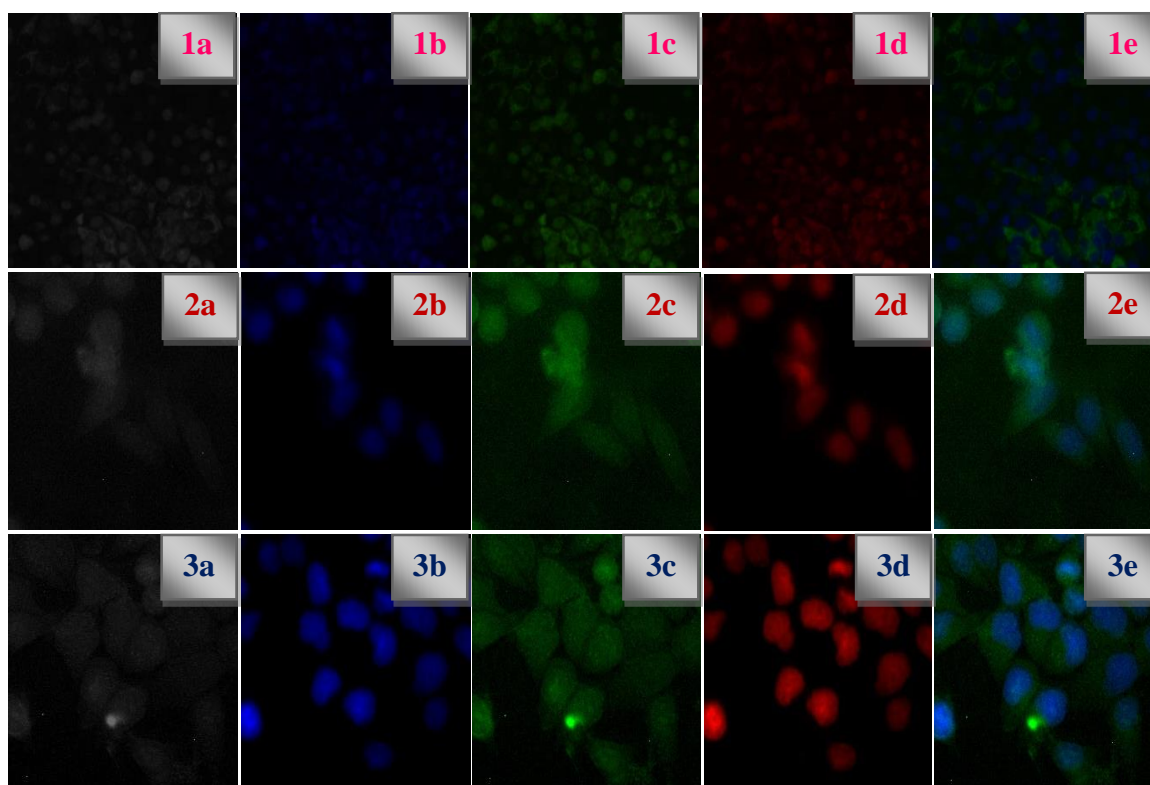


Fig 22. Confocal microscopic fluorescence images of HepG2 cells treated compound **A3** (1a-1e) treated $\text{Fe}(\text{NO}_3)_2$ (top: 2a-2e) with and $\text{Ni}(\text{NO}_3)_3$ (bottom: 3a-3e) (a) Bright field images, (b) fluorescence images of **A3**, (c) fluorescence images of **A3-Mⁿ⁺**, (d) overlapping images of **A3** & **A3-Mⁿ⁺** and (e) merged images

HepG2 cells were used to validate the cytocompatibility of **A3-Fe³⁺** and **A3-Ni²⁺** ions complexes in vitro. The fluorescence and bright field pictures overlap, demonstrating that the fluorescence signals are restricted to the intracellular area, indicating that the permeability of the **A3** cell membrane is good. After repeated treatment with the ions **A3-Fe³⁺** and **A3-Ni²⁺**, the fluorescence vanished. When the concentration of **A3-Fe³⁺** and **A3-Ni²⁺** ions uptake increased, the signal intensity rose as well. The probe fluoresced when it was taken up by the cells, confirming its ability to detect Fe^{3+} and Ni^{2+} ions in vitro.

Table 2. Mulliken atomic charges of **A3**

Position	Charge a.u
C1	-0.100
C2	-0.065
C3	0.123
C4	0.125
C5	-0.064
C6	-0.102
C11	0.112
C12	-0.051
C13	-0.104
C14	-0.057
C15	0.056
C16	0.121
N20	-0.312
N21	-0.346
N22	-0.282
C23	-0.195
C24	0.230
C25	-0.093
C26	-0.006
C27	-0.190
C28	0.040
C31	0.138
O33	-0.337
H34	0.245
Br35	0.003
Br36	0.001

5.3.7. Computational Analysis

In DFT, the **A3** and **A3-Fe³⁺**/**A3-Ni²⁺** ions geometry was optimised using the B3LYP/6-31G (d,p) basis set. The improved **A3** structure is shown in **Figure 23**.

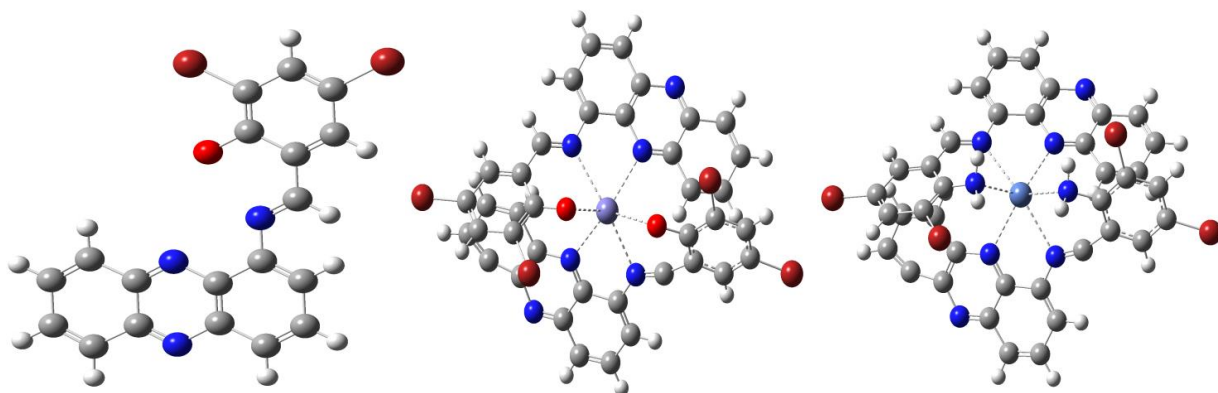


Fig 23. Optimize structure of **A3** and **A3-Fe³⁺**/**A3-Ni²⁺** ions

5.3.7.1. Mulliken charge analysis

The Mulliken atomic charges are calculated by determining the electron population of each individual atom using the basis function. The **A3** molecule was examined by B3LYP using the 6-31G (d,p) basis set, as shown in **Table 2**. Calculation plays an essential role in the application of computer calculations of chemical compounds. C3, C4, C11, C15, C16, C24, C28, C31, H34, Br35, and Br6 in **A3** have positive charges. Above C24 and H34 atoms have a stronger positive charge than other atoms due to the existence of mostly electronegative C atoms in the vicinity. Nitrogen (N20, N21, and N23) and oxygen (O2) have more negative charges (O33). C1, C2, C5, C6, C12, C13, C14, C23, C25, C26, and C27 are some of the carbon atoms in the title chemical that carry a negative charge. Based on the results given in **Fig 24**, we infer that our synthesised compounds are suitable for substitution processes.

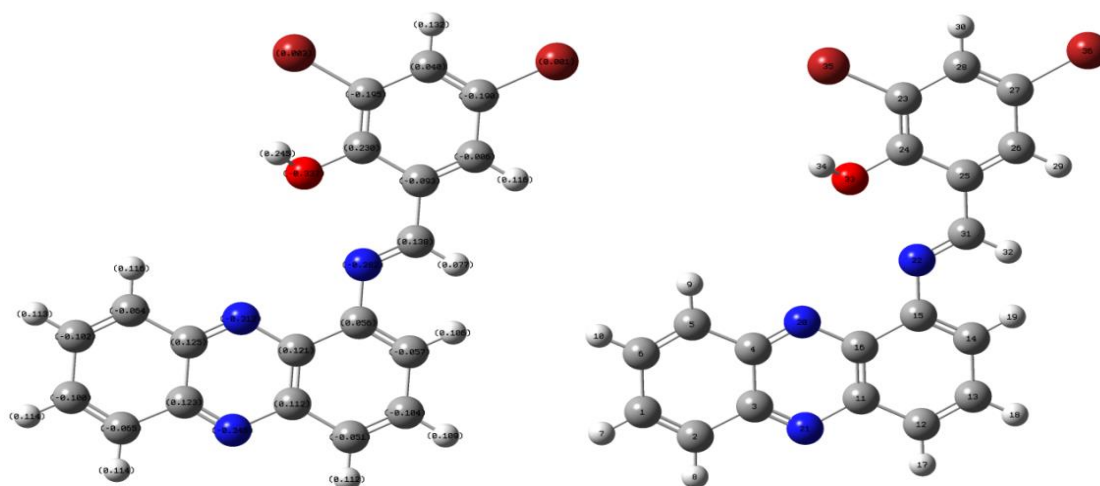


Fig 24. Mulliken atomic Charge of **A3**

5.3.7.2. Molecular Electrostatic Potential of **A3**

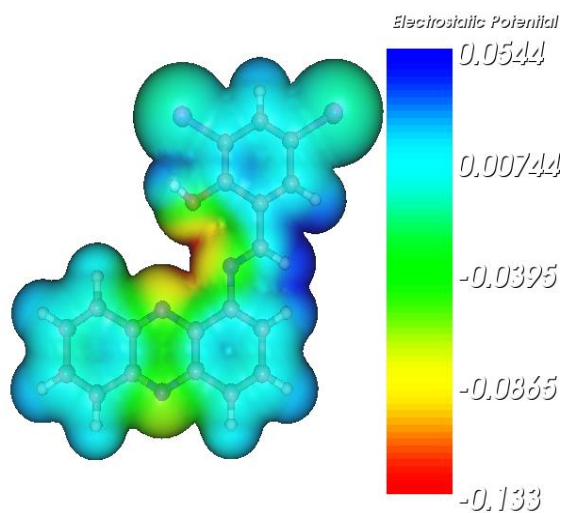


Fig 25. MEP diagram of **A3**

Even though it is concerned with the electrical density, MEP is a particularly effective descriptor in accepting places for electrophilic attack, nucleophilic reaction, and hydrogen bonding interactions. It also shows the molecule's relative polarity in a visual form. The electrostatic surface potential of **A3** was calculated using the B3LYP/6-31G (d,p) level of theory. The colour red represents negative electrostatic potential, whereas the colour blue represents positive (+) electrostatic potential and the colour green represents zero

potential. In **Fig 25**, the negative (-) regions above the O and N atoms are plainly evident. The presence of the O atom also contributes to the positive potential of C24 and H34. The found molecule, as illustrated in **Figure 24**, has multiple possible locations for nucleophilic and electrophilic attack.

5.3.7.3. FMO analysis of A3

Chemical reactivity, chemical compound stability, electrical, chemical processes, and optical features are all influenced by the HOMO-LUMO band gap. LUMO energy refers to the ability to recognise an electron, whereas HOMO energy refers to the ability to donate an electron. The HOMO-LUMO gap in the conjugated molecule is created by intermolecular charge transfer from the end-capping electron-donor groups to the efficient electron-acceptor groups through a π -conjugated channel. The B3LYP level with a 6-31G (d,p) basis set is used to determine the HOMO energy, LUMO energy, and energy gap of **A3** in **Table 3**. **Fig 26** shows the HOMO-LUMO molecular orbitals and energies, with the positive and negative phases of orbitals highlighted in green and red, respectively. As seen in the figure, the HOMO is -6.4226 eV while the LUMO is -2.5956 eV. The HOMO-LUMO gap for the title chemical is 3.827 eV. Inside the molecule, the HOMO-LUMO energy gap resolves the final charge transfer contacts.

Table 3. Calculated energy values (eV) of **A3**

B3LYP	A3
E_{HOMO}	-6.4226
E_{LUMO}	-2.5956
E_{LUMO-HOMO}	3.827

To get a better understanding of the internal charge transfer that occurred between the receptor **A3** and the respective metal ions during complex formation, the density

functional theory technique was employed to predict the structure of the metal complexes, **A3-Fe³⁺** and **A3-Ni²⁺** ions (**Fig 26**). The computations were carried out using the computational code Gaussian 03W and the exchange-correlation functional B3LYP with the basis sets 6-31G(d,p) for C, H, N, and O atoms, and LANL2DZ for Fe³⁺ and Ni²⁺ atoms. The experimental and computational structures of the **A3** receptor were discovered to be identical, with the receptor generating a pseudo cavity with three donors, O and N atoms, to form a complex with Fe³⁺ and Ni²⁺ ions (**Fig 26**). Furthermore, the bandgap between the HOMO and LUMO becomes smaller for **A3 Fe³⁺** and **A3-Ni²⁺** complexes (**Fig 26**). The nonradiative decay of the excited state of the **A3-Fe³⁺** and **A3-Ni²⁺** complexes was caused by a putative charge transfer mechanism that occurred between the receptor **A3** and the metal ions, lowering the bandgap.

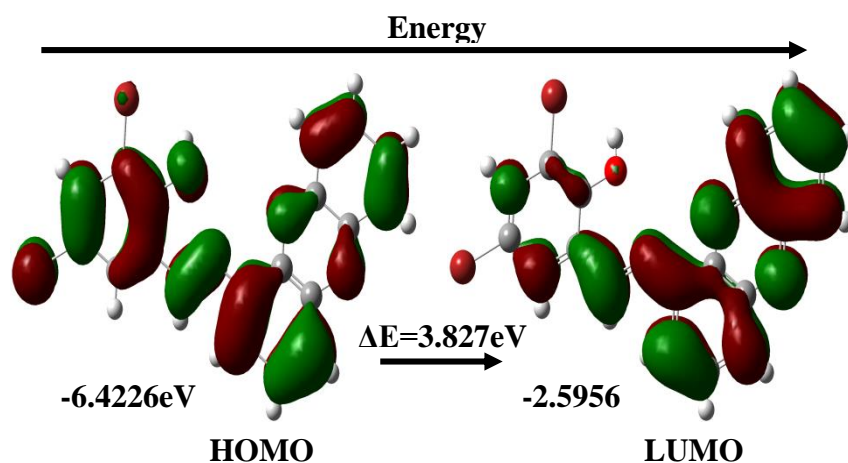


Fig 26. Molecular orbitals and energies for the HOMO and LUMO diagram of **A3**

5.3.8. NLO activity

Organic NLO molecules have been demonstrated to benefit from DFT analysis. According to new study, organic materials exhibit greater optical non-linearity than inorganic ones. In the presence of an applied electric field, a system's energy may be working in the electric field.

Table 4. Dipole moment, Polarisability, Hyperpolarisability of **A3** calculated using B3LYP method using 6-31G (d,p) basis set.

Parameter	Dipolemoment (Debye)
	A3
μ_x	-0.7042
μ_y	-0.2820
μ_z	-0.6372
μ_{total}	0.9907
Parameter	Polarisability (a.u)
α_{xx}	-157.6107
α_{yy}	-141.9841
α_{zz}	-174.5903
α_{xy}	-8.4922
α_{xz}	0.1634
α_{yz}	1.6685
Parameter	Hyperpolarisability (a.u)
β_{xxx}	158.3019
β_{yyy}	44.6192
β_{zzz}	0.2870
β_{xyy}	40.9995
β_{xxy}	109.7542
β_{xxz}	-1.2518
β_{xzz}	108.8402
β_{yzz}	25.2936
β_{yyz}	3.4921
β_{xyz}	0.3592
β_0 (esu)x10 ⁻³⁰	3.08
α_0 (esu)x10 ⁻²³	2.3
$\Delta\alpha$ (esu)x10 ⁻²⁴	4.79

Hyperpolarizabilities and polarizabilities describe how a system reacts to an applied electric field. They are in charge of the system's NLO properties as well as the strength of molecular interactions. During this inquiry, the electronic dipole moment, polarizability, anisotropy of polarizability, and molecular first hyperpolarizability of the present chemical were investigated. The electric dipole moment, polarizability, hyperpolarizability, and first-order hyperpolarizability of the **A3** are estimated using finite field method and the B3LYP/6-31(d,p) level of theory. As shown in **Table 4**, the calculated mean linear polarizability and initial hyperpolarizability values are 2.3×10^{-23} and 3.08×10^{-30} esu, respectively. According to the data, the title compound material's initial hyperpolarizability is 11 times more than that of the NLO reference substance Urea. **A3** may be the optimum material for NLO applications, based on the studies above.

5.4. CONCLUSIONS

We introduce **A3** phenazine-based chemosensors for the selective detection of Fe^{3+} and Ni^{2+} ions. The probes reveal fluorescence excitation in the visible area during the sensing experiment. The probes' large Stoke shift in the presence of Fe^{3+} and Ni^{2+} ions suggests that they could be used in a variety of domains, including biological processes, pathological research, and therapeutic effects over long periods of time, implying that they can detect Fe^{3+} and Ni^{2+} ions in biological systems. Both metal ions' affinity for chemosensors, as well as the values of quantum yield of metal connected chemosensors, demonstrate that the probes have a significant affinity for the respective metal ions. The PET-On process is demonstrated by the structure of **A3** chemosensors connected to Ni^{2+} and Fe^{3+} ions. This is the first time, to our knowledge; a Ni^{2+} and Fe^{3+} hydroxyl phenazine-based chemosensor combination has been reported. We were able to foresee the practical application of our produced chemosensors **A3** by conducting bio-imaging experiments in live HepG2 cells. Our probes can detect intracellular Fe^{3+} and Ni^{2+} ions without generating significant damage in cancer cells. Furthermore, the **A3** complexes have potential anticancer characteristics by inducing apoptosis.

5.5. REFERENCES

1. J. Yin, Y. Hu and J. Yoon, *Chem. Soc. Rev.*, 2015, 44, 4619–4644.
2. X. H. Li, X. H. Gao, W. Shi and H. M. Ma, *Chem. Rev.*, 2014, 114, 590–659.
3. J. Sun, B. Ye, G. Xia, X. Zhao and H. Wang, *Sens. Actuators, B*, 2016, 233, 76–82.
4. X. Zhou, S. Lee, Z. Xu and J. Yoon, *Chem. Rev.*, 2015, 115, 7944–8000.
5. X. X. Hu, X. L. Zheng, X. X. Fan, Y. T. Su, X. Q. Zhan and H. Zheng, *Sens. Actuators, B*, 2016, 227, 191–197.
6. K. P. Carter, A. M. Young and A. E. Palmer, *Chem. Rev.*, 2014, 114, 4564–4601.
7. O. Anderson, *Chem. Rev.*, 1999, 99, 2683–2710.
8. W. Qin, W. Dou, V. Leen, W. Dehan, M. W. Auweraer and N. Boens, *RSC Adv.*, 2016, 6, 7806–7816.
9. S. Sinha, T. Mukherjee, J. Mathew, S. K. Mukhopadhyay and S. Ghosh, *Anal. Chim. Acta*, 2014, 822, 60–68.
10. C. Li, J. Qin, G. Wang, B. Wang, A. Fu and Z. Zhang, *Inorg. Chim. Acta*, 2015, 430, 91–95.
11. H. Matthias, U. M. Martina, G. Bruno and C. Clara, *Cell*, 2010, 142, 24–38.
12. S. K. Danuta and R. R. Des, *Pharmacol. Rev.*, 2015, 57, 547–583.
13. R. Meneghini, *Free Radical Biol. Med.*, 1997, 23, 783–792.
14. P. Aisen, M. Resnick and E. A. Leibold, *Curr. Opin. Chem. Biol.*, 1999, 3, 200–206.
15. R. S. Eisenstein, *Annu. Rev. Nutr.*, 2000, 20, 627–662.
16. T. A. Rouault, *Nat. Chem. Biol.*, 2006, 2, 406–414.
17. C. Brugnara, *Clin. Chem.*, 2003, 49, 1573–1578.
18. S. Lunvongsa, M. Oshima and S. Motomizu, *Talanta*, 2006, 68, 969–973.
19. D. C. Gomes, M. A. Segundo, J. C. Lima and A. S. Rangel, *Talanta*, 2005, 66, 703–711.
20. R. Timerbaev, E. Dabek-Zlotorzynska and A. G. T. Marc van den Hoop, *Analyst*, 1999, 124, 811–826.

21. P. Vanloot, B. Coulomb, C. Brach-Papa, M. Sergent and J. L. Boudenne, *Chemosphere*, 2007, 69, 1351–1360.
22. T. Shamspur, I. Sheikhsaie and M. H. Mashhadizadeh, *J. Anal. At. Spectrom.*, 2005, 20, 476–478.
23. L. Hu, Y. F. Zhang, L. Nie, C. G. Xie and Z. Q. Yan, *Spectrochim. Acta, Part A*, 2013, 104, 87–91.
24. Z. Q. Yan, S. Y. Guang, H. Y. Xu and X. Y. Liu, *Analyst*, 2011, 136, 1916–1921.
25. D. B. Wei, Y. L. Sun, J. X. Yu, G. H. Wei and Y. G. Du, *Sens. Actuators, B*, 2011, 160, 1316–1321.
26. L. Hu, L. Nie, G. N. Xu, H. Shi, X. Q. Xu, X. Z. Zhang and Z. Q. Yan, *RSC Adv.*, 2014, 4, 19370–719374.
27. Singh, S. Sinha, R. Kaur, N. Kaur and N. Singh, *Sens. Actuators, B*, 2014, 204, 617–621.
28. Y. W. Ma, T. H. Leng, Y. R. Qu, C. Y. Wang, Y. J. Shen and W. H. Zhu, *Tetrahedron*, 2017, 73, 14–20.
29. L. Qiu, C. C. Zhu, H. C. Chen, H. C. Chen, M. Hu, W. J. He and Z. J. Guo, *Chem. Commun.*, 2014, 50, 4631–4634.
30. T. Nandhini, P. Kaleeswaran and K. Pitchumani, *Sens. Actuators, B*, 2016, 230, 199–205.
31. N. R. Chereddy, K. Suman, P. S. Korrapati, S. Thennarasu and A. B. Mandal, *Dyes Pigm.*, 2012, 95, 606–613.
32. H. Kim, B. A. Rao, J. Jeong, S. Angupillai, J. S. Choi, J. O. Nam, C. S. Lee and Y. A. Son, *Sens. Actuators, B*, 2016, 224, 404–412.
33. Y. Xiang and A. J. Tiong, *Org. Lett.*, 2006, 8, 1549–1552.
34. L. Dong, C. Xu, X. Zeng, L. Mu, S. F. Xue, Z. Tao and J. X. Zhang, *Sens. Actuators, B*, 2010, 145, 433–437.
35. J. Mao, L. N. Wang, W. Dou, X. L. Tang, Y. Yan and W. S. Liu, *Org. Lett.*, 2007, 9, 4567–4570.
36. N. V. Ghule, R. S. Bhosale, A. L. Bhosale, S. V. Bhosale and S. V. Bhosale, *Sens. Actuators, B*, 2016, 227, 17–23.
37. P. Kaur and D. Sareen, *Dyes Pigm.*, 2011, 88, 296–300.

38. T. B. Wei, P. Zhang, B. B. Shi, P. Chen, Q. Lin, J. Liu and Y. M. Zhang, *Dyes Pigm.*, 2013, 97, 297–302.
39. Bansal, M.; Singh, D.; Garg, V. K.; Rose, P. *World Acad. Sci. Eng. Technol.* 2009, 3, 174 –180.
40. N.Gupta, D.Singhal, A. K. Singh, *New J. Chem.*, 2016, 40, 641 –650.
41. Z.Krejpcio, R. W. Wojciak, *Pol. J. Environ. Stud.*, 2002, 11, 251 –254.
42. J. Barcelo, C. Poschenrieder, *Environ. Exp. Bot.*, 2002, 48, 75 –92.
43. B. Valeur, I. Leray, *Coord. Chem. Rev.*, 2000, 205, 3 –40.
44. M. Cempel, G. Nickel, *Pol. J. Environ. Stud.*, 2006, 15, 375 – 382.
45. IARC, International Agency for Research on Cancer: Lyon, France., 1990, 49, 257 –445.
46. H. Li, S. J. Zhang, C. L. Gong, Y. F. Li, Y. Liang, Z. G. Qi, S. Chen, *Analyst.*, 2013, 138, 7090 –7093.
47. M. Shamsipur, T. Poursaberi, A. R. Karami, M.Hosseini, A.Momeni, N.Alizadeh, M.Yousefi, M. R. Ganjali, *Anal. Chim. Acta.*, 2004, 501, 55–60.

Summary

The thesis deals with studies on Schiff base ligand based fluorescence chemosensor application. The Schiff base ligand were synthesized and characterized by UV-Spectrophotometer, Spectrofluorometer, Infra-red spectroscopy, Nuclear Magnetic resonance spectroscopy, and High resolution mass spectroscopy, theoretical calculation, anticancer activity and some metal nitrate and chloride involved fluorescent chemosensor applications.

Chapter 1

This chapter deals with the introduction about the need for Fluorescent chemosensor. Further, the information about the mechanism of Schiff base ligand in fluorescent properties. Basic principle mechanism involved in photochemistry was also outlined. The aim and scope of the present investigation also included in this chapter.

Chapter 2

In this chapter, the fluorescent chemosensor has been successfully designed and we synthesized as a simple Schiff-base of (E)-N-(1-(1H-phenothiazin-2yl)-ethylidene)-3-((E)-(2-phenylhydrazono) methyl) aniline and studied their PET mechanisms. The experiments indicated report chemosensor **AT** was a highly sensitive and selective chemosensor for Cr^{3+} and Pb^{2+} in a HEPES buffer solution in EtOH: H_2O (1:4, v/v, pH=7.0). Significantly, the probe showed a “turn-on” fluorescence response to Cr^{3+} and Pb^{2+} and emission intensity at 428 nm (excitation wavelength 290). The fluorescence improvement with high selectivity and sensitivity was attributed to photoinduced electron transfer (PET) and also competitive metal studies. The Job plot of **AT** binding with Cr^{3+} and Pb^{2+} demonstrated a 1:1 stoichiometry complex predicted at 0.6 μM concentration. Further, the binding constant was calculated and found to be $2.13 \times 10^4 \text{ M}^{-1}$ ($R^2=0.9991$) and $2.37 \times 10^4 \text{ M}^{-1}$ ($R^2=0.9996$)

according to the Benesi-Hildebrand equation and detection limit at 8.63×10^{-7} M ($R^2=0.9992$) and 7.42×10^{-7} M ($R^2=0.9990$) towards using this equation $3\sigma/k$ due to WHO (World Health Organization) allowed ($7.4 \mu\text{M}$) in drinking water. The pH experiment covered a range from 4-10 in sensing application. EDTA titration was examined and was found to be reversible and irreversible due to Cr^{3+} and Pb^{2+} added into **AT** solution. The theoretical calculation was carried out by B3LYP/6-31*G in Gaussian 09 program. The **AT** has a potent in-vitro HepG2 cell line against the cytotoxic, living cell images. It is worth noting that the receptor **AT** would be a beneficial addition to academia for its optical properties and functional application to biomedical industries which will open door to the establishment of these findings. The molecule is useful in sensing and drug-carrying applications.

Chapter 3

In this chapter, the benzenesulfonamide based Schiff base of **BT** characterized by FT-IR, ^1H NMR, and ^{13}C NMR spectroscopy and mass spectrometry. The compound **BT** exhibited recognition for Al^{3+} in ethanol/ water HEPES buffer solution (5 mM, 1: 4, v/v, pH 7.4) at room temperature in a UV-Visible and fluorescence spectroscopy. The fluorescence emission intensity at 516 nm (excitation wavelength at 290 nm), fluorescence “turn-on” due to the presence of Al^{3+} ion with a high peak below all metal ions. Photoinduced Electron Transfer (PET) and stimulating the Chelation Enhanced Fluorescence (CHEF) process for **BT**+ Al^{3+} is coordinated through the NH group and imine nitrogen inhibited and blocked. Job’s plot was shown by 1:1 stoichiometric for **BT**- Al^{3+} . The binding constant (K) was determined as $3.27 \times 10^7 \text{ M}^{-1}$ (Al^{3+}), the detection limit of **BT** for Al^{3+} was observed $R^2=0.9965$. Competitive metal ions extensively studied for the presence of Al^{3+} , whereas, after the EDTA solution added into **BT**+ Al^{3+} proved to be reversible and irreversible. The theoretical calculation used in Gaussian 09 program was followed by the B3LYP/6-31G(d,p) basis set.

Chapter 4

In this chapter, a new and simple water-soluble fluorescent chemosensors namely asymmetrical azine derivatives viz., (E)-4-(((bis(4-chlorophenyl)methylene) hydrazono)methyl)-2,6-dimethoxyphenol (**A1**), and (E)-4-(((bis(4-bromophenyl)methylene) hydrazono)methyl)-2,6-dimethoxyphenol (**A2**) were synthesized. The synthesized compounds have been elucidated by Fourier-Transform infrared, ^1H , and ^{13}C NMR and ESI-MS spectral studies. The Mass spectra of **A1** and **A2** are in excellent confirmation with the proposed molecular formula of the respective compounds. In presence of Zn^{2+} and Al^{3+} ions, chemosensors **A1** and **A2** exhibit enhancement of emission intensity. The detection limit (LOD) of **A1** and **A2** against Zn^{2+} and Al^{3+} ions are $1.062 \times 10^5 \text{ M}^{-1}$ and $1.13 \times 10^5 \text{ M}^{-1}$, respectively which clearly indicate that the probes can be used to detect Zn^{2+} and Al^{3+} ions in biological system. Binding affinity of both metal ions towards the chemosensors and the values of k_a of metal bound chemosensors suggest that the probes have significant affinity towards the respective metal ions. The structure of **A1** and **A2** both Zn^{2+} and Al^{3+} ions bound chemosensors prove PET OFF-CHEF On mechanism. Theoretical calculation was conceded out for all compounds **A1** and **A2** using DFT/6-31G (d,p) basis set and their optimized bond parameters were calculated. Molecular electrostatic potential and Mulliken analysis revealed that oxygen atom will be the most reactive site for electrophilic attack and the hydrogen atom will be reactive site for nucleophilic attack. The investigation on docking studies for compounds **A1-A2** was carried with 3ERT protein. The docking results showed an outstanding docking score -6.45 and -6.32 (kcal/mol) for compounds **A1** and **A2**. Cytotoxic activity by MTT assay revealed that the compounds **A1-A2** exhibited broad inhibition on the MCF-7 cell line with IC_{50} values of 50.51 and 63.19 μM respectively. The observed IC_{50} values revealed that compound **A1** possessed a more inhibitory effect against the cancer cells.

Chapter 5

This chapter introduces A1C4 phenazine-based chemosensors for the selective detection of Fe^{3+} and Ni^{2+} ions. The probes reveal fluorescence excitation in the visible area during the sensing experiment. The probes' large Stoke shift in the presence of Fe^{3+} and Ni^{2+} ions suggests that they could be used in a variety of domains, including biological processes, pathological research, and therapeutic effects over long periods of time, implying that they can detect Fe^{3+} and Ni^{2+} ions in biological systems. Both metal ions' affinity for chemosensors, as well as the values of quantum yield of metal connected chemosensors, demonstrate that the probes have a significant affinity for the respective metal ions. The PET-On process is demonstrated by the structure of A1C4 chemosensors connected to Ni^{2+} and Fe^{3+} ions. This is the first time, to our knowledge; a Ni^{2+} and Fe^{3+} hydroxyl phenazine-based chemosensor combination has been reported. We were able to foresee the practical application of our produced chemosensors A1C4 by conducting bio-imaging experiments in live HepG2 cells. Our probes can detect intracellular Fe^{3+} and Ni^{2+} ions without generating significant damage in cancer cells. Furthermore, the A1C4 complexes have potential anticancer characteristics by inducing apoptosis.

LIST OF PUBLICATIONS

1. Novel schiff base synthesis of E-N-(1-(1H-phenothiazin-2-yl)-ethylidene)-3-((E)-(2-phenylhydrazono) methyl) aniline “Turn-on” fluorescent chemosensor for sensitivity and selectivity of detection of Cr³⁺ and Pb²⁺ ions. **P. Vijayakumar** E. Dhineshkumar M. Arockia doss S. Nargis Negar R. Renganathan. *Materials Today: Proceedings* .2021,42 1050–1064.
2. Fluorescence Recognition of Al(III) Ions by a New Chemosensor Based E-4-((1-(10H-Phenothiazin-2-yl)ethylidene)amino)-N-(pyrimidin-2-yl) benzenesulfonamide. **P.Vijayakumar**, M.Arockia Doss, S. Nargis Negar R. Renganathan. *Asian Journal of Chemistry*; 2021, Vol. 33, No.7, 1563-1572.
3. Synthesis of Schiff base of (Z)-4-methyl-N'-(phenyl(2-(4-substituted)-1H benzo[d]imidazol-6-yl)methylene) benzenesulfonohydrazide and their role as chemosensor for Zn²⁺ and Al³⁺. **P.Vijayakumar**, R.Renganathan. (**Under Review in Chemical Papers**)
4. Novel Dual Chemosensor for Fe³⁺/ Ni²⁺ ions and its Multi Applications. **P.Vijayakumar**, R.Renganathan. (**Communicated to Journal of molecular structure**)
5. Synthesis, DNA-binding study, and antioxidant activity of 14-aryl-14H-dibenzo[a,j]xanthene derivatives. Andivelu Ilangovan, Karnambaram Anandhan , Kaushik Mahabir Prasad, **Pakkiri Vijayakumar**, Rajalingam Renganathan , Devanesan Arul Ananth ,Thilagar Sivasudha. *Med Chem Res.*, 2015, 24, 344–355.
6. Spectroscopic investigation and computational studies on the interaction of Acriflavine with various estrogens. C.Manivannan, S.Baskaran, **P.Vijayakumar**, R.Renganathan. *Spectrochimica Acta Part A: Molecular and Biomolecular Spectroscopy.*, 2019, 206, 622-629.
7. A comparative study on the electron transfer reaction (ETR) of surfactant cobalt(III) complexes of aliphatic/aromatic ligands in micro heterogeneous media: a thermodynamic approach. Kannan Sugumar, Karuppiyah Nagaraj, Krishnan Senthil Murugan, Pilavadi Thangamuniyandi, Subramanian Sakthinathan, **Pakkiri Vijayakumar**. *RSC Adv.*, 2015, 5, 48079.

8. Bioengineered Metal and Metal Oxide Nanoparticles for Photocatalytic and Biological Applications (Review), Geetha Palani, Karthik Kannan, D. Radhika, **P. Vijayakumar**, K. Pakiyaraj. *Physics and Chemistry of solid state*. 2020, 21, 571-583.
9. Synthesis and characterization of porphyrin derivatives and photophysical properties, AIE study and its biological evaluation. **P.Vijayakumar**, R.Renganathan. (**Under Preparation**)
10. Synthesis and characterization of imidazole derivatives and photophysical, electrochemical properties, AIE study. P.Vijayakumar, R.Renganathan (Under Preparation)

Presentation in Conference

1. **P.Vijayakumar**, R.Renganathan, Novel Schiff base Synthesis of *E-N-(1-(1H-phenothiazin-2-yl)-ethylidene)-3-((E)-(2-phenylhydrazono) methyl) aniline* “Turn-on” fluorescent chemosensor for sensitivity and selectivity of detection of Cr³⁺ and Pb²⁺. 2020 Second International Conference on Recent Advances in Materials and Manufacturing (ICRAMM 2020), 20-21, November 2020, Velalar College of Engineering & Technology, Erode. (**Oral Presentation**)
2. **P.Vijayakumar**, R.Renganathan, Synthesis of Schiff base of (Z)-4-methyl-N'-(phenyl(2-(4-substituted)-1H-benzo[d]imidazol-6-yl)methylene)benzenesulfonohydrazide and their role as chemosensor for Zn²⁺ and Al³⁺. Recent innovations in chemical sciences (RICS 2022), March 24-25, Periyar University, Salem. (**Poster Presentation**)
3. **P.Vijayakumar**, R.Renganathan, Synthesis and characterization of porphyrin derivatives and photophysical study and its biological evaluation, Recent Advances in nanomaterials(NSRAN – 2015), Jeyaram Arts and Science College, Karur, 15 October, 2015. (**Best Poster Award**).
4. **P.Vijayakumar**, R.Renganathan, Studies on the synthesis, photophysical and biological evaluation of Porphyrins. International Conference on Research Initiatives in chemistry for sustainable Development (RICS-2019), 18-19, March 2019. Department of Chemistry, Gandhigram Rural Institute, Gandhigram, Dindigul. (**Poster Presentation**)



Novel schiff base synthesis of *E-N*-(1-(1H-phenothiazin-2yl)-ethylidene)-3-((E)-(2-phenylhydrazono) methyl) aniline “Turn-on” fluorescent chemosensor for sensitivity and selectivity of detection of Cr^{3+} and Pb^{2+} ions

P. Vijayakumar^a, E. Dhineshkumar^b, M. Arockia doss^c, S. Nargis Negar^d, R. Renganathan^{a,*}

^aSchool of Chemistry, Bharathidasan University, Tiruchirappalli 620024, India

^bDepartment of Chemistry, Annamalai University, Annamalainagar 608002, Tamilnadu, India

^cDepartment of Chemistry, St. Joseph University, Nagaland 797 115, India

^dDepartment of Nanoengineering, Center for Physical Sciences and Technology, Savanoriu Ave. 231, LT-02300 Vilnius, Lithuania

ARTICLE INFO

Article history:

Received 5 October 2020

Received in revised form 29 November 2020

Accepted 4 December 2020

Available online 23 January 2021

Keywords:

Chemosensor

PET

EDTA

pH

HepG2

Cytotoxic

DFT

ABSTRACT

The Synthesized *E-N*-(1-(1H-phenothiazin-2yl)-ethylidene)-3-((E)-(2-phenylhydrazono)methyl)aniline (**AT**) was characterized by FT-IR, MS, ^1H , and ^{13}C spectroscopy instruments. The chemosensor demonstrates fluorescent performance with high sensitivity and selectivity detection of Cr^{3+} and Pb^{2+} over other coexistent metal ions in 100% aqueous solution, and even with a visual fluorescence change from light yellow to light blue. The probe shows “turn-on” fluorescence intensity at 428 nm (excitation wavelength 290) in HEPES buffer solution in EtOH: H_2O (1:4, v/v, pH = 7.0). Significantly, the fluorescence enhancement was attributed to photoinduced electron transfer (PET). The Job plot for showed Cr^{3+} and Pb^{2+} complex formation for both metal ions with 1:1 stoichiometry and was predicted at 0.6 μM concentration. Additionally the binding constant was found to be $2.13 \times 10^4 \text{ M}^{-1}$ ($R^2 = 0.9991$) and $2.37 \times 10^4 \text{ M}^{-1}$ ($R^2 = 0.9996$) according to Benesi-Hildebrand equation and detection limit at $8.63 \times 10^{-7} \text{ M}$ ($R^2 = 0.9992$) and $7.42 \times 10^{-7} \text{ M}$ ($R^2 = 0.9990$) and WHO (World Health Organization) allowed (7.4 μM) for drinking water. The pH experiments range from 4 to 10 in sensing application and reversible and irreversible due to EDTA + Cr^{3+} and EDTA + Pb^{2+} added into **AT** solution. The theoretical calculation was performed by B3LYP/6-31*G in Gaussian 09 program. The CYGD has strong cytotoxic in-vitro activity against cell line HepG2. We believe that our protocol receptor would be a valuable addition in academia for its optical properties and also excellent practical applications in biomedical industries.

© 2020 Elsevier Ltd. All rights reserved.

Selection and peer-review under responsibility of the scientific committee of the Second International Conference on Recent Advances in Materials and Manufacturing 2020.

1. Introduction

The selection of transition metal ions has potential applications in many fields such as biology, chemistry, medicine, and the environment [1–5]. A variety of effectively fluorescent chemosensors for alkali and alkaline earth metal ions have been developed [1,3–5]. The soft transition metal ions are fluorescence chemosensors and particularly necessary much attention is paid because of their impact on the environment [6,7]. Our body could be affected by the direct disease due to excess or deficiency of a metal ion [8].

The metal ion Cr^{3+} is a trivalent form and plays a vital role in various biological processes and it assists the metabolism of carbohydrates, nucleic acids, proteins, and fats through stimulated enzymes as well as by stabilizing the nucleic acids and proteins [9]. Therefore, it is very important to develop a chemosensor for detection of Cr^{3+} ions in biological and also ecological samples. Cr^{3+} could be detected using various instrumentation techniques like reversed phase-high performance liquid chromatography coupled to different spectrometric detection methods, stripping voltammetric analysis, and atomic absorption spectrophotometers [10–12]. Costly instrumentation and time consumption for analysis made chemosensors a significantly analytical tool that can be used to detect ionic species. In current years, fluorescent

* Corresponding author.

E-mail address: rrengas@gmail.com (R. Renganathan).

chemosensors for Cr^{3+} have been reported [13–17]. As a result, the high sensitivity and selectivity to detecting Cr^{3+} ion very quickly in the development of material for ease, and due to it is very simplicity, low cost, and convenience, extensive attention is received by small organic fluorescence basic methods for chemosensors [18]. Fluorescent chemosensor has several acceptable sensing properties for Pb^{2+} has drawn considerable much attention because of spread of poisonous lead a heavy toxic metal ion from batteries, metallurgy, gasoline, mining, and pigments damage to human health neurological damage, inducing anemia, nerve disorders, kidney disorder, physical growth impairments, memory loss and inhibition of brain developing existing in children [19–23]. However, all reports about the sensing properties of Pb^{2+} ions is only in basic condition that coordinate or substitute effectively for sensor Pb^{2+} ions [24–33]. The Pb^{2+} heavy poisoning could lead the irreversible harm to the growth of teenagers, cognitive development, fetal growth, psychological and behavioral [34–38]. The drinking water can limit to 10 ppm, according to the World Health Organization (WHO) [39]. Fluorescence chemosensors are interesting in the recognition of various anions, cations and different neutral molecules in number of fields including molecular devices, environmental sensors, biological probes, and detection of nerve gases due to their excellent properties as real-time detection, low cost, low detection limit, operational simplicity high sensitivity and selectivity and adaptability to different platforms [40–46]. The detection of fluorescence signal interacting with a chemical species in fluorescence probes occurs through [47] various mechanisms such as chelation-enhanced fluorescence (CHEF) [48], intramolecular charge transfer (ICT) [49], photoinduced electron/energy transfer (PET) [50], metal–ligand charge transfer (MLCT) [51], excited-state resonance energy transfer (FRET) [52], excimer/excimer formation [53], intramolecular and intermolecular proton transfer (ESIPT) [54] and C = N isomerization [55]. Schiff-base compounds can be used as fluorescence chemosensors due to simple synthesized procedure [56,57]. In this work we successfully designed fluorescence chemosensor for high sensitively and selectively of Cr^{3+} and Pb^{2+} for “turn-on” platform in aqueous media. Schiff-base-based fluorescent chemosensors, (*E*)-*N*-(1-(1*H*-phenothiazin-2yl)-

thylidene)-3-((*E*)-(2-phenylhydrazono)methyl)aniline was synthesized and characterized by FT-IR, ESI-MS, ^1H NMR, and ^{13}C NMR spectroscopy. The probe **AT** showed an excellent fluorescence enrichment towards Cr^{3+} and Pb^{2+} , and sensing mechanisms was proposed based on UV-Vis, Fluorescence titrations, ESI-mass spectrometry analysis, ^1H NMR titrations, molecular docking, living cell imaging, cytotoxicity, and DFT.

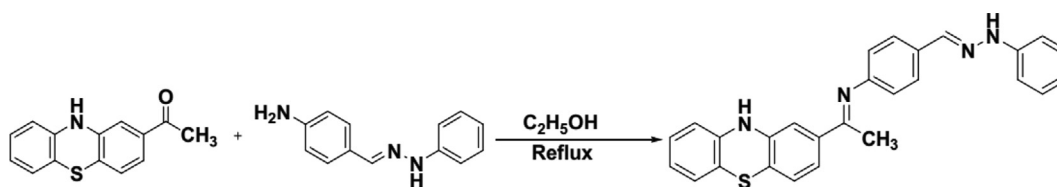
2. Experimental methods

2.1. Materials and instruments

All chemical compounds were purchased and used after purification. Distilled water was used for all experiments. The synthesized compound was characterized by using FT-IR, ^1H & ^{13}C NMR, and ESI-MS spectroscopy. Infrared measurement was made at 4000–400 cm^{-1} region on an Agilent Carry 630 FT-IR (Fourier Transfer Infrared) spectrometer. The ^1H NMR spectrum and ^{13}C NMR were recorded on a Bruker-400 MHz and TMS as an internal standard working in $\text{DMSO } d_6$, respectively. UV and fluorescence measurements were carried out with Perkin-Elmer LS45 fluorescence spectrophotometer at a scan rate of 1200 nm range at room temperature. A Varian RF-5310PC fluorescence spectrometer was used to record fluorescence at ambient temperature.

2.2. Synthesis of Schiff base AT

1-(10*H*-phenothiazin-8-yl)ethanone (0.48 g, 2 mmol) and 4-(*P*henyl-hydrazonomethyl)-phenylamine (0.42 g, 2 mmol) were dissolved in absolute ethanol and the refluxed for 24 under 60 °C atmosphere. Then, the reaction was confirmed by TLC plate with benzene solvent. This solution was poured in distil water and light yellow precipice appeared, and filter dried for 2 days. The sample was recrystallized from absolute ethanol and finally got the product **AT** shown in Scheme 1. Yield: 83%. FT-IR; (C = N) 1597 cm^{-1} , (NH) 3345 cm^{-1} . ^1H NMR (500 MHz, $\text{DMSO } d_6$) δ 10.14 (s, 1H), 8.06 (s, 1H), 7.30 (s, 1H), 7.284–7.282 (d, $J = 0.8$, 2H), 7.18–7.15 (m, $J = 9.2$, 4H), 7.093–9.055 (m, $J = 1.6$, 4H), 6.985–6.966 (d,



Scheme 1. Synthesis of compound AT.

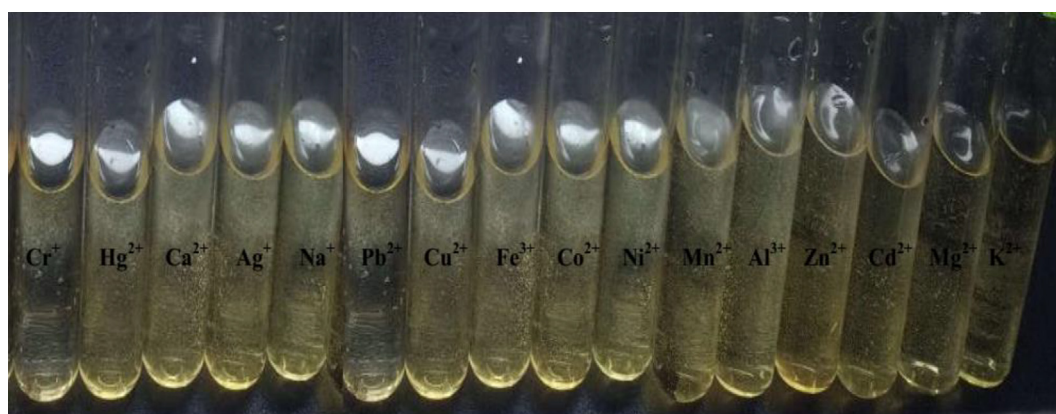


Fig. 1. The colourless of metal solution made in compound of AT.

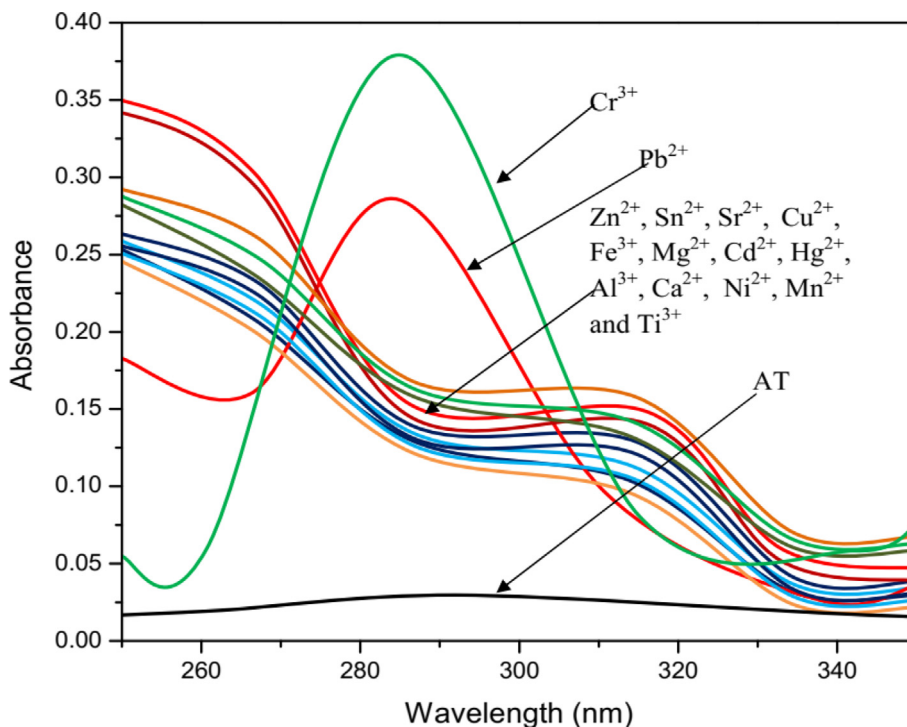


Fig. 2. Absorption spectrum of AT (100 μM) with different metal ion (100 μM) used in HEPES buffer solution in EtOH:H₂O (1:4, v/v) pH = 7.0.

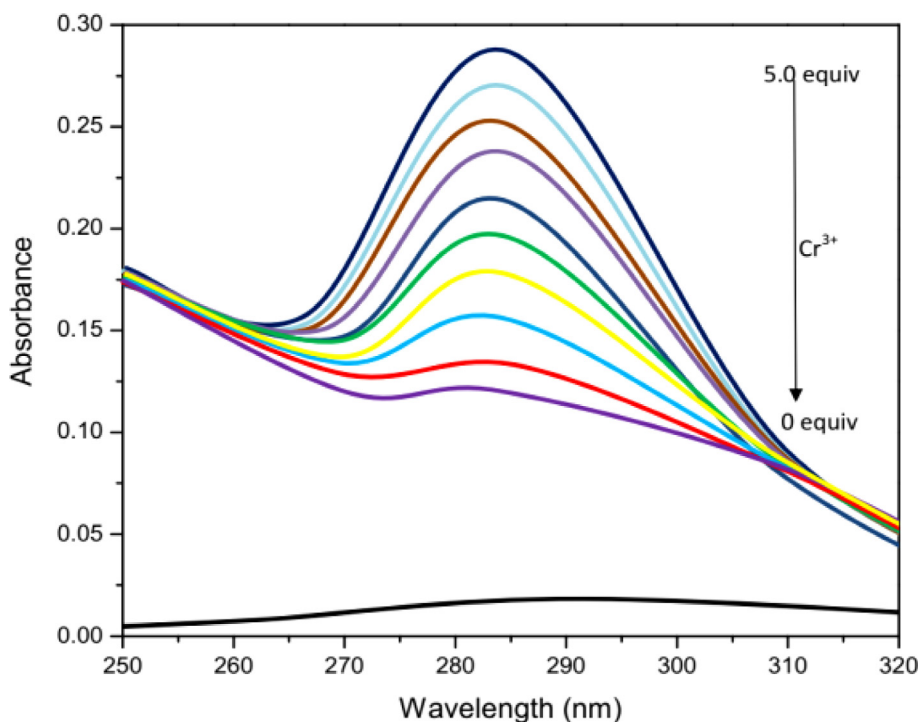


Fig. 3. UV-visible titration spectra of AT (10 μM) and in the presence of different concentrations of Cr³⁺ (10 μM) in ethanol.

$J = 7.6, 2H), 6.88 (s, 1H), 6.797-6.771 (m, J = 10.4, 4H), 6.644-6.605 (m, J = 15.4, 4H), 2.566-2.557 (t, J = 36, 3H)$. ¹³C NMR (100 MHz, DMSO *d*₆), δ (ppm): 196.88, 158.23, 157.15, 152.98, 146.25, 145.16, 141.59, 130.54, 129.18, 128.43, 118.33, 116.49, 115.26, 114.91, 111.41, 26.44. ESI-MS (m/z): calculated for C₂₇H₂₂N₄S [M + H]⁺: 434.1600; found: 435.2747.

2.3. UV-vis and fluorescence experimentation

The stock solutions (0.025 M) of different metal ions (nitrate or chloride salts) were prepared in distilled water. A 1×10^{-5} M stock solution of AT prepared in distilled water was used for spectroscopic studies. The absorption and fluorescence spectra

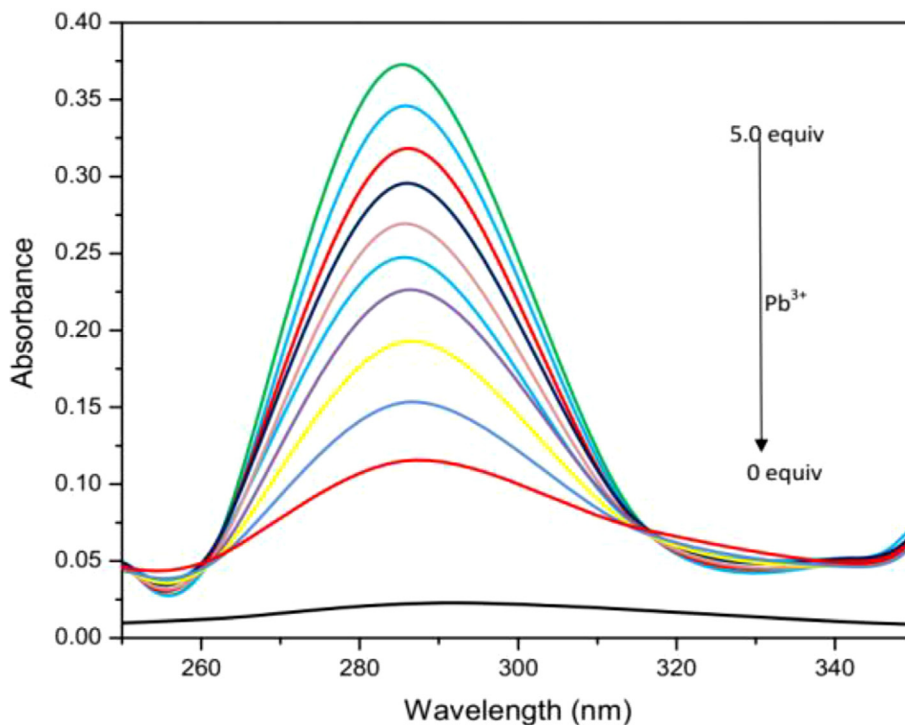


Fig. 4. UV-visible titration spectra of AT (10 μM) and in the presence of different concentrations of Pb²⁺ (10 μM) in ethanol.

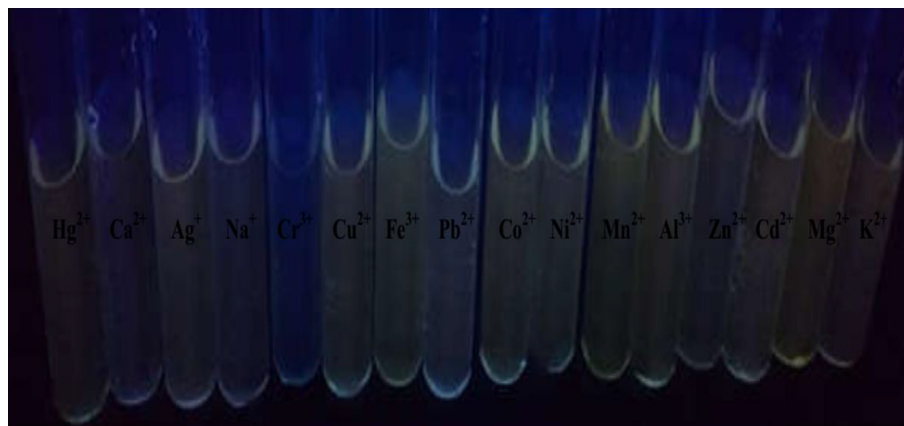


Fig. 5. The colourless of metal solution made in compound of AT.

measurements were carried out by using a 5 mL mixed solution of **AT** and metal ion in a quartz cell at room temperature. All fluorescence experiments were conducted upon excitation wavelength at 369 nm.

2.4. Cell culture

The human hepatocellular liver carcinoma cells (HepG2 cell lines) (NCCS, Pune, India) were grown in DMEM by addition of 10% of FBS and antibiotics (streptomycin-50 μg/mL; penicillin-100 μg/mL), at 37 °C, 5% CO₂ incubator, cells were produced at 95%.

2.5. Anticancer activity, cell viability assay

The cytotoxicity of **AT** was tested using a 3-(4, 5-dimethylthiazole-2-yl)-2, 5-diphenyl tetrazolium bromide (MTT) assay against HepG2 cell lines. Cells were seeded onto a 96-well plate at a cell density per dis 1.5×10^4 and incubated at varying

concentrations from 1.5 to 500 μM to last 48 h in a medium containing **AT**. Triplicate wells with 100 μL of MTT added to each well are retained for each operation. It was incubated at 37 °C for 4 h, allowing MTT reaction and metabolically active cells to form crystals of formazan. The medium for MTT was cautiously discarded from the wells. To extract intracellular formazan crystals, 100 μL of DMSO was applied to each well and the dishes shaken for 10 min. Using ELISA, at 428 nm, the absorbance was readouts. Using a fluorescent microscope, the photographs of the cells were analyzed. The survival percentage was determined using formula: %survival = [live cell number (test)/live cell number (control)] × 100.

2.6. Fluorescence microscopic study

For in-vitro fluorescence imaging of **AT**, the cells were seeded in a 35 mm culture dish at a density of 3×10^5 cells per dish. After completion, 60% confluence for fluorescence microscopy was

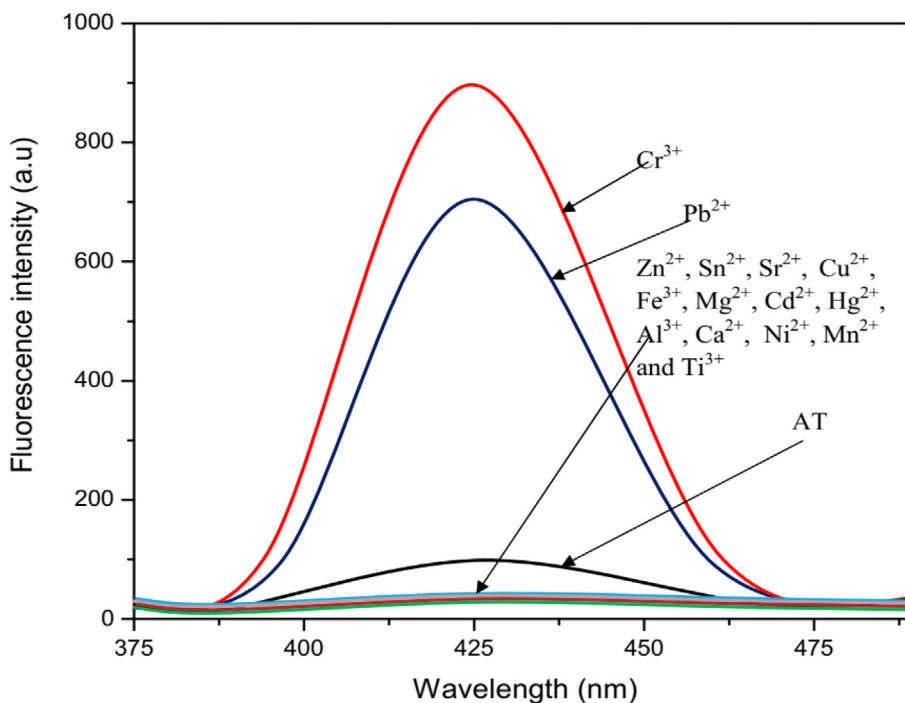


Fig. 6. Fluorescence spectrum of AT (100 μM) with different metal ion (100 μM) used in 10 mM HEPES buffer solution in EtOH: H₂O (1:4, v/v) pH = 7.0.

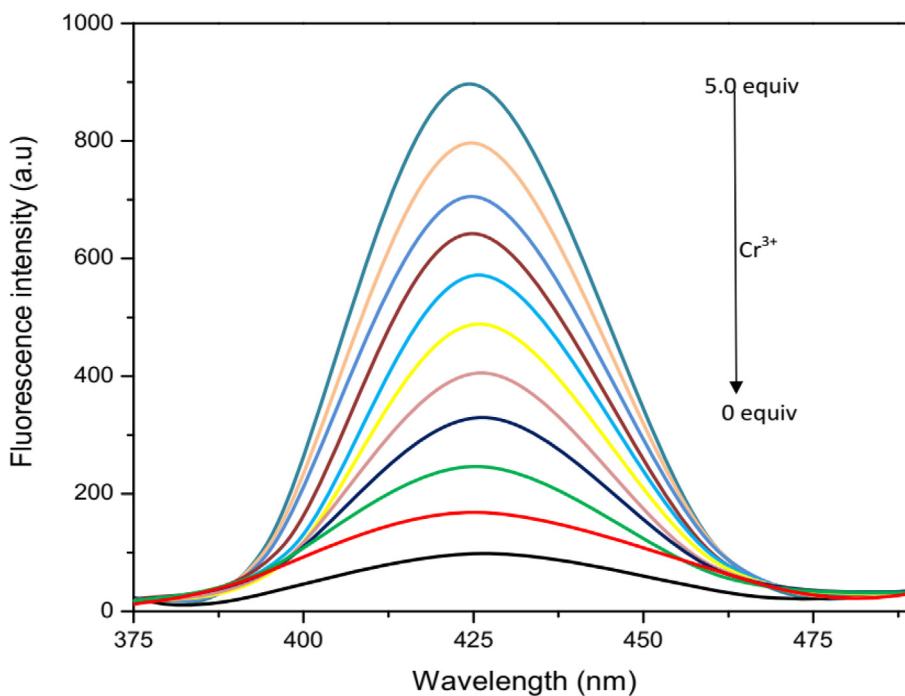


Fig. 7. Fluorescence titration spectra of AT (20 μM) in the presence of different concentrations of 0.5 equiv. Cr³⁺ (20 μM) in ethanol.

replaced by mercury nitrate and zinc nitrate (0.3 μM and 0.5 μM) augmented with the serum to absorb Cr³⁺/Pb²⁺ ions by 40-hours developing cells, **AT** (5.0 μM), dissolved in DMSO/H₂O (99/1), in addition to new media to allow **AT** to be absorbed by cells to form the Cr³⁺/Pb²⁺ - **AT** complex. Under a fluorescence microscope, both excitations of Cr³⁺/Pb²⁺ ions were trypsinized and examined for **AT** images at 428 nm using a 10x fluorescent target. The bright and Fluorescence field knowledge was obtained using the fluorescence microscope 40x-Olympus FV1000-LX81.z, Camedia software, and

Adobe Photoshop version 10.0 processed using. For the control trial, the media was stripped off Cr³⁺/Pb²⁺ ions.

3. Results and discussion

As shown in [Scheme 1](#), Schiff base compounds based on the fluorescent chemosensor **AT** *E-N*-(1-(1H-phenothiazin-2yl)-ethylidene)-3-((E)-(2-phenylhydrazono)methyl)aniline were designed

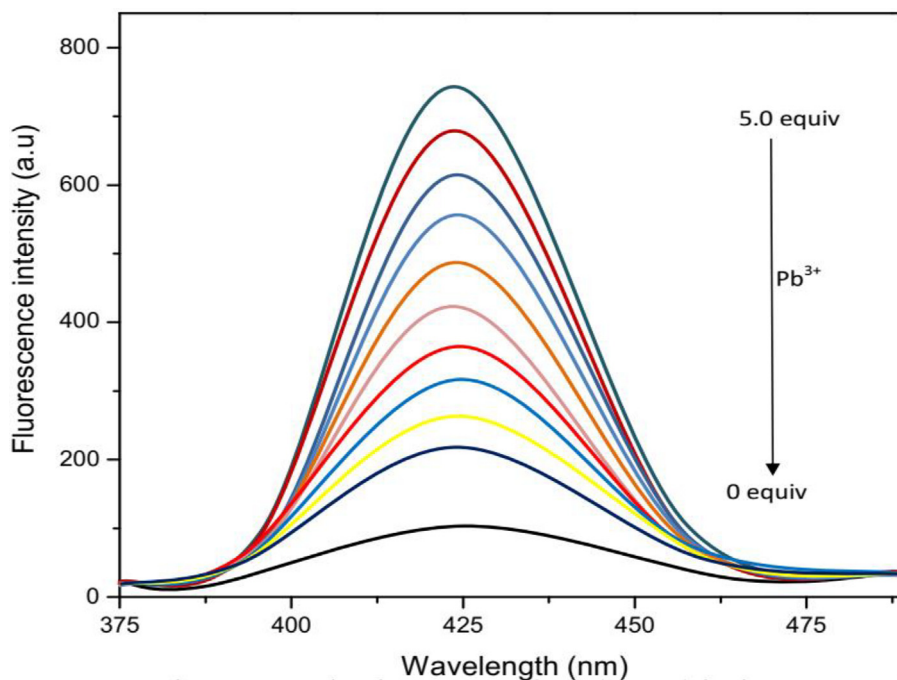


Fig. 8. Fluorescence titration spectra of AT (20 μM) in the presence of different concentrations of 0.5 equiv Pb^{3+} (20 μM) in ethanol.

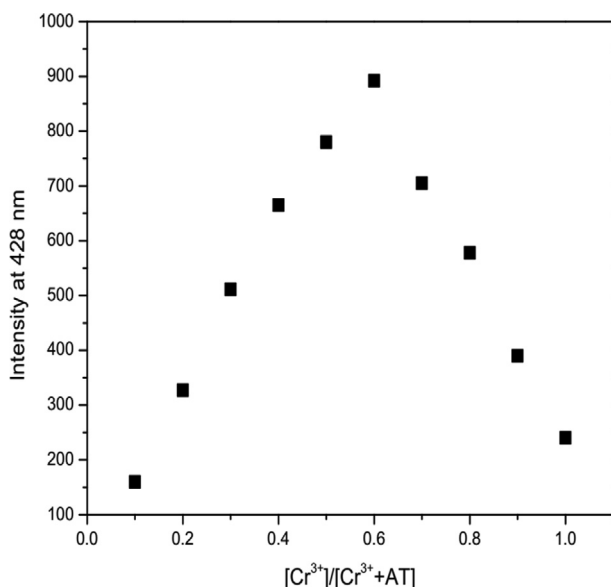


Fig. 9. Job's plot of AT (20 μM) solution with Cr^{3+} (20 μM) ion.

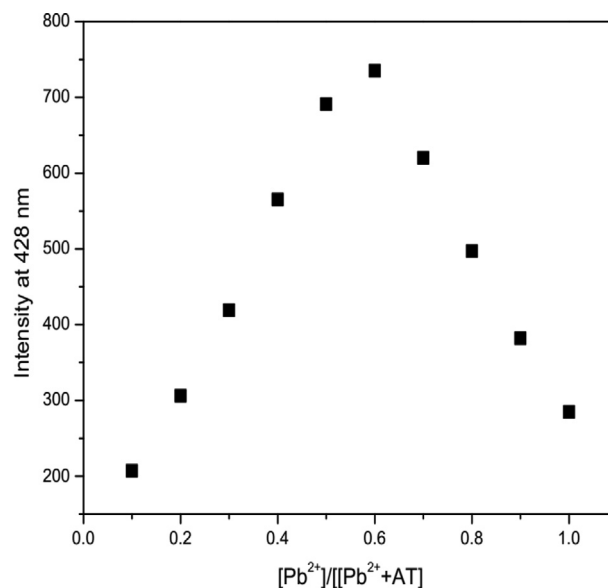


Fig. 10. Job's plot of AT (20 μM) solution with Pb^{2+} (20 μM) ion.

and characterized by FT-IR, ESI-MS, ^1H and ^{13}C NMR spectroscopic methods. Further studies namely UV-vis and fluorescence microscopy were performed HEPES buffer solution in EtOH: H_2O (1:4, v/v, pH = 7.0) and under excitation wavelength at 290 nm. The fluorescence intensity at 428 nm was measured for sensitivity and selectivity of Cr^{3+} and Pb^{2+} ions.

3.1. Absorption studies

The sensing behavior of AT ($1.0 \times 10^{-5} \text{ M}^{-1}$) towards various metal ions such as Zn^{2+} , Sn^{2+} , Sr^{2+} , Cu^{2+} , Fe^{3+} , Mg^{2+} , Cr^{3+} , Cd^{2+} , Hg^{2+} , Al^{3+} , Ca^{2+} , Ni^{2+} , Mn^{2+} , Pb^{2+} , and Ti^{3+} ($1.0 \times 10^{-3} \text{ M}^{-1}$) have been studied in HEPES buffer solution in EtOH: H_2O (1:4, v/v, pH = 7.0) investigated by UV-Vis absorption spectroscopy in 100% aqueous

solution. The AT solution exhibited yellow color to colorless solution in the naked eye under UV-Vis lamp (Fig. 1) in the presence of two alkali metal ions (Ca^{2+} , Mg^{2+}), one alkali earth metal ion (Mg^{2+}), and transition metal ions (Ag^+ , Cu^{2+} , Fe^{3+} , Co^{2+} , Ni^{2+} , Mn^{2+} , Zn^{2+} , Cd^{2+} , and Mg^{2+}). The AT solution demonstrated a strong absorption band around 284 nm observed due to π - π^* electronic transition with detection of Cr^{3+} and Pb^{2+} and without any interference by other metal ions. When AT (100 μM) solution was added into different metal ion (100 μM) solutions showed a new absorption band centred at 315 nm observed by blue (hypsochromic) shift and absorption peaks at 284 nm shown in hyperchromic shift (Fig. 2) The Cr^{3+} and Pb^{2+} (10 μM) solutions was added incrementally to AT (10 μM) in HEPES buffer solution in EtOH: H_2O (1:4, v/v, pH = 7.0) (Fig. 3 and Fig. 4). Then gradually the absorbance

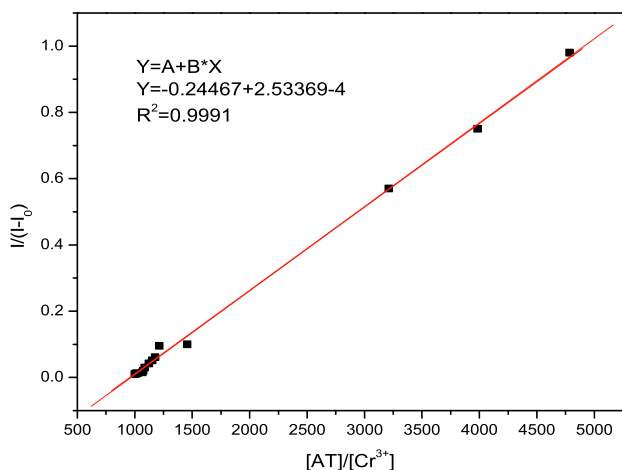


Fig. 11. Benesi-Hildebrand equation of AT (10 mM) with different concentration Cr³⁺ (10 mM) ion used in 10 mM HEPES buffer solution in EtOH:H₂O (1:4, v/v) pH = 7.0.

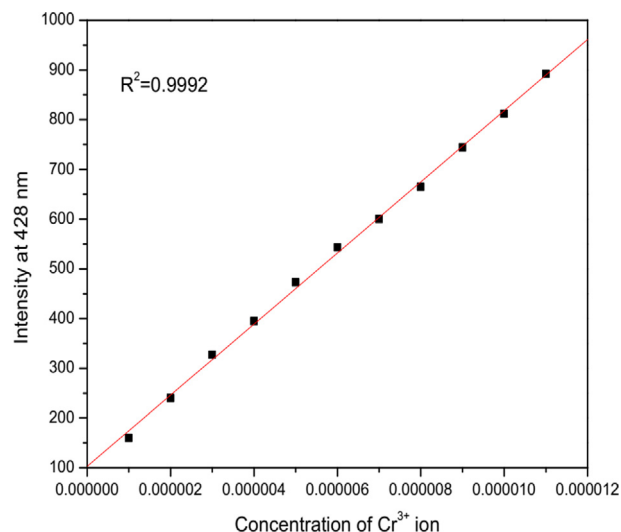


Fig. 13. Detection limit of AT (10 μM) with different Cr³⁺ (10 μM) used in 10 mM HEPES buffer solution in EtOH:H₂O (1:4, v/v) pH = 7.0.

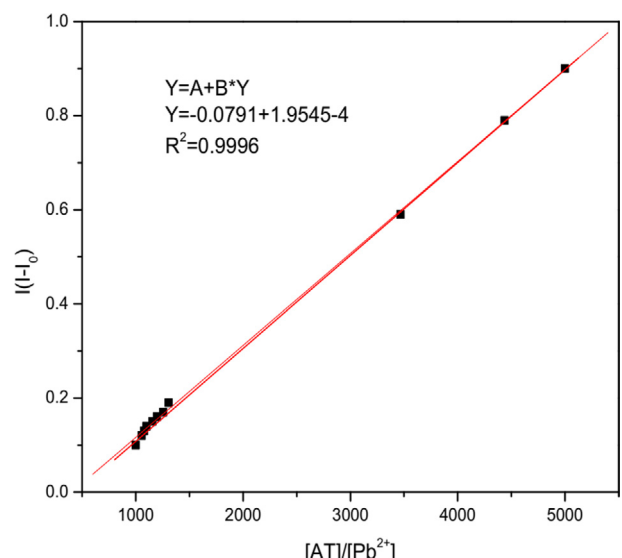


Fig. 12. Benesi-Hildebrand equation of AT (10 μM) with different concentration Pb²⁺ (10 μM) ion used in 10 mM HEPES buffer solution in EtOH:H₂O (1:4, v/v) pH = 7.0.

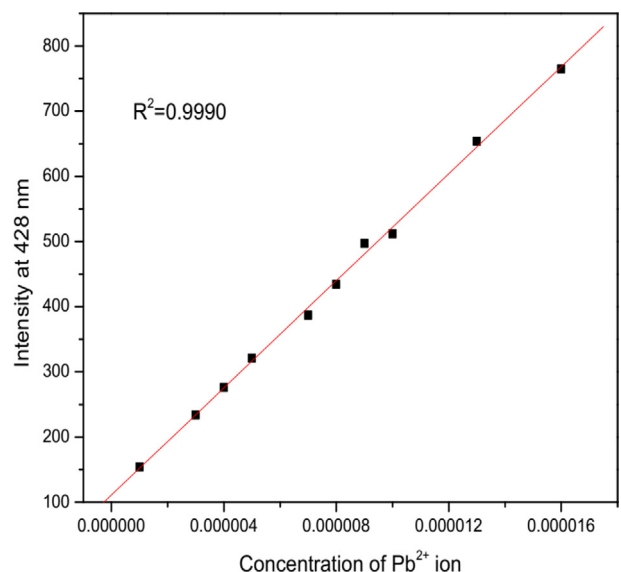


Fig. 14. Detection limit of AT (10 μM) with different Pb²⁺ (10 μM) used in 10 mM HEPES buffer solution in EtOH:H₂O (1:4, v/v) pH = 7.0.

intensity at 315 nm was decreased after increasing concentration of 0, 0.5, 1.0, 1.5, 2.0, 2.5, 3.0, 3.5, 4.0, 4.5, and 5.0 of Cr³⁺ and Pb²⁺. For Pb²⁺, two isobestic points at 260 and 317 nm were noticed depending on the increased concentration of Pb²⁺.

3.2. Emission studies

The fluorescence measurements were carried out with excitation wavelength at 290 nm AT (1.0 × 10⁻⁵ M⁻¹) and metal ions (1.0 × 10⁻⁶ M⁻¹) in (10 mM) HEPES buffer solution of EtOH: H₂O (1:4, v/v, pH = 7.0) in 100% aqueous solutions. The pale yellow solution of AT changed to light blue for Cr³⁺ ions and colorless for Pb²⁺ ions (Fig. 5). The probe AT (100 μM) solution exhibited enormously weak fluorescence intensity at 428 nm and significantly changed due to role as for dual chemosensor for Cr³⁺ (100 μM) and Pb²⁺ (100 μM) were shifted to longer wavelength due to bathochromic shift (Fig. 6). Other metal ions had no influence on the

emission intensity. The highly sensitive and selective detection of Cr³⁺ and Pb²⁺ was determined by “turn-on” fluorescence performed in a 100% aqueous solution. This is possibly due to PET (Photoinduced Electron Transfer) mechanism. Upon addition of 5.0 equiv. of Cr³⁺ and Pb²⁺ (20 μM) to AT (20 μM) solution displayed fluorescence enhancement at 428 nm and was successively decreased after adding higher conc. of Cr³⁺ and Pb²⁺ metal ion (Fig. 7 and Fig. 8). The job plot was constructed by probe AT binding with Cr³⁺ and Pb²⁺, 1:1 stoichiometry complex (0.5 equiv. of Cr³⁺ and Pb²⁺ with AT (0.5 equiv.)) has been predicted as 0.6 μM concentration (Fig. 9 and Fig. 10). The binding constant of AT (10 μM) with Cr³⁺ and Pb²⁺ (10 μM) was calculated using fluorescence titration data and found to be 2.13 × 10⁴ M⁻¹ (R² = 0.9991) and 2.37 × 10⁴ M⁻¹ (R² = 0.9996) according to Benesi-Hildebrand equation (Fig. 11 and Fig. 12). Furthermore, the detection limit was 8.63 × 10⁻⁷ M (R² = 0.9992) and 7.42 × 10⁻⁷ M (R² = 0.9990) towards using this equation 3σ/k (Fig. 13 and Fig. 14) [58,59]. Consequently, the performance of AT to WHO (World Health Orga-

nization) allowed different concentrations of Cr^{3+} and Pb^{2+} in (7.4 μM) in drinking water. Different metal ions (0.5 equiv of Sn^{2+} , Sr^{2+} , Cu^{2+} , Fe^{3+} , Mg^{2+} , Cr^{3+} , Cd^{2+} , Hg^{2+} , Al^{3+} , Ca^{2+} , Ni^{2+} , Mn^{2+} , Pb^{2+}

and Ti^{3+}) were added into AT (10 μM) solution of 20 mM of HEPES buffer solution in EtOH:H₂O (1:4, v/v, pH = 7.0) in 100% aqueous solutions (Fig. 15 and Fig. 16). The emission intensity at 428 nm

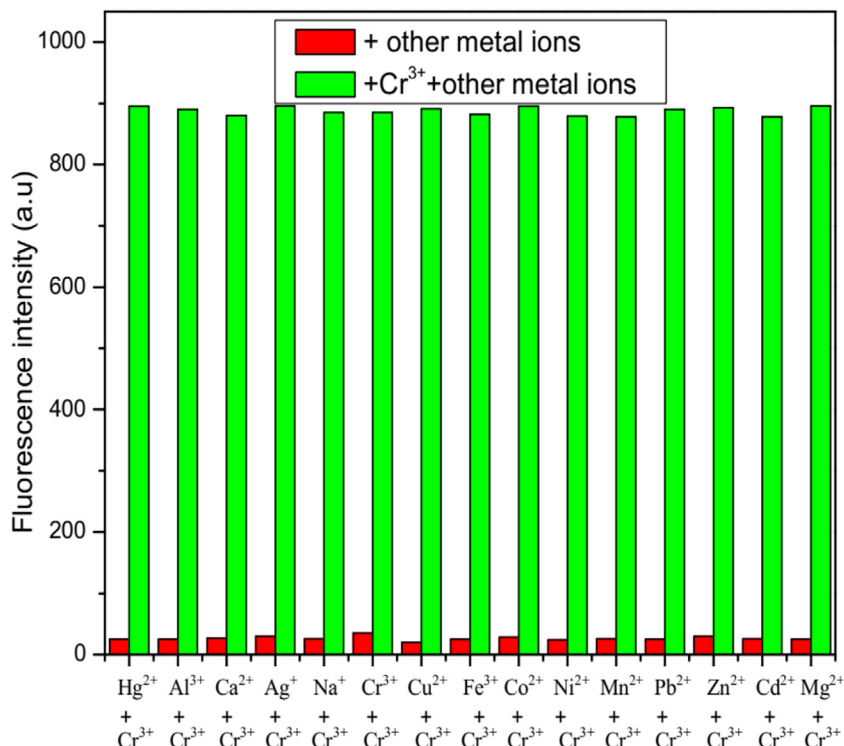


Fig. 15. The fluorescence changes of AT (10 μM) with Cr^{3+} (5 equiv.) and upon addition of Hg^{2+} , Al^{3+} , Ca^{2+} , Ag^+ , Na^+ , K^+ , Cu^{2+} , Fe^{3+} , Co^{2+} , Ni^{2+} , Mn^{2+} , Pb^{2+} , Zn^{2+} , Cd^{2+} , and Mg^{2+} were prepared in 20 mM of HEPES buffer solution EtOH:H₂O (1:4, v/v) pH = 7.0.

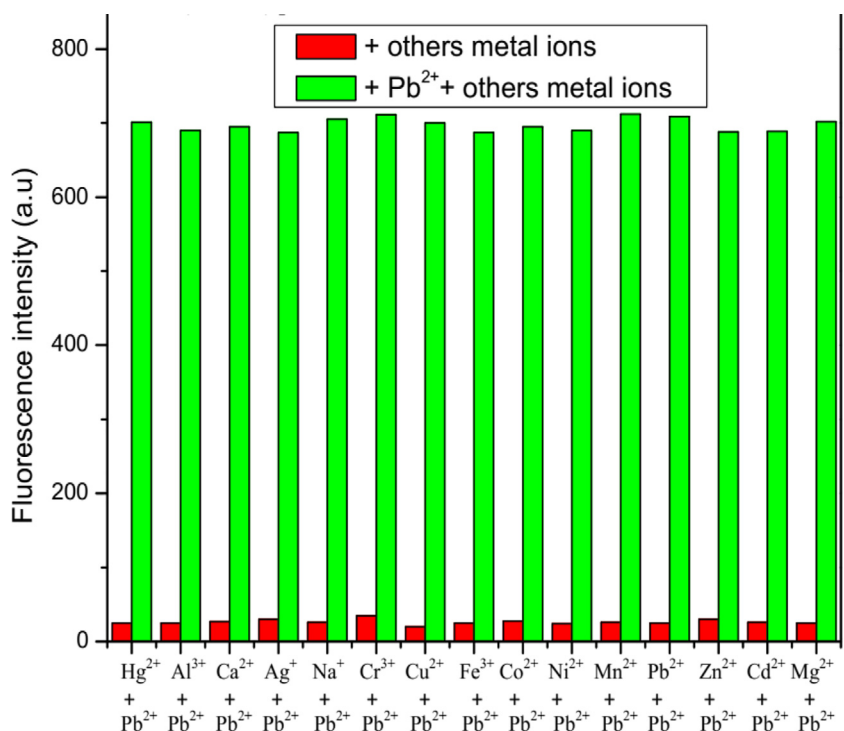
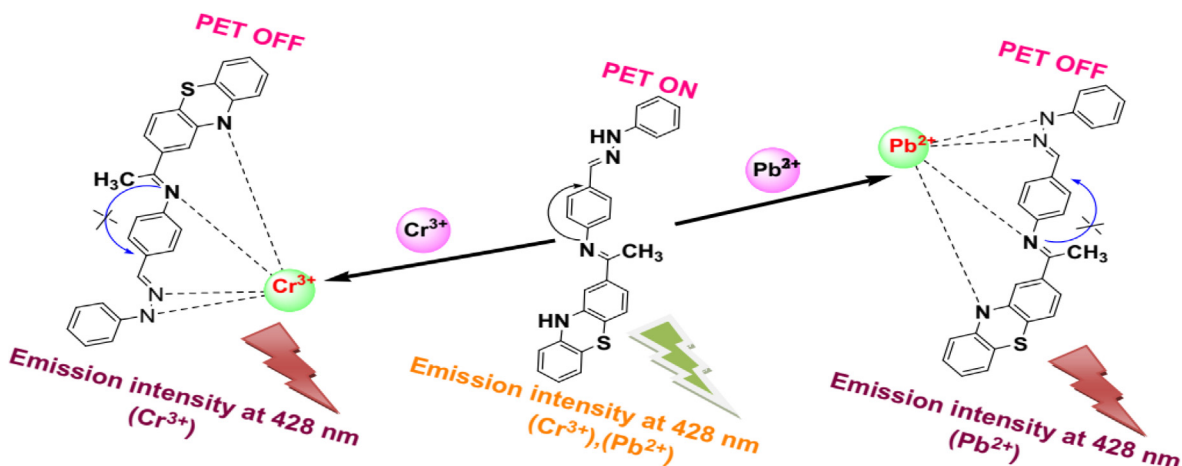
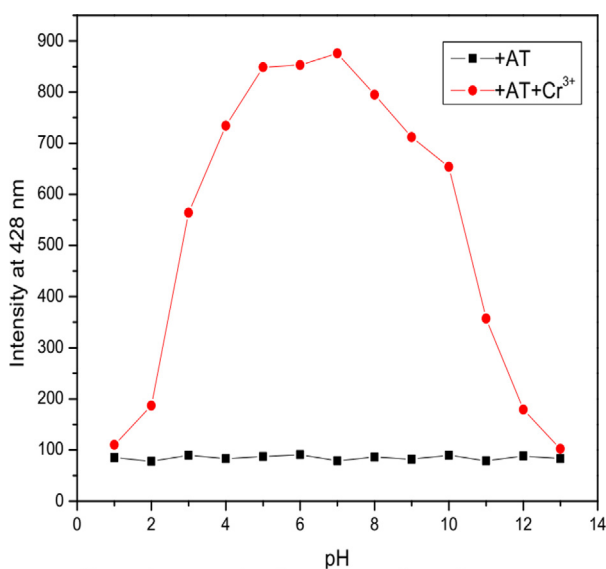
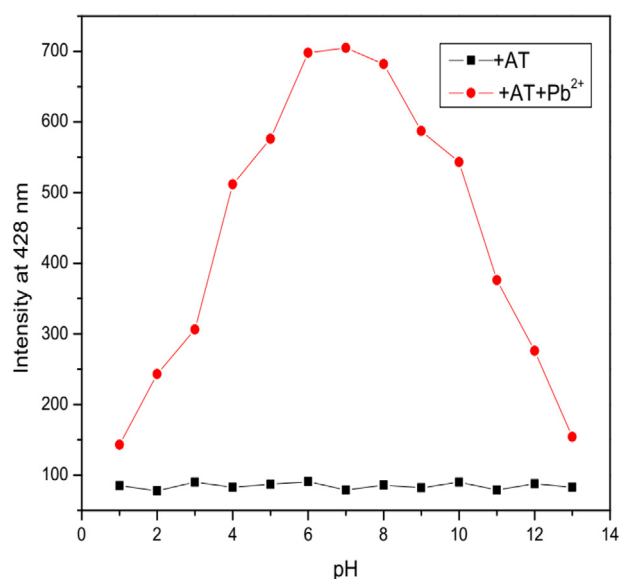


Fig. 16. The fluorescence changes of AT (10 μM) with Pb^{3+} (5 equiv.) and upon addition of Hg^{2+} , Al^{3+} , Ca^{2+} , Ag^+ , Na^+ , K^+ , Cu^{2+} , Fe^{3+} , Co^{2+} , Ni^{2+} , Mn^{2+} , Pb^{2+} , Zn^{2+} , Cd^{2+} , and Mg^{2+} were prepared in 20 mM of HEPES buffer solution EtOH:H₂O (1:4, v/v) pH = 7.0.

Scheme 2. Synthesis of compound AT-Cr³⁺ and Pb²⁺ ions.Fig. 17. Effect of pH on the fluorescence intensity at 428 nm of AT (10 μ M) in 2 M aqueous solution in the presence of Cr³⁺.Fig. 18. Effect of pH on the fluorescence intensity at 428 nm of AT (10 μ M) in aqueous solution in the presence of Pb²⁺.

for 0.3 equiv of Cr³⁺ and Pb²⁺ shows high values, however, the presence of Cr³⁺ and Pb²⁺ binding with others metal ions did not affect the sensing ability of AT (10 μ M) against Cr³⁺ and Pb²⁺.

3.3. Binding mechanism

The fluorescence results indicated photoinduced electron transfer (PET) pathway, and it was caused by the stable complex formation AT-Cr³⁺ and AT-Pb²⁺ via complex formation involving imine bond -CH=N- and NH resulting due to contribution of lone pairs of imine nitrogen which inhibited PET process. Further, after binding complex Cr³⁺ and Pb²⁺ to AT, C=N isomerization and the photoinduced electron transfer (PET) effect were hindered [60,61]. Enhancement of the fluorescence intensity for Cr³⁺ and Pb²⁺ can be explained by PET-ON to PET-OFF with binding. The ESI-mass spectrum confirmed by binding complex and exact molecular weight present at 485.32 m/z shifted from 434.16 m/z after adding 0.5 equiv of Cr³⁺ into AT solution, whereas, after added 0.5equiv. Pb²⁺ concentration into AT solution, which provided value at 640.43 m/z , however, it was changed and enormous shifted due to the normal mass value at 434.16 m/z , therefore -CH=N- and

NH group much potentially participated in complexation of AT-Cr³⁺ and AT-Pb²⁺ as in Scheme 2.

3.4. Effect of pH

The scope of chemosensor would be much affected by pH value sensing capability Hence it is necessary to suitably increment pH value in AT solution to detect Cr³⁺ and Pb²⁺ very efficiently. This is revealed in (Fig. 17 and Fig. 18). Over the pH range of 1–13, AT solution of Cr³⁺ and Pb²⁺ shows no significant change. The changes in fluorescence intensity under strong acid condition indicates inhibition of complex formation between AT and Cr³⁺ and Pb²⁺ ions due to protonation of Schiff base compound AT. Whereas, under the strong basic condition the formation complexes of AT binding with Cr³⁺ and Pb²⁺ prove was inhibited because of sufficiently methyl atom is performed. However, AT exhibited great sensing action to Cr³⁺ and Pb²⁺ over the pH range from 4 to 10, and may successfully detect Cr³⁺ and Pb²⁺ in sensible applications in this large pH range.

3.5. Reversibility study

The reversible response is important for a suitable fluorescent chemosensor. The fluorescence spectrum of **AT** (10 μM) solution with an alternating increase of 3 equiv. of Cr^{3+} and Pb^{2+} and EDTA solution in $\text{EtOH}:\text{H}_2\text{O}$ (1:4, v/v, pH = 7.0, 10 mM HEPES buffer) was measured. The emission intensity measured at 436 nm in 100% aqueous solu-

tions, upon addition and it was restored on addition of Cr^{3+} and Pb^{2+} solution to **AT**. Moreover, the fluorescence ON-OFF-ON responsibility upon alternate addition of Cr^{3+} and Pb^{2+} to EDTA solution of **AT** under the UV lamp 365 nm was reversible and could be used and the reversible cycle for at least four times (Fig. 19 and Fig. 20). Thus, **AT** can be used as an excellent reversible fluorescent chemosensor detecting Cr^{3+} and Pb^{2+} in 100% aqueous solution.

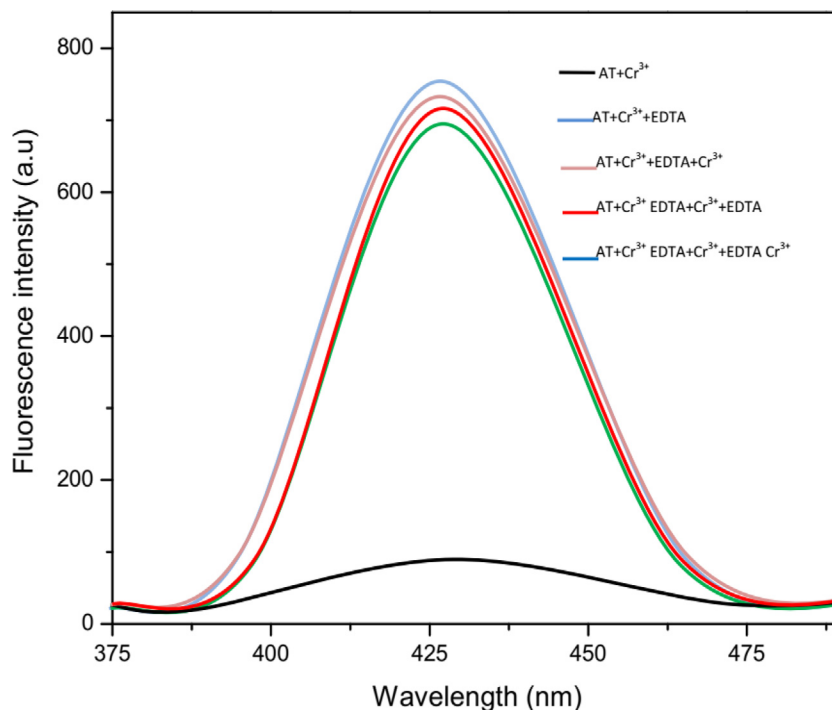


Fig. 19. Fluorescence spectrum of AT (10 μM) solution upon addition of Cr^{3+} (3 equiv.) and EDTA (3 equiv.) in HEPES buffer solution $\text{EtOH}:\text{H}_2\text{O}$ (1:4, v/v).

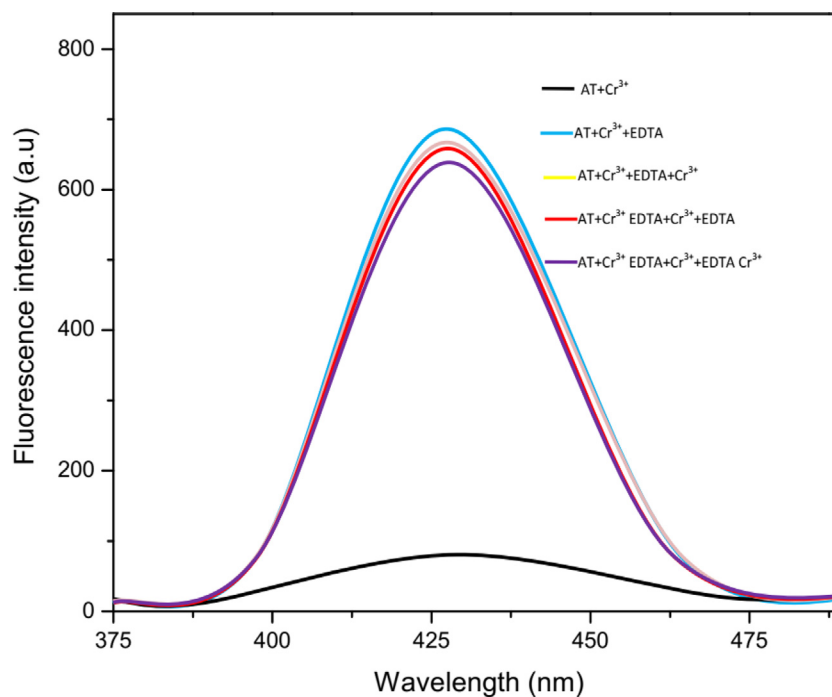


Fig. 20. Fluorescence spectrum of AT (10 μM) solution upon addition of Pb^{2+} (3 equiv.) and EDTA (3 equiv.) in HEPES buffer solution $\text{EtOH}:\text{H}_2\text{O}$ (1:4, v/v).

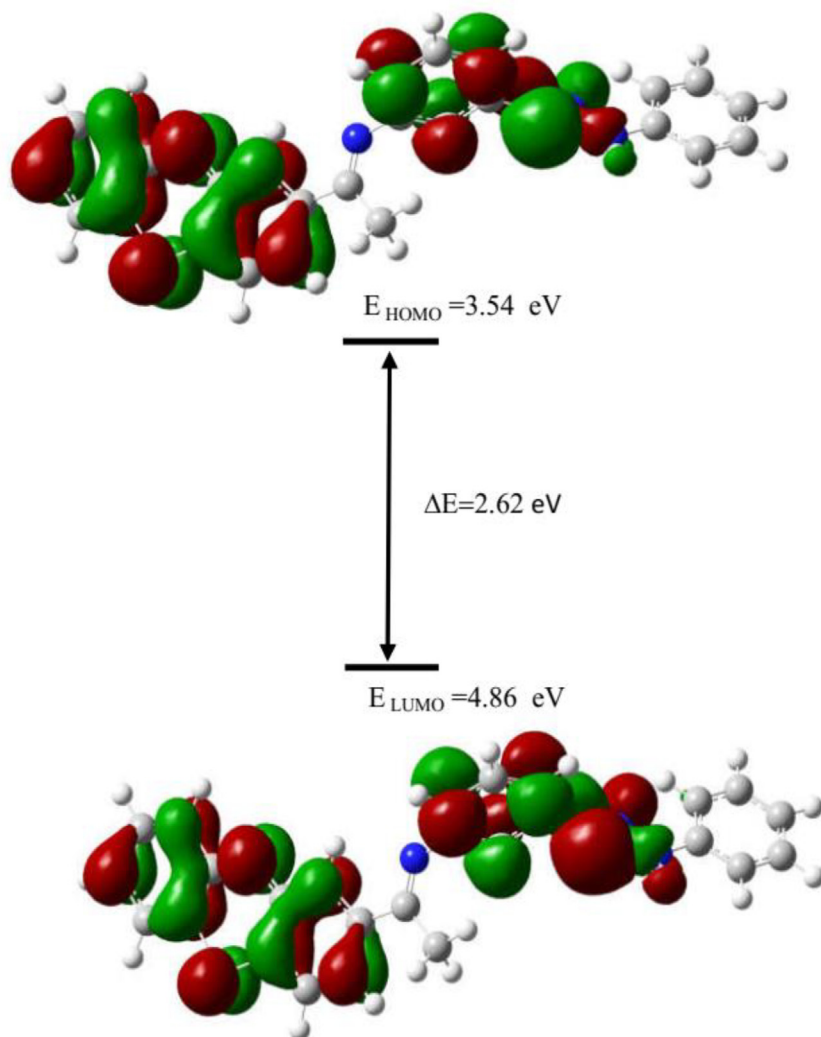


Fig. 21. Energy diagram of HOMO and LUMO orbital of AT and its corresponding metal complexes calculated at the DFT level using a B3LYP/6-31G* basis set.

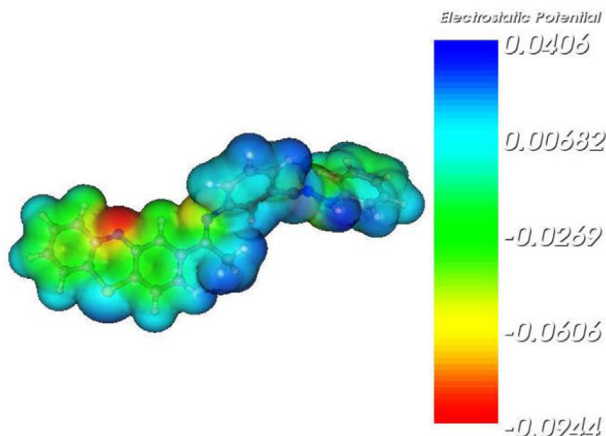


Fig. 22. Molecular electrostatic potential surface of AT.

3.6. Theoretical studies

3.6.1. HOMO and LUMO analysis

The theoretical calculation studies HOMO-LUMO predict the energy gap value investigated in Gaussian 09. HOMO energy means

that the electron-donating ability, whereas, LUMO means that electron-accepting ability for the HOMO-LUMO energy gap as shown in Fig. 21. The calculated lowest energetic gap is ($\Delta E_{\text{gap}} = 2.62$ eV), while the HOMO energy is ($E_{\text{HOMO}} = -3.54$ eV) and the lowest LUMO energy is ($E_{\text{LUMO}} = -4.38$ eV), Therefore, higher energy allowed the greatest electron donor and electron acceptor respectively, and HOMO and LUMO has two parameters and which is related to the orbital energy.

3.6.2. Molecular electrostatic potential (MEP) and Mulliken charge

Molecular electrostatic potential (MEP) is sensitive to the charge distribution and depends on the name of electrophilic and nucleophilic reaction. The MEP commonly is used to study hydrogen bonding interaction and even biological detection. The surface complex shows different energy of the molecular electrostatic potential. The result of AT expressed increase with potential order blue > green > yellow > red, where blue color is the highest electrostatic potential energy, red color is the lowest electrostatic potential energy and green color is neutral stability as shown in Fig. 22. The Mulliken charge calculations carried out by computational chemistry are shown in Fig. 23, C19 atom is the highest atomic molecular orbital, N10 is the lowest atomic molecular orbital due to decreased atomic charge and all molecular orbital range is C2 to C25 (Fig. 23).

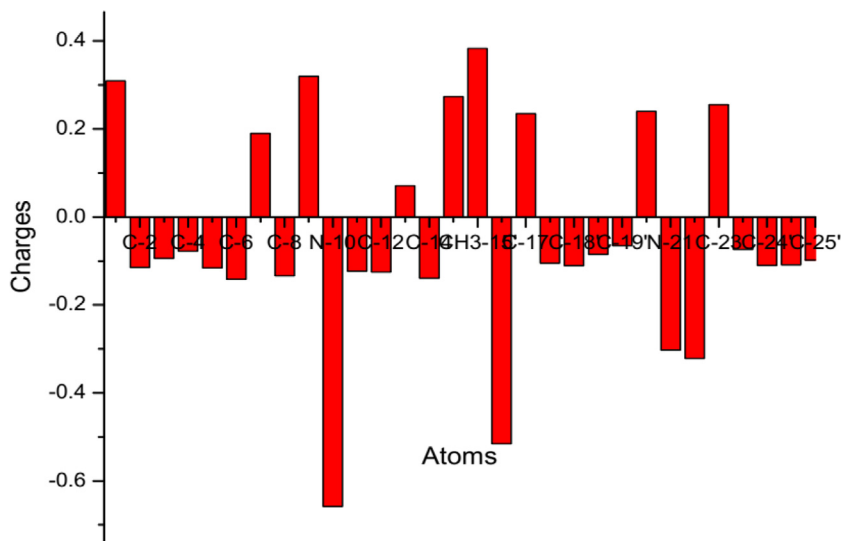


Fig. 23. Mulliken atomic charges for AT.

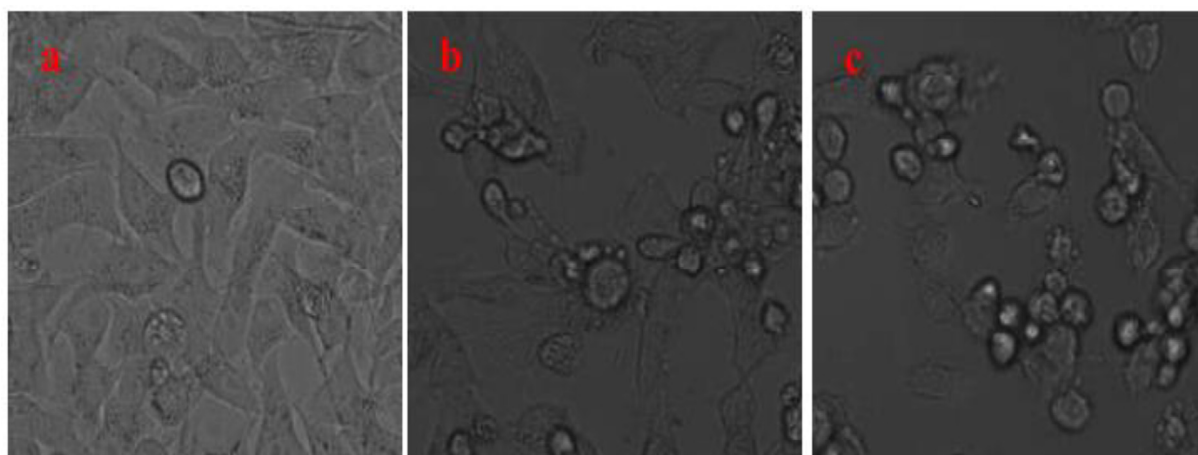


Fig. 24. Live cell images of AT: (a) before and (b and c) after treatment with AT examined by fluorescence microscopy.

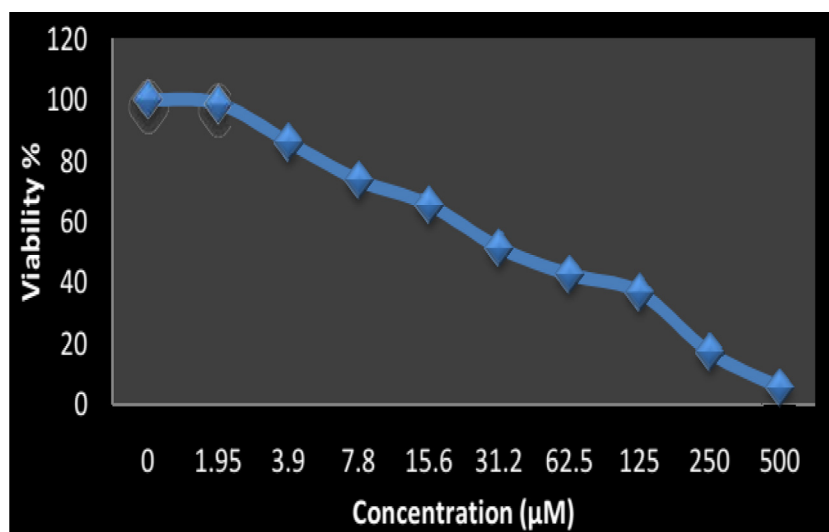


Fig. 25. The IC₅₀ values of AT against HepG2 cell lines.

Table 1
The IC₅₀ values of AT against HepG2 cell lines.

Anticancer effect of AT on HepG2 cell line	
Concentration (μM)	Viability %
AT	
0	100
1.95	98.81
3.9	86.15
7.8	73.66
15.6	65.59
31.2	51.45
62.5	42.67
125	36.77
250	17.11
500	5.45

3.7. Cytotoxicity

The cytotoxicity responses of AT were studied with various concentrations. This is evident from cellular imaging. Thus, these results show AT as an efficient candidate under intracellular concentration for certain biological conditions and justify its cytotoxic effect and MTT assay in AT-treated HepG2 cancer cells for up to 5 h. The 20 μM concentrations of AT demonstrated important cyto-

toxic effects at least up to 4 h on HepG2 cells. The synthesized AT was investigated for cytotoxic activity using the cell line HepG2 in the MTT study, which tests the impact of cellular mitochondrial metabolism on complexes. Tested compounds of ever-increasing concentrations with two days for cells tested. Microscopic images of cancer control cells and morphological changes apoptotic in the AT-treated HepG2 cell line presented in Fig. 24. The tests showed limited cell death at compound AT. At 77% of IC₅₀ values, the demonstrated good inhibition on the HepG2 cell. The AT-IC₅₀ values (Fig. 25) show that an inhibitory action against cancer cells is more potent. The NH group that carries the phenyl group shows the highest IC₅₀ value, convincing us that the electronic effect may be one of the determinants of anticancer activity in the compound AT. The IC₅₀ values of AT against HepG2 cell lines are given in Table 1.

3.8. Living cell imaging

The AT chemosensor is also being tested for imagery of living cells. First, a strong AT fluorescence view of HepG2 cell-incubated human liver cancer cells (Fig. 26). The overlap of fluorescence and the picture of the bright field reveal the emission of fluorescence within the intracellular region. Good cell membrane

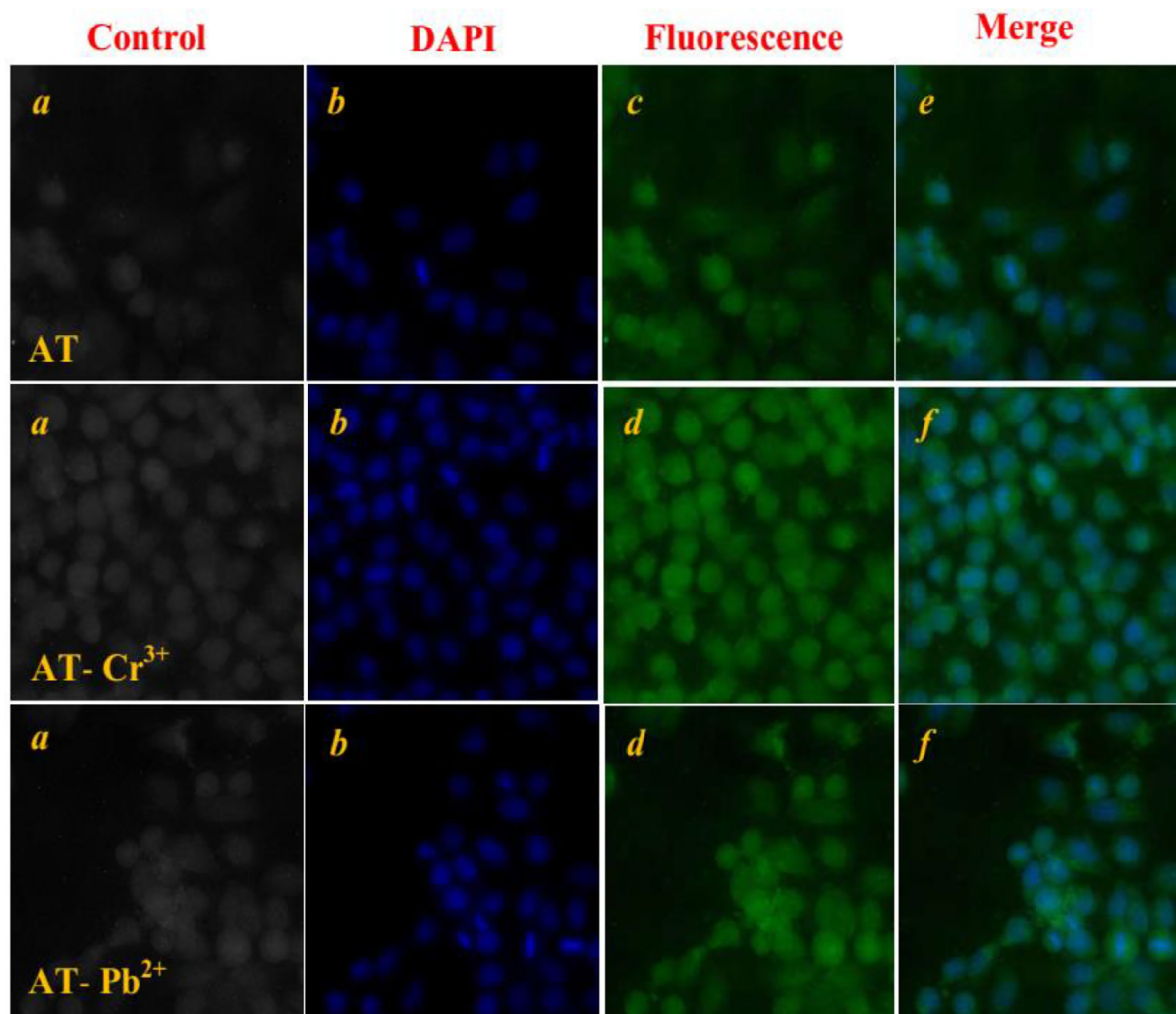


Fig. 26. Confocal fluorescence and merged images of HepG2 cells were stained with DAPI, AT-Cr³⁺ and AT-Pb²⁺, respectively. (a) HepG2 cells incubated with AT-Cr³⁺ and AT-Pb²⁺ (5 μM) only, (b) HepG2 cells pre-incubated with AT-Cr³⁺ and AT-Pb²⁺ (5 μM) followed by 0.1 mM AT, (c) cells were stained with both DAPI and 5 μM AT-Pb²⁺ and AT-Cr³⁺; (d) cells of (c) further incubated with AT (0.1 mM) for another 30 min, (e) and (f) were merged images. Scale bar, 30 μm.

permeability was noted for the chemosensor **AT**. The visualization of fluorescence of living cells followed additional treatment with $\text{Cr}^{3+}/\text{Pb}^{2+}$ ions. These observations suggest an efficient binding of chemo-sensors with **AT** to $\text{Cr}^{3+}/\text{Pb}^{2+}$ ions.

4. Conclusion

In summary, the fluorescent chemosensor has been successfully designed and we synthesized a simple Schiff-base of (E)-N-(1-(1H-phenothiazin-2yl)-ethylidene)-3-((E)-(2-phenylhydrazono)methyl) aniline and studied their PET mechanisms. The experiments indicated report chemosensor **AT** was a highly sensitive and selective chemosensor for Cr^{3+} and Pb^{2+} in a HEPES buffer solution in EtOH: H_2O (1:4, v/v, pH = 7.0). Significantly, the probe showed a “turn-on” fluorescence response to Cr^{3+} and Pb^{2+} and emission intensity at 428 nm (excitation wavelength 290). The fluorescence improvement with high selectivity and sensitivity was attributed to photoinduced electron transfer (PET) and also competitive metal studies. The Job plot of **AT** binding with Cr^{3+} and Pb^{2+} demonstrated a 1:1 stoichiometry complex predicted at 0.6 μM concentration. Further, the binding constant was calculated and found to be $2.13 \times 10^4 \text{ M}^{-1}$ ($R^2 = 0.9991$) and $2.37 \times 10^4 \text{ M}^{-1}$ ($R^2 = 0.9996$) according to the Benesi-Hildebrand equation and detection limit at $8.63 \times 10^{-7} \text{ M}$ ($R^2 = 0.9992$) and $7.42 \times 10^{-7} \text{ M}$ ($R^2 = 0.9990$) towards using this equation $3\sigma/k$ due to WHO (World Health Organization) allowed (7.4 μM) in drinking water. The pH experiment covered a range from 4 to 10 in sensing application. EDTA titration was examined and was found to be reversible and irreversible due to Cr^{3+} and Pb^{2+} added into **AT** solution. The theoretical calculation was carried out by B3LYP/6–31*G in Gaussian 09 program. The **AT** has a potent in-vitro HepG2 cell line against the cytotoxic, living cell images. It is worth noting that the receptor **AT** would be a beneficial addition to academia for its optical properties and functional application to biomedical industries which will open door to the establishment of these findings. The molecule is useful in sensing and drug-carrying applications.

CRedit authorship contribution statement

P. Vijayakumar: Conceptualization, Methodology, Writing - original draft. **E. Dhineshkumar:** Software, Validation, Writing - review & editing. **M. Arockia doss:** Software, Validation, Writing - review & editing. **S. Nargis Negar:** Software, Validation, Writing - review & editing. **R. Renganathan:** Supervision, Writing - review & editing.

Declaration of Competing Interest

The authors declare that they have no known competing financial interests or personal relationships that could have appeared to influence the work reported in this paper.

Acknowledgement

P.V thanks University Grands Commission (UGC) F.4-1/2006 (BSR)/7-22/2007(BSR) dated 02.01.2013. R. R. thanks to DST Nanomission (SR/NM/NS/1256/2013) for the project and UGC (UGC-2013-35169/2015) for project and Emeritus Fellowship (F.6/2016-17/EMERITUS-2015-17-OBC7855/ (SA-II)).

References

- [1] A.P. de Silva, H.Q.N. Gunaratne, T. Gunnlaugsson, A.J.M. Huxley, C.P. McCoy, J.T. Rademacher, T.E. Rice, Signaling recognition events with fluorescent sensors and switches, *Chem. Rev.* 97 (5) (1997) 1515–1566, <https://doi.org/10.1021/cr960386p>.
- [2] L. Prodi, F. Bolletta, M. Montalti, N. Zaccheroni, Luminescent chemosensors for transition metal ions, *Coord. Chem. Rev.* 205 (2000) 59–83.
- [3] J.P. Desvergne, A.W. Czarnik (Eds.), *Chemosensors of Ions and Molecular Recognitions*; NATO ASI Series, Kluwer Academic Dordrecht, the Netherlands, 1997.
- [4] B. Valeur, I. Leray, Design principles of fluorescent molecular sensors for cation recognition, *Coord. Chem. Rev.* 205 (2000) 3–40.
- [5] L. Fabbrizzi, A. Poggi, Sensors and switches from supramolecular chemistry, *Chem. Soc. Rev.* 24 (3) (1995) 197, <https://doi.org/10.1039/cs9952400197>.
- [6] W. Kaim, B. Schwederski, *Bioinorganic Chemistry: Inorganic Elements in Chemistry of Life, an Introduction and Guide*, Wiley Interscience, New York, 1991.
- [7] C.D. Klassen, M.D. Amdur, J. Dull, Casarett and Doull's Toxicology, 3rd Ed., MacMillan, New York, 1986.
- [8] (a) Y.Li, J. Wu, X. Jin, J.Wang, S.Han, W.Wu, J.Xu, W.Liu, X.Yao and Y.Tang, *Dalton Trans* 43 (2014) 1881. (b) Z.Zhanga, S.Lu, C.Sha, D.Xu, *Sens. Actuators B* 208 (2015) 258. (c) J.M. Junga, S. Y. Lee, C. Kim, *Sens. Actuators B* 251(2017) 291. (d) Jo, T. G. Jo, M.Jung, J.Han, M. H. Lim, C.Kim, *RSC Adv* 7 (2017) 28723.
- [9] (a) A. Levina, P. A. Lay, *The Nutritional Biochemistry of Chromium (III)*, Elsevier, 2nd edn, 2019, pp. 281–321 (b) S.Mishra, R. N. Bharagava, *J. Environ. Sci. Health, Part C Environ. Carcinog. Ecotoxicol. Rev* 34 (2016) 1 (c) H.Arakawa, R. Ahmad, M.Naoui, H. A. Tajmir- Riahi, *J. Biol. Chem* 275 (2000) 10150.
- [10] E. Jorge, M. Rocha, I. Fonseca, M. Neto, *Talanta* 81 (2010) 556–564.
- [11] C. Capellos B.H. Bielski Kinetic systems: mathematical description of chemical kinetics in solution 1972.
- [12] M.C. Pannain, R.E. Santelli, *Talanta* 42 (1995) 1609–1617.
- [13] V. Bravo, S. Gil, A.M. Costero, M.N. Kneeteman, U. Llaosa, P.M. Mancini, L.E. Ochando, M. Parra, *Tetrahedron* 68 (2012) 4882–4888.
- [14] J.Y. Jung, S.J. Han, J. Chun, C. Lee, J. Yoon, *Dyes Pigm* 94 (2012) 423–426.
- [15] D. Li, C.-Y. Li, H.-R. Qi, K.-Y. Tan, Y.-F. Li, *Sens. Actuators B* 223 (2016) 705–712.
- [16] M. Sarkar, S. Banthia, A. Samanta, *Tetrahedron. Lett.* 47 (2006) 7575–7578.
- [17] S. Goswami, K. Aich, K. Das, A. Manna, S. Das, *RSC Adv.* 3 (2013) 2412–2416.
- [18] (a) T. Q. Lai, L. G. Xiao, K.Deng, T. X. Liang, X. B. Chen, X. B. Peng, Y. Cao, *ACS Appl. Mater. Interfaces* 1 (2018) 668– 675 (b) M.Trobe, M.D.Burke, *Angew. Chem. Int. Ed* 16 (2018) 4192–4214 (c) J. Feist, J. Galego, F. J. G. Vidal, *ACS Photonics* 1 (2018) 205–216.
- [19] D. Bellinger, H.L. Needleman, in *Human Lead Exposure*, ed. H. L. Needleman, CRC Press, Boca Raton, 1992, p. 191.
- [20] H. Needleman, *Annu. Rev. Med.* 55 (2004) 209.
- [21] M.L. Riess, J.K. Halm, *J. Gen. Intern. Med.* 22 (2007) 1212.
- [22] H.N. Kim, W.X. Ren, J.S. Kim, J. Yoon, *Chem. Soc. Rev.* 41 (2012) 3210.
- [23] V.M. Cangelosi V.L. Pecoraro, in *Binding, Transport and Storage of Metal Ions in Biological Cells*, ed. W. Maret, A.Wedd, Royal Society of Chemistry, Cambridge, 2014, p. 843.
- [24] J.Y. Kwon, Y.J. Yoon, Y.J. Lee, K.M. Kim, M.S. Seo, W. Nam, J. Yoon, *J. Am. Chem. Soc.* 127 (2005) 10107.
- [25] L. Marbella, B. Serli-Mitasev, P. Basu, *Angew. Chem. Int. Ed* 48 (2009) 3996.
- [26] H. Lee, D. Bae, J. Park, H. Song, W. Han, J. Jung, *Angew. Chem. Int. Ed* 48 (2009) 1239.
- [27] T. Li, S. Dong, E. Wang, *J. Am. Chem. Soc.* 132 (2010) 13156.
- [28] A. Thakur, D. Mandal, S. Ghosh, *Anal. Chem.* 85 (2013) 1665.
- [29] H. Zhu, T. Yu, H. Xu, K. Zhang, H. Jiang, Z. Zhang, Z. Wang, S. Wang, *ACS Appl. Mater. Interfaces* 6 (2014) 21461.
- [30] B. Zhang, L. Lu, Q. Hu, F. Huang, Z. Lin, *Biosens. Bioelectron.* 56 (2014) 243.
- [31] V. Luxami, R. Rani, A. Sharma, K. Paul, *J. Photochem. Photobiol. A* 311 (2015) 68.
- [32] S. Kuo, H. Li, P. Wu, C. Chen, Y. Huang, Y. Chan, *Anal. Chem.* 87 (2015) 4765.
- [33] S. Deo, H.A. Godwin, *J. Am. Chem. Soc.* 122 (2000) 174–175.
- [34] S. Araki, H. Sato, K. Yokoyama, K. Murata, *Am. J. Ind. Med.* 37 (2000) 193–204.
- [35] N. Rifai, G. Cohen, M. Wolf, et al., *Ther. Drug Monit.* 15 (1993) 71–74.
- [36] H. Xue, X.J. Tang, L.Z. Wu, L.P. Zhang, C.H. Tung, *J. Org. Chem.* 70 (2005) 9727–9734.
- [37] S. Sirilaksanapong, M. Sukwattanasinitt, P. Rashatasakhon, *Chem. Commun.* 48 (2012) 293–295.
- [38] K.M. Lee, X. Chen, W. Fang, J.M. Kim, J. Yoon, *Macromol. Rapid Commun.* 32 (2011) 497–500.
- [39] Second ed. Guidelines for Drinking Water Quality, Vol. 2. Geneva: World Health Organization, 1996.
- [40] X.H. Li, X.H.S. Gao, W.H.M. Ma, *Chem. Rev.* 114 (2014) 590–659.
- [41] Y.M. Yang, Q. Zhao, W. Feng, F.Y. Li, *Chem. Rev.* 113 (2013) 192–270.
- [42] Z.P. Liu, Z.P.Z.P. He, Z.J. Guo, *Chem. Soc. Rev.* 42 (2013) 1568–1600.
- [43] L.E. Kreno, K. Leong, O.K. Farha, M. Allendorf, R.P. Van Duyne, J.T. Hupp, *Chem. Rev.* 112 (2012) 1105–1125.
- [44] O. Adegoke, P.B.C. Forbes, *Anal. Chim. Acta* 862 (2015) 1–13.
- [45] V.K. Gupta, A.K. Singh, M.R. Ganjali, P. Norouzi, F. Faridbod, N. Mergu, *Sens. Actuators B Chem.* 182 (2013) 642–651.
- [46] J. Cheng, K. Wei, X. Ma, X. Zhou, H. Xiang, *J. Phys. Chem. C* 117 (2013) 16552–16563.
- [47] B. Valeur, *Molecular Fluorescence Principles and Applications*, Wiley-VCH Verlag GmbH, New York, 2001, p. 341.
- [48] M. Mameli, M.C. Aragoni, M. Arca, C. Caltagirone, F. Demartin, G. Farruggia, G. deFilippo, F.A. Devillanova, A. Garau, F. Isaia, A selective, nontoxic, OFF-ON fluorescent molecular sensor based on 8-hydroxyquinoline for probing Cd^{2+} in living cells, *Chem. Eur. J.* 16 (2010) 919–930.

- [49] Z. Xu, Y. Xiao, X. Qian, J. Cui, D. Cui, Ratiometric and selective fluorescent sensor for CuII based on internal charge transfer (ICT), *Org. Lett.* 7 (2005) 889.
- [50] R. Alam, T. Mistri, P. Mondal, D. Das, S.K. Mandal, A.R. Khuda-Bukhsh, M. Ali, Anovel copper (II) complex as a nitric oxide turn-on fluorosensor: intracellular applications and DFT calculation, *Dalton Trans.* 43 (2014) 2566.
- [51] P.D. Beer, Transition-metal receptor systems for the selective recognition and sensing of anionic guest species, *Acc. Chem. Res.* 31 (1998) 71.
- [52] H. Ueyama, M. Takagi, S.A. Takenaka, Novel potassium sensing in aqueous media with a synthetic oligonucleotide derivative fluorescence resonance energy transfer associated with guanine quartet–potassium ion complex formation, *J. Am. Chem. Soc.* 124 (2002) 14286–14287.
- [53] B. Schazmann, N. Alhashimy, D. Diamond, Chloride selective calix [4]arene optical sensor combining urea functionality with pyrene excimer transduction, *J. Am. Chem. Soc.* 128 (2006) 8607.
- [54] X. Zhang, L. Guo, F.Y. Wu, Y.B. Jiang, Development of fluorescent sensing of anions under excited-state intermolecular proton transfer signaling mechanism, *Org. Lett.* 5 (2003) 2667.
- [55] J.S. Wu, W.M. Liu, X.Q. Zhuang, F. Wang, P.F. Wang, S.L. Tao, X.H. Zhang, S.K. Wu, S.T. Lee, Fluorescence turn on of coumarin derivatives by metal cations: A new signaling mechanism based on C=N isomerization, *Org. Lett.* 9 (2007) 33–36.
- [56] S. Kim, J.Y. Noh, K.Y. Kim, J.H. Kim, H.K. Kang, S. Nam, S.H. Kim, S. Park, C. Kim, *J. Inorg. Chem.* 51 (2012) 3597–3602.
- [57] M. Shyamal, P. Mazumdar, S. Maity, G.P. Sahoo, A. Misra, *J. Phys. Chem. A* 120 (2016) 210–220.
- [58] V. Thomsen, D. Schatzlein, D. Mercurio, *Spectroscopy* 18 (2003) 112–114.
- [59] C.R. Lohani, J.M. Kim, S.Y. Chung, J. Yoon, K.H. Lee, *Analyst* 135 (2079) (2010) 2084.
- [60] S. Sinha, B. Chowdhury, P. Ghosh, *Inorg. Chem.* 55 (2016) 9212–9220.
- [61] L. McDonald, J. Wang, N. Alexander, H. Li, T. Liu, Y. Pang, *J. Mater. Chem. B* 120 (2016) 766–772.



Fluorescence Recognition of Al(III) Ions by a New Chemosensor Based *E*-4-((1-(10*H*-Phenothiazin-2-yl)ethylidene)amino)-*N*-(pyrimidin-2-yl)benzenesulfonamide

P. VIJAYAKUMAR¹, M. AROCKIA DOSS², S. NARGIS NEGAR³ and R. RENGANATHAN^{1,*}

¹School of Chemistry, Bharathidasan University, Tiruchirappalli-620024, India

²Department of Chemistry, St. Joseph University, Nagaland-797115, India

³Department of Nanoengineering, Center for Physical Sciences and Technology, Savanoriu Ave. 231, LT-02300 Vilnius, Lithuania

*Corresponding author: E-mail: rrengas@gmail.com

Received: 25 March 2021;

Accepted: 28 April 2021;

Published online: 26 June 2021;

AJC-20398

A novel Schiff base derivative *E*-4-((1-(10*H*-phenothiazin-2-yl) ethylidene)amino)-*N*-(pyrimidin-2-yl)benzenesulfonamide (**BT**) was synthesized and characterized by ¹H & ¹³C NMR, FT-IR and mass spectrometry. Compound **BT** acts as a detector for Al³⁺ in ethanol/water HEPES buffer solution (5 mM, pH 7.4, v/v 1:4) at room temperature. The fluorescence intensity observed at 516 nm was increased due to Al³⁺ ion present with a fluorescence response “turn-on” process, when excited at 290 nm. This shows compound **BT** is coordinated to Al³⁺ ion through the NH group and C=NH of the Schiff base blocking the photoinduced transfer (PET) and chelation induced enhanced fluorescence (CHEF) process, to increase the fluorescence intensity of **BT**. The detection limit of **BT** was in a micro-molar range for Al³⁺ ion, confirming high selectivity and sensitivity of **BT**. The **BT**-Al³⁺ ion binding mode and the recognition mechanism of chemosensor were explored by EDTA titration, Job’s plot, Mass and FT-IR analysis. The theoretical support was established by DFT calculations.

Keywords: Benzenesulfonamide, Chemosensor, Photoinduced electron transfer, EDTA, DFT.

INTRODUCTION

The fluorescence chemosensors for the development of recognition of transition metal cations are an important area of research for industrial, biological and environmental purposes [1,2]. Owing to their facile syntheses, high sensitivity and selectivity, flexibility and cost-effectiveness, such fluorescence chemosensors have gained exceptional attention [3,4]. One of the main concerns among researchers is the sensitive and selective detection of metal cations in the production of chemosensors. In general, chemosensors have three components: receptor (capable of guest binding selectivity), spacer (which interfaces receptor and signaling), an active unit (capable of altering its properties during metal complexation). Different chemosensors of polycyclic aromatic hydrocarbons, aromatic ring, thiocarbazole, heterocyclic rings, carbazole and even silatrane are reported [5-7]. Aluminium is the most plentiful metal ingredient and biological non-essential ingredient and too much used in manufacturing and everyday life such as food additives, water treatment devices, packaging products, cosmetics

and prescription drugs [8-11]. Compared to other metal ions the highly efficient identification of Al³⁺ ions in aqueous solutions are important due to its strong hydrated ability, lack of spectroscopic characteristics and poor coordination power [12-14]. Due to their high coordination power, excellent photo-physical performance and ease of synthesis, Schiff base fluorescent chemosensors have recently attracted a lot of attention [15-17]. Aluminum accumulation in the brain induces neuron degeneration, which is followed by various diseases such as Alzheimer, Parkinson disease, lateral amyotrophic sclerosis, dialysis-induced encephalopathy and also multiple sclerosis [18-21]. Thus it has encouraged ongoing studies on the potentially harmful impact of the atmosphere to enhance effective tools for Al³⁺ identification. These techniques include mass spectrometry, spectrophotometer, electrochemistry, graphite furnace atomic absorption spectrometry, inductively coupled plasma mass spectrometry, voltammetry and liquid chromatography [22-24]. Sensing mechanisms such as fluorescence resonance energy transfer, chelation-induced enhanced fluorescence, intermolecular charge transfer and photoinduced

electron transfer are very relevant in fluorescence chemosensors [25-29]. For several years, the Schiff base compound was used in chemistry [30]. There has been substantial use of non-transition metal complexes [30]. Several complexes of Schiff bases have found interesting uses in materials science [31]. In this case, in turn-on chemosensors, the benzenesulfonamide moieties received considerable attention owing to the formation of excimers and high quantum yield [32,33] due to their ability to show a peculiar shift in their emission wavelengths. Comparison with conventional analytical approaches requires, for example, colorimetric methods that could be accomplished by UV-visible spectra with specific benefits, such as detection and even ease of operation, which could be carried out using on-site tests [34].

Benzenesulfonamide type Schiff base ligand (*E*)-4-((1-(10*H*-phenothiazine-2-yl) ethylidene)amino)-*N*-(pyrimidine-2-yl)benzene sulfonamide (**BT**) was studied in this work. The chemosensor activity for Al³⁺ ions in ethanol/water HEPES buffer (5 mM, pH 7.4, v/v 1:4) solution was demonstrated by the UV-visible and fluorescent spectroscopy at ambient temperature. Complexation of **BT** within the Al³⁺ ion was analyzed by FT-IR and ESI-MS spectroscopy.

EXPERIMENTAL

All the chemicals were purchased commercially and used after purification. Throughout the experiments, only distilled water was used. Solutions of different metal ions salts, such as chloride or nitrate salts of Cr³⁺, Sn²⁺, Cu²⁺, Cd²⁺, Ti³⁺, Ca²⁺, Hg²⁺, Fe³⁺, Al³⁺, Ni²⁺, Sr²⁺, Mn²⁺, Zn²⁺, Pb²⁺ and Al³⁺ ions were prepared. The FT-IR, ¹H & ¹³C NMR and ESI-MS spectroscopy were used to validate the synthesized compound. An Agilent Carry 630 FT-IR spectrometer was used to test infrared at 4000-400 cm⁻¹. The ¹H & ¹³C NMR spectra were obtained using a Bruker 400 MHz instrument with TMS as the internal norm and DMSO-*d*₆ as solvent. At room temperature, fluorescence measurements were taken with a Perkin-Elmer LS45 fluorescence spectrophotometer with a scan rate of 1200 nm.

Synthesis of Schiff base derivative BT: 2-Acetylphenothiazine (0.48 g, 2 mmol) and 4-amino-*N*-(pyrimidin-2-yl)benzene sulfonamide (0.42 g, 2 mmol) were dissolved in absolute ethanol and refluxed for 24 h at 60 °C. Then, the reaction was confirmed by TLC plate. This solution mixture was poured in distilled H₂O and light brownish yellow precipitate appeared and then filtered and dried for 2 to 3 days. It was recrystallized from absolute ethanol and finally got the product (**Scheme-I**). Yield: 88%. FT-IR (KBr, ν_{max}, cm⁻¹): (C=N) 1591, (NH) 3345; ¹H NMR (DMSO-*d*₆, 400 MHz) δ ppm: 8.53 (s, 1H), 8.54 (s,

1H), 8.83 (s, 1H), 7.682-7.661 (d, *J* = 8.4 Hz, 2H), 7.409-7.404 (d, *J* = 2.0 Hz, 2H), 7.389-7.384 (d, *J* = 2.0 Hz, 2H), 7.099-7.039 (*J* = 2.4 Hz, 7H), 6.980-6.961 (d, *J* = 7.6 Hz, 2H), 6.841-6.820 (m, *J* = 8.4 Hz, 4H), 6.723-6.700 (m, *J* = 10.4 Hz, 4H), 6.632-6.610 (2, *J* = 8.0 Hz, 2H). ¹³C NMR (DMSO-*d*₆, 100 MHz) δ ppm: 196.88, 158.23, 157.15, 152.98, 141.97, 141.16, 136.06, 129.77, 126.25, 126.11, 124.76, 123.25, 122.52, 122.17, 114.53, 112.62, 112.09, 26.44. m.f.: C₂₇H₁₉N₅O₅S₂; ESI-MS (*m/z*): calculated for [M + H]⁺: 473.16; found: 473.27.

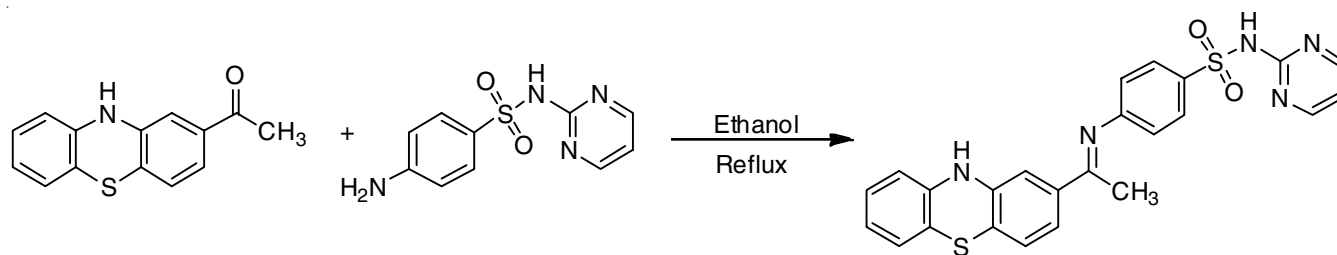
UV-vis and fluorescence analysis: In aqueous water, stock solutions of various metal ions, such as nitrate or chloride salts, were prepared. For spectroscopic tests, a stock solution of **BT** (10 μM) was prepared in aqueous water. The absorption and fluorescence spectra were measured in a quartz cell in an ethanol/water HEPES buffer solution (5 mM, pH 7.4, v/v 1:4) at room temperature using a 5 mL mixed solution of **BT** (10 μM) and metal ion solution with an accurate concentration. Both fluorescence experiments were carried out at a wavelength of 290 nm.

Cell culture: The HepG2 cell lines (NCCS, Pune, India) were grown in DMEM with 10% FBS and antibiotics (streptomycin: 50 μg/mL; penicillin: 100 μg/mL) at 37 °C, 5% CO₂ incubator and cells were developed at 95%.

Anticancer activity and cell viability assay: The cytotoxicity of **BT** was investigated in HepG2 cell lines using a 3-(4,5-dimethylthiazole-2-yl)-2,5-diphenyl tetrazolium bromide (MTT) assay. Cells were seeded onto a 96-well plate with a cell density per disc of 1.5 × 10⁴ and incubated in a medium containing **BT** for 48 h at various concentrations ranging from 0.0 to 500 μL. For each process, triplicate wells with 100 μL of MTT were used. It was incubated for 4 h at 37 °C, allowing the MTT reaction and metabolically active cells to form formazan crystals. The MTT medium was carefully removed from the wells. DMSO (100 μL) was added to each well and the dishes were shaken for 10 min to remove intracellular formazan crystals. The absorbance was measured using ELISA at 365 nm. The cells images were studied under a fluorescent microscope. The percentage survival was estimated using the following formula:

$$\text{Survival (\%)} = \frac{\text{Live cell number (test)}}{\text{Live cell number (control)}} \times 100$$

Fluorescence microscopic study: The cells were seeded at a density of 3 × 10⁵ cells per dish in a 35 mm culture dish for *in vitro* fluorescence imaging of **BT**. After completion, 60% confluence for fluorescence microscopy was replaced with aluminum nitrate supplemented with the serum to absorb Al³⁺ ion by 40 h forming cells, **BT** (5.0 M), dissolved in DMSO/



Scheme-I: Synthesis of compound **BT**

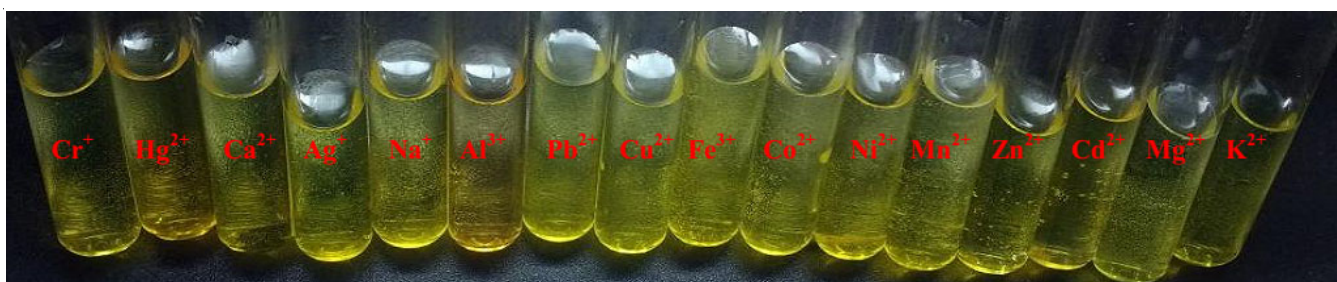


Fig. 1. The colorimetric studies for **BT**

H₂O (99/1), by addition of new media to allow **BT** to be absorbed by cells to form the Al³⁺-**BT** complex. After that there was a 3 h incubation period. Al³⁺ ions were trypsinized and analyzed for **BT** images at 365 nm using a 10× fluorescent target under a fluorescence microscope. The fluorescence microscope 40x-Olympus FV1000-LX81.z, Camedia software and Adobe Photoshop version 10.0 were used to obtain the bright and fluorescence field information. The Al³⁺ ion was removed from the media for the control trial.

Theoretical studies: The Gaussian09 program [35] was used to perform the computations. The B3LYP method was used to perform the geometry optimization. The molecular electrostatic potentials (MEPs) and Mulliken atomic charges of benzene sulfonamide were plotted in a 3D diagram using optimized structures at the same level theory. Furthermore, the energy gap for benzenesulfonamide was determined using the B3LYP method with a 6-31G (d,p) basis range, as well as HOMO and LUMO energy values. Furthermore, theoretical measurements were used to determine the dipole moment, polarizability and hyper polarizability of molecular polarizabilities.

RESULTS AND DISCUSSION

The fluorescent chemosensor **BT**, *E-4-(1-(10H-phenothiazin-2-yl)ethylidene)amino)-N-(pyrimidin-2-yl)benzenesulfonamide* (**BT**) was synthesized (**Scheme-I**) and characterized using FT-IR, ESI-MS, ¹H&¹³C NMR spectroscopic methods. Colorimetric experiments with naked eye UV-vis and fluorescence spectroscopy in HEPES buffer solution of EtOH:H₂O (1:4 v/v, pH = 7.0) and excitation at 290 nm were also carried out. For different metal ions, the fluorescent chemosensor **BT** solution was investigated and the fluorescence intensity at 516 nm for Al³⁺ ion was investigated further.

Absorption studies: The interaction of analytes with chemosensors was tested using the UV-visible absorption technique [36-39]. At room temperature, experiments were performed in an ethanol/water HEPES buffer (5 mM, pH 7.4, v/v 1:4). Under a UV lamp, the colorimetric tests for **BT** solution showed a bright yellow to medium yellow colour to the naked eye (Fig. 1).

Compound **BT** has three absorption bands with maximum at 252, 272 and 295 nm, which are caused by intra-ligand $\pi \rightarrow \pi^*$ electronic transitions and another absorption band at 327 nm, which may be caused by $n \rightarrow \pi^*$ electronic transitions from non-bonding orbitals on the heteroatoms to π^* orbitals of **BT** (Fig. 2). The absorbance of **BT** was explored with different metal ions such as alkali metal ions (Mg²⁺, Ca²⁺) and transition

metal ions (Cd²⁺, Cu²⁺, Ag⁺, Co²⁺, Mg²⁺, Ni²⁺, Fe³⁺, Zn²⁺ and Mn²⁺) in ethanol/water HEPES buffer (5 mM, pH 7.4, v/v 1:4) at ambient temperature. The presence of Al³⁺ ion caused a noticeable shift in wavelength in the absorption spectra of **BT**, while the other metal ions did not cause any significant shifts in the absorption spectrum (Fig. 2). The spectrum of **BT** reveals a new absorption at 415 nm and two new isosbestic points at 308 nm and 340 nm after the addition of Al³⁺ ions (Fig. 3).

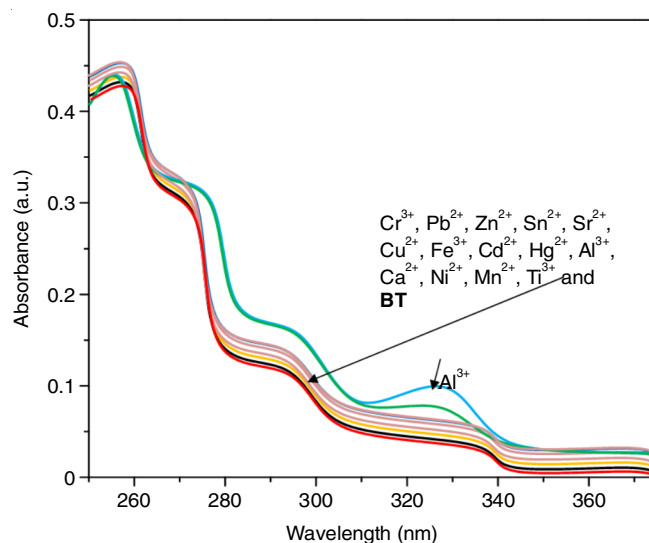


Fig. 2. Absorption spectrum of **BT** (10 μ M) with different metal ion (5 equiv.) used in ethanol/water HEPES buffer solution in EtOH:H₂O (5 mM, pH 7.4, v/v 1:4)

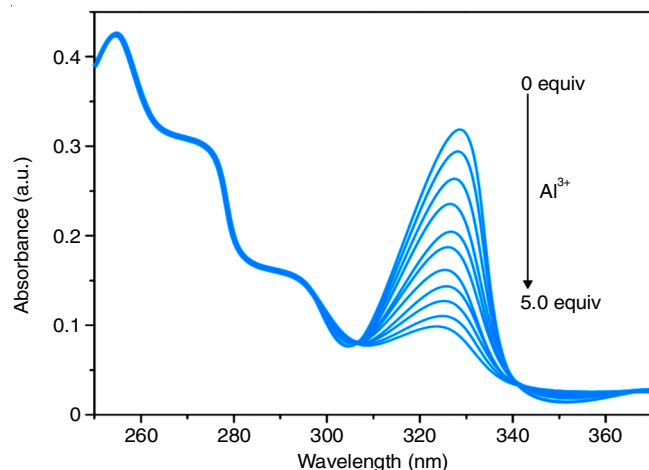
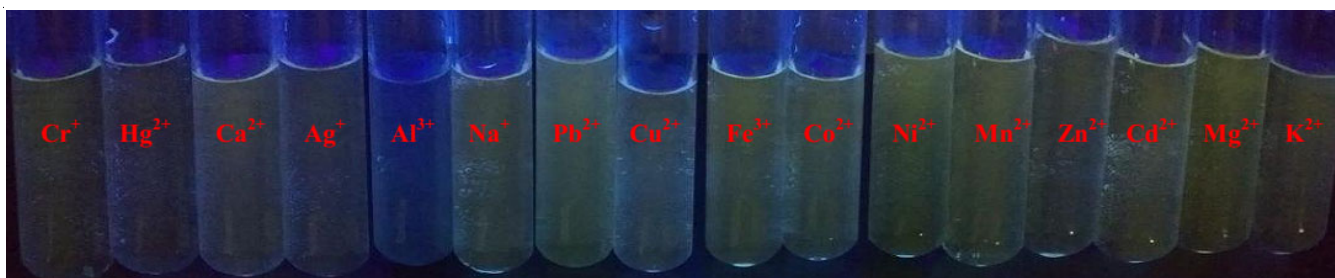


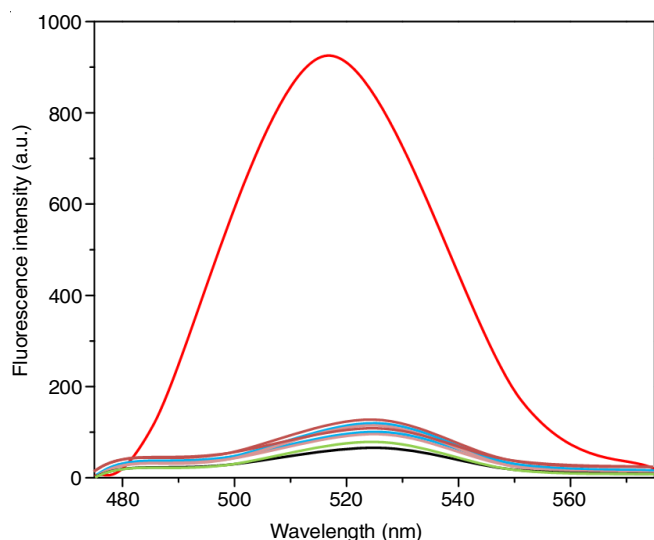
Fig. 3. Absorption spectrum of **BT** (10 μ M) with increase concentration of Al³⁺ ion used in ethanol/water HEPES buffer solution (5 mM, pH 7.4, v/v 1:4)

Fig. 4. Fluorometric studies for **BT**

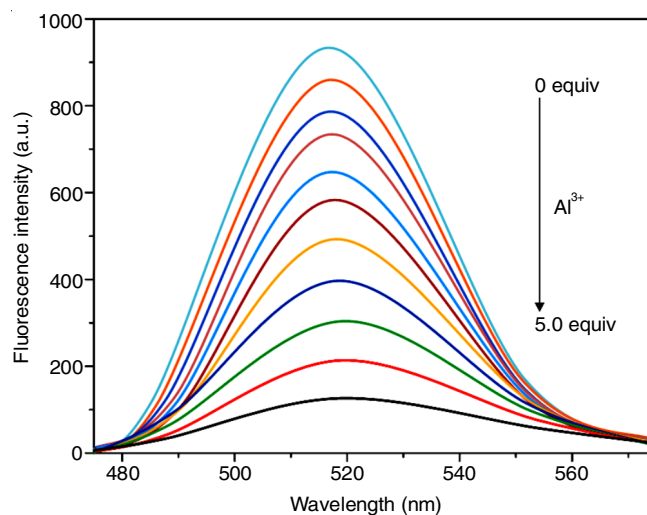
The redshift (bathochromic) in absorption is due to the donor atoms in **BT** binding to Al^{3+} to form a chelate ring, which causes the spectrum to be expanded in conjugation, which may explain the red shift in absorption strength.

Fluorescence studies: The selectivity of **BT** was revealed by pale yellow colour change to blue colour of Al^{3+} because with all metal ions no colour change was observed by fluorescence lamp under 365 nm (Fig. 4).

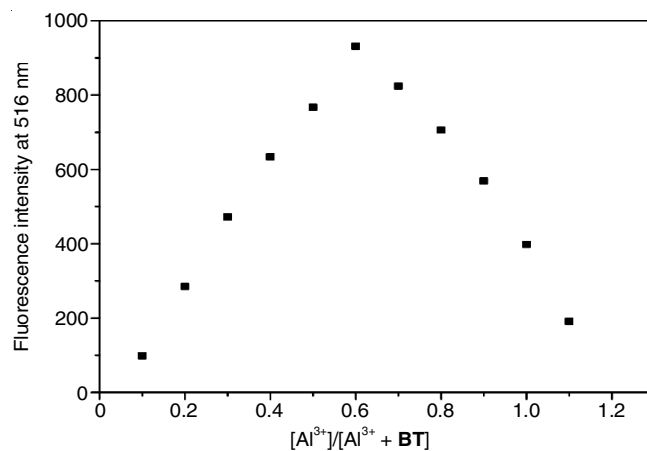
An equimolar solutions of **BT** ($10 \mu\text{M}$) was added to solutions of different heavy transition metal ions such as Cr^{3+} , Sn^{2+} , Cu^{2+} , Cd^{2+} , Ti^{3+} , Ca^{2+} , Hg^{2+} , Fe^{3+} , Al^{3+} , Ni^{2+} , Sr^{2+} , Mn^{2+} , Zn^{2+} , Pb^{2+} and Al^{3+} ion in ethanol/water HEPES buffer (2 mM 1:4, v/v, pH = 7.0) at ambient temperature. The emission study demonstrated that the compound **BT** shows weak emission maximum intensity at 516 nm observed on excitation at 290 nm (Fig. 5).

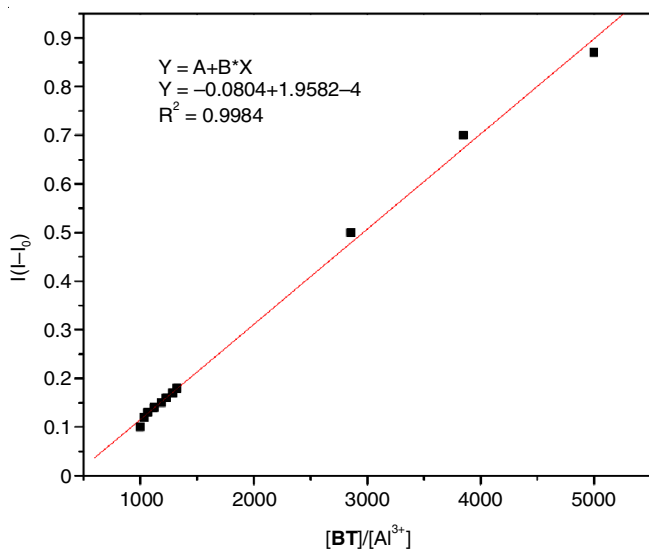
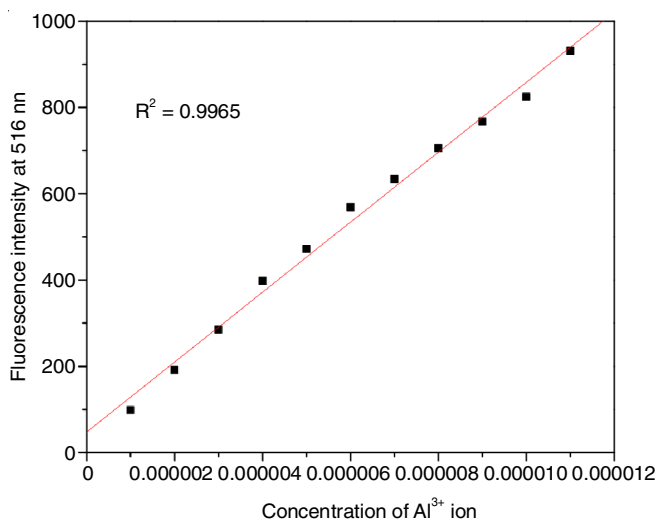
Fig. 5. Fluorescence spectrum of **BT** ($10 \mu\text{M}$) with different metal ion (5 equiv.) used in ethanol/water HEPES buffer solution in EtOH: H_2O (5 mM, pH 7.4, v/v 1:4)

The emission intensity at 516 nm was red shifted when Al^{3+} ions was added, but no other metal ions made a noticeable difference in the fluorescence spectrum. The switch-ON fluorescence of **BT** caused by metal-ligand binding was fully selective for Al^{3+} ions. Various spectroscopic techniques were used to investigate the binding of the **BT**- Al^{3+} complex. The fluorescence emission intensity at 516 nm gradually decreased with the addition of 2 equiv. of Al^{3+} ion (Fig. 6) becoming stable, reflecting the coordination of **BT** (10M) with Al^{3+} in stoichiometric complex 1:1 binding mode.

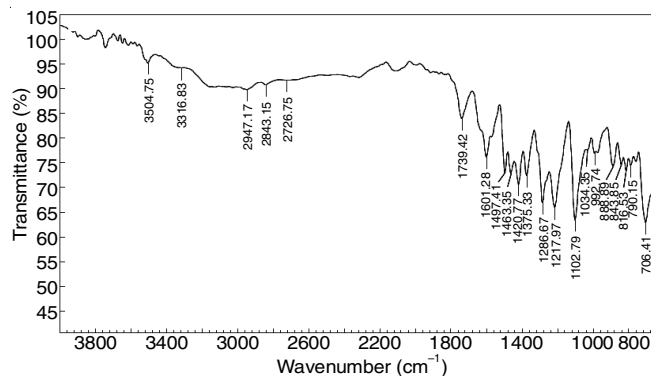
Fig. 6. Fluorescence spectrum **BT** ($10 \mu\text{M}$) with increase concentration of Al^{3+} ion used in ethanol/water HEPES buffer solution (5 mM, pH 7.4, v/v 1:4)

The complexation of **BT**- Al^{3+} ion was found to be 1:1 stoichiometric using job plots based on fluorescence results (Fig. 7). The binding constant (K) determined from fluorescence intensity at 516 nm using the Benesi-Hildebrand plot was $3.27 \times 10^7 \text{M}^{-1}(\text{Al}^{3+})$, indicating that **BT** would bind to Al^{3+} ion (Fig. 8). The detection limit of Al^{3+} ion was calculated using the equation $\text{DL} = 3/k$, where k is the slope of intensity versus sample concentration and $R_2 = 0.9965$ is the standard deviation (Fig. 9). Titration of **BT** as a receptor for Al^{3+} ion was carried out to better understand the binding of **BT** as a receptor for Al^{3+} ions.

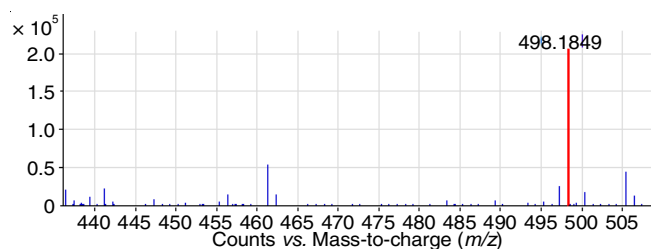
Fig. 7. Job's plot of **BT** + Al^{3+} ion

Fig. 8. Benesi-Hildebrand plot from fluorescence titration of **BT** + Al³⁺ ionFig. 9. Determination of limit **BT** (10 μM) with different concentration of Al³⁺ ion

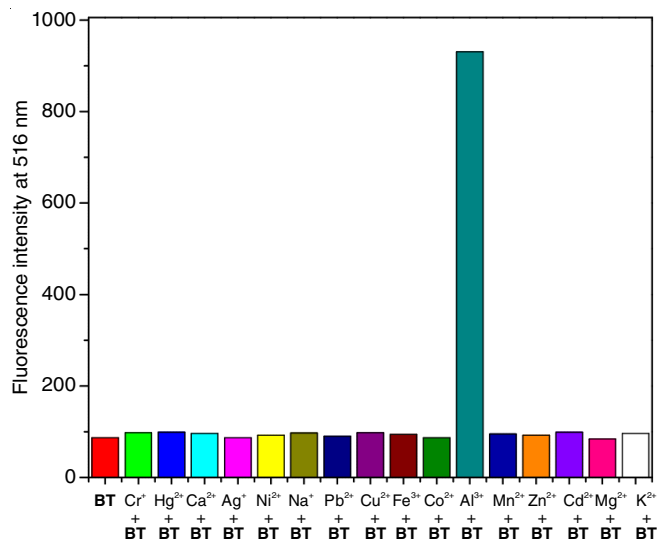
Binding mechanism: Binding studies demonstrate that **BT** is sensitive and selective for Al³⁺ ion as shown by fluorescence changes observed at 516 nm. The inhibition of rotation around the azomethine nitrogen increases the rigidity of the molecular association (CHEF) when Al³⁺ ion is chelated with O and N donors of **BT**. The photoinduced electron transfer (PET) mechanism causes the fluorescence of **BT** to be quenched due to the delocalization of accessible lone pairs of electrons on the imine (C=N) nitrogen atom to the aromatic moiety. Two effects (PET and CHEF), which are responsible for titration processes, were found to increase emission. Further experiments, such as FT-IR and mass spectroscopy, supported the PET process. Due to the addition of 0.5 equiv. of Al³⁺, the NH stretching peak at 3345 cm⁻¹ vanished and a new peak appeared at 3316 cm⁻¹, the functional group of the imine peak at 1591 cm⁻¹ vanished and a new peak at 1601 cm⁻¹ appeared (Fig. 10). After applying Al³⁺ (1 equiv.) to **BT** solution, the ESI-MS spectrum revealed the exact molecular weight at 498.18 m/z, which was compared to the original compound exact mass at

Fig. 10. FT-IR spectrum of **BT** + Al³⁺ ion

473.27 m/z (**BT**), confirming the 1:1 stoichiometry for **BT**-Al³⁺ (Fig. 11).

Fig. 11. ESI-MS spectrum of **BT** + Al³⁺ ion

Competitive metal studies: The fluorescence intensity of **BT**-Al³⁺ was examined with other interfering metal ions such as Cr³⁺, Sn²⁺, Cu²⁺, Cd²⁺, Ti³⁺, Ca²⁺, Hg²⁺, Fe³⁺, Ni²⁺, Sr²⁺, Mn²⁺, Zn²⁺, Pb²⁺ and Al³⁺ ions in ethanol/water HEPES buffer (5 mM, pH 7.4, v/v 1:4) at ambient temperature. Fig. 12 showed that λ_{ex} wavelength 290 used and λ_{em} intensity at 516 nm was observed.

Fig. 12. Emission intensity of **BT** (10 μM) at λ_{em} = 516 nm and the presence of various metal ions (5 equiv.) in ethanol/water HEPES buffer (5 mM, pH 7.4, v/v 1:4) at room temperature

In the presence of Al³⁺ ions (λ_{ex} = 290 nm), the fluorescence intensity of **BT** increased at 516 nm, but other metal ions had no discernible effect on the emission intensity of **BT**

at 516 nm. When **BT** was combined with Al^{3+} ion, the fluorescence intensity at 516 nm ($\lambda_{\text{ex}} = 290$ nm) was monitored to estimate the main effect of different metal ions (Fig. 13). In the presence of other metal ions, the fluorescence emission strength of **BT** mixed with Al^{3+} did not change significantly. The obtained results show that **BT** can be used to detect Al^{3+} ions in a relatively simple manner.

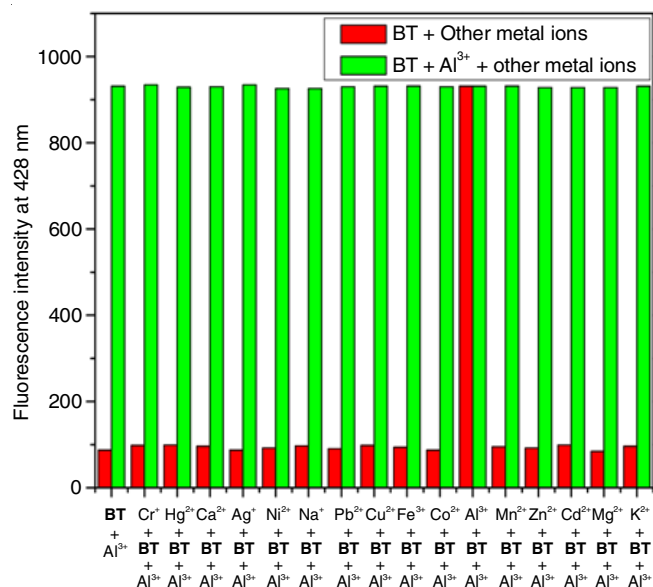


Fig. 13. Competitive metal studies **BT** (10 μM) at $\lambda_{\text{em}} = 516$ nm and the presence of various metal ions (5 equiv.) in ethanol/water HEPES buffer (5 mM, pH 7.4, v/v 1:4) at room temperature

Reversibility: The probe's reusability is a notable attribute for its use and reversibility tests of **BT** with Al^{3+} ions were performed at room temperature in an ethanol/water HEPES buffer (5 mM, pH 7.4, v/v 1:4) (Fig. 14). The fluorescence spectra of **BT** were observed at 516 nm with 2 equiv. of Al^{3+} ion. After applying a higher concentration of the chelating

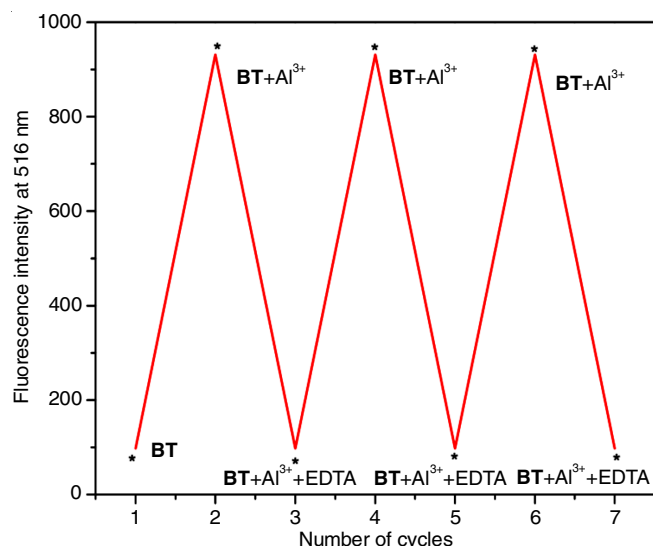


Fig. 14. Emission intensity of **BT** (10 μM) at $\lambda_{\text{em}} = 516$ nm and the presence of various metal ions (5 equiv.) in ethanol/water HEPES buffer (5 mM, pH 7.4, v/v 1:4) temperature

agent EDTA solution, the emission intensity of metal complexes was decreased, suggesting that the free **BT** was being regenerated. The addition of Al^{3+} ion to the **BT** solution mixture induced fluorescence enhancement within 5 min a second time and the addition of the chelating agent EDTA solution caused fluorescence intensity to be quenched. By gradually adding suitable strong chelating reagents such as EDTA, the obtained results showed that **BT** was a reversible and reusable sensor for Al^{3+} ions for up to three cycles.

Cytotoxic activity: The anticancer effects of newly synthesized materials on liver cancer cells (HepG2) were assessed using the MTT-based metabolic assay mentioned previously [40]. The cells (approximately 10,000 cells) were seeded in a well (96-well plate) containing 100 μL of fresh medium and incubated for 24 h. The cells were then treated with 100 μL of various concentrations (ranging from 0.0-500 μM concentration) of the newly generated compound in each well. MTT (100 μL) was applied after 24 h of treatment and incubated for 2-4 h. Then, the reaction was arrested using 100 μL volumes of DMSO and the measurement was carried at 360 nm. The cytotoxicity of active compound was determined by the concentration of extracts that inhibited cell growth by 50% (IC_{50}) as shown in Table-1. The anticancer activity results revealed that the synthesized compound showed potent inhibition of liver cancer cell proliferation.

TABLE-1 IC_{50} VALUES OF BT AGAINST HepG2 CELL LINES	
Anticancer effect of BT on HepG2 cell line	
Concentration (μM)	Cell viability (%)
0	100
0.9	95
1.9	82
3.9	75
7.8	61
15.6	43
31.25	27
62.5	18
125	11
250	7
500	3

Cell imaging: The HepG2 cancer cells were exposed to compound **BT** for 30 min at 37 $^{\circ}\text{C}$ after being incubated with Al^{3+} ions (0-100 $\mu\text{g}/\text{mL}$). Because of their high emission intensity in the presence of the probe, compound **BT**- Al^{3+} ions were chosen for the cell imaging procedure. The confocal fluorescence images of HepG2 cell lines after treatment with DAPI, metal salts, probe and its complexes. For Al^{3+} complex, a proportional increase in sensor concentration (0, 20, 50 and 100 $\mu\text{g}/\text{mL}$) follows a proportional relationship with fluorescence intensity. The linking motif within the living cell can be clearly seen in magnified images (Fig. 15). As a result, the receptor **BT** has a strong cell-permeable property and can be used to detect Al^{3+} ions within living cells. Furthermore, when HepG2 cell lines were used instead of HepG2 cells, a similarity in cell imaging was observed (Fig. 15).

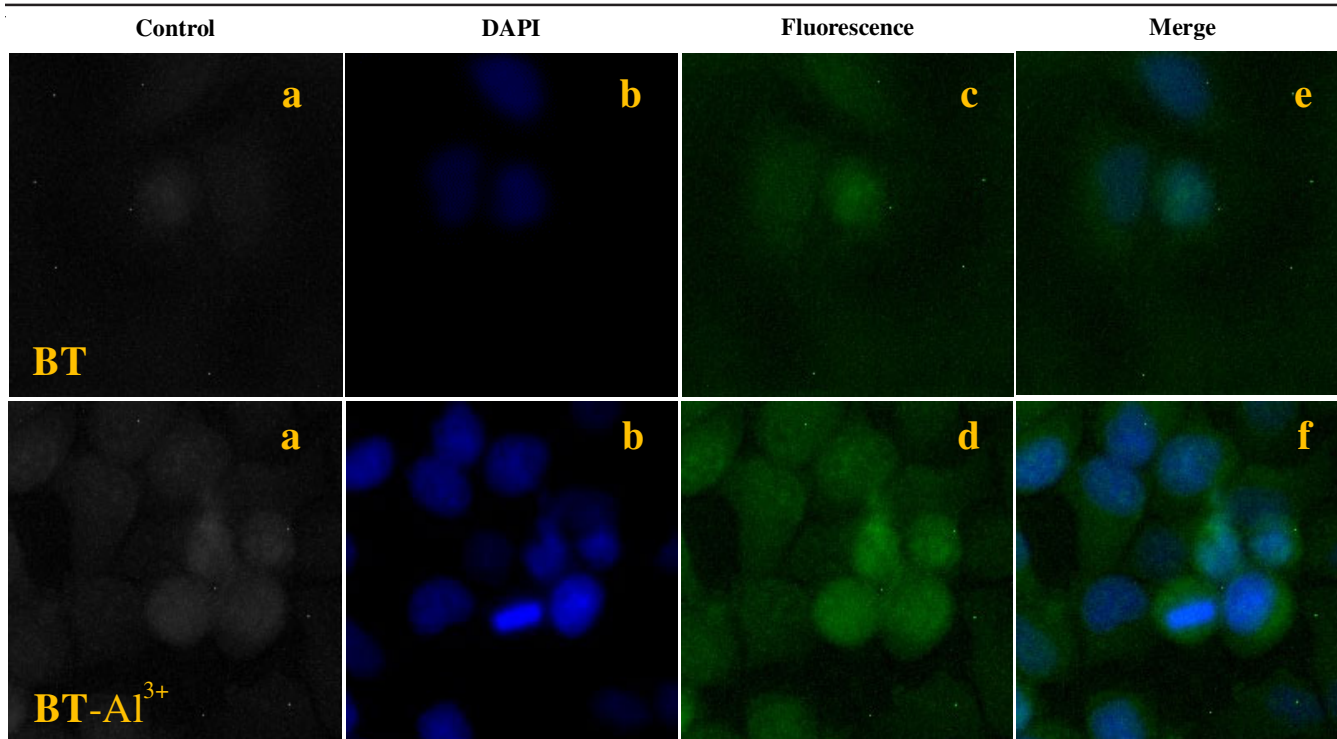


Fig. 15. Confocal fluorescence and merged images of HepG2 cells were stained with DAPI, BT-Al³⁺, respectively. (a) HepG2 cells incubated with BT-Al³⁺ (5 μM) only, (b) HepG2 cells pre-incubated with BT-Al³⁺ (5 μM) followed by 0.1 mM BT, (c) cells were stained with both DAPI and 5 μM BT-Al³⁺; (d) cells of (c) further incubated with BT (0.1 mM) for another 30 min, (e) and (f) were merged images. Scale bar, 30 μm

Theoretical studies

HOMO and LUMO analysis: For all the experiments performed on Schiff base compound, the HOMO and LUMO are delocalized from the entire molecule. The energy level of HOMO and LUMO is an extremely important parameter to define the reactivity of molecules because they generally take part in chemical reactions. The lower E_{HOMO} has a weak electron donating capability. However, the higher E_{HOMO} means the good electron donor [41]. In the B3LYP/6-31G(d,p) basis set, the DFT method was used to measure the energy level. The substituted benzenesulfonamide molecules with a methyl group and an NH group in the ring. The largest E_{HOMO} value at 3.24 eV and the lowest E_{LUMO} value at 2.43 eV for compound BT, both calculated the band gap energy level at 1.64 eV, because of the decrease in the LUMO value (Fig. 16).

This compound has a stronger electron-donating ability than other Schiff bases. In the meantime, the other calculation method include is dipole moment, polarizability and hyperpolarizability are presented in Table-2. The present work shows the existence of a structure resembling benzenesulfonamide ring increase the HOMO orbitals.

MEP analysis: The MEP is a crucial method for analyzing molecular interactions within a molecule. Hydrogen-bonding reactions, as well as electrophilic and nucleophilic attacking, are extremely helpful in predicting and understanding relevant reactivity sites [42-44]. The optimized structure of molecules at the B3LYP/6-31G(d,p) basis set was used to measure the 3D plot of the MEP diagram for the Schiff molecules (BT). Different colours reflected the molecular electrostatic potentials

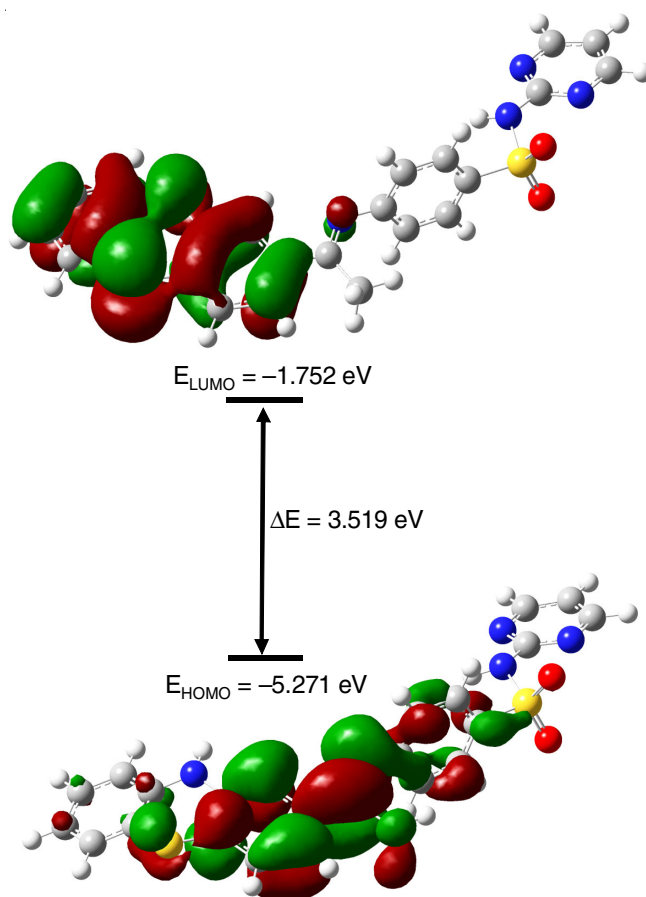


Fig. 16. Energy level diagram of BT

TABLE-2
CALCULATED ENERGY VALUES (eV) OF
COMPOUND **BT** IN GAS PHASE

B3LYP/6-31G(d,p)	BT
E_{HOMO}	-5.2715
E_{LUMO}	-1.752
$E_{\text{LUMO-HOMO}}$	3.5194
Electronegativity	-3.5118
Hardness	1.7595
Electrophilicity index	3.5042
Softness	7.731

at the surface of **BT** molecule. The negative electrostatic potential indicates proton attraction, while the positive electrostatic potential indicates proton repulsion shows in Fig. 17.

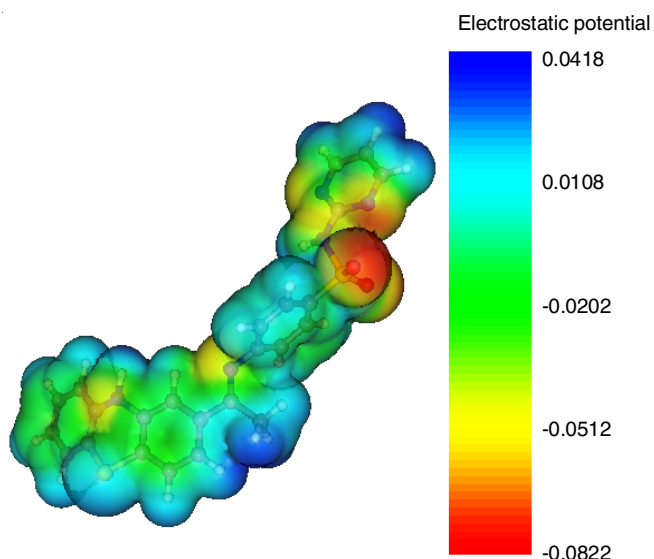


Fig. 17. Molecular electrostatic potential surface of **BT**

Mulliken charge distribution analysis: Mulliken charge population investigation leads to the same conclusion on charge distributions of all Schiff bases of organic compounds. The charge distributions above all atoms propose the formation of donor and acceptor paired relatively the charge transfer in this molecule. The highest negative charge density which is placed on O and N atoms, further responsible for a strong bond between the substrate surface and Schiff base. The Mulliken charge distribution of the molecule is calculated by B3LYP at 6-31G (d,p) level theory. The synthesized compound **BT**, charge distribution shows that all the nitrogen and oxygen highly negative charges and Mulliken charges are very low compared with natural charges (Fig. 18).

Further negative charge could spread all over C1, C3, C5, C6, C8, C11, C15, C18' and C19', therefore due to these atoms attached all the molecules. While, other atoms attached to a molecule such as N10, CH₃15', N16, N22, S21, N22, N24 and N24' are given in Table-3, indicated that compound **BT** can undergo nucleophilic substitution.

NLO Effects: Table-4 shows the approximate hyperpolarizability values for the synthesized compound **BT**. Urea is used as a reference molecule to assess NLO properties and for comparison purposes. Compound **BT** exhibited first hyperpol-

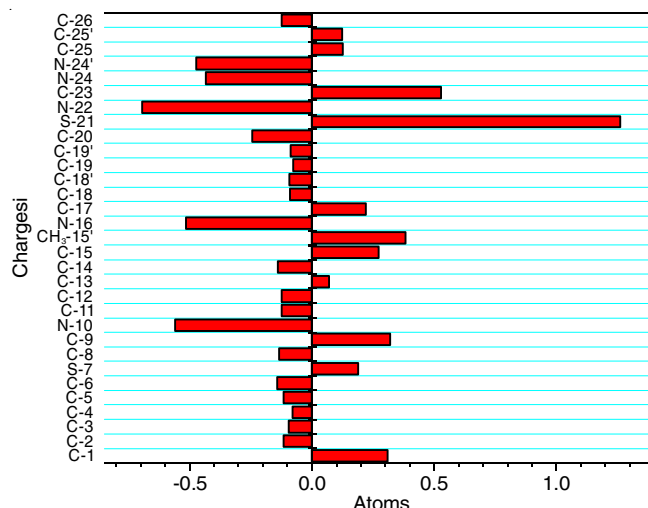


Fig. 18. Mulliken atomic charges for **BT**

TABLE-3
MULLIKEN ATOMIC CHARGES OF COMPOUND **BT**

Atom	BT	Atom	BT
C-1	0.309	N-16	-0.513
C-2	-0.115	C-17	0.22
C-3	-0.094	C-18	-0.089
C-4	-0.078	C-18'	-0.09
C-5	-0.115	C-19	-0.075
C-6	-0.142	C-19'	-0.086
S-7	0.189	C-20	-0.243
C-8	-0.134	S-21	1.259
C-9	0.32	N-22	-0.693
N-10	-0.559	C-23	0.529
C-11	-0.123	N-24	-0.434
C-12	-0.125	N-24'	-0.472
C-13	0.072	C-25	0.125
C-14	-0.139	C-25'	0.122
C-15	0.274	C-26	-0.124
CH ₃ -15'	0.384		

TABLE-4
DIPOLE MOMENT, POLARIZABILITY,
HYPERPOLARIZABILITY VALUES OF COMPOUND **BT**

Parameter	Dipolemoment (Debye)	Hyperpolarizability (a.u)	
μ_x	9794.942	β_{xxx}	-159.606
μ_y	4546.899	β_{yyy}	4.3205
μ_z	5231.86	β_{zzz}	1.0394
μ_{total}	139.906	β_{xyy}	-47.817
Parameter	Polarisability (a.u)	β_{xxy}	
α_{xx}	-204.44	β_{xxx}	59.3327
α_{yy}	-175.20	β_{xzz}	-68.893
α_{zz}	-183.08	β_{zzz}	108.453
α_{xy}	-9.77	β_{yyz}	-2.432
α_{xz}	4.56	β_{yyz}	3.7775
α_{yz}	4.26	β_{xyz}	-4.4776
α_0 (esu) $\times 10^{-23}$	2.8	β_0 (esu) $\times 10^{-30}$	1.21
		$\Delta\alpha$ (esu) $\times 10^{-24}$	4.42

arizability (β_{tot}) as 139.906×10^{-30} esu, which is six times higher than that of urea ($\beta_0 1.21 \times 10^{-30}$). As a result, this molecule may be used as a non-linear optical substance in a future building block.

Conclusion

In present work, Schiff base derivative was synthesized and characterized by FT-IR, mass and ^1H & ^{13}C NMR analysis. The synthesized *E*-4-((1-(10*H*-phenothiazin-2-yl)ethylidene)-amino)-*N*-(pyrimidin-2-yl)benzenesulfonamide (**BT**) exhibited recognition for Al^{3+} in ethanol/water HEPES buffer solution (5 mM, pH 7.4, v/v 1:4) at ambient temperature in a UV-visible and fluorescence spectroscopy. The fluorescence λ_{em} intensity at 516 nm (λ_{ex} wavelength at 290 nm), fluorescence “turn-on” due to the presence of Al^{3+} ion with a high peak below all metal ions. The PET and stimulating CHEF process for **BT**+ Al^{3+} ion was coordinated through the NH group and imine nitrogen inhibited and blocked. Job's plot was shown by 1:1 stoichiometric for **BT**- Al^{3+} ion. The binding constant (*K*) was determined as $3.27 \times 10^7 \text{ M}^{-1}$ (Al^{3+}), the limit of detection **BT** for Al^{3+} ion was observed $R^2 = 0.9965$. Competitive metal ions extensively studied for the presence of Al^{3+} ion, whereas, after the EDTA solution added into **BT**+ Al^{3+} ion proved to be reversible and irreversible. The theoretical calculation used in Gaussian 09 program was followed by the B3LYP/6-31G(d,p) basis set.

ACKNOWLEDGEMENTS

One of the authors (PV) thanks to UGC for providing the fellowship (F4-1/2006(BSR)/7-22/2007(BSR) dated 02.01.2013). Another author (RR) thanks DST Nanomission (SR/NM/NS/1256/2013) and UGC (UGC-2013-35169/2015) for sanctioning the project and Emeritus Fellowship (F.66/2016-17/EMERITUS-2015-17-OBC7855/(SA-II)).

CONFLICT OF INTEREST

The authors declare that there is no conflict of interests regarding the publication of this article.

REFERENCES

- D. Wu, A.C. Sedgwick, T. Gunnlaugsson, E.U. Akkaya, J. Yoon and T.D. James, *Chem. Soc. Rev.*, **46**, 7105 (2017); <https://doi.org/10.1039/C7CS00240H>
- D. Udhayakumari and V. Inbaraj, *J. Fluoresc.*, **30**, 1203 (2020); <https://doi.org/10.1007/s10895-020-02570-7>
- Y.M. Yang, Q. Zhao, W. Feng and F.Y. Li, *Chem. Rev.*, **113**, 192 (2013); <https://doi.org/10.1021/cr2004103>
- D.C.E. Persch, D.C.O. Dumele and F. Diederich, *Angew. Chem. Int. Ed.*, **54**, 3290 (2015); <https://doi.org/10.1002/anie.201408487>
- G. Singh, A. Singh, P. Satija, G. Sharma, J. Shilpy, J. Singh, J. Singh, K.N. Singh and A. Kaur, *New J. Chem.*, **43**, 5525 (2019); <https://doi.org/10.1039/C9NJ00288J>
- G. Singh, J. Singh, S.S. Mangat, J. Singh and S. Rani, *RSC Adv.*, **5**, 12644 (2015); <https://doi.org/10.1039/C4RA14329A>
- G. Singh, S. Rani, A. Saroa, S. Girdhar, J. Singh, A. Arora, D. Aulakh and M. Wriedt, *RSC Adv.*, **5**, 65963 (2015); <https://doi.org/10.1039/C5RA09004K>
- B. Naskar, R. Modak, Y. Sikdar, D.K. Maiti, A. Bauzá, A. Frontera, A. Katarkar, K. Chaudhuri and S. Goswami, *Sens. Actuators B Chem.*, **239**, 1194 (2017); <https://doi.org/10.1016/j.snb.2016.08.148>
- K. Boonkitpatarakul, J. Wang, N. Niamnont, B. Liu, L. McDonald, Y. Pang and M. Sukwattanasinitt, *ACS Sens.*, **1**, 144 (2016); <https://doi.org/10.1021/acssensors.5b00136>
- S. Gui, Y. Huang, F. Hu, Y. Jin, G. Zhang, L. Yan, D. Zhang and R. Zhao, *Anal. Chem.*, **87**, 1470 (2015); <https://doi.org/10.1021/ac504153c>
- E. Yildiz, S. Saçmaci, M. Saçmaci and A. Ülgen, *Food Chem.*, **237**, 942 (2017); <https://doi.org/10.1016/j.foodchem.2017.06.055>
- K.S. Ku, P. Muthukumar, S. Angupillai and Y.A. Son, *Sens. Actuators B Chem.*, **236**, 184 (2016); <https://doi.org/10.1016/j.snb.2016.05.143>
- L. Tang, S. Ding, K. Zhong, S. Hou, Y. Bian and X. Yan, *Spectrochim. Acta A*, **174**, 70 (2017); <https://doi.org/10.1016/j.saa.2016.11.026>
- Z. Li, W. Chen, L. Dong, Y. Song, R. Li, Q. Li, D. Qu, H. Zhang, Q. Yang and Y. Li, *New J. Chem.*, **44**, 3261 (2020); <https://doi.org/10.1039/C9NJ06309A>
- S. Wang, G. Men, L. Zhao, Q. Hou and S. Jiang, *Sens. Actuators B Chem.*, **145**, 826 (2010); <https://doi.org/10.1016/j.snb.2010.01.060>
- H.Y. Jeong, S.Y. Lee, J. Han, M.H. Lim and C. Kim, *Tetrahedron*, **73**, 2690 (2017); <https://doi.org/10.1016/j.tet.2017.03.069>
- Y. Xu, L. Yang, H. Wang, Y. Zhang, X. Yang, M. Pei and G. Zhang, *J. Photoch. Photobio. A*, **391**, 112372 (2020); <https://doi.org/10.1016/j.jphotochem.2020.112372>
- J.A. Edwardson, J.M. Candy, P.G. Ince, F.K. McArthur, C.M. Morris, A.E. Oakley, G.A. Taylor and E. Bjertness, *Ciba Found. Symp.*, **169**, 165 (1992).
- M. Kawahara, *J. Alzheimers Dis.*, **8**, 171 (2005); <https://doi.org/10.3233/JAD-2005-8210>
- J. Savory, M.M. Herman, C.D. Katsetos and M.R. Wills, in Eds.: M. Nicolini, P.F. Zatta and B. Corain, *Aluminum in Chemistry Biology and Medicine*, Cortina International/Raven Press: Verona, New York, p. 45 (1991).
- C. Exley, G. Mamutse, O. Korchazhkina, E. Pye, S. Strekopytov, A. Polwart and C. Hawkins, *Mult. Scler.*, **12**, 533 (2006); <https://doi.org/10.1177/1352458506071323>
- S. Mondal, A.K. Bhanja, D. Ojha, T.K. Mondal, D. Chattopadhyay and C. Sinha, *RSC Adv.*, **5**, 73626 (2015); <https://doi.org/10.1039/C5RA11548E>
- S.Y. Li, D.B. Zhang, J.Y. Wang, R.M. Lu, C.H. Zheng and S.Z. Pu, *Sens. Actuators B Chem.*, **245**, 263 (2017); <https://doi.org/10.1016/j.snb.2017.01.149>
- G. Bartwal, K. Aggarwal and J.M. Khurana, *New J. Chem.*, **42**, 2224 (2018); <https://doi.org/10.1039/C7NJ04194B>
- S.K. Sahoo, G.D. Kim and H.J. Choi, *J. Photochem. Photobiol. Chem.*, **27**, 30 (2016); <https://doi.org/10.1016/j.jphotochemrev.2016.04.004>
- Y. Dong, R. Fan, W. Chen, P. Wang and Y. Yang, *Dalton Trans.*, **46**, 6769 (2017); <https://doi.org/10.1039/C7DT00956A>
- K.P. Carter, A.M. Young and A.E. Palmer, *Chem. Rev.*, **114**, 4564 (2014); <https://doi.org/10.1021/cr400546e>
- W.N. Lipscomb and N. Sträter, *Chem. Rev.*, **96**, 2375 (1996); <https://doi.org/10.1021/cr950042j>
- A.K. Bhanja, C. Patra, S. Mondal, D. Ojha, D. Chattopadhyay and C. Sinha, *RSC Advances*, **5**, 48997 (2015); <https://doi.org/10.1039/C5RA06193H>
- K. Zhang, L. Zhang, S. Zhang, Y. Hu, Y. Zheng and W. Huang, *Inorg. Chem.*, **54**, 5295 (2015); <https://doi.org/10.1021/acs.inorgchem.5b00283>
- X. Liu and J.-R. Hamon, *Coord. Chem. Rev.*, **389**, 94 (2019); <https://doi.org/10.1016/j.ccr.2019.03.010>
- T. Simon, M. Shellaiiah, V. Srinivasadesikan, C.-C. Lin, F.-H. Ko, K.W. Sun and M.-C. Lin, *Sens. Actuators B Chem.*, **231**, 18 (2016); <https://doi.org/10.1016/j.snb.2016.02.136>
- A. Singh, R. Singh, M. Shellaiiah, E.C. Prakash, H.-C. Chang, P. Raghunath, M.-C. Lin and H.-C. Lin, *Sens. Actuators B Chem.*, **207**, 338 (2015); <https://doi.org/10.1016/j.snb.2014.09.105>

34. J. Wan, K. Zhang, C. Li, Y. Li and S. Niu, *Sens. Actuators B Chem.*, **246**, 696 (2017); <https://doi.org/10.1016/j.snb.2017.02.126>
35. M.J. Frisch, G.W. Trucks, H.B. Schlegel, G.E. Scuseria, M.A. Robb, J.R. Cheeseman, G. Scalmani, V. Barone, B. Mennucci, G.A. Petersson, H. Nakatsuji, M. Caricato, X. Li, H.P. Hratchian, A.F. Izmaylov, J. Bloino, G. Zheng, J.L. Sonnenberg, M. Hada, M. Ehara, K. Toyota, R. Fukuda, J. Hasegawa, M. Ishida, T. Nakajima, Y. Honda, O. Kitao, H. Nakai, T. Vreven, J.A. Montgomery Jr., J.E. Peralta, F. Ogliaro, M. Bearpark, J.J. Heyd, E. Brothers, K.N. Kudin, V.N. Staroverov, T. Keith, R. Kobayashi, J. Normand, K. Raghavachari, A. Rendell, J.C. Burant, S.S. Iyengar, J. Tomasi, M. Cossi, N. Rega, J.M. Millam, M. Klene, J. E. Knox, J.B. Cross, V. Bakken, C. Adamo, J. Jaramillo, R. Gomperts, R.E. Stratmann, O. Yazyev, A.J. Austin, R. Cammi, C. Pomelli, J.W. Ochterski, R.L. Martin, K. Morokuma, V.G. Zakrzewski, G.A. Voth, P. Salvador, J.J. Dannenberg, S. Dapprich, A.D. Daniels, O. Farkas, J.B. Foresman, J.V. Ortiz, J. Cioslowski and D.J. Fox, GAUSSIAN 09, revision B.01.; Gaussian Inc.: Wallingford, CT (2010).
36. Z. Wang, N. Wang, X. Han, R. Wang and J. Chang, *J. Biomol. Struct. Dyn.*, **36**, 3388 (2018); <https://doi.org/10.1080/07391102.2017.1388287>
37. Z. Li, Z. Wang, N. Wang, X. Han, W. Yu, R. Wang and J. Chang, *J. Pharm. Biomed. Anal.*, **149**, 290 (2018); <https://doi.org/10.1016/j.jpba.2017.11.007>
38. T. Ren, Z. Wang, L. Zhang, N. Wang, X. Han, R. Wang and J. Chang, *J. Fluoresc.*, **27**, 1467 (2017); <https://doi.org/10.1007/s10895-017-2086-2>
39. L. Zhang, T. Ren, X. Tian, Z. Wang, W. Yu, R. Wang and J. Chang, *J. Fluoresc.*, **27**, 369 (2017); <https://doi.org/10.1007/s10895-016-1965-2>
40. T. Mosmann, *J. Immunol. Methods*, **65**, 55 (1983); [https://doi.org/10.1016/0022-1759\(83\)90303-4](https://doi.org/10.1016/0022-1759(83)90303-4)
41. S. Antonczak, *J. Mol. Struct.*, **856**, 38 (2008); <https://doi.org/10.1016/j.theochem.2008.01.014>
42. I. Lukovits, E. K'alm'an and F. Zucchi, *Corrosion*, **57**, 3 (2001); <https://doi.org/10.5006/1.3290328>
43. E. Scrocco and J. Tomasi, *Adv. Quantum Chem.*, **11**, 115 (1978); [https://doi.org/10.1016/S0065-3276\(08\)60236-1](https://doi.org/10.1016/S0065-3276(08)60236-1)
44. V. Arjunan, P.S. Balamourougane, C.V. Mythili, S. Mohan and V. Nandhakumar, *J. Mol. Struct.*, **1006**, 247 (2011); <https://doi.org/10.1016/j.molstruc.2011.09.015>